EISSN 1305-3612

DIR

Diagnostic and Interventional Radiology

TSR 1924
TURKISH SOCIETY OF RADIOLOGY

dirjournal.org

VOLUME 29
ISSUE 5
SEPTEMBER 2023

Diagnostic and Interventional Radiology

Official Journal of the Turkish Society of Radiology

E-ISSN: 1305-3612
www.dirjournal.org

Diagnostic and Interventional Radiology

Official Journal of the Turkish Society of Radiology

E-ISSN: 1305-3612
www.dirjournal.org

Diagnostic and Interventional Radiology (Diagn Interv Radiol) is a bimonthly periodical of the Turkish Society of Radiology and the content of the journal is available at https://www.dirjournal.org/. It is peer-reviewed and adheres to the highest ethical and editorial standards. The editors of the journal endorse the Editorial Policy Statements Approved by the Council of Science Editors Board of Directors (https://cse.memberclicks.net/march-31--2000-draft-editorial-policies). The journal is in compliance with the Recommendations for the Conduct, Reporting, Editing and Publication of Scholarly Work in Medical Journals published by the International Committee of Medical Journal Editors (updated May 2022, www.icmje.org).

First ten volumes of Diagnostic and Interventional Radiology have been published in Turkish under the name of Tanısal ve Girişimsel Radyoloji (Index Medicus® abbreviation: Tani Girisim Radyol), the current title's exact Turkish translation.

Diagnostic and Interventional Radiology is indexed in **Science Citation Index Expanded, Pubmed/MEDLINE, PubMed Central, Web of Science, DOAJ, TUBITAK ULAKBIM TR Index, HINARI, EMBASE, CINAHL, Scopus, Gale** and **CNKI**.

Contact Information

Diagnostic and Interventional Radiology Turkish Society of Radiology
Hoşdere Cad., Güzelkent Sok., Çankaya Evleri, F/2, 06540
Ankara, Turkey
E-mail: info@dirjournal.org
Phone: +90 (312) 442 36 53 **Fax:** +90 (312) 442 36 54

Publisher Contact

Address: Molla Gürani Mah. Kaçamak Sk.
No: 21/1 34093 İstanbul, Turkey
Phone: +90 (530) 177 30 97
E-mail: info@galenos.com.tr/yayin@galenos.com.tr
Web: www.galenos.com.tr **Publisher Certificate Number:** 14521
Online Publication Date: September 2023
EISSN 1305-3612
International scientific journal published bimonthly.

Turkish Society of Radiology is one of the foremost medical specialty organizations in Turkey. It was formed by the merger of the two main radiology societies of Turkey, one of which was founded in 1924. The Society is based in Ankara, Turkey.

TSR 1924
TURKISH SOCIETY OF RADIOLOGY

Diagnostic and Interventional Radiology

Instructions to Authors

Diagnostic and Interventional Radiology (Diagn Interv Radiol) is a medium for disseminating scientific information based on research, clinical experience, and observations pertaining to diagnostic and interventional radiology. The journal is the double-blind peer-reviewed, bimonthly, open-access publication organ of the Turkish Society of Radiology and its publication language is English. Diagnostic and Interventional Radiology is currently indexed by Science Citation Index Expanded, PubMed MEDLINE, Web of Science, PubMed Central, DOAJ, TUBITAK ULAKBIM TR Index, HINARI, EMBASE, CINAHL, Scopus, Gale and CNKI.

The journal is a medium for original articles, reviews, pictorial essays, technical notes related to all fields of diagnostic and interventional radiology.

The editorial and publication process of the Diagnostic and Interventional Radiology are shaped in accordance with the guidelines of the International Committee of Medical Journal Editors (ICMJE), World Association of Medical Editors (WAME), Council of Science Editors (CSE), Committee on Publication Ethics (COPE), European Association of Science Editors (EASE), and National Information Standards Organization (NISO). The journal is in conformity with the Principles of Transparency and Best Practice in Scholarly Publishing.

Authorship

Each individual listed as an author should fulfill the authorship criteria recommended by the International Committee of Medical Journal Editors (ICMJE - www.icmje.org). To be listed as an author, an individual should have made substantial contributions to all four categories established by the ICMJE: (a) conception and design, or acquisition of data, or analysis and interpretation of data, (b) drafting the article or revising it critically for important intellectual content, (c) final approval of the version to be published, and (d) agreement to be accountable for all aspects of the work in ensuring that questions related to the accuracy or integrity of any part of the work are appropriately investigated and resolved. Individuals who contributed to the preparation of the manuscript but do not fulfill the authorship criteria should be acknowledged in an acknowledgements section, which should be included in the title page of the manuscript. If the editorial board suspects a case of "gift authorship", the submission will be rejected without further review.

Ethical standards

For studies involving human or animal participants, the authors should indicate whether the procedures followed were in accordance with the ethical standards of the responsible committee on human and animal experimentation (institutional or regional) and with the Helsinki Declaration. Application or approval number/year of the study should also be provided. The editorial board will act in accordance with COPE guidelines if an ethical misconduct is suspected.

It is the authors' responsibility to carefully protect the patients' anonymity and to verify that any experimental investigation with human subjects reported in the submission was performed with informed consent and following all the guidelines for experimental investigation with human subjects required by the institution(s) with which all the authors are affiliated with. For photographs that may reveal the identity of the patients, signed releases of the patient or of his/her legal representative should be enclosed.

Prospective human studies require both an ethics committee approval and informed consent by participants. Retrospective studies require an ethics committee approval with waiver of informed consent. Authors may be required to document such approval.

All submissions are screened by a similarity detection software (iThenticate by CrossCheck). Manuscripts with an overall similarity index of greater than 20%, or duplication rate at or higher than 5% with a single source are returned back to authors without further evaluation along with the similarity report.

In the event of alleged or suspected research misconduct, e.g., plagiarism, citation manipulation, and data falsification/fabrication, the Editorial Board will follow and act in accordance with COPE guidelines.

Withdrawal Policy

Articles may be withdrawn under certain circumstances.

The article will be withdrawn if it;

- violates professional ethical codes,
- is subject to a legal dispute,
- has multiple submissions,
- includes fake claims of authorship, plagiarism, misleading data, and false data that may pose a severe health risk.

The editorial board will follow the principles set by COPE (Committee on Publication Ethics) in case of an article withdrawal.

Manuscript Preparation

The manuscripts should be prepared in accordance with ICMJE-Recommendations for the Conduct, Reporting, Editing, and Publication of Scholarly Work in Medical Journals (updated in May 2022 - https://www.icmje.org/recommendations/).

Original Investigations and Reviews should be presented in accordance with the following guidelines: randomized study – CONSORT, observational study – STROBE, study on diagnostic accuracy – STARD, systematic reviews and meta-analysis PRISMA, nonrandomized behavioral and public health intervention studies – TREND.

Diagnostic and Interventional Radiology will only evaluate manuscripts submitted via the journal's self-explanatory online manuscript submission and evaluation system available at mc04.manuscriptcentral.com/dir. Evaluation process of submitted manuscripts takes 4 weeks on average.

Manuscripts are evaluated and published on the understanding that they are original contributions, and do not contain data that have been published elsewhere or are under consideration by another journal. Authors are required to make a full statement at the time of submission about all prior reports and submissions that might be considered duplicate or redundant publication, and mention any previously published abstracts for meeting presentations that contain partial or similar material in the cover letter. They must reference any similar previous publications in the manuscript.

Authors must obtain written permission from the copyright owner to reproduce previously published figures, tables, or any other material in both print and electronic formats and present it during submission. The original source should be cited within the references and below the reprinted material.

Cover letter: A cover letter must be provided with all manuscripts. This letter may be used to emphasize the importance of the study. The authors should briefly state the existing knowledge relevant to the study and the contributions their study make to the existing knowledge. The correspondent author should also include a statement in the cover letter declaring that he/she accepts to undertake all the responsibility for authorship during the submission and review stages of the manuscript.

Diagnostic and Interventional Radiology

Instructions to Authors

Title page: A separate title page should be submitted with all manuscripts and should include the title of the manuscript, name(s), affiliation(s), and major degree(s) of the author(s). The name, address, telephone (including the mobile phone number) and fax numbers and e-mail address of the corresponding author should be clearly listed. Grant information and other sources of support should also be included. Individuals who contributed to the preparation of the manuscript but do not fulfill the authorship criteria should also be acknowledged in the title page. Manuscripts should not be signed by more than 6 authors unless they are multicenter or multidisciplinary studies.

Main document

Abstract: All submissions (except for Letters to the Editor) should be accompanied by an abstract limited to 400 words. A structured abstract is only required with original articles and it should include the following subheadings: PURPOSE, METHODS, RESULTS, CONCLUSION.

Main points: Each submission should be accompanied by 3 to 5 "main points", which should emphasize the most striking results of the study and highlight the message that is intended to be conveyed to the readers. As these main points would be targeting radiology residents, experts and residents of other fields of medicine, as well as radiology experts, they should be kept as plain and simple as possible. These points should be constructed in a way that provides the readers with a general overview of the article and enables them to have a general idea about the article.

The main points should be listed at the end of the main text, above the reference list.

Example: Liu S, Xu X, Cheng Q, et al. Simple quantitative measurement based on DWI to objectively judge DWI-FLAIR mismatch in a canine stroke model. Diagn Interv Radiol 2015;(4)21:348–354.

• The relative diffusion-weighted imaging signal intensity (rDWI) of ischemic lesions might be helpful to identify the status of fluid attenuated inversion recovery (FLAIR) imaging in acute ischemic stroke.

• The relative apparent diffusion coefficient (rADC) value appears not useful to identify the status of FLAIR imaging in the acute period.

• Based on our embolic canine model, rDWI increased gradually in the acute period, while the rADC kept stable, which might explain why rDWI is helpful to identify the status of FLAIR imaging, while rADC is not.

Main text

Original Articles

Original articles should provide new information based on original research. The main text should be structured with Introduction, Methods, Results, and Discussion subheadings. The number of cited references should not exceed 50 and the main text should be limited to 4500 words. Number of tables included in an original article should be limited to 4 and the number of figures should be limited to 7 (or a total of 15 figure parts).

Introduction

State briefly the nature and purpose of the work, quoting the relevant literature.

Methods

Include the details of clinical and technical procedures.

Research ethics standards compliance

All manuscripts dealing with human subjects must contain a statement indicating that the study was approved by the Institutional Review Board or a comparable formal research ethics review committee. If none is present at your institution, there should be a statement that the research was performed according to the Declaration of Helsinki principles (www.wma.net/e/policy/b3.htm). There should also be a statement about whether informed consent was obtained from research subjects.

Results

Present these clearly, concisely, and without comment. Statistical analysis results should also be provided in this section to support conclusions when available.

Discussion

Explain your results and relate them to those of other authors; define their significance for clinical practice. Limitations, drawbacks, or shortcomings of the study should also be stated in the discussion section before the conclusion paragraph. In the last paragraph, a strong conclusion should be written.

Review Articles

Review articles are scientific analyses of recent developments on a specific topic as reported in the literature. No new information is described, and no opinions or personal experiences are expressed. Reviews include only the highlights on a subject. Main text should be limited to 4000 words and the number of cited references should not exceed 75. Number of tables included in a review article should be limited to 4 and the number of figures should be limited to 15 (or a total of 30 figure parts).

Pictorial Essay

This is a continuing medical education exercise with the teaching message in the figures and their legends. Text should include a brief abstract; there may be as many as 30 figure parts. No new information is included. The value of the paper turns on the quality of the illustrations. Authors can submit dynamic images (e.g. video files) or include supplemental image files for online presentation that further illustrate the educational purpose of the essay. Maximums: Pages of text – 4 (1,500 words); References – 20; Figures – 15 or total of 30 images; No table Main text should be limited to 1500 words and the number of cited references should not exceed 15.

Technical Notes

Technical note is a brief description of a specific technique, procedure, modification of a technique, or new equipment of interest to radiologists. It should include a brief introduction followed by Technique section for case reports or Methods section for case series, and Discussion is limited to the specific message, including the uses of the technique, equipment, or software. Literature reviews and lengthy descriptions of cases are not appropriate.

Main text should be limited to 1500 words and the number of cited references should not exceed 8. Number of tables included in a technical note should be limited to 4 and the number of figures should be limited to 3 (or a total of 6 figure parts).

Diagnostic and Interventional Radiology

Instructions to Authors

Letter to the Editor and Reply

Letters to the Editor and Replies should offer objective and constructive criticism of published articles within last 6 months. Letters may also discuss matters of general interest to radiologists and may include images. Material being submitted or published elsewhere should not be duplicated in letters.

Main text should be limited to 500 words and the number of cited references should not exceed 6. No tables should be included and the number of figures should be limited to 2 (or a total of 4 figure parts).

Recommendations for Manuscripts:

Type of manuscript	Word limit	Abstract word limit	Reference limit	Author limit	Table limit	Figure limit
Original Article	4500	400 (Structured)	50	6*	4	7 or total of 15 images
Review Article	4000	200	75	5	4	15 or total of 24 images
Pictorial Essay	1500	400	20	5	1	15 figures or total of 30 figure parts
Technical Note	1500	200	8	5	2	3 figures or total of 6 figure parts
Letter	500	N/A	6	4	No tables	2 figures or total of 4 figure parts

*Manuscripts should not be signed by more than 6 authors unless they are multicenter or multidisciplinary studies.
**Considering the specific condition of the manuscript, minor flexibilites may be applied for the recommendations upon the decision of Editor-in-Chief or the Section Editors.

References

Both in-text citations and the references must be prepared according to the AMA Manual of style.

While citing publications, preference should be given to the latest, most up-to-date publications. Authors are responsible for the accuracy of references If an ahead-of-print publication is cited, the DOI number should be provided. Journal titles should be abbreviated in accordance with the journal abbreviations in Index Medicus/MEDLINE/PubMed. When there are six or fewer authors, all authors should be listed. If there are seven or more authors, the first three authors should be listed followed by "et al." In the main text of the manuscript, references should be cited in superscript after punctuation. The reference styles for different types of publications are presented in the following examples.

Journal Article: Economopoulos KJ, Brockmeier SF. Rotator cuff tears in overhead athletes. Clin Sports Med. 2012;31(4):675-692.

Book Section: Fikremariam D, Serafini M. Multidisciplinary approach to pain management. In: Vadivelu N, Urman RD, Hines RL, eds. Essentials of Pain Management. New York, NY: Springer New York; 2011:17-28.

Books with a Single Author: Patterson JW. Weedon's Skin Pahology. 4th ed. Churchill Livingstone; 2016.

Editor(s) as Author: Etzel RA, Balk SJ, eds. Pediatric Environmental Health. American Academy of Pediatrics; 2011.

Conference Proceedings: Morales M, Zhou X. Health practices of immigrant women: indigenous knowledge in an urban environment. Paper presented at: 78th Association for Information Science and Technology Annual Meeting; November 6-10; 2015; St Louis, MO. Accessed March 15, 2016. https://www.asist.org/files/meetings/am15/proceedings/openpage15.html

Thesis: Maiti N. Association Between Behaviours, Health Charactetistics and Injuries Among Adolescents in the United States. Dissertation. Palo Alto University; 2010.

Online Journal Articles: Tamburini S, Shen N, Chih Wu H, Clemente KC. The microbiome in early life: implications for health outcometes. Nat Med. Published online July 7, 2016. doi:10.1038/nm4142

Epub Ahead of Print Articles: Websites: International Society for Infectious Diseases. ProMed-mail. Accessed February 10, 2016. http://www.promedmail.org

Tables

Tables should be included in the main document and should be presented after the reference list. Tables should be numbered consecutively in the order they are referred to within the main text. A descriptive title should be provided for all tables and the titles should be placed above the tables. Abbreviations used in the tables should be defined below by footnotes (even if they are defined within the main text). Tables should be created using the "insert table" command of the word processing software and they should be arranged clearly to provide an easy reading. Data presented in the tables should not be a repetition of the data presented within the main text but should be supporting the main text.

Figures and figure legends

Figures, graphics, and photographs should be submitted as separate files (in TIFF or JPEG format) through the submission system. The files should not be embedded in a Word document or the main document. When there are figure subunits, the subunits should not be merged to form a single image. Each subunit should be submitted separately through the submission system. Images should not be labelled (a, b, c, etc.) to indicate figure subunits. Thick and thin arrows, arrowheads, stars, asterisks, abbreviations and similar marks can be used on the images to support figure legends. Like the rest of the submission, the figures too should be blind. Any information within the images that may indicate the institution or the patient should be removed.

Figure legends should be listed at the end of the main document.

General

All acronyms and abbreviations used in the manuscript should be defined at first use, both in the abstract and in the main text. The abbreviation should be provided in parenthesis following the definition.

Statistical analysis should be performed in accordance with guidelines on reporting statistics in medical journals (Altman DG, Gore SM, Gardner MJ, Pocock SJ. Statistical guidelines for contributors to medical journals. Br Med J 1983: 7; 1489–1493.). Information on the statistical analysis process of the study should be provided within the main text.

When a drug, product, hardware, or software mentioned within the main text product information, the name and producer of the product should be provided in parenthesis in the following format: "Discovery St PET/CT scanner (GE Healthcare)."

All references, tables, and figures should be referred to within the main text and they should be numbered consecutively in the order they are referred to within the main text.

Initial evaluation and peer review process

Manuscripts submitted to Diagnostic and Interventional Radiology will first go through a technical evaluation process where the editorial office staff will ensure that the manuscript is prepared and submitted in accordance with the journal's guidelines. Submissions that do not conform the journal's guidelines will be returned to the submitting author with technical correction requests.

All submissions are screened by a similarity detection software (iThenticate by CrossCheck), and those with an overall similarity index of greater than 20%, or duplication rate at or higher than 5% with a single source are returned back to authors without further evaluation along with the similarity report.

Manuscripts meeting the requirements mentioned in journal's guideline will go under the review process. The initial review will be performed by Editor-in-Chief and the Section Editor, which include the evaluation of the manuscript for its originality, importance of the findings, scientific merit, interest to readers and compliance with the policy of the journal in force. Manuscripts with insufficient priority for publication are not sent out for further review and rejected promptly at this level to allow the authors to submit their work elsewhere without delay.

Manuscripts that pass through the initial review are sent to peer review, which is performed in a blinded manner by least two external and independent reviewers. During the review process, all original articles are evaluated by at least one senior consultant of statistics for proper handling and consistency of data, and use of correct statistical method. The Section Editor and / or Editor-in-Chief are the final authority in the decision-making process for all submissions.

Revisions

When submitting a revised version of a paper, the author must submit a detailed "Response to reviewers" that states point by point how each issue raised by the reviewers has been covered and where it can be found (each reviewer's comment followed by the author's reply and line numbers where the changes have been made) as well as an annotated copy, and a clear copy of the main document.

Revised manuscripts must be submitted within 30 days from the date of the decision letter. If the revised version of the manuscript is not submitted within the allocated time, the revision option will be automatically cancelled by the submission system. If the submitting author(s) believe that additional time is required, they should request an extension before the initial 30-day period is over.

Proofs and DOI Number

Accepted manuscripts are copy-edited for grammar, punctuation, and format by professional language editors. Following the copyediting process, the authors will be asked to review and approve the changes made during the process. Authors will be contacted for a second time after the layout process and will be asked to review and approve the PDF proof of their article for publication. Once the production process of a manuscript is completed it is published online on the journal's webpage as an ahead-of-print publication before it is included in its scheduled issue.

Publication Fee Policy

Diagnostic and Interventional Radiology (DIR) applies an Article Processing Charge (APCs) for only accepted articles. No fees are requested from the authors during submission and evaluation process. All manuscripts must be submitted via Manuscript Manager.

An APC fee of and local taxes will be applied depending on the article type (see Table 1)

Review	$ 1250
Original Article	$ 1000
Pictorial Essay	$ 750
Technical Note	

Table 1. Article Types and Fees

The APCs will be accepted through the link that will be sent to the corresponding author of each article via the online article system. In the next step, the authors will be receiving a receipt of their payment.

*Please note that the Article Processing Charge (APC) will not affect neither the editorial and peer-review process nor the priority of the manuscripts by no means. All submissions will be evaluated by the Editorial Board and the external reviewers in terms of scientific quality and ethical standards.

Refund Policy:

Returning the article to the author; Diagnostic and Interventional Radiology (DIR) will refund the submission fees with a coupon code if the article is returned to the author. Using this code, authors can use the submission fees of different articles without making a new payment.

Article Retraction:

Infringements of publication/research ethics, such as multiple submissions, bogus claims of authorship, plagiarism, and fraudulent use of data could lead to article retraction.

A retraction statement titled "Retraction: [article title]" must be signed by the authors and/or the editor. The original article is marked as retracted but a PDF version remains available to readers, and the retraction statement is linked to the original published paper.

Diagnostic and Interventional Radiology

Volume 29 • Issue 5

September 2023

www.dirjournal.org

Contents

Full text of these articles can be accessed online at www.dirjournal.org or through PubMed (https://www.ncbi.nlm.nih.gov/pmc/journals/2754/).

Diagn Interv Radiol 2023; DOI: 10.4274/dir.2023.232186

ABDOMINAL IMAGING

ORIGINAL ARTICLE

Can the Gleason score be predicted in patients with prostate cancer? A dynamic contrast-enhanced MRI, $^{(68)}$Ga-PSMA PET/CT, PSA, and PSA-density comparison study

Hüseyin Akkaya
Okan Dilek
Selim Özdemir
Zeynel Abidin Taş
İhsan Sabri Öztürk
Bozkurt Gülek

PURPOSE

The present study aims to evaluate whether perfusion parameters in prostate magnetic resonance imaging (MRI), $^{(68)}$Ga-prostate-specific membrane antigen (PSMA) positron emission tomography (PET)/computed tomography (CT), prostate-specific antigen (PSA), and PSA density can be used to predict the lesion grade in patients with prostate cancer (PCa).

METHODS

The study included a total of 137 PCa cases in which 12-quadrant transrectal ultrasound-guided prostate biopsy (TRUSBx) was performed, the Gleason score (GS) was determined, and pre-biopsy multiparametric prostate MRI and $^{(68)}$Ga-PSMA PET/CT examinations were undertaken. The patient population was evaluated in three groups according to the GS: (1) low risk; (2) intermediate risk; (3) high risk. The PSA, PSA density, pre-TRUSBx $^{(68)}$Ga-PSMA PET/CT maximum standardized uptake value (SUV_{max}), perfusion MRI parameters [maximum enhancement, maximum relative enhancement, T0 (s), time to peak (s), wash-in rate (s^{-1}), and wash-out rate (s^{-1})] were retrospectively evaluated.

RESULTS

There was no significant difference between the three groups in relation to the PSA, PSA density, and $^{(68)}$Ga-PSMA PET/CT SUV_{max} ($P > 0.05$). However, the values of maximum enhancement, maximum relative enhancement (%), T0 (s), time to peak (s), wash-in rate (s^{-1}), and wash-out rate (s^{-1}) significantly differed among the groups. A moderate positive correlation was found among the prostate volume, PSA (r = 0.490), and $^{(68)}$Ga-PSMA SUV_{max} (r = 0.322) in the patients. The wash-out rate (s^{-1}) and wash-in rate (s^{-1}) had the best diagnostic test performance (area under the curve: 89.1% and 78.4%, respectively).

CONCLUSION

No significant correlation was found between the $^{(68)}$Ga-PSMA PET/CT SUV_{max} and the GS. The wash-out rate was more successful in estimating the pretreatment GS than the $^{(68)}$Ga-PSMA PET/CT SUV_{max}.

KEYWORDS

$^{(68)}$Ga-PSMA PET/CT, prostate perfusion MRI, wash-out rate, wash-in rate, PSA, PSA density

From the Clinic of Radiology (H.A. ✉ dr.hsynakkaya@gmail.com, O.D., S.Ö., B.G.), University of Health Sciences Turkey, Adana City Training and Research Hospital, Adana, Turkey; Clinic of Pathology (Z.A.T.), University of Health Sciences Turkey, Adana City Training and Research Hospital, Adana, Turkey; Clinic of Nuclear Medicine (İ.S.Ö.), University of Health Sciences Turkey, Adana City Training and Research Hospital, Adana, Turkey.

Received 07 March 2023; revision requested 09 April 2023; last revision received 17 May 2023; accepted 22 May 2023.

Epub: 03.07.2023

Publication date: 05.09.2023

DOI: 10.4274/dir.2023.232186

The prostate-specific antigen (PSA) and digital rectal examination are the most commonly used parameters in the early diagnosis and screening of prostate cancer (PCa).[1,2] The Gleason score (GS) is globally the most widely used and accepted pathology staging criterion in determining the prostate adenocarcinoma tumor grade. This score is also associated with the prognosis of PCa.[3,4]

The Prostate Imaging–Reporting and Data System (PI-RADS) version 2.1 is based on the contrast enhancement of lesions, diffusion-weighted imaging (DWI) findings, and T2-weighted signal characteristics.[5,6] Dynamic contrast-enhanced (DCE)-magnetic resonance imaging

You may cite this article as: Akkaya H, Dilek O, Özdemir S, Taş ZA, Öztürk İS, Gülek B. Can the Gleason score be predicted in patients with prostate cancer? A dynamic contrast-enhanced MRI, $^{(68)}$Ga-PSMA PET/CT, PSA, and PSA-density comparison study. *Diagn Interv Radiol*. 2023;29(5):647-655.

(MRI) is a technique used to measure perfusion, blood flow, and tissue vascularity by examining the signal generation curve of the tissue.[7] Quantitative DCE-MRI (as seen in the Tofts model),[8] assumes two chambers representing the extravascular extracellular space and blood plasma in the examined tissue to provide absolute and, therefore, more objective values for perfusion. Semi-quantitative parameters that can be obtained using DCE-MRI can be derived from the signal intensity curve and subsequently calculated.[9,10] These parameters are the maximum enhancement, maximum relative enhancement, T0 (s), time to peak (s), wash-in rate (s^{-1}), and wash-out rate (s^{-1}).[9,11]

Molecular PCa imaging is a useful tool for systematic evaluation in tumor biology.[11] In their study, Demirci et al.[12] showed (1) a correlation between the $^{(68)}$Ga-prostate-specific membrane antigen (PSMA) maximum standardized uptake value (SUV_{max}) and the tumor grade, and (2) that intraprostatic accumulation sites may be capable of predicting clinically significant cancer, giving it the potential to serve as a target for biopsy sampling together with multi-parametric MRI (mpMRI) in selected patients. Kwan et al.[13] retrospectively compared the final pathology results of radical prostatectomy (RP) cases with positron emission tomography (PET)/computed tomography (CT) results. According to the results obtained in the study, the International Society of Urological Pathology (ISUP) grade group from the final RP was predicted using the SUV_{max}; this was also true to a lesser extent in PSA and the maximal dimension of PET-avid lesions. The SUV_{max} monotonically increased in the ISUP grade group.[13] In their retrospective study, Donato et al.[14] showed that $^{(68)}$Ga-PSMA PET/CT was successful in predicting the cancer grade after MRI and prostate biopsy.

Main points

- A moderate positive correlation was found between the prostate volume and $^{(68)}$Ga-prostate-specific membrane antigen (PSMA) maximum standardized uptake value (SUV_{max}) values.
- Prostate-specific antigen and $^{(68)}$Ga-PSMA SUV_{max} values were affected by prostate volume.
- Semi-quantitative dynamic contrast-enhanced (DCE)-magnetic resonance imaging (MRI) data were successful in predicting the extent of intraprostatic tumor lesions.
- The most valuable parameter in predicting Gleason grade among the DCE-MRI parameters was the wash-out rate, followed by the wash-in rate.

The present study aimed to investigate the performance of the PSA, PSA density, $^{(68)}$Ga-PSMA PET/CT, and perfusion MRI values as the most commonly used PCa diagnostic methods in cancer grade prediction.

Methods

Patient selection and study design

The present study was conducted in full accordance with the guidelines of the Declaration of Helsinki, revised in 2000 in Edinburgh. Approvals for the study were obtained from the Ethics Committee of University of Health Sciences Turkey, Adana City Training and Research Hospital and the Turkish Ministry of Health (2022/2115). The requirement for informed consent from the patients was waived due to the retrospective nature of the study.

In this study, a total of 207 patients with PI-RADS 4–5 lesions detected using prostate mpMRI examinations, performed between January 2018 and August 2022, were identified. Transrectal ultrasonography-guided 12-quadrant prostate biopsy (TRUSBx) was performed by urologists and interventional radiologists, and GSs were determined. Patients who underwent prostate mpMRI, $^{(68)}$Ga-PSMA PET/CT, and serum PSA examinations before biopsy were included in the study. First, PI-RADS categorization was performed for all patients included in the study; next, quantitative perfusion measurements from DCE-MRI sections of PI-RADS 4–5 lesions were made (Table 1).

The inclusion criterion was as follows: patients with a GS of ≥6 without extracapsular extension.

The exclusion criteria were as follows: (1) Patients without $^{(68)}$Ga-PSMA PET/CT or PSA examinations; (2) patients with a history of prostate surgery or pelvic radiotherapy; (3) patients with insufficient pathology result material; (4) patients without non-adenocarcinoma according to the pathology report; (5) patients with poor MRI quality; (6) patients with suspected extra-prostatic extension in mpMRI; (7) patients with unavailable biopsy results; (8) patients without pre-biopsy mpMRI (Figure 1).

A total of 137 patients met the study criteria and were eligible for evaluation.

Due to the older age of the patients and the low urooncology cooperative group performance, there were few cases of RP. Therefore, transrectal ultrasound-guided prostate biopsy results were included in the study instead of RP diagnoses.

The PSA density was obtained by dividing the PSA value by the prostate volume. In the calculation of prostate volume, the following formulas were applied: (1) ellipsoid volume = length × width × height × $\pi/6$, and (2) bullet (cylinder + half ellipsoid) volume = length × width × height × $5\pi/24$.[15,16] Depending on the shape of the lesion measured, either an ellipsoid or bullet volume measurement method was used.

The grading guidelines for PCa were issued by the ISUP, based on a consensus conference held in 2014.[17] Prostate grading was divided into five separate groups. However, in some oncology studies, certain subgroups were combined and examined as three groups according to tumor aggressiveness

Table 1. Median (min–max) values of the parameters evaluated in the study

	Median (min–max)
Age	69 (53–90)
$^{(68)}$Ga-PSMA SUV_{max}	6.72 (2.12–35.42)
PSA (μg/L)	7.71 (0.79–36.22)
PSA density (ng/mL^2)	0.17 (0.01–0.55)
Prostate volume (cm^3)	44 (14–124)
Maximum enhancement	987.32 (145.81–2646.77)
Maximum relative enhancement (%)	114.04 (48.72–211.54)
T0 (s)	30.25 (16.32–48.21)
Time to peak (s)	51.33 (24.19–234.9)
Wash-in rate (s^{-1})	9.18 (2.94–92.55)
Wash-out rate (s^{-1})	5.12 (0.15–31.26)
Gleason score (radical prostatectomy)	3 (1–7)
Gleason score (biopsy)	2 (1–7)

min, minimum; max, maximum; PSMA, prostate-specific membrane antigen; SUV_{max}, maximum standardized uptake value; PSA, prostate-specific antigen.

and recurrency risk.[4,6,9,13] In the present study, the number of patients in the three groups was determined according to the GSs to achieve homogeny: (1) GS: 3 + 3, low/very low risk (group 1); (2) GS: 3 + 4 or 4 + 3, intermediate risk (group 2); (3) GS: 8–10 high/very high risk (group 3) (Table 2).

MRI acquisition

Imaging was performed using a 3-Tesla scanner (Ingenuity; Philips Healthcare, the Netherlands) with a body-parallel array coil (SENSE Torso/cardiac coil; USA Instruments, Gainesville, FL, USA). The MRI sequences comprised essential T2-weighted images in three planes and DWIs. For contrast enhancement, 0.1 mmol/kg of gadobutrol (Gadovist, Bayer Schering Pharmaceuticals, Mississauga, Canada) was injected through the antecubital vein at a rate of 3.0 mL/s, followed by 30 mL normal saline flushing at the same injection rate. The acquisition parameters of the MRI protocols are provided in Table 3.

Acquisition of $^{(68)}$Ga-PSMA PET/CT

After the preparation and quality control of the radiotracer, all the patients received 113–384 MBq (mean: 215.3 ± 67.2 MBq, <2 nmol PSMA ligand) of $^{(68)}$Ga-PSMA-11 according to the yield of radiolabeling. Whole-body images were captured with a radiotracer using a PET/CT scanner (Ingenuity; Philips Healthcare, the Netherlands) at 40–60 minutes after injection. The patients were placed on the scanner table in a supine position, and a CT transmission scan without intravenous contrast enhancement was acquired using a low tube current (130 kVp, 48–76 mAs), 4.0 mm slice thickness, 0.6 s gantry rotation, and 6 × 3 mm collimator width. Then, PET emission scanning was performed for 3 min per bed position, with the identical transverse

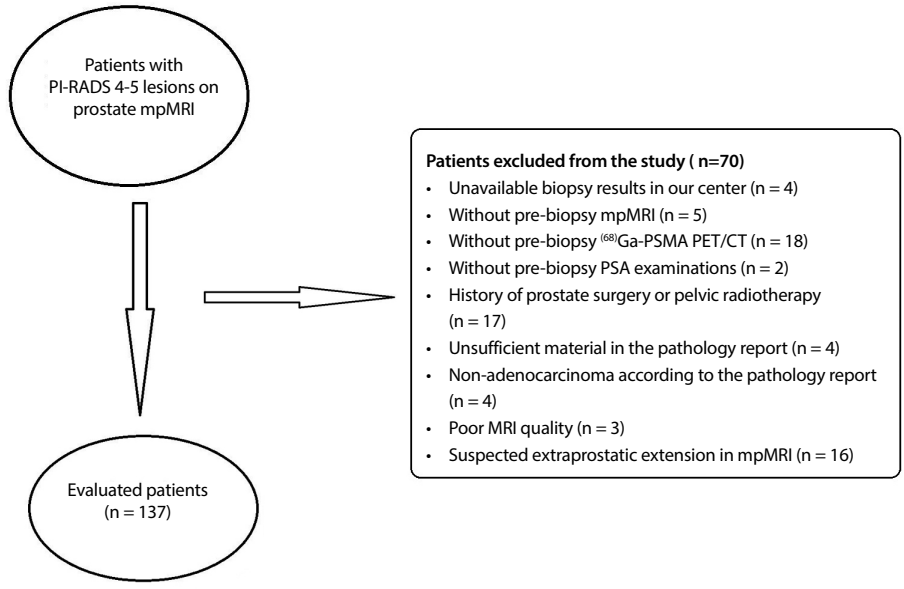

Figure 1. The initial overall number of patients, together with the number of patients included in the study, is demonstrated. The number of patients excluded from the study and exclusion criteria of the study are shown. mpMRI, multi-parametric magnetic resonance imaging; PSMA, prostate-specific membrane antigen; PET, positron emission tomography; CT, computed tomography; PI-RADS, Prostate Imaging–Reporting and Data System.

Table 2. Distribution of patients according to the Gleason score

	Frequency (n)	Percentage (%)
Group		
Gleason score, low risk	36	26.28
Gleason score, intermediate risk	50	36.50
Gleason score, high risk	51	37.22
Gleason score		
3 + 3	36	26.28
3 + 4	36	26.28
4 + 3	14	10.21
4 + 4	25	18.25
4 + 5	17	12.41
5 + 4	5	3.65
5 + 5	4	2.92

Table 3. Multiparametric examination protocol

Parameter	T2-weighted axial/coronal/sagittal	DWI axial	Pre-contrast T1 FFE axial	Dynamic contrast-enhanced T1 FFE axial	Post-contrast T1 SPIR axial
TR (msec)	3.500/3.600/4.300	4.3	10.0	5.5	524.3
TE (msec)	100/110/110	86	1.6	1.2	9.0
Slice thickness (mm)	3	3	4	4	3
Interslice gap (mm)	0.3	0.3	0	0	0
Matrix size	316 × 272/308 × 272/316 × 255 (respectively)	120 × 118	216 × 166	216 × 166	308 × 266
Flip angle (degree)	–	–	5/15	10	–
FOV (mm × mm)	220 × 220	180 × 180	300 × 300	300 × 300	220 × 220
b values (s/mm^2)	–	0, 600,1500	–	–	–
Number of slices	30/30/26	30	24	39	30
Acquisition time (minute/second)	2 min 15 sec/2 min 24 sec/2 min 25 sec	7 min 9 sec	10 sec/11 sec	4 min 13 sec	2 min 26 sec

DWI, diffusion-weighted imaging; SPIR, spectral pre-saturation with inversion recovery; FFE, fast-field echo; TR, repetition time; TE, echo time; FOV, field of view.

field of view in the caudocranial direction. The visual analysis included four-point certainty scoring (definitely negative, equivocal: probably negative, equivocal: probably positive, and definitely positive), as well as the evaluation of the anatomic site and lesion size. Semi-quantitative analysis was undertaken using the SUV_{max}. Due to the retrospective nature of the study, SUV_{max} measurements were retrospectively reproduced by the nuclear medicine specialist included in the study; the specialist who performed the measurements was blinded to all remaining information.

MRI evaluation

Lesions included in the study were primarily evaluated in DWI and T2-weighted MRI sequences according to the PI-RADS version 2.1 guidelines, and semiquantitative measurements were obtained from the perfusion sequence of the lesions with PI-RADS 4–5 scores (Figures 2, 3). The images were confirmed by the $^{(68)}$Ga-PSMA PET/CT examination. There were mismatches between the two tests of 11 patients; these patients were excluded from the study.

For the measurements, all the images obtained from the software were used. Regions of interest (ROIs) were defined as areas with an abnormal signal on MRI images and were manually drawn. The ROIs were inputted using the oval-shaped function. Using these ROIs, the time-intensity curve and time-to-peak values were automatically generated. These images were evaluated on a workstation (Intelli Space Philips, the Netherlands). The following perfusion parameters were evaluated: (1) maximum enhancement; (2) maximum relative enhancement; (3) T0 (s); (4) time to peak (s); (5) wash-in rate (s^{-1}); (6) wash-out rate (s^{-1}). Maximum relative enhancement was obtained as follows: maximum signal difference (MSD)/signal baseline (SB), where MSD is the difference between the signal intensity at its maximum and SB (Figures 2, 3). The T0 (s) was calculated as the time elapsed until the contrast agent appeared on the vessel wall. Semi-quantitative DCE-MRI was exploited to achieve the parameters of maximal enhancement, maximal relative enhancement, T0, time to peak, wash-in rate, wash-out rate, brevity of enhancement, and area under the curve (AUC). The T0 was defined as the baseline duration of the curve (sec). The time to peak (s) was defined as the time elapsed between the arterial peak enhancement and the end of the steepest portion of enhancement; the wash-in rate was determined as the maximum slope between the time of onset of contrast inflow and the time of peak intensity, and the wash-out rate was determined as the fitted line slope between the start of the wash-out and the end of the measurement. Maximum enhancement was defined as the difference between the maximum signal intensity of a pixel over all dynamics and the signal intensity of the same pixel in the reference dynamic. The relative maximum enhancement was defined as the maximum signal intensity of a pixel over all dynamics relative to the same pixel in the reference dynamic: 0% indicated the same signal intensity as the reference dynamic (%).

Statistical analysis

The data were analyzed using SPSS Statistics version 25.0 (IBM Inc. Armonk, NY, USA). Categorical measurements were summarized as numbers and percentages and continuous measurements as a median (min–max) where necessary. The Shapiro–Wilk test was used to determine whether the parameters in the study showed normal distribution, the Dunn–Bonferroni test was used to determine the source of the difference among the groups, and the Kruskal–Wallis test was used in the analysis of more than two groups of parameters that did not show normal distribution.

Fleiss' kappa (κ) was used to evaluate the agreement between TRUSBx and RP:

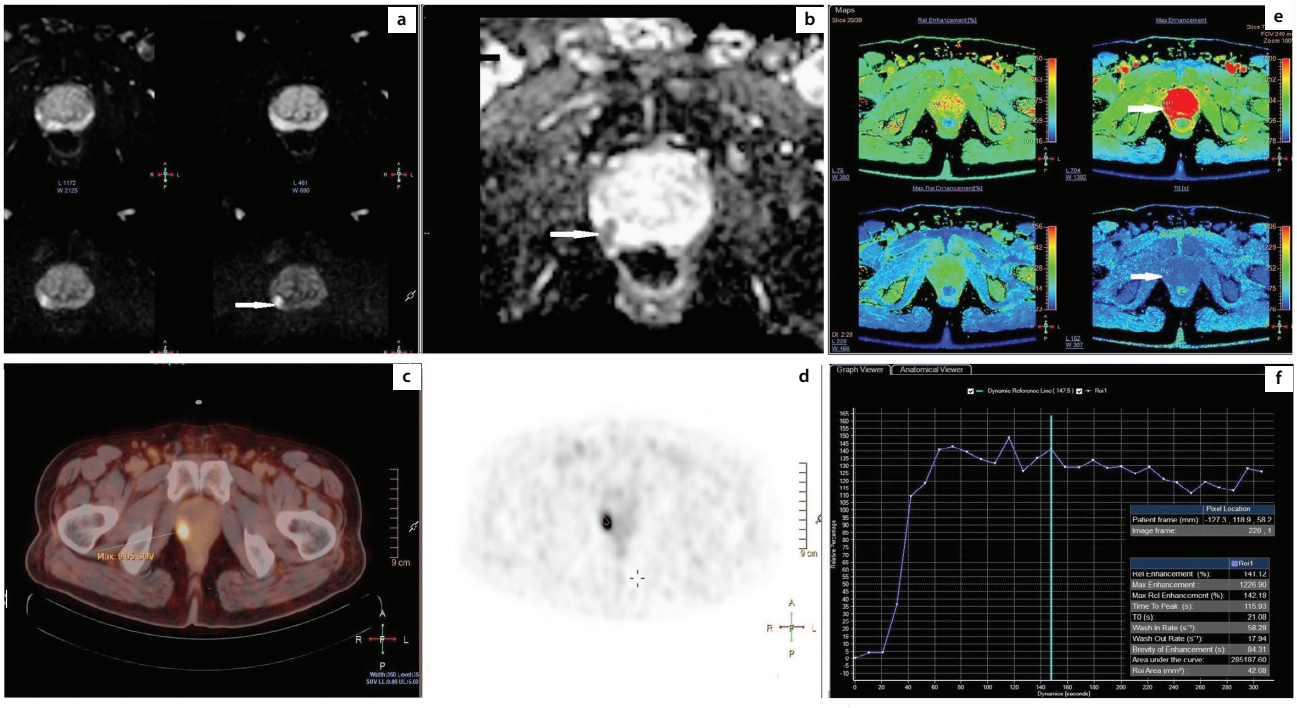

Figure 2. Peripheral zone with a PI-RADS 4 lesion, Gleason score 4 + 5, PSA: 5.72 µg/L, PSA-D: 0.23 ng/mL^2. **(a)** DWI (b = 0,600,1500 s/mm^2) shows a marked hyperintense signal (arrow) above the background. **(b)** Apparent diffusion coefficient map reveals decreased signal intensity (arrow) in the lesion. **(c, d)** $^{(68)}$Ga-PSMA-11 PET/CT images show avid uptake of radiotracer, with a SUV_{max} of 9.95. **(e, f)** DCE-MRI time-intensity curve demonstrates a decline after initial up-slope enhancement. TTP: 115.93 s^{-1}; wash-in rate; 58.28 s^{-1}, wash-out rate; 17.94 s^{-1}. PI-RADS, Prostate Imaging–Reporting and Data System; PSA, prostate-specific antigen; DWI, diffusion-weighted imaging; PSMA, prostate-specific membrane antigen; PET, positron emission tomography; CT, computed tomography; SUV_{max}, maximum standardized uptake value; DCE, dynamic contrast-enhanced; MRI, magnetic resonance imaging.

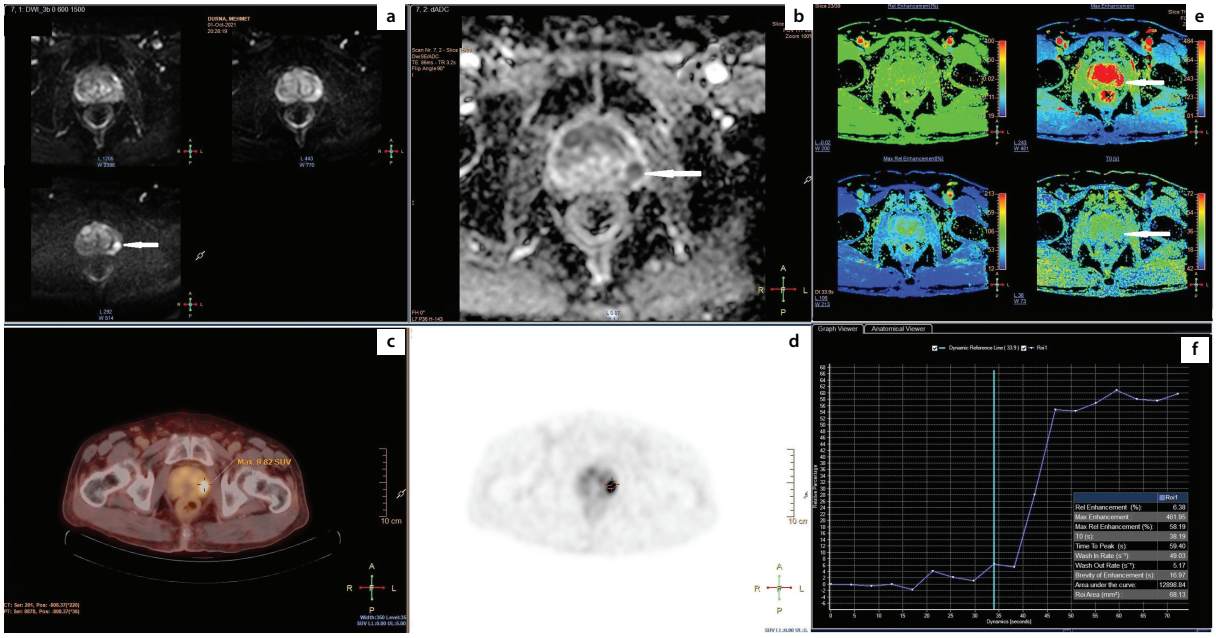

Figure 3. Peripheral zone with a PI-RADS 5 lesion, Gleason score 3 + 3, PSA: 6.84 µg/L, PSA-D: 0.21 ng/mL^2 **(a)** DWI (b = 0,600,1500 s/mm^2) shows a marked hyperintense signal (arrow) above the background. **(b)** Apparent diffusion coefficient map reveals decreased signal intensity (arrow) in the lesion. **(c, d)** $^{(68)}$Ga-PSMA-11 PET/CT images show avid uptake of radiotracer, with SUV_{max} of 9.82. **(e, f)** DCE-MRI time-intensity curve demonstrates a decline after initial up-slope enhancement. TTP: 59.4 s^{-1} ; wash in rate; 49.03 s^{-1}, wash out rate; 5.17 s^{-1}. PI-RADS, Prostate Imaging–Reporting and Data System; PSA, prostate-specific antigen; DWI, diffusion-weighted imaging; PSMA, prostate-specific membrane antigen; PET, positron emission tomography; CT, computed tomography; SUV_{max}, maximum standardized uptake value; DCE, dynamic contrast-enhanced; MRI, magnetic resonance imaging.

(1) 0.01–0.20, non-significant; (2) 0.21–0.40, weak; (3) 0.41–0.60, moderate; (4) 0.61–0.80, good; (5) 0.81–1.00, very good.[18]

The sensitivity and specificity values of the prostate volume (cm^3), maximum enhancement, maximum relative enhancement (%), T0 (s), time to peak (s), wash-in rate (s^{-1}), and wash-out rate were calculated according to the GS variable, and the cut-off values of these parameters were determined by examining the receiver operating characteristic (ROC) AUC. A ROC analysis was performed to differentiate between patients with a GS of 6 and two groups with a score of ≥7. The cut-off value was calculated according to these two groups using Youden's index. The Spearman correlation coefficient was used to determine the relationship between continuous measurements. Statistical significance was defined as $P < 0.050$.

Results

There was no significant difference among the three groups in terms of age, PSA, PSA density, and $^{(68)}$Ga-PSMA SUV_{max} values ($P > 0.05$) (Table 4); however, there were significant differences in the maximum enhancement, maximum relative enhancement (%), T0 (s), time to peak (s), wash-in rate (s^{-1}), and wash-out rate (s^{-1}) values among the groups. When the differences among the groups were further examined using the Dunn–Bonferroni test, it was observed that the patients in group 3 had a higher prostate volume (cm^3) than those in group 1. The time to peak (s) parameter had a lower mean value in group 3 compared with groups 1 and 2 ($P < 0.05$). It was observed that the patients in group 3 had higher maximum enhancement, maximum relative enhancement (%), wash-in rate (s^{-1}), and wash-out rate (s^{-1}) values than those in group 1 and group 2. The T0 (s) value was higher in group 1 than in groups 2 and 3. No significant difference was observed among the groups concerning the remaining parameters shown in Table 4 ($P > 0.05$).

The prostate volume had a moderate positive correlation with the PSA (r = 0.490) and $^{(68)}$Ga-PSMA SUV_{max} (r = 0.322) values and a weak negative correlation with PSA density (ng/mL^2) (r = –0.251) ($P < 0.001$, $P < 0.001$, and $P = 0.003$, respectively) (Table 5).

The AUC values of maximum enhancement, maximum relative enhancement (%), T0 (s), time to peak (s), wash-in rate (s^{-1}), and wash-out rate (s^{-1}), evaluated according to the GS variable, were determined as 65.3%, 65.8%, 71.9%, 72.1%, 78.4%, and 89.1%, respectively, at their optimal cut-off values. Accordingly, the wash-out rate (s^{-1}) had the best diagnostic test performance (Table 6).

The diagnostic test performances of the time to peak (s), wash-in rate (s^{-1}), and wash-out rate (s^{-1}) values, which had high AUC values, are examined in Table 7. Accordingly, it was determined that the value of the wash-out rate (s^{-1}) was stronger in predicting diagnostic test performance than the wash-in rate (s^{-1}) and the time to peak (s) ($P = 0.005$ and $P = 0.003$, respectively) (Table 7).

The multivariate ROC curves of the investigated prostate perfusion MRI parameters are shown in Figure 4 and Table 6.

The number of RP cases was small, but the Kappa analysis agreement between the GSs of TRUSBx and RP was obtained as 0.796, ($P < 0.001$) (Figure 5).

Discussion

The main purpose of this study was to compare $^{(68)}$Ga-PSMA SUV_{max}, DCE-MRI, and PSA density values, which are the most-used parameters for GS prediction in the literature. Based on the information obtained in the present study, DCE-MRI parameters, respectively, the wash-out rate, wash-in rate, and time to peak, were quite successful in predicting the GS; meanwhile, the $^{(68)}$Ga-PSMA SUV_{max} and PSA failed to predict the GS.

In the current study, no correlation was found between the PCa grade and the PSA; however, a moderate correlation was observed between the prostate volume and the PSA. Recent studies that investigated whether the addition of prostate volume to the

Table 4. Analysis of the investigated parameters according to the three patient groups, based on the Gleason score

	Group 1 (low risk) Median (min–max)	Group 2 (intermediate risk) Median (min–max)	Group 3 (high risk) Median (min–max)	*P*	Dunn-Bonferroni test
Age	69 (57–80)	68.5 (57–89)	70 (53–90)	**0.777**	
$^{(68)}$Ga-PSMA SUV_{max}	5.34 (2.18–31.84)	6.35 (2.41–35.42)	7.15 (2.12–28.91)	**0.178**	
PSA (μg/L)	6.78 (0.87–20.7)	7.40 (0.79–23.81)	8.60 (0.86–36.20)	**0.186**	
PSA density (ng/mL^2)	0.16 (0.01–0.45)	0.165 (0.01–0.44)	0.17 (0.03–0.55)	**0.717**	
Prostate volume (cm^3)	39.5 (14–122)	44 (17–116)	55 (14–124)	**0.032**	1-2; $P = 0.412$ 2-3; $P = 0.412$ 3-1; $P = 0.048$
Maximum enhancement	885.59 (145.81–1852.36)	964.38 (351.12–1785.69)	1235.23 (512.85–2646.77)	**0.001**	1-2; $P = 0.659$ 3-1; $P < 0.001$ 3-2; $P = 0.008$
Maximum relative enhancement (%)	98.49 (51.65–185.12)	111.33 (48.72–201.33)	143.12 (68.45–211.54)	**<0.001**	1-2; $P = 0.952$ 3-1; $P < 0.001$ 3-2; $P = 0.008$
T0 (s)	34.28 (20.66–48.21)	30.43 (18.31–47.28)	28.22 (16.32–43.68)	**<0.001**	1-2; $P = 0.011$ 1-3; $P < 0.001$ 2-3; $P = 0.477$
Time to peak (s)	63.03 (36.12–234.9)	53.76 (24.19–210.19)	42.19 (24.51–137.80)	**<0.001**	1-3. $P = 0.035$ 2-3; $P = 0.021$ 1-2; $P = 1.000$
Wash-in rate (s^{-1})	7.12 (2.94–85.90)	8.93 (4.26–43.19)	13.24 (6.56–92.55)	**<0.001**	1-2; $P = 1.000$ 3-1; $P = 0.001$ 3-2; $P = 0.003$
Wash-out rate (s^{-1})	3.13 (0.15–5.54)	4.62 (2.11–10.21)	8.87 (3.14–31.26)	**<0.001**	1-2; $P = 0.143$ 3-1; $P < 0.001$ 3-2; $P < 0.001$

min, minimum; max, maximum; PSA, prostate-specific antigen.

Table 5. Analysis of the correlation of prostate volume with PSA, PSA density, and $^{(68)}$Ga-PSMA SUV_{max}

	Prostate volume (cm^3)	
	r	*P*
PSA (μg/L)	0.490	**<0.001**
PSA density (ng/mL^2)	–0.251	**0.003**
$^{(68)}$Ga-PSMA SUV_{max}	0.322	**<0.001**

PSMA, prostate-specific membrane antigen; SUV_{max}, maximum standardized uptake value; PSA, prostate-specific antigen.

PSA calculation could better distinguish false from true positives showed that PSA density supplied more information for biopsy decisions than PSA alone. In tests performed on different PSA density threshold levels as predictors of PCa, a PSA density value of 0.15 remained the most accepted value for distinguishing clinically significant diseases from clinically insignificant diseases. Recent literature studies showed that PSA density had a high sensitivity in the diagnosis of PCa in small (<50 mL) and medium-sized (50–75 mL) prostates; however, the sensitivity of this parameter was significantly lower in large (>75 mL) prostates.[2,15] In the current study, the ability of PSA density to predict the GS was evaluated, and it was determined to have no significant value for this purpose. The prostate volume of patients with a high tumor grade was greater than in those with a low tumor grade, suggesting that PSA density might be misleading in PCa diagnosis.

The clinical use of $^{(68)}$Ga-PSMA PET/CT appears to have replaced CT; it also seems superior to MRI in the detection of metastatic diseases.[19] In addition, an increasing number of studies advocate that $^{(68)}$Ga-PSMA PET/CT is superior to mpMRI in detecting PCa. However, there are also studies arguing that, particularly in patients with a large prostate volume, $^{(68)}$Ga-PSMA SUV_{max} increases PSMA expression independently of the GS.[20,21] In the present study, it was observed that the prostate volume and PSMA SUV_{max} values had a moderate correlation; however, there was no correlation between GS and the PSMA SUV_{max} values of the lesions. Uprimny et al.[22] reported that the tracer uptake in a primary tumor increases with the increase in GS and PSA levels. They also analyzed the GS and SUV_{max} values obtained from biopsy samples, as in this study, but not from the final results of all-gland pathology, based on RP.[23,24] However, in an immunohistochemical study evaluating the correlation between SUV_{max} values and PSMA expression in tissue samples, it was shown that the tracer uptake was directly related to the intensity of PSMA expression. However, in the same study, it was found that the tracer uptake did not show the GS.[25] Donato et al.[14] showed that $^{(68)}$Ga-PSMA PET/CT could predict the cancer grade but was still less sensitive than prostate mpMRI and prostate biopsy. It is necessary to increase the number of histopathological examinations including correlation analysis to determine whether the number of tumor cells or tumor grade is more effective for increasing the PSMA SUV_{max}.

van Niekerk et al.[26] reported that micro-vascularity increased as the lesion grade increased in patients with PCa. DCE-MRI is an important diagnostic method in the detection of focal PCa, as it increases the accuracy of the examination for the detection and evaluation of intraprostatic tumor lesions.[27] The contribution of perfusion parameters to the detection of intraprostatic lesions has

Table 6. ROC analysis of the DCE-MRI parameters according to the Gleason score variable

	Maximum enhancement	Maximum relative enhancement (%)	T0 (s)	Time to peak (s)	Wash-in rate (s^{-1})	Wash-out rate (s^{-1})
AUC (s.e.) (95% CI)	0.653 (0.051) (0.566–0.732)	0.658 (0.051) (0.572–0.737)	0.719 (0.049) (0.636–0.792)	0.721 (0.045) (0.638–0.794)	0.784 (0.046) (0.705–0.850)	0.891 (0.028) (0.826–0.938)
Cut-off	≤1354.3	≤132.67	>32.15	>51.32	≤8.59	≤4.11
Sensitivity % (95% CI)	97.2 (85.5–99.9)	83.3 (67.2–93.6)	72.22 (54.8–85.8)	88.89 (73.9–96.9)	86.11 (70.5–95.3)	80.56 (64–91.8)
Specificity (95% CI)	27.7 (19.3–37.5)	45.54 (35.6–55.8)	72.28 (55.2–74.5)	63.37 (53.2–72.7)	73.27 (63.5–81.6)	86.14 (77.8–92.2)
PPV % (95% CI)	32.1 (29.3–35)	35.3 (30.2–40.7)	42.6 (34.7–51)	46.4 (39.5–53.4)	53.4 (44.8–61.9)	67.4 (55.4–77.6)
NPV % (95% CI)	96.4 (79.2–99.5)	88.5 (78.2–94.3)	86.8 (79.3–91.9)	94.1 (86.3–97.6)	93.7 (86.7–97.1)	92.6 (86.4–96)
P	**0.003**	**0.002**	**<0.001**	**<0.001**	**<0.001**	**<0.001**

ROC, receiver operating characteristic; DCE, dynamic contrast-enhanced; MRI, magnetic resonance imaging; AUC, area under the curve; NPV, negative predictive value; PPV, positive predictive value; CI, confidence interval.

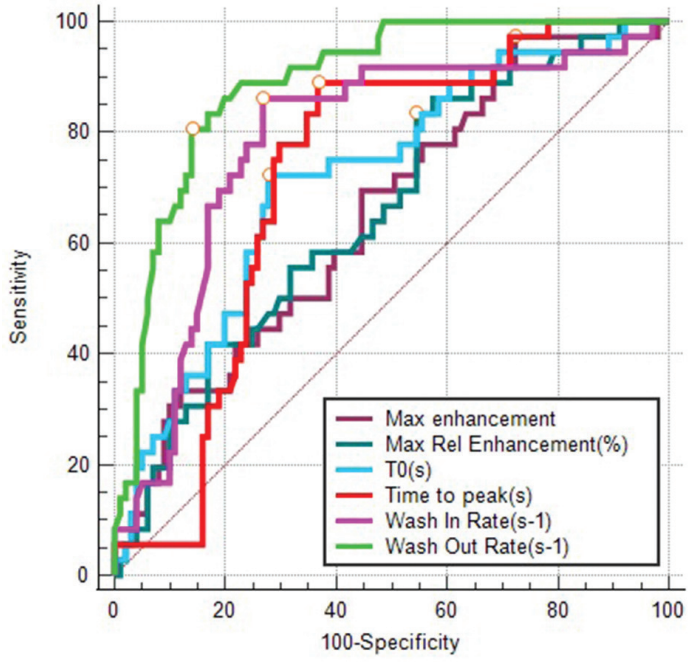

Figure 4. Multivariate ROC curve analysis of quantitative prostate perfusion parameters on MRI. ROC, receiver operating characteristic; MRI, magnetic resonance imaging.

been investigated in numerous studies.[28,29] In one of the largest series of these studies, Zhao et al.[25] demonstrated that shortening of the time to reach peak value in patients with PCa was the most sensitive DCE-MRI parameter. Ren et al.[30] indicated that DCE-MRI curves increase the ability to distinguish benign tissue from malignant prostate tissue, based on T2-weighted imaging, and that the absence of DCE-MRI causes some aggressive lesions to be missed. Boesen et al.[3] showed that the combination of measuring PSA density and performing prostate mpMRI before biopsy in patients with a GS of 7–10 increased diagnostic sensitivity and reduced the risks of unnecessary biopsy procedures.

Chen et al.[31] determined that the wash-out value had a significant correlation with GS in the evaluation of prostate tumor aggressiveness. In a similar study, Vos et al.[32] reported that quantitative parameters and semi-quantitative parameters, derived from DCE-MRI using a 3.0 T device, could assist in the evaluation of PCa aggressiveness in the peripheral zone.

In the present study, the most valuable parameter in predicting the tumor grade among the DCE-MRI parameters was the wash-out rate, followed by the wash-in rate. In tumor biology, it is known that, as the amount of non-differentiation increases, angiogenesis increases, and the microvascular bed expands.[9] Therefore, as the GS of a tumor increases, the rates of non-differentiation and angiogenesis also increase; this is represented by higher wash-out and wash-in rates in DCE-MRI evaluation.[26,32] It can be stated that the correlation between angiogenesis and the wash-out rate is more valuable than the correlation between PSMA expression and angiogenesis. However, further studies involving multimodalities are required to evaluate the correlation between angiogenesis and PSMA expression, as well as DCE-MRI parameters.

An important aspect of this study is the analysis of the lesions' multimodal characteristics. While DCE-MRI parameters reflect the microvascular nature of lesions, the SUV_{max} indicates their PSMA concentration. Thus, their combined evaluation contributes to a comprehensive assessment of tumor status and the selection of an appropriate treatment plan.

There were limitations to the present study.

(1) Kim et al.[33] reported that there was a difference in the DCE-MRI semi-quantitative parameters of lesions in peripheral and transition zones, although this did not affect the sensitivity of lesion detection. Ziayee et al.[34] determined that perfusion parameters and lesion detection rates were satisfactory for lesions in the peripheral zone but significantly reduced in those in the transition zone. In the present study, the lesions were not evaluated separately for the peripheral or transition zone; this could be considered a limitation.

Table 7. Analysis of the diagnostic test performances of wash-out rate (s^{-1}), wash-in rate (s^{-1}), and time to peak (s)

	Wash-out rate (s^{-1})	Wash-in rate (s^{-1})	Time to peak (s)	p1	p2	p3
AUC (s.e.) 95%-CI (%)	0.891 (0.028) (0.826–0.938)	0.784 (0.046) (0.705–0.850)	0.721 (0.045) (0.638–0.794)			
Cut-off	<4.11	<8.59	>51.32			
Sensitivity (%) 95%-CI (%)	80.56 (64–91.8)	86.11 (70.5–95.3)	88.89 (73.9–96.9)			
Specificity 95%-CI (%)	86.14 (77.8–92.2)	73.27 (63.5–81.6)	63.37 (53.2–72.7)	**0.005**	**0.003**	0.386
PPV 95%-CI (%)	67.4 (55.4–77.6)	53.4 (44.8–61.9)	46.4 (39.5–53.4)			
NPV 95%-CI (%)	92.6 (86.4–96)	93.7 (86.7–97.1)	94.1 (86.3–97.6)			
P	**<0.001**	**<0.001**	**<0.001**			

ROC curve test; p1, wash-out rate (s^{-1})-wash-in rate (s^{-1}); p2, wash-out rate (s^{-1})-time to peak (s); p3, wash-in rate (s^{-1})-time to peak (s). ROC, receiver operating characteristic; AUC, area under the curve; CI, confidence interval; NPV, negative predictive value; PPV, positive predictive value.

(2) In the current literature, k_{trans}, v_e, and k_{ep} calculations are used to describe DCE-MRI parameters. Although k_{trans} correlates with the initial slope (wash-in rate) of the time-intensity curve, v_e correlates with the peak height and time to peak of the time-intensity curve; k_{ep} controls the shape of the curve (reflected in the relative contributions of its independent components, K_{trans} and v_e). The authors of the present study were unable to use these parameters, since no application capable of calculating these values is available in hospital; this can be regarded as a limitation concerning the integration of the study with existing literature.

(3) In hospital, $^{(68)}$Ga-PSMA PET/CT examinations are performed on PI-RADS 4-5 lesions or in cases with a distant metastasis risk. Therefore, low PI-RADS category lesions were not included in the study in the absence of $^{(68)}$Ga-PSMA PET/CT examinations. This is accepted as a limitation due to the risk of bias.

(4) We evaluated the 3 + 4 (intermediate favorable) and 4 + 3 (intermediate unfavorable) groups as a common group in order to ensure a homogeneous distribution among the patient groups.

(5) The small number of patients who underwent RP is a limitation.

In conclusion, the semi-quantitative DCE-MRI data, especially the wash-out rate, wash-in rate, and time-to-peak values, are important diagnostic parameters for predicting the grade of intraprostatic tumor lesions. There was a moderate correlation between the prostate volume and PSMA SUV_{max} values; this may be a misleading factor for PSMA SUV_{max} prediction and GS determination.

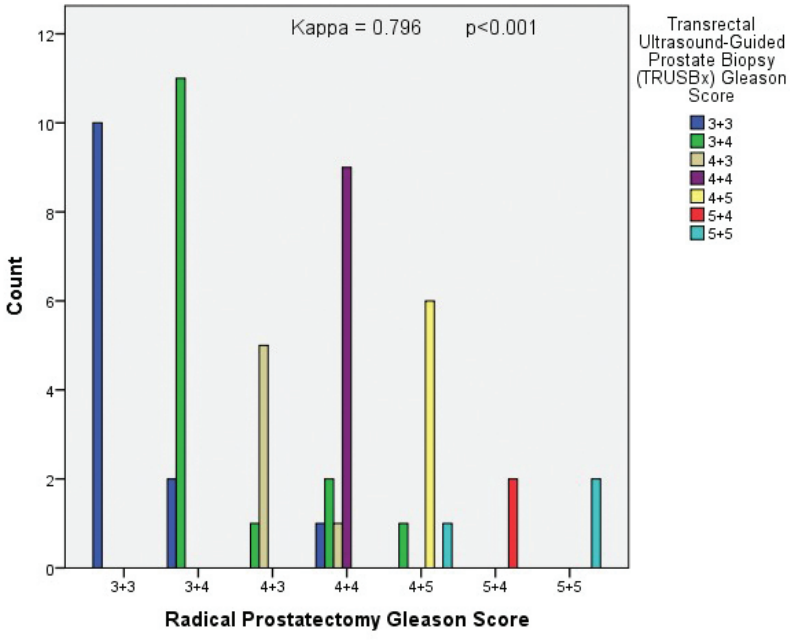

Figure 5. Kappa analysis agreement between transrectal ultrasound-guided prostate biopsy and radical prostatectomy.

Conflict of interest disclosure

The authors declared no conflicts of interest.

References

1. Turkbey B, Rosenkrantz AB, Haider MA, et al. Prostate imaging reporting and data system version 2.1: 2019 update of prostate imaging reporting and data system version 2. *Eur Urol*. 2019;76(3):340-351. [CrossRef]
2. Sauter G, Steurer S, Clauditz TS, et al. Clinical utility of quantitative Gleason grading in prostate biopsies and prostatectomy specimens. *Eur Urol*. 2016;69(4):592-598. [CrossRef]
3. Boesen L, Nørgaard N, Løgager V, et al. Prebiopsy biparametric magnetic resonance imaging combined with prostate-specific antigen density in detecting and ruling out Gleason 7-10 prostate cancer in biopsy-naïve men. *Eur Urol Oncol*. 2019;2(3):311-319. [CrossRef]
4. Godtman RA, Kollberg KS, Pihl CG, Månsson M, Hugosson J. The association between age, prostate cancer risk, and higher Gleason score in a long-term screening program: results from the Göteborg-1 Prostate Cancer Screening Trial. *Eur Urol*. 2022;82(3):311-317. [CrossRef]
5. Tan CH, Hobbs BP, Wei W, Kundra V. Dynamic contrast-enhanced MRI for the detection of prostate cancer: meta-analysis. *AJR Am J Roentgenol*. 2015;204(4):W439-W448. [CrossRef]
6. Winkel DJ, Heye TJ, Benz MR, et al. Compressed sensing radial sampling MRI of prostate perfusion: utility for detection of prostate cancer. *Radiology*. 2019;290(3):702-708. [CrossRef]
7. Tofts PS, Brix G, Buckley DL, et al. Estimating kinetic parameters from dynamic contrast-

enhanced T(1)-weighted MRI of a diffusable tracer: standardized quantities and symbols. *J Magn Reson Imaging*. 1999;10(3):223-232. [CrossRef]

8. Zhao J, Mangarova DB, Brangsch J, et al. Correlation between intraprostatic PSMA Uptake and MRI PI-RADS of [68Ga]Ga-PSMA-11 PET/MRI in patients with prostate cancer: comparison of PI-RADS version 2.0 and PI-RADS version 2.1. *Cancers (Basel)*. 2020;12(12):3523. [CrossRef]
9. Singanamalli A, Rusu M, Sparks RE, et al. Identifying in vivo DCE MRI markers associated with microvessel architecture and gleason grades of prostate cancer. *J Magn Reson Imaging*. 2016;43(1):149-158. [CrossRef]
10. Michallek F, Huisman H, Hamm B, Elezkurtaj S, Maxeiner A, Dewey M. Prediction of prostate cancer grade using fractal analysis of perfusion MRI: retrospective proof-of-principle study. *Eur Radiol*. 2022;32(5):3236-3247. [CrossRef]
11. Zhao J, Hamm B, Brenner W, Makowski MR. Lesion-to-background ratio threshold value of SUVmax of simultaneous [68Ga]Ga-PSMA-11 PET/MRI imaging in patients with prostate cancer. *Insights Imaging*. 2020;11(1):137. [CrossRef]
12. Demirci E, Kabasakal L, Şahin OE, et al. Can SUVmax values of Ga-68-PSMA PET/CT scan predict the clinically significant prostate cancer? *Nucl Med Commun*. 2019;40(1):86-91. [CrossRef]
13. Kwan TN, Spremo S, Teh AYM, McHarg D, Thangasamy I, Woo HH. Performance of Ga-68 PSMA PET/CT for diagnosis and grading of local prostate cancer. *Prostate Int*. 2021;9(2):107-112. [CrossRef]
14. Donato P, Morton A, Yaxley J, et al. 68Ga-PSMA PET/CT better characterises localised prostate cancer after MRI and transperineal prostate biopsy: Is 68Ga-PSMA PET/CT guided biopsy the future? *Eur J Nucl Med Mol Imaging*. 2020;47(8):1843-1851. [CrossRef]
15. Yusim I, Krenawi M, Mazor E, Novack V, Mabjeesh NJ. The use of prostate specific antigen density to predict clinically significant prostate cancer. *Sci Rep*. 2020;10(1):20015. [CrossRef]
16. Aminsharifi A, Howard L, Wu Y, et al. Prostate specific antigen density as a predictor of clinically significant prostate cancer when the prostate specific antigen is in the diagnostic gray zone: defining the optimum cutoff point stratified by race and body mass index. *J Urol*. 2018;200(4):758-766. [CrossRef]
17. Egevad L, Delahunt B, Srigley JR, Samaratunga H. International Society of Urological Pathology (ISUP) grading of prostate cancer - an ISUP consensus on contemporary grading. APMIS. 2016;124(6):433-435. [CrossRef]
18. Fleiss JL, Cohen J. The equivalence of weighted kappa and the intraclass correlation coefficient as measures of reliability. *Educ Psychol Meas*. 1973;33(3):613-619. [CrossRef]
19. Tulsyan S, Das CJ, Tripathi M, Seth A, Kumar R, Bal C. Comparison of 68Ga-PSMA PET/CT and multiparametric MRI for staging of high-risk prostate cancer 68Ga-PSMA PET and MRI in prostate cancer. *Nucl Med Commun*. 2017;38(12):1094-1102. [CrossRef]
20. Jochumsen MR, Sörensen J, Tolbod LP, et al. Potential synergy between PSMA uptake and tumour blood flow for prediction of human prostate cancer aggressiveness. *EJNMMI Res*. 2021;11(1):12. [CrossRef]
21. Lennartz S, Täger P, Zopfs D, et al. Lymph node assessment in prostate cancer: evaluation of iodine quantification with spectral detector CT in correlation to PSMA PET/CT. *Clin Nucl Med*. 2021;46(4):303-309. [CrossRef]
22. Uprimny C, Kroiss AS, Decristoforo C, et al. 68Ga-PSMA-11 PET/CT in primary staging of prostate cancer: PSA and Gleason score predict the intensity of tracer accumulation in the primary tumour. *Eur J Nucl Med Mol Imaging*. 2017;44(6):941-949. [CrossRef]
23. Budäus L, Leyh-Bannurah SR, Salomon G, et al. Initial experience of (68)Ga-PSMA PET/CT imaging in high-risk prostate cancer patients prior to radical prostatectomy. *Eur Urol*. 2016;69(3):393-396. [CrossRef]
24. Barbosa FG, Queiroz MA, Nunes RF, Marin JFG, Buchpiguel CA, Cerri GG. Clinical perspectives of PSMA PET/MRI for prostate cancer. *Clinics (Sao Paulo)*. 2018;73(Suppl 1):e586s. [CrossRef]
25. Zhao J, Kader A, Mangarova DB, et al. Dynamic contrast-enhanced mri of prostate lesions of simultaneous [68Ga]Ga-PSMA-11 PET/MRI: comparison between intraprostatic lesions and correlation between perfusion parameters. *Cancers (Basel)*. 2021;13(6):1404. [CrossRef]
26. van Niekerk CG, van der Laak JA, Hambrock T, et al. Correlation between dynamic contrast-enhanced MRI and quantitative histopathologic microvascular parameters in organ-confined prostate cancer. *Eur Radiol*. 2014;24(10):2597-2605. [CrossRef]
27. Winkel DJ, Heye TJ, Benz MR, et al. Compressed sensing radial sampling MRI of prostate perfusion: utility for detection of prostate cancer. *Radiology*. 2019;290(3):702-708. [CrossRef]
28. Cai W, Li F, Wang J, et al. A comparison of arterial spin labeling perfusion MRI and DCE-MRI in human prostate cancer. *NMR Biomed*. 2014;27(7):817-825. [CrossRef]
29. Sung YS, Kwon HJ, Park BW, et al. Prostate cancer detection on dynamic contrast-enhanced MRI: computer-aided diagnosis versus single perfusion parameter maps. *AJR Am J Roentgenol*. 2011;197(5):1122-1129. [CrossRef]
30. Ren J, Huan Y, Wang H, et al. Dynamic contrast-enhanced MRI of benign prostatic hyperplasia and prostatic carcinoma: correlation with angiogenesis. *Clin Radiol*. 2008;63(2):153-159. [CrossRef]
31. Chen YJ, Chu WC, Pu YS, Chueh SC, Shun CT, Tseng WY. Washout gradient in dynamic contrast-enhanced MRI is associated with tumor aggressiveness of prostate cancer. *J Magn Reson Imaging*. 2012;36(4):912-919. [CrossRef]
32. Vos EK, Litjens GJ, Kobus T, et al. Assessment of prostate cancer aggressiveness using dynamic contrast-enhanced magnetic resonance imaging at 3 T. *Eur Urol*. 2013;64(3):448-455. [CrossRef]
33. Kim JK, Hong SS, Choi YJ, et al. Wash-in rate on the basis of dynamic contrast-enhanced MRI: usefulness for prostate cancer detection and localization. *J Magn Reson Imaging*. 2005;22(5):639-646. [CrossRef]
34. Ziayee F, Mueller-Lutz A, Gross J, et al. Arterial input function for quantitative dynamic contrast-enhanced MRI to diagnose prostate cancer. *Diagn Interv Radiol*. 2022;28(2):108-114. [CrossRef]

Diagn Interv Radiol 2023; DOI: 10.4274/dir.2023.232188

ABDOMINAL IMAGING

ORIGINAL ARTICLE

Field-of-view optimized and constrained undistorted single-shot study of intravoxel incoherent motion and diffusion-weighted imaging of the uterus during the menstrual cycle: a prospective study

Xiaodan Li
Tianzhu Liu
Jun Chen
Jiahui Tang
Wanchun Zhang
Juan Du
Lina Li
Lesheng Huang

PURPOSE

This study aimed to compare the variability of the uterus during the menses phase (MP), follicular phase (FP), and luteal phase (LP) of the menstrual cycle using intravoxel incoherent motion diffusion-weighted imaging (IVIM-DWI).

METHODS

This prospective study was conducted at the Guangdong Provincial Hospital of Traditional Chinese Medicine between January 2022 and January 2023. Women of childbearing age (18–45 years) with appropriate progesterone levels were included in this study. Conventional magnetic resonance imaging and IVIM-DWI scans were performed during the MP, FP, and LP. The differences in IVIM-DWI-derived parameters between these phases were then compared, and the overlap was quantitatively described.

RESULTS

The apparent diffusion coefficient (ADC) and pure molecular diffusion coefficient (*D*) values from the endometrium, uterine junctional zone (UJZ), and myometrium indicated statistical differences between the MP and FP and the MP and LP (ADC: endometrium, both $P < 0.001$; UJZ, $P = 0.008$ and $P < 0.001$, respectively; myometrium, $P = 0.033$ and $P = 0.006$, respectively; *D*: endometrium, both $P < 0.001$; UJZ, $P = 0.008$ and $P = 0.006$, respectively; myometrium, $P = 0.041$ and $P = 0.045$, respectively). The perfusion-related diffusion coefficient (*D**) values from the myometrium indicated statistical differences between the FP and MP and the FP and LP (*D**: myometrium, $P = 0.049$ and $P = 0.009$, respectively). The overlapping endometrium ratios between the MP and FP or LP were lower than 50% in the ADC and *D* values (ADC: overlapping of MP and FP: 33.33%, overlapping of MP and LP: 23.33%; *D*: overlapping of MP and FP: 40.00%, overlapping of MP and LP: 43.33%).

CONCLUSION

The ADC and IVIM-derived parameters indicated differences in the uterus in diverse phases of the menstrual cycle, especially in the endometrium in relation to ADC and *D* values.

KEYWORDS

Intravoxel incoherent motion diffusion-weighted imaging, uterus, menses phase, follicular phase, luteal phase, menstrual cycle

From the Department of Gynecology (X.L., J.D., L.L.), Guangdong Hospital of Traditional Chinese Medicine, Zhuhai, China; Department of Radiology (T.L., J.C., J.T., W.Z., L.H. ✉ huanglesheng2008@163.com), Guangdong Hospital of Traditional Chinese Medicine, Zhuhai, China.

Received 09 March 2023; revision requested 14 April 2023; last revision received 21 June 2023; accepted 10 July 2023.

Epub: 09.08.2023

Publication date: 05.09.2023

DOI: 10.4274/dir.2023.232188

You may cite this article as: Li X, Liu T, Chen J, et al. Field-of-view optimized and constrained undistorted single-shot study of intravoxel incoherent motion and diffusion-weighted imaging of the uterus during the menstrual cycle: a prospective study. *Diagn Interv Radiol.* 2023;29(5):656-663.

The observable morphological and signal changes in the uterus on conventional magnetic resonance imaging (MRI) have been clearly described in the literature.[1-3] With the development and application of quantitative MRI sequences, researchers have become interested in the correlation between periodic morphological changes in the uterus and those displayed using quantitative MRI technologies. Kido et al.[4] revealed that the apparent diffusion coefficient (ADC) values of diffusion-weighted imaging (DWI) for the myometrium and endometrium are lower during the menses phase (MP), and the degree of these differences is similar to those reported between malignant and non-malignant tissues. Kılıçkesmez et al.[5] also noted that ADC values increase significantly. Fractional anisotropy values on diffusion tensor imaging tend to decrease in all zones in the secretory phase, with the exception of the uterine junctional zone (UJZ). Recently, Li et al.[6] demonstrated that the T2* values in the endometrium during the ovulatory phase (OP) and luteal phase (LP) are significantly higher than those in the UJZ and myometrium.

The ADC is a quantitative parameter derived from DWI[7] and has been commonly used and validated as a potential imaging biomarker for evaluating diffuse or focal uterogenic disease[8,9] and monitoring the treatment response of malignant tumors.[10] However, because the ADC represents the degree of mobility of water molecules in tissue, it may not fully account for the tissue characteristics that can be interrogated using DWI techniques.[7,11] However, intravoxel incoherent motion (IVIM) imaging has been approved to help evaluate uterogenic diseases.[9,10,12,13] The IVIM imaging technique is based on DWI using various *b* values,[7] allowing for the separate analysis of two components of random water motion in biological tissues (pure molecular diffusion and perfusion) using the parameters of the pure molecular diffusion coefficient (*D*), perfusion fraction (*f*), and perfusion-related diffusion coefficient (*D**).[14] However, the reliability of IVIM imaging for evaluating uterogenic diseases can be influenced by several factors; for instance, the menstrual cycle of women of childbearing age may influence DWI or IVIM parameters.[4] Previous studies have reported DWI or IVIM-derived parameter measurement errors resulting from this issue.[9,13,15-17]

Main points

- Statistical differences between the menses phase (MP) and follicular phase (FP)/luteal phase (LP) were identified in the endometrium, uterine junctional zone, and myometrium in relation to apparent diffusion coefficient (*D*) and pure molecular *D* values in intravoxel incoherent motion diffusion-weighted imaging (IVIM-DWI).
- Statistical differences in perfusion-related *D* values were identified between the LP and MP/FP in the myometrium through IVIM-DWI.
- The differences in the uterine structure observed through IVIM-DWI can provide experimental evidence for the inclusion/exclusion criteria or layered analysis in future IVIM-DWI uterus studies in women of childbearing age.

Whether the uterine structure can cause significant changes in IVIM values during the menstrual cycle affects the feasibility, accuracy, and credibility of IVIM clinical diagnoses. Therefore, this study aimed to compare the diagnostic performance of different IVIM-DWI-derived parameters for the phases of the menstrual cycle to explore the degree of changes during the menstrual cycle presented in IVIM-DWI.

Methods

Study design and setting

This field-of-view (FOV) optimized and constrained undistorted single-shot (FOCUS) study was a prospective investigation conducted in the Guangdong Provincial Hospital of Traditional Chinese Medicine between January 2022 and January 2023. The FOCUS study protocol has been approved by our institutional Research Ethics Board (approval ZF2022-379) and adhered to the tenets of the Declaration of Helsinki. Signed informed consent was obtained from each participant. The study flowchart is provided in Figure 1.

Participants and screening

Healthy female volunteers were recruited and screened in our hospital during the study period. The inclusion criteria were as follows: (1) healthy women aged 18–45 years, (2) premenopausal status with a regular menstrual cycle (28 ± 7 days), (3) biphasic basal body temperature, (4) no history of gynecologic diseases, and (5) no oral contraceptives or hormone replacement therapy in the previous 12 months. The exclusion criteria were as follows: (1) congenital uterine abnormalities, (2) leiomyoma, (3) history of adenomyosis, (4) abnormal serum hormone levels, (5) pregnancy, (6) age <18 or >45 years, (7) usual contraindications to MRI, or (8) refusal to sign the informed consent form.

To ensure the patients had normal serum hormone levels, we tested the progesterone levels of the recruited patients. We set the progesterone level at <2.84 nmol/L during the LP and >5.8 nmol/L during the MP. If the progesterone level was inconsistent with the menstrual cycle phase, the gynecologist rechecked the participant's progesterone levels during the next menstrual cycle. However, participants were excluded if the results remained inconsistent with the menstrual cycle phases.

After screening with the progesterone test, a color Doppler ultrasound (US) (Volunson S10; GE Healthcare, MA, USA) examination of the female reproductive system was performed to ensure the patient fit the inclusion criteria. The US examination included the following: 1) exclusion of lesions in the

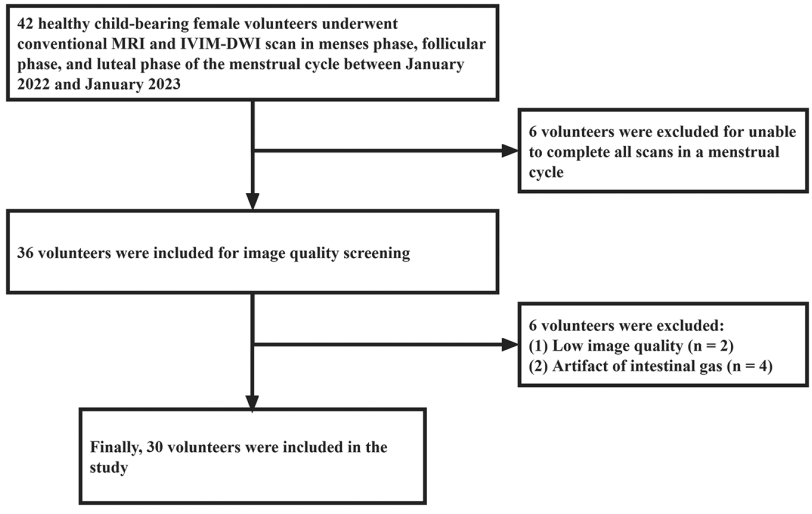

Figure 1. Flowchart of the screening process of female volunteers of childbearing age. MRI, magnetic resonance imaging; IVIM, intravoxel incoherent motion diffusion; DWI, diffusion-weighted imaging.

uterus, bilateral fallopian tubes, and ovaries; 2) assessment of the size and position of the uterus; 3) evaluation of the uniformity of the myometrium layer echo; 4) measurement of endometrial thickness; and 5) analysis of uterine blood flow signals.

Magnetic resonance imaging examination

All participants underwent repeated MRIs over multiple time points during the menstrual cycle. Time point one (T_1) was from days 1 to 4 of the menstrual cycle, time point two (T_2) was from days 7 to 12, and time point three (T_3) was from days 16 to 24; T_1, T_2, and T_3 represent the MP, follicular phase (FP), and LP, respectively. Because the precise time window of the OP is too short to measure accurately, we did not examine the uterus for OP.

The MRI examinations were performed using a 3.0-T scanner (Signa Discovery 750 w; GE Healthcare) with a 16-channel abdominal coil. Participants were required to undertake bowel preparation, including a low-fiber diet for one day, an 8-hour fast before the test, and an enema with 500 mL of saline 30 min before the MRI. For all participants, the following five standard sequences were performed: (1) sagittal T2-weighted short TI inversion recovery (STIR) sequence, (2) axial T1-weighted turbo spin-echo sequence, (3) axial STIR sequence, (4) sagittal FOCUS DWI sequence, and (5) sagittal FOCUS IVIM sequence.

An IVIM-DWI using a FOCUS protocol was performed on all participants in the sagittal plane in a supine position. The scan range covered the whole uterus and extended 5–8 cm beyond the distal border of the uterus. Spatial saturation bands were applied to remove the signal from the overlying fat and nearby tissues. In addition, the following 12 *b* values were applied: 0, 25, 50, 75, 100, 150, 200, 300, 400, 500, 600, and 800 s/mm^2.

Participants were asked to breathe freely during the examination, resulting in the following: average repetition time: 3007 ms; average echo time: 69 ms; slice thickness: 4 mm; inter-slice gap: 1 mm; matrix: 48 × 48; FOV: 240 × 240 mm; number of excitations = 2; number of slices = 16–20 (based on the size of the uterus). Two *b* values (0 and 800 s/mm^2) were applied to the FOCUS DWI sequence, and diffusion-weighted gradients were applied in three orthogonal directions. The remaining scan parameters were consistent with the FOCUS IVIM sequence. The total scan time was approximately 30–35 min.

Image analysis

The IVIM parameters and ADC maps were generated and calculated using FuncTool (GE AW4.6 advantage; GE Healthcare). A quantitative analysis of DWI data was performed using mono-exponential and bi-exponential models for IVIM data. The ADCs were calculated through the mono-exponential linear fitting technique using the following equation:[18]

$$\frac{S(b)}{S_0} = \exp\left(-b \times \mathrm{ADC}\right),$$

where $S(b)$ corresponds to the mean signal intensity at a given b value and S_0 is the mean signal intensity at $b = 0$ s/mm^2.

For the bi-exponential model, the IVIM-derived parameters were calculated using the following equation:[19]

$$\frac{S(b)}{S_0} = [(1-f) \times \exp(-b \times D)] + [f \times \exp(-b \times D^*)],$$

where D is pure water diffusion, D^* represents pseudo diffusion, and f values are the intravascular water fractions in a selected area. The values were calculated using b values >200 and <200 s/mm^2, respectively.

The quality of the IVIM, DWI, and routine T1-weighted and T2-weighted images was evaluated by a single examiner (JC) with 17 years abdominal MRI experience. Moreover, a trained examiner (LT) with ten years experience in female reproductive system MRI-based diagnosis post-processed all qualified images and then measured the study parameters quantitatively at the post-processing workstation. The examiner was blinded to the participants' age, menstrual cycle phases, body mass index (BMI), and previous reproductive history.

To minimize measurement errors, three non-overlapping regions of interest (ROIs) were determined, avoiding visible vessels, uterine borders, and artifacts: (1) the endometrium, anterior, and posterior region of the UJZ; (2) the anterior, posterior, and fundus of the myometrium; and (3) the anterior and posterior region of the cervical muscularis. The size of each ROI was adjusted according to the measurable range of the anatomical structure [endometrium: 15 (mean) and 12–20 mm^2 (range); UJZ: 8 (mean) and 5–12 mm^2 (range); myometrium and cervical muscularis: 20 (mean) and 15–25 mm^2 (range)], and the position was maintained on the different parametric maps (Figure 2). The mean ADC, D, D^*, and f values for each anatomical structure (endometrium, UJZ, myometrium, and cervical muscularis) were obtained by averaging the measurements in the ROIs (Figure 2).

Statistical analysis

Statistical analyses were performed using SPSS version 26.0 (Chicago, IL, USA). We tested continuous variables for normal distribution using the Kolmogorov–Smirnov test. Variables with a normal distribution were expressed as mean ± standard deviation, those with a non-normal distribution were expressed as the median (minimum–maximum), and categorical variables were presented as frequencies with percentages. A chi-squared test was applied to analyze

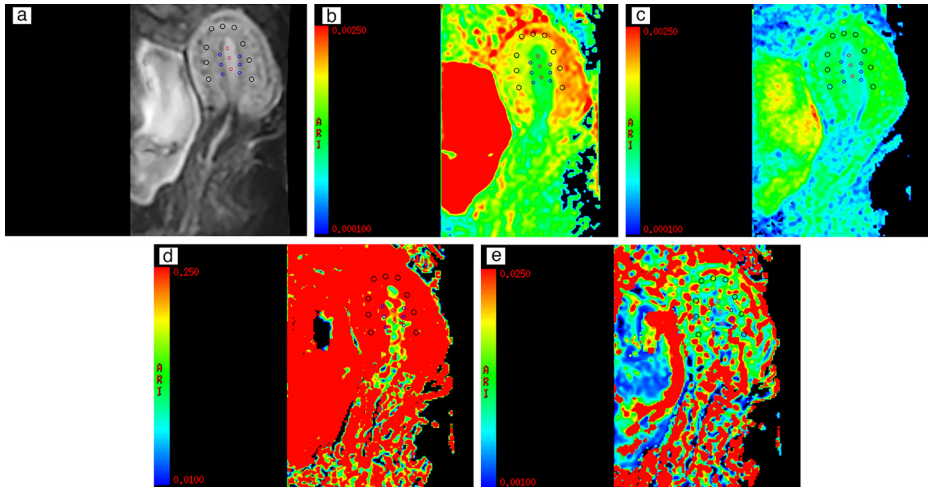

Figure 2. A 25-year-old healthy female participant in the follicular phase. **(a)** Sagittal view of a diffusion-weighted image with *b*: 0 s/mm^2; **(b)** apparent diffusion coefficient map; **(c)** pure molecular diffusion coefficient map; **(d)** perfusion-related diffusion coefficient map; **(e)** perfusion fraction map. Examiner-measured endometrium (red circles, **a-e**), uterine junctional zone (blue circles, **a-e**), and myometrium (black circles, **a-e**) in sagittal view.

categorical variables. Based on the variable distribution and homogeneity of variance, a Student's t-test or Mann–Whitney U test was applied to compare the differences in each DWI or IVIM-derived parameter between the three menstrual cycle phases.

To quantitatively describe the overlapping conditions and differentiation in menstrual cycle phases in relation to IVIM-DWI parameters, we divided the continuous data into intervals, and based on the order of magnitudes, we set the interval ranges as follows: (1) the interval ranges of the ADC and *D* were 0.10×10^{-3} (e.g., an ADC interval of 1.20×10^{-3} mm²/s including data between 1.15×10^{-3} and 1.25×10^{-3} mm²/s (1.15×10^{-3} mm²/s ≤ x <1.25×10^{-3} mm²/s); (2) the interval range of *D** was 10×10^{-3} mm²/s; (3) the interval range of *f* was 10.00%. After the data intervals were processed, the frequencies of each interval were calculated; overlapping intervals and overlapping ratios between the phases were then calculated within the range of a 95% confidence interval of the intervals. In this study, clinical differences were identified when overlapping ratios between the phases were <50%, and $P < 0.05$ was considered statistically significant.

Results

Characteristics of participants

We recruited 42 healthy female volunteers of childbearing age (18–45 years). Six participants (14.29%) were unable to complete all the scans in a menstrual cycle, two (4.76%) were excluded because of low image quality in screening, and four (9.52%) were excluded because they had artifacts in the form of intestinal gas. Finally, 30 participants (71.4%), with a mean age of 29.33 ± 5.76 years, were included in this study.

The characteristics of the participants are summarized in Table 1. Seventeen participants (56.67%) had not given birth, seven (23.33%) had one child (two cesareans and five eutocia), and six (20.00%) had two children (four cesareans and eight eutocia); menstrual cycles were 30 days (26–35 days). The mean BMI of the participants was 20.48 ± 2.55 kg/m², and none were obese.

Endometrium

During the menstrual cycle, the endometrium ADC and *D* values indicated a statistically significant decrease in the MP compared with the FP and LP (ADC: both $P < 0.001$, *D*: both $P < 0.001$). However, no statistical differences among the MP, FP, and LP were identified in the endometrium *D** and *f* values (*D**: MP and FP: $P = 0.171$, MP and LP: $P = 0.061$, FP and LP: $P = 0.753$; *f*: MP and FP: $P = 0.770$, MP and LP: $P = 0.651$, LP and FP: $P = 0.410$) (Tables 2, 3 and Figure 3).

The endometrium exhibited low overlapping ratios between the MP and FP/LP in the ADC (MP and FP: 33.33%; MP and LP: 23.33%) and *D* (MP and FP: 40.00%; MP and LP: 43.33%), and the overlapping intervals between the MP, FP, and LP in the ADC (MP and FP: $1.0–1.3 \times 10^{-3}$ mm²/s; MP and LP: $1.0–1.3 \times 10^{-3}$ mm²/s) and *D* (MP and FP: $0.6–1.1 \times 10^{-3}$ mm²/s; MP and LP: $0.7–1.1 \times 10^{-3}$ mm²/s) were less than those between the FP and LP (FP and LP: ADC, $1.0–1.6 \times 10^{-3}$ mm²/s; *D*, $0.7–1.4 \times 10^{-3}$ mm²/s) (Table 4, Figure 4).

Uterine junction zone

During the menstrual cycle, the UJZ ADC and *D* values demonstrated a statistically significant decrease in the MP compared with the FP and LP (ADC: MP and FP, $P = 0.008$, and MP and LP, $P < 0.001$; *D*: MP and FP, $P = 0.008$, MP and LP: $P = 0.006$). However, no statistical difference was identified among the MP, FP, and LP in the UJZ *D** and *f* values (*D**: MP and FP, $P = 0.753$, MP and LP, $P = 0.703$, LP and FP,

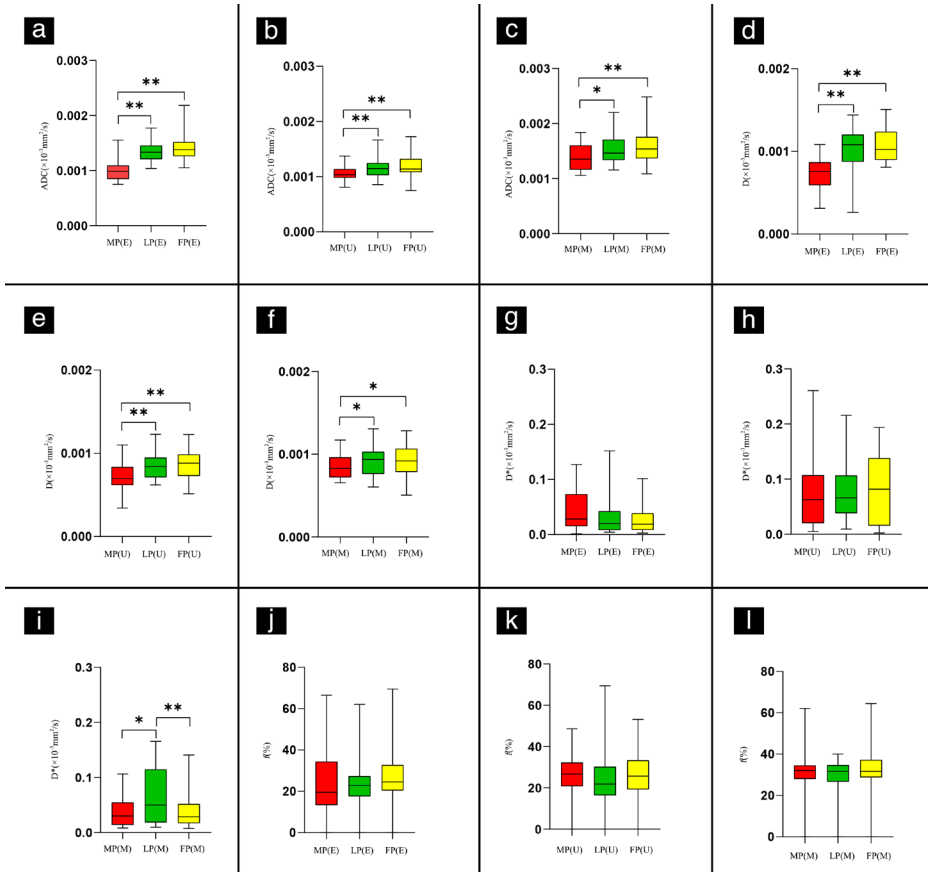

Figure 3. Box plots of different phases [menses (MP), luteal (LP), and follicular (FP)] in the endometrium, uterine junctional zone (UJZ), and myometrium using parameters derived from intravoxel incoherent motion diffusion-weighted imaging. Apparent diffusion coefficient and pure molecular diffusion coefficient values in the endometrium, UJZ, and myometrium, revealing differences between the MP and LP/FP (**a-f**, $P < 0.05$), especially in the endometrium (**a**, **d**, $P < 0.001$ all). Perfusion-related diffusion coefficient values in the myometrium, which differ for LP and MP/FP (F, $P < 0.05$) (E = endometrium; U = UJZ; M = myometrium).

Table 1. Demographic data of participants

Characteristics	Participants (n = 30)
Age (years), mean ± standard deviation	29.33 ± 5.76
Procreation (N/O/T)	17/7/6 (56.67%/23.33%/20.00%)
Birth mode (none/cesarean/eutocia)	17/6/13 (47.22%/16.67%/36.11%)
Menstrual cycle (days), median (minimum–maximum)	30 (26–35)
BMI (kg/m²)	20.48 ± 2.55

N, none; O, one; T, two; BMI, body mass index.

P = 0.873; f: MP and FP, P = 0.370, MP and LP, P = 0.794, LP and FP, P = 0.256) (Tables 2, 3 and Figure 3).

The UJZ exhibited high overlapping ratios (60.00%–80.00%) and no apparent differences in the overlapping interval between phases in the IVIM-DWI-derived parameters (Table 4, Figure 4).

Myometrium

During the menstrual cycle, the myometrium ADC and D values demonstrated a statistically significant decrease in the MP compared with the FP and LP (ADC: MP and FP, P = 0.033, MP and LP, P = 0.006; D: MP and FP, P = 0.041, MP and LP, P = 0.045) but no statistically significant change in the LP and FP (ADC: LP and FP, P = 0.168; D: LP and FP, P = 0.624). However, D* values indicated a statistically significant increase in the FP compared with the MP and LP (FP and MP, P = 0.049; FP and LP, P = 0.009). Moreover, the myometrium f values indicated no statistical difference in the MP, FP, and LP (MP and FP, P = 0.284; MP and LP, P = 0.997; LP and FP, P = 0.282) (Tables 2, 3 and Figure 3).

The myometrium had highly overlapping ratios (60.00%–86.67%) and no apparent differences in overlapping intervals between phases in the IVIM-DWI parameters (Table 4, Figure 4).

Table 2. Comparison of ADC, *D*, *D**, and f values in different periods of the menstrual cycle in the endometrium, UJZ, and myometrium

Value of IVIM-DWI parameter	ADC ($\times10^{-3}$ mm²/s)	D ($\times10^{-3}$ mm²/s)	D* ($\times10^{-3}$ mm²/s)	f (%)
Endometrium				
MP of endometrium	0.98 ± 0.18	0.74 ± 0.19	28.30 (1.51–127.23)	19.80 (4.59–66.47)
LP of endometrium	1.34 ± 0.18	1.08 ± 0.24	20.07 (4.41–151.90)	23.47 (6.14–62.10)
FP of endometrium	1.42 ± 0.25	1.08 ± 0.21	18.97 (2.82–101.63)	28.00 ± 12.37
UJZ				
MP of UJZ	1.06 ± 0.14	0.73 ± 0.17	73.12 ± 60.28	27.87 ± 9.67
LP of UJZ	1.15 ± 0.17	0.85 ± 0.17	77.75 ± 51.65	24.79 ± 12.30
FP of UJZ	1.14 (0.75–1.72)	0.85 ± 0.17	80.16 ± 64.69	27.08 ± 10.61
Myometrium				
MP of myometrium	1.40 ± 0.25	0.85 ± 0.14	30.16 (8.39–106.26)	32.33 (17.97–62.10)
LP of myometrium	1.52 ± 0.25	0.90 ± 0.17	50.03 (9.60–165.53)	30.91 ± 5.53
FP of myometrium	1.58 ± 0.30	0.92 ± 0.20	28.63 (7.68–140.80)	31.87 (13.90–64.40)

IVIM-DWI, intravoxel incoherent motion diffusion-weighted imaging; ADC, apparent diffusion coefficient; *D*, pure molecular diffusion coefficient; *D**, perfusion-related diffusion coefficient; *f*, perfusion fraction; MP, menses phase; FP, follicular phase; LP, luteal phase; UJZ, uterine junctional zone.

Discussion

The endometrium is divided into basal and functional layers, with changes to the endometrium occurring in the functional layer.[20] The thickness of the endometrium is approximately 1–4, 12–13, and 16–18 mm in the MP, LP, and FP, respectively.[21] During the MP, changes in phenotype involve the release of proinflammatory cytokines, chemokines, and matrix metalloproteinases, leading to the collapse of the shallow endometrial layer, focal bleeding, and menstrual shedding.[22] Conversely, mesenchyme cells have relatively high or high edema and

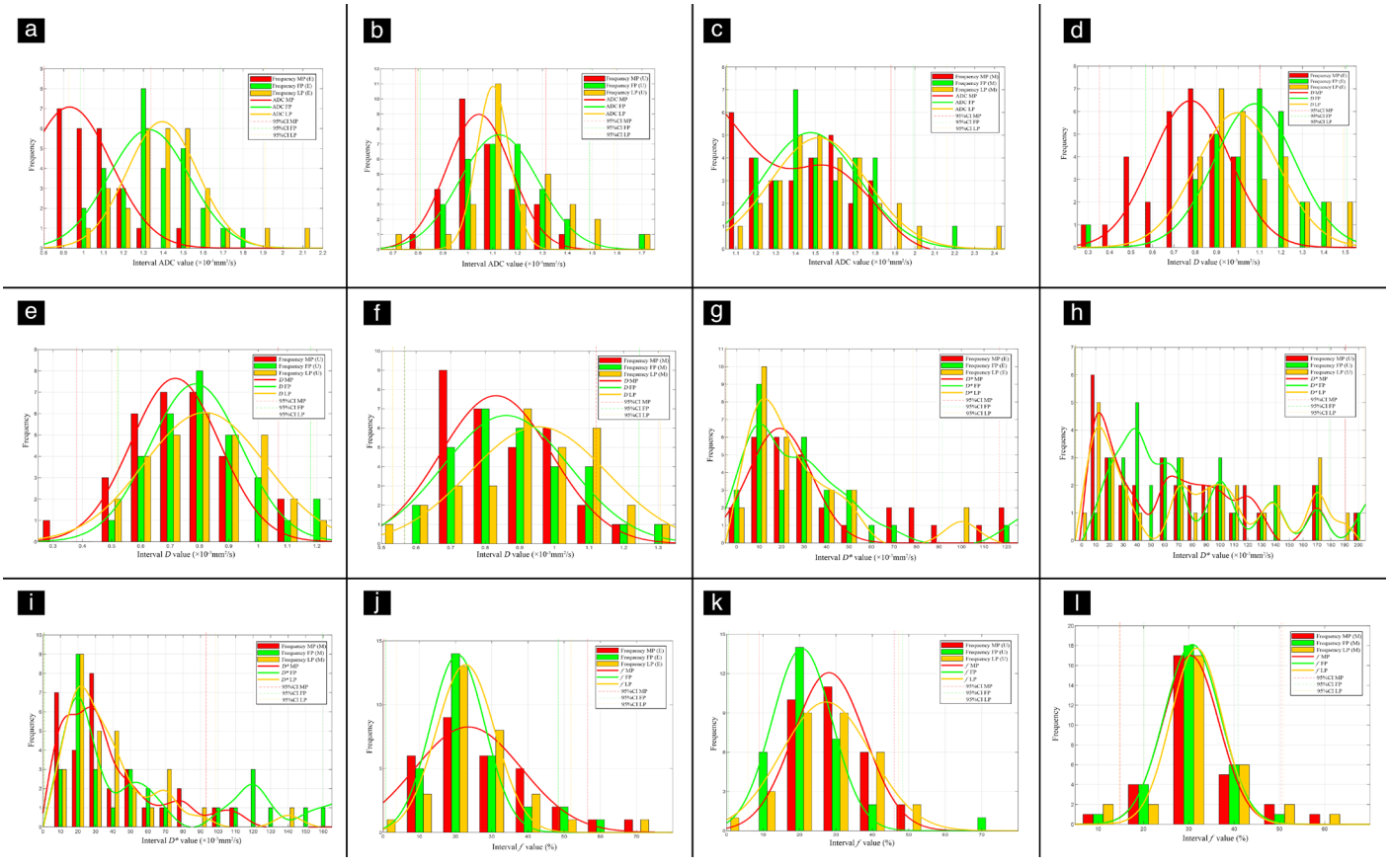

Figure 4. (a-l) Histogram and fitted curve graph of the overlapping conditions. MP, menses phase; FP, follicular phase; LP, luteal phase; ADC, apparent diffusion coefficient, CI, confidence interval.

are lost during spiral arteriole hyperplasia in the LP and FP.[23-25] In this study, we found that lower ADC and *D* values produced offset fitted curves for the MP and smaller overlapping intervals and lower overlapping ratios in the MP and LP/FP in terms of ADC and *D* values, consistent with endometrial physiology. These findings support the rationale that water molecule diffusion in endometrial cells decreases with the shedding of edematous mesenchyme cells in the functional layer.

After the demise of the corpus luteum and progesterone level decrease, UJZ-dominated and myometrium-involved anterograde (from the fundus of the uterus to the cervix) contractility increases with an increase in uterine contraction (UC) breadth, frequency, and resting tone. Unlike retrograde contraction during the LP and FP, anterograde contraction in the MP significantly increases in intensity and frequency to empty the uterine contents.[26] UCs are often felt by women during the MP, sometimes experienced as an aching feeling (dysmenorrhea). Furthermore, UC can cause the endometrium to be drawn into the myometrium, leading to endometriosis.[27] Substantial constriction from the UJZ and myometrium may cause the blood to flow out of the muscular layer, with the decrease in blood volume leading to a decrease in water content. Contraction forces the smooth muscle cells to tighten, which may be why the ADC and *D* values reduce during the MP.[28] The myometrium exhibits decreased signal intensity under conventional MRI, and the UJZ is unclear in T2-weighted images during the MP. However, the myometrium has higher signal intensity and the UJZ architecture is clearly defined during the LP.[1] This phenomenon may indirectly indicate that the myometrium and UJZ have tight myometrium structures. UC during the MP reduces water molecules in tissues. In the present study, although the UJZ and myometrium ratios overlapped by more than 50%, the fitted curve and highest frequencies were also offset to the left for lower ADC and *D* values in the MP (Figure 4), similar to the endometrium.

Tan et al.[29] reported that the pulsatility index peaked on the day of the luteinizing hormone surge in the dominant and non-dominant uterine arteries during the FP. The dominant uterine artery pulsatility index then declined from the peak to a low level in the mid-LP. The hemodynamic changes correlated with the variations in serum estradiol and progesterone concentrations. Fur-

Table 3. *P* value of the parameter comparison between different menstrual cycle phases in the endometrium, UJZ, and myometrium

P value of IVIM-DWI parameter	ADC	D	*D**	f
Endometrium				
MP vs. FP	<0.001	<0.001	0.171	0.770
MP vs. LP	<0.001	<0.001	0.061	0.651
LP vs. FP	0.133	0.668	0.753	0.410
UJZ				
MP vs. FP	0.008	0.008	0.753	0.370
MP vs. LP	<0.001	0.006	0.703	0.794
LP vs. FP	0.203	0.954	0.873	0.256
Myometrium				
MP vs. FP	0.033	0.041	0.049	0.284
MP vs. LP	0.006	0.045	0.980	0.997
LP vs. FP	0.168	0.624	0.009	0.282

IVIM-DWI, intravoxel incoherent motion diffusion-weighted imaging; ADC, apparent diffusion coefficient; *D*, pure molecular diffusion coefficient; *D**, perfusion-related diffusion coefficient; f, perfusion fraction; MP, menses phase; FP, follicular phase; LP, luteal phase; UJZ, uterine junction zone.

Table 4. Overlapping conditions during different phases of the menstrual cycle based on IVIM-DWI parameters and uterine structure

	Overlapping interval of M (ADC, *D*, *D**: $\times10^{-3}$ mm²/s; *f*: %)	Overlapping interval of UJZ (ADC, *D*, *D**: $\times10^{-3}$ mm²/s; *f*: %)	Overlapping interval of E (ADC, *D*, *D**: $\times10^{-3}$ mm²/s; *f*: %)	Overlapping ratios of M (%)	Overlapping ratios of UJZ (%)	Overlapping ratios of E (%)
ADC						
MP vs. FP	1.2–1.8	0.9–1.3	1.0–1.3	73.33	76.67	33.33
MP vs. LP	1.2–1.8	0.9–1.3	1.0–1.3	70.00	70.00	23.33
FP vs. LP	1.2–1.8	0.9–1.4	1.0–1.6	70.00	66.67	76.67
D						
MP vs. FP	0.7–1.1	0.6–1.0	0.6–1.1	83.33	73.33	40.00
MP vs. LP	0.7–1.1	0.6–1.0	0.7–1.1	60.00	63.33	43.33
FP vs. LP	0.5–1.2	0.6–1.1	0.7–1.4	66.67	80.00	76.67
D*						
MP vs. FP	10–70	10–130	10–70	53.33	60.00	66.67
MP vs. LP	10–70	10–140	10–50	60.00	73.33	70.00
FP vs. LP	10–70	10–140	0–50	66.67	63.33	80.00
f						
MP vs. FP	20–40	20–40	10–40	86.67	63.33	73.33
MP vs. LP	20–50	20–40	10–50	80.00	80.00	73.33
FP vs. LP	20–40	10–40	10–40	86.67	70.00	73.33

IVIM-DWI, intravoxel incoherent motion diffusion-weighted imaging; ADC, apparent diffusion coefficient; *D*, pure molecular diffusion coefficient; *D**, perfusion-related diffusion coefficient; *f*, perfusion fraction; M, myometrium; U, uterine junctional zone; E, endometrium; MP, menses phase; FP, follicular phase; LP, luteal phase.

thermore, Raine-Fenning et al.[30] noted that both the endometrial and sub-endometrial vascularization index and vascularization flow index increased during the FP, peaking 3 days before ovulation before decreasing to the lowest point 5 days post-ovulation. Similar to Tan et al.[29], our study revealed that *D** values, which denote the level of the tissue body fluid or blood perfusion, were high during the FP; however, no obvious differences were observed in the histogram and fitted curve graph. This may be due to the low sample size and discrete interval of *D** values. Differences in the myometrium were also identified during the menstrual cycle in the T2-weighted MRI scans.[1] The UJZ did not exhibit a similar variation in our study, possibly due to the priority levels of the uterine artery blood supply.

IVIM imaging is a new method for probing tissue perfusion and diffusion without using a contrast agent and has been applied in clinical studies of uterus lesions.[13,15,16,31] However, most studies[13,15,31] fail to explain or describe menstrual cycle details. From the results of our study, the different phases of the menstrual cycle demonstrated significant differences in IVIM-derived parameters, especially in the endometrium for low overlapping ratios between phases, which could undermine the credibility of studies. Therefore, based on the rigor of clinical research, we suggest that studies of the uterus and IVIM should be conducted during the same phase of the menstrual cycle, if possible.

This study has some strengths. First, we presented explainable results for DWI and IVIM for the uterus during the menstrual cycle that are consistent with current physiology and similar research. Therefore, DWI and IVIM can be used as techniques for human clinical research for the functional or metabolic change in the menstrual cycle based on the premise of social ethics. Second, although DWI and IVIM have been widely used in the diffuse and focal lesions of the uterus, few studies have considered changes in the menstrual cycle. We considered that the stability of the DWI and IVIM parameters in the uterus were reliable indicators for relevant studies. Because DWI and IVIM can change during the menstrual cycle, choosing an appropriate phase of the menstrual cycle for clinical research using the DWI and IVIM can ensure the relative stability of the baseline characteristics of participants; completing the relevant research during the same phase of the menstrual cycle would be more effective.

We acknowledge several limitations in our study. First, this is a single-center and small sample study. Our findings need validation through large-scale studies. Second, due to the small sample size and limited space, a subgroup analysis based on age and fertility was not applied. Third, subjective bias may exist for one observer, especially in *D** values.[11,32,33] Finally, although we applied enema and FOCUS technology in multiple *b*-value scans, artifacts from gas in the rectum or colon may still have occurred, affecting the quality of the DWI and IVIM mappings.

In conclusion, our findings demonstrate that parameters derived from ADCs and IVIM can detect differences in the uterus in diverse phases of the menstrual cycle, especially regarding ADC and *D* values in the endometrium, which could have a baseline impact on DWI and IVIM.

Acknowledgments

We thank Medjaden Inc. for the scientific editing of this manuscript.

Conflict of interest disclosure

The authors declared no conflicts of interest.

Funding

This study was funded by the Zhuhai Medical Research Project in 2022 (2220009000170).

References

1. Takeuchi M, Matsuzaki K, Nishitani H. Manifestations of the female reproductive organs on MR images: changes induced by various physiologic states. *Radiographics*. 2010;30(4):1147. [CrossRef]
2. Demas BE, Hricak H, Jaffe RB. Uterine MR imaging: effects of hormonal stimulation. *Radiology*. 1986;159(1):123-126. [CrossRef]
3. McCarthy S, Tauber C, Gore J. Female pelvic anatomy: MR assessment of variations during the menstrual cycle and with use of oral contraceptives. *Radiology*. 1986;160(1):119-123. [CrossRef]
4. Kido A, Kataoka M, Koyama T, Yamamoto A, Saga T, Togashi K. Changes in apparent diffusion coefficients in the normal uterus during different phases of the menstrual cycle. *Br J Radiol*. 2010;83(990):524-528. [CrossRef]
5. Kılıçkesmez Ö, Fırat Z, Oygen A, et al. Diffusion tensor imaging of the uterine zones related to the menstrual cycle and menopausal status at 3 tesla MRI. *Balkan Med J*. 2016;33(6):607-613. [CrossRef]
6. Li Y, Lai M, Li Q, Fu C, Zhang Q. Cyclic changes in T2* relaxometry of human uterus during the menstrual cycle using BOLD MR imaging. *Eur J Radiol*. 2022;156:110563. [CrossRef]
7. Tao YY, Zhou Y, Wang R, et al. Progress of intravoxel incoherent motion diffusion-weighted imaging in liver diseases. *World J Clin Cases*. 2020;8(15):3164-3176. [CrossRef]
8. Nougaret S, Horta M, Sala E, et al. Endometrial cancer MRI staging: updated guidelines of the european society of urogenital radiology. *Eur Radiol*. 2019;29(2):792-805. [CrossRef]
9. Jha RC, Zanello PA, Ascher SM, Rajan S. Diffusion-weighted imaging (DWI) of adenomyosis and fibroids of the uterus. *Abdom Imaging*. 2014;39(3):562-569. [CrossRef]
10. Inoue C, Fujii S, Kaneda S, et al. Correlation of apparent diffusion coefficient value with prognostic parameters of endometrioid carcinoma. *J Magn Reson Imaging*. 2015;41(1):213-219. [CrossRef]
11. Lee Y, Lee SS, Kim N, et al. Intravoxel incoherent motion diffusion-weighted MR imaging of the liver: effect of triggering methods on regional variability and measurement repeatability of quantitative parameters. *Radiology*. 2015;274(2):405-415. [CrossRef]
12. Meng N, Fang T, Feng P, et al. Amide proton transfer-weighted imaging and multiple models diffusion-weighted imaging facilitates preoperative risk stratification of early-stage endometrial carcinoma. *J Magn Reson Imaging*. 2021;54(4):1200-1211. [CrossRef]
13. Liu J, Wan Y, Wang Z, Qi Y, Qu P, Liu Y. Perfusion and diffusion characteristics of endometrial malignancy based on intravoxel incoherent motion MRI at 3.0 T: comparison with normal endometrium. *Acta Radiol*. 2016;57(9):1140-1148. [CrossRef]
14. Li YT, Cercueil JP, Yuan J, Chen W, Loffroy R, Wáng YX. Liver intravoxel incoherent motion (IVIM) magnetic resonance imaging: a comprehensive review of published data on normal values and applications for fibrosis and tumor evaluation. *Quant Imaging Med Surg*. 2017;7(1):59-78. [CrossRef]
15. Satta S, Dolciami M, Celli V, et al. Quantitative diffusion and perfusion MRI in the evaluation of endometrial cancer: validation with histopathological parameters. *Br J Radiol*. 2021;94(1125):20210054. [CrossRef]
16. Hu Q, Jiang P, Feng Y, et al. Noninvasive assessment of endometrial fibrosis in patients with intravoxel incoherent motion MR imaging. *Sci Rep*. 2021;11(1):12887. [CrossRef]
17. Zhang Q, Ouyang H, Ye F, et al. Feasibility of intravoxel incoherent motion diffusion-weighted imaging in distinguishing adenocarcinoma originated from uterine corpus or cervix. *Abdom Radiol (NY)*. 2021;46(2):732-744. [CrossRef]
18. Yoshimaru D, Miyati T, Suzuki Y, et al. Diffusion kurtosis imaging with the breath-

hold technique for staging hepatic fibrosis: a preliminary study. *Magn Reson Imaging*. 2018;47:33-38. [CrossRef]

19. Le Bihan D, Breton E, Lallemand D, Aubin ML, Vignaud J, Laval-Jeantet M. Separation of diffusion and perfusion in intravoxel incoherent motion MR imaging. *Radiology*. 1988;168(2):497-505. [CrossRef]
20. Critchley HOD, Maybin JA, Armstrong GM, Williams ARW. Physiology of the endometrium and regulation of menstruation. *Physiol Rev*. 2020;100(3):1149-1179. [CrossRef]
21. Giri SK, Nayak BL, Mohapatra J. Thickened endometrium: when to intervene? A clinical conundrum. *J Obstet Gynaecol India*. 2021;71(3):216-225. [CrossRef]
22. Blanks AM, Brosens JJ. Progesterone action in the myometrium and decidua in preterm birth. *Facts Views Vis Obgyn*. 2012;4(3):33-43. [CrossRef]
23. Demir R, Yaba A, Huppertz B. Vasculogenesis and angiogenesis in the endometrium during menstrual cycle and implantation. *Acta Histochem*. 2010;112(3):203-214. [CrossRef]
24. Dey SK, Lim H, Das SK, et al. Molecular cues to implantation. *Endocr Rev*. 2004;25(3):341-373. [CrossRef]
25. Gellersen B, Brosens IA, Brosens JJ. Decidualization of the human endometrium: mechanisms, functions, and clinical perspectives. *Semin Reprod Med*. 2007;25(6):445-453. [CrossRef]
26. de Ziegler D, Bulletti C, Fanchin R, Epiney M, Brioschi PA. Contractility of the nonpregnant uterus: the follicular phase. *Ann N Y Acad Sci*. 2001;943:172-184. [CrossRef]
27. Salamanca A, Beltrán E. Subendometrial contractility in menstrual phase visualized by transvaginal sonography in patients with endometriosis. *Fertil Steril*. 1995;64(1):193-195. [CrossRef]
28. Togashi K, Nakai A, Sugimura K. Anatomy and physiology of the female pelvis: MR imaging revisited. *J Magn Reson Imaging*. 2001;13(6):842-849. [CrossRef]
29. Tan SL, Zaidi J, Campbell S, Doyle P, Collins W. Blood flow changes in the ovarian and uterine arteries during the normal menstrual cycle. *Am J Obstet Gynecol*. 1996;175(3 Pt 1):625-631. [CrossRef]
30. Raine-Fenning NJ, Campbell BK, Kendall NR, Clewes JS, Johnson IR. Quantifying the changes in endometrial vascularity throughout the normal menstrual cycle with three-dimensional power Doppler angiography. *Hum Reprod*. 2004;19(2):330-338. [CrossRef]
31. Bhosale P, Ramalingam P, Ma J, et al. Can reduced field-of-view diffusion sequence help assess microsatellite instability in FIGO stage 1 endometrial cancer? *J Magn Reson Imaging*. 2017;45(4):1216-1224. [CrossRef]
32. Lecler A, Savatovsky J, Balvay D, et al. Repeatability of apparent diffusion coefficient and intravoxel incoherent motion parameters at 3.0 Tesla in orbital lesions. *Eur Radiol*. 2017;27(12):5094-5103. [CrossRef]
33. Pieper CC, Sprinkart AM, Kukuk GM, Mürtz P. Short-term measurement repeatability of a simplified intravoxel incoherent motion (IVIM) analysis for routine clinical diffusion-weighted imaging in malignant liver lesions and liver parenchyma at 1.5T. *Rofo*. 2019;191(3):199-208. [CrossRef]

Diagn Interv Radiol 2023; DOI: 10.4274/dir.2023.232149

ARTIFICIAL INTELLIGENCE AND INFORMATICS

ORIGINAL ARTICLE

Deep learning reconstruction for brain diffusion-weighted imaging: efficacy for image quality improvement, apparent diffusion coefficient assessment, and intravoxel incoherent motion evaluation in *in vitro* and *in vivo* studies

Satomu Hanamatsu
Kazuhiro Murayama
Yoshiharu Ohno
Kaori Yamamoto
Masao Yui
Hiroshi Toyama

PURPOSE

Deep learning reconstruction (DLR) to improve imaging quality has already been introduced, but no studies have evaluated the effect of DLR on diffusion-weighted imaging (DWI) or intravoxel incoherent motion (IVIM) in *in vitro* or *in vivo* studies. The purpose of this study was to determine the effect of DLR for magnetic resonance imaging (MRI) in terms of image quality improvement, apparent diffusion coefficient (ADC) assessment, and IVIM index evaluation on DWI through *in vitro* and *in vivo* studies.

METHODS

For the *in vitro* study, a phantom recommended by the Quantitative Imaging Biomarkers Alliance was scanned and reconstructed with and without DLR, and 15 patients with brain tumors with normal-appearing gray and white matter examined using IVIM and reconstructed with and without DLR were included in the *in vivo* study. The ADCs of all phantoms for DWI with and without DLR, as well as the coefficient of variation percentage (CV%), and ADCs and IVIM indexes for each participant, were evaluated based on DWI with and without DLR by means of region-of-interest measurements. For the *in vitro* study, using the mean ADCs for all phantoms, a t-test was adopted to compare DWI with and without DLR. For the *in vivo* study, a Wilcoxon signed-rank test was used to compare the CV% between the two types of DWI. In addition, the Wilcoxon signed-rank test was used to compare the ADC, true diffusion coefficient (*D*), pseudodiffusion coefficient (*D**), and percentage of water molecules in micro perfusion within 1 voxel (*f*) with and without DLR; the limits of agreement of each parameter were determined through a Bland–Altman analysis.

RESULTS

The *in vitro* study identified no significant differences between the ADC values for DWI with and without DLR ($P > 0.05$), and the CV% was significantly different for DWI with and without DLR ($P < 0.05$) when *b* values ≥250 s/mm^2 were used. The *in vivo* study revealed that *D** and *f* with and without DLR were significantly different ($P < 0.001$). The limits of agreement of the ADC, *D*, and *D** values for DWI with and without DLR were determined as $0.00 \pm 0.51 \times 10^{-3}$, $0.00 \pm 0.06 \times 10^{-3}$, and $1.13 \pm 4.04 \times 10^{-3}$ mm^2/s, respectively. The limits of agreement of the *f* values for DWI with and without DLR were determined as −0.01 ± 0.07.

CONCLUSION

Deep learning reconstruction for MRI has the potential to significantly improve DWI quality at higher *b* values. It has some effect on *D** and *f* values in the IVIM index evaluation, but ADC and *D* values are less affected by DLR.

KEYWORDS

Brain, magnetic resonance imaging, diffusion, intravoxel incoherent motion, deep learning reconstruction

From the Department of Radiology (S.H. ✉ shana@fujita-hu.ac.jp, K.M., Y.O., H.T.), Fujita Health University School of Medicine, Toyoake, Japan; Joint Research Laboratory of Advanced Medicine Imaging (Y.O.), Fujita Health University School of Medicine, Toyoake, Japan; Canon Medical Systems Corporation (K.Y., M.Y.), Otawara, Japan.

Received 21 February 2023; revision requested 05 April 2023; last revision received 29 May 2023; accepted 23 June 2023.

Epub: 09.08.2023

Publication date: 05.09.2023

DOI: 10.4274/dir.2023.232149

You may cite this article as: Hanamatsu S, Murayama K, Ohno Y, Yamamoto K, Yui M, Toyama H. Deep learning reconstruction for brain diffusion-weighted imaging: efficacy for image quality improvement, apparent diffusion coefficient assessment, and intravoxel incoherent motion evaluation in *in vitro* and *in vivo* studies. *Diagn Interv Radiol.* 2023;29(5):664-673.

The clinical application of artificial intelligence is expanding with a variety of targets not only for detection or diagnostics but also for image noise reduction for computed tomography (CT) and magnetic resonance imaging (MRI).[1-10] In recent years, some MRI suppliers have introduced deep learning reconstruction (DLR) for denoising and improving imaging quality, which has been tested for MRI of the central nervous system as well as of the body.[1-10] Moreover, in the late 1980s, Le Bihan et al.[11] developed intravoxel incoherent motion (IVIM), a non-invasive approach that measures perfusion-related parameters using diffusion-weighted imaging (DWI) for MR examinations.[12-22] This method exploits the fact that the signal acquired using a DWI sequence is affected by the incoherent motion of water resulting not only from thermal energy but also blood circulation in the microvasculature.[11-22] To date, however, no studies have evaluated the efficacy of DLR for apparent diffusion coefficient (ADC) evaluation or IVIM index assessments in *in vivo* or *in vitro* studies.

We hypothesized that DLR may affect IVIM index measurements, possibly without influencing ADC measurements, by denoising and improving DWI quality. The purpose of this study was therefore to determine the efficacy of DLR for MRI on image quality improvement, ADC assessment, and IVIM index evaluation in DWI through *in vitro* and *in vivo* studies using a 3 Tesla (T) MR system.

Main points

- The *in vitro* study identified no significant differences in apparent diffusion coefficient values for diffusion-weighted imaging (DWI) with and without deep learning reconstruction (DLR) ($P > 0.05$).
- There were significant differences in coefficient of variation percentages between the DWI with and without DLR ($P < 0.05$) when b values of 250, 500, 750, 1000, and 1500 s/mm^2 were used.
- There were significant differences in the pseudodiffusion coefficient and percentage of water molecules in micro perfusion within 1 voxel values between the DWI with and without DLR ($P < 0.001$).

Methods

Research ethics standards compliance

The *in vivo* study was a retrospective study and was approved by the Institutional Review Board (IRB) of Fujita Health University, Japan (research registration: HM22-328; IRB-approval number: CI22-647); it is compliant with the Health Insurance Portability and Accountability Act of Japan. Written informed consent was waived for each participant enrolled in this study. This study was also technically and financially supported by the Canon Medical Systems Corporation. Two of the authors are employees of the Canon Medical Systems Corporation (KY and MY) but did not have control over any of the data used in this study.

Quantitative diffusion phantom for *in vitro* study

The *in vitro* study quantitatively assessed an ADC evaluation of DWI obtained with and without using the DLR method. For this study, the quantitative diffusion phantom (High Precision Devices, Boulder, CO, USA), which was developed by the National Institute of Standards and Technology/Quantitative Imaging Biomarker Alliance (QIBA) of the Radiological Society of North America and is commercially available, consisting of 13 vials filled with varying concentrations of polyvinylpyrrolidone (PVP) in an aqueous solution, was used to evaluate ADC measurement accuracy.[23,24] The phantom was specifically designed to quantitatively map the isotropic Gaussian diffusion of water molecules and generate physiologically relevant ADC values.[25] The distribution of PVP concentrations in the phantom was as follows: 0% (vials 1–3), 10% (vials 4 and 5), 20% (vials 6 and 7), 30% (vials 8 and 9), 40% (vials 10 and 11), and 50% (vials: 12 and 13) in an aqueous solution.[24] The vials were stored in an ice-water bath at 0°C to eliminate thermal variability across scanner locations and timepoints for the ADC measurements.[23]

Participants in the *in vivo* study

The *in vivo* study involved 314 consecutive patients (146 men, 168 women; mean age: 59.8 years; age range: 18–91 years) who had been diagnosed with a suspected brain tumor at nearby hospitals. The participants visited the outpatient clinic in our department of neurosurgery between March and August 2019, where they were examined using brain MRI with IVIM. The exclusion criteria were 1) mass effect of a brain tumor or peritumoral edema on a slice at the basal-ganglia level, 2) contraindications for MR examination, 3) contraindication for gadolinium (Gd) contrast media because of asthma, 4) renal dysfunction, and 5) severe motion artifact. Of the 314 patients originally included in this study, 299 were excluded because of the mass effect of brain tumor or peritumoral edema on a slice at basal-ganglia level (n = 287), contraindications for MR examination because of claustrophobia (n = 2) and having a cardiac pacemaker device (n = 1), contraindication for Gd contrast media because of asthma (n = 2) and renal disfunction (n = 4), and severe motion artifact (n = 3). The remaining 15 patients with brain tumors with normal-appearing gray and white matter (8 men, 7 women; mean age: 49.6 years; age range: 31–82 years) were included in this study. The patient selection chart is presented in Figure 1, and details of patient characteristics are summarized in Table 1.

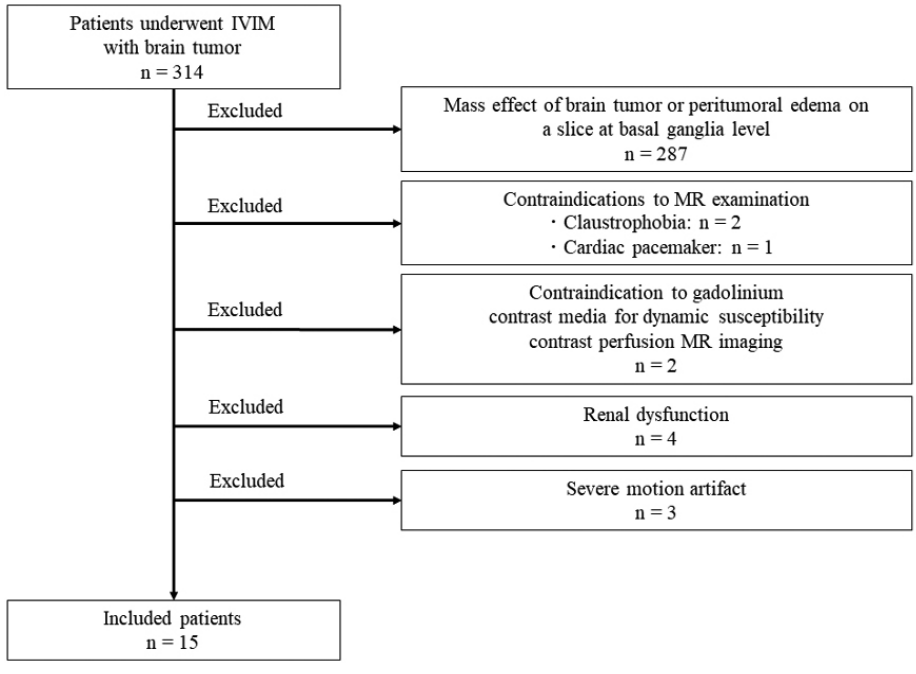

Figure 1. Patient selection chart. Patient selection for the final study population. IVIM, intravoxel incoherent motion; MR, magnetic resonance.

Magnetic resonance examinations

All MR examinations for the *in vitro* and *in vivo* studies were performed using a 3T clinical MR scanner (Vantage Galan 3T/ZGO, Canon Medical Systems Corporation, Otawara, Tochigi, Japan) with a 32-channel phased-array surface coil (32 ch Head SPEEDER, Canon Medical Systems). The maximal gradient specifications were 100 mT/m for amplitude and 200 mT/m/msec for slew rate.

In vitro study

For the *in vitro* study, DWI was acquired in the axial planes using a two-dimensional spin-echo (SE)-type echo-planar imaging (EPI) sequence with a parallel imaging technique (SPEEDER, Canon Medical Systems) and the following parameters: repetition time (TR)/echo time (TE), 4500/66 ms; field of view (FOV), 220 × 220 mm; acquisition matrix, 144 × 144; slice thickness, 4 mm; reduction factor (SPEEDER factor), 3; number of acquisition (NAQ), 1; *b* values, 0, 10, 25, 50, 75, 100, 250, 500, 750, 1000, 1500, 2000, and 3000 s/mm^2. All MRI was then reconstructed with and without the DLR method (Advanced Intelligent Clear-IQ Engine, Canon Medical Systems), which is consistent with other studies,[3,5,10] and operated using an MRI system (version 6 SP0003, Canon Medical Systems).

Table 1. Patient characteristics

Variables		Values
Sex (count, %)	Male	8 (53.3%)
	Female	7 (46.7%)
Age as mean ± standard deviation (years, range)		49.6 ± 17.6 (28–82)
Diagnosis (count)	Low-grade gliomas (grade 1, 2)	5
	Schwannomas	4
	Meningiomas	2
	Central neurocytoma	1
	Arachnoid cyst	1
	Metastases	1
	Malignant peripheral nerve sheath tumor	1

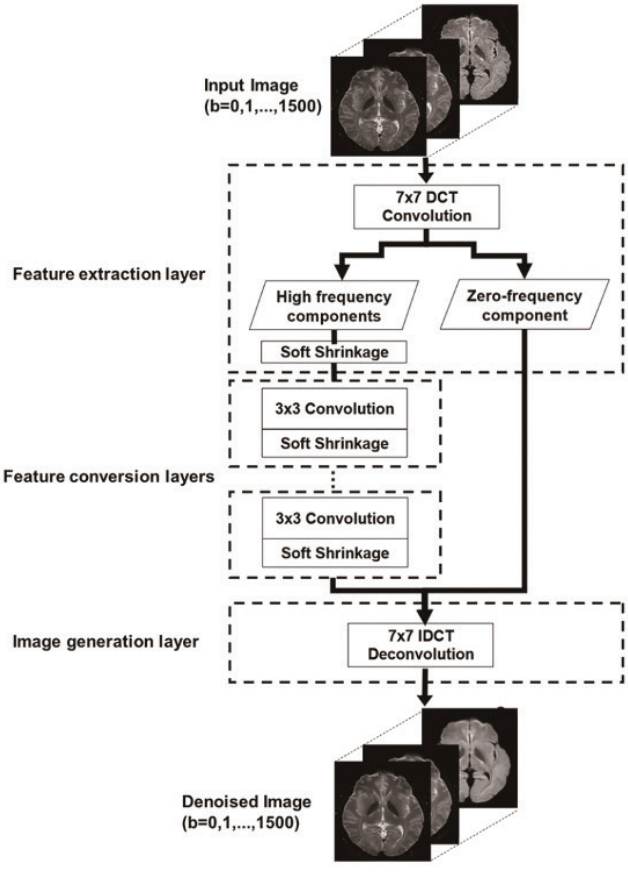

Figure 2. Deep learning reconstruction network. In the first feature extraction layer, input images (b = 0, 1, …, 1500) are convolved using a 7 × 7 discrete cosine transform (DCT) kernel. After the initial soft shrinkage, 48 high frequency components undergo a 3 × 3 convolution repeatedly and soft shrinkage in the feature conversion layers. Finally, the denoised output images (b = 0, 1, …, 1500) are generated through the inverse DCT deconvolution of both the bypassed zero-frequency component and output data from the feature conversion layers.

In vivo study

For the *in vivo* study, DWI was acquired in the axial planes using the SE-EPI sequence with SPEEDER and the following parameters: TR/TE, 4500/72 ms; echo train spacing, 0.9 ms; number of slices, 30; slice thickness; 5 mm; FOV, 220 × 220 mm; acquisition matrix, 160 × 160; NAQ, 1; flip angle, 90/180; SPEEDER factor, 3; *b* values, 0, 5, 10, 20, 30, 50, 75, 100, 250, 500, 750, 1000, and 1500 s/mm^2. All MRI data were then reconstructed with and without DLR, as in the *in vitro* study.[3,5,10] The examination time including reconstruction time with and without DLR was recorded for each participant.

Deep learning reconstruction method for brain diffusion-weighted imaging

The DLR method used in this study is based on a convolutional neural network (CNN), and the details have been published in the literature.[3] Figure 2 provides a diagram of the DLR method. A study has proposed CNN denoising using soft shrinkage, which adapts to the amount of noise by introducing a variable threshold of an inactive section, as an activation function;[26] noise-adaptive soft shrinkage is also applied to the neural network in the DLR method.[1] The present study used the same trained DLR network described in the literature.[3] The network was trained and validated using conventional contrast images (T2 weighted, T1 weighted, etc.) of the brain and knees of several human volunteers.[3] The quality of the different contrast images reconstructed using the DLR method was clinically evaluated in several body regions, such as the brain,[3] pelvis,[5] and abdominal arteries.[27] The DLR details, including information on training and validation data sets, are provided in the literature.[3,5,10]

Image analysis

In vitro study

First, an ADC map was generated from the DWI for all *b* values. Signal intensity data obtained from each voxel on the DWI for all *b* values were fitted to a mono-exponential model to calculate the ADC using a built-in Tensor application (System software version 6.0, Canon Medical Systems). The ADC for each phantom was then measured by a neuroradiologist (SH) with 3-years' experience using ImageJ version 1.52p (https://imagej.nih.gov/ij/). Five circular regions of interest (ROIs) with a diameter of 10 mm were placed on the center slice and two additional slices, one obtained 1 cm before and the other 1 cm after the center slice, as well as on each phantom, after which the mean ADC value within each phantom was calculated.

In vivo study

An ADC map was generated for each patient from the DWI reconstructed with and without DLR for *b* values of 0 s/mm^2 and others (i.e., *b* = 5, 10, 20, 30, 50, 75, 100, 250, 500, 750, 1000, and 1500 s/mm^2) by means of commercially available software (IVIM) using a mono-exponential model on a Vitrea workstation (version 7.4, Canon Medical Systems). In addition, IVIM parameters were determined using commercially available software (IVIM) on the same workstation and based on the theory described in other studies.[11-15] Based on a bi-exponential model derived from DWI with different *b* values, the true diffusion coefficient (*D*), pseudodiffusion coefficient (*D**), and percentage of water molecules in micro perfusion within 1 voxel (*f*) were determined using the following previously published formula:[11-15]

$$S(b)/S_0 = f_{ivim} \exp\left[-b\left(D^* + D_{blood}\right)\right] + \left(1 - f_{ivim}\right) \exp\left(-bD_{tissue}\right) \quad [1]$$

where *S(b)* is the signal intensity for each *b* value and S_0 is the signal intensity at a *b* value of zero.

To quantitatively evaluate the influence of DLR on the DWI obtained at each *b* value for all patients, ROIs were measured using the Vitrea workstation. A center line was first placed manually on each slice. Subsequently, ROIs with a diameter of 10 mm were automatically placed on the normal cortex and white matter of a slice at basal-ganglia level obtained from each brain hemisphere (total of 10 ROIs = 5 ROIs × right and left hemisphere) to determine the mean signal intensity and standard deviation for ROIs on each slice. An example of ROI placements is provided in Supplementary Figure 1. For a quantitative image quality comparison of DWI obtained for each *b* value and reconstructed with and without DLR, the coefficient of variation percentages (CVs%) of the DWI for each *b* value with and without DLR were calculated by means of the following previously published formula:[10,28-30]

CV% = standard deviation within ROI/mean signal intensity within ROI × 100% [2]

To determine the influence of DLR on all DWI parameter evaluations, ADC, *D*, *D**, and *f* values from the automatically copied ROIs were measured on the same slices on ADC, *D*, *D**, and *f* maps for each patient.

Statistical analysis

In vitro study

To determine the influence of DLR on ADC measurements, mean ADCs measured within each phantom on DWIs with and without DLR were correlated with standard references and with each other using Spearman's correlation coefficient. To determine the effect of DLR on ADC evaluation, mean ADCs for each phantom were then compared in DWI with and without DLR by means of a t-test. A Bland–Altman analysis was then performed to determine the limits of agreement between the DWI with and without DLR.[31,32]

In vivo study

To compare the IVIM examination time, including reconstruction with and without DLR, the mean IVIM examination time with DLR and that without DLR was compared using Wilcoxon's signed-rank test.

To determine the utility of DLR for image quality improvement on the DWI at each *b* value, the Wilcoxon signed-rank test was used to compare CV% in the DWI with and without DLR. To determine the influence of DLR on ADC and IVIM index evaluations, ADC, *D**, *D*, and *f* values were compared in the DWI with and without DLR by means of the Wilcoxon signed-rank test. Finally, the Bland–Altman analysis was used to evaluate the limits of agreement of the ADC and each IVIM index for DWI with and without DLR.[31,32]

Results

In vitro study

The correlations of ADC values for DWI with and without DLR with nominal ADC values as standard references are presented in Figure 3. The ADC values for DWI with and without DLR significantly and strongly correlated with those for standard references (with DLR: r = 0.99, $P < 0.0001$; without DLR: r = 0.99, $P < 0.0001$) and between DWI with and without DLR (r = 0.99, $P < 0.0001$).

Table 2 provides a comparison of ADC values for DWI with and without DLR for the *in vitro* study. The ADC values for DWI with and without DLR in the *in vitro* study were not significantly different ($P > 0.05$).

The results of the Bland–Altman analysis are presented in Figure 4. The limit of agreement between the ADC values for DWI with and without DLR and standard reference values was determined as $-0.03 \pm 0.04 \times 10^{-3}$ mm^2/s. In addition, the limit of agreement of ADC values for DWI with and without DLR was determined as $-0.00 \pm 0.01 \times 10^{-3}$ mm^2/s.

Table 2. Comparison of ADC values within each phantom for DWI with and without DLR

Concentration of phantom (%)	ADC with DLR ($\times 10^{-3}$ mm^2/s)	ADC without DLR ($\times 10^{-3}$ mm^2/s)	Upper and lower limits of agreement ($\times 10^{-3}$ mm^2/s)	*P* value
0	1.18 ± 0.01	1.17 ± 0.01	0.00 ± 0.02	0.09
10	0.89 ± 0.01	0.88 ± 0.01	0.00 ± 0.01	0.43
20	0.64 ± 0.01	0.63 ± 0.01	0.00 ± 0.01	0.37
30	0.42 ± 0.01	0.42 ± 0.01	0.00 ± 0.01	0.99
40	0.26 ± 0.01	0.26 ± 0.01	0.00 ± 0.01	0.83
50	0.14 ± 0.01	0.14 ± 0.01	0.00 ± 0.01	0.75

ADC, apparent diffusion coefficient; DLR, deep learning reconstruction; DWI, diffusion-weighted imaging.

In vivo study

An example case is presented in Figure 5.

The mean examination time, including reconstruction time, of DLR (256 ± 4 s, range: 247–261 s) was significantly different from that without DLR (208 ± 4 s, range: 199–213 s, $P < 0.001$).

The results of the comparison of CV% of each phantom for DWI with and without DLR are summarized in Table 3. The CV% was significantly different for DWI with and without DLR ($P < 0.05$) when *b* values equal to or higher than 250 s/mm^2 were used.

The results of the comparisons of ADC, *D*, *D**, and *f* for DWI with and without DLR are presented in Table 4, and the results for the limits of agreements for ADC, *D*, *D**, and *f* for DWI with and without DLR are illustrated in Figure 6; *D** and *f* were significantly different for DWI with and without DLR ($P < 0.001$). The limit of agreement of ADC values for DWI with and without DLR was determined as 0.00 ± 0.51 × 10^{-3} mm^2/s, the limit of agreement of *D* values for DWI with and without DLR was determined as 0.00 ± 0.06 × 10^{-3} mm^2/s, the

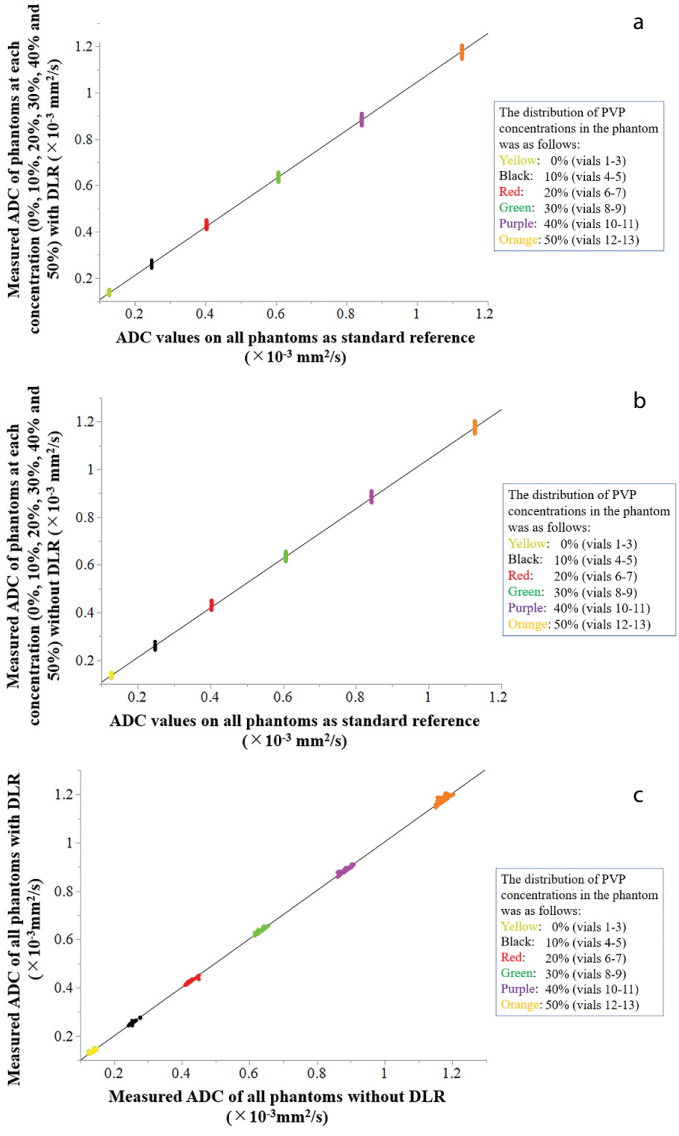

Figure 3. Correlations between apparent diffusion coefficient (ADC) values for diffusion-weighted imaging (DWI) with and without deep learning reconstruction (DLR) and standard reference values and between DWI with and without DLR [yellow: polyvinylpyrrolidone (PVP) concentration within the phantom of 0%, black: PVP concentration within the phantom of 10%, red: PVP concentration within the phantom of 20%, green: PVP concentration within the phantom of 30%, purple: PVP concentration within the phantom of 40%, and orange: PVP concentration within the phantom of 50%]. **(a)** ADC values for DWI with DLR and the standard reference values exhibit significant and strong correlations (r = 0.99, $P < 0.0001$). **(b)** ADC values for DWI without DLR and the standard reference values reveal significant and strong correlations (r = 0.99, $P < 0.0001$). **(c)** ADC values for DWI with and without DLR demonstrate significant and strong correlations (r = 0.99, $P < 0.0001$).

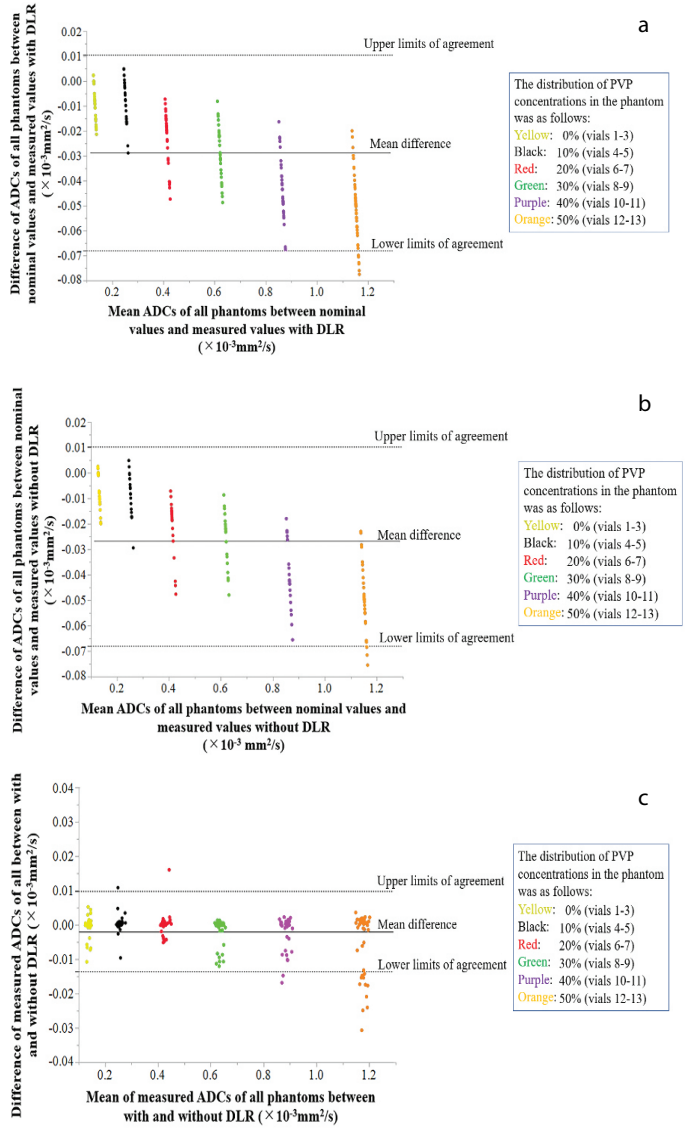

Figure 4. Mean differences and the limits of agreement of apparent diffusion coefficient (ADC) values for diffusion-weighted imaging (DWI) with and without deep learning reconstruction (DLR) and standard reference values and between DWI with and without DLR [yellow: polyvinylpyrrolidone (PVP) concentration within the phantom of 0%, black: PVP concentration within the phantom of 10%, red: PVP concentration within the phantom of 20%, green: PVP concentration within the phantom of 30%, purple: PVP concentration within the phantom of 40%, and orange: PVP concentration within the phantom of 50%]. Mean differences are indicated by solid lines; upper and lower limits of agreement are indicated as dotted lines at the top and bottom, whereas plotted dots indicate data points. **(a)** Limits of agreement of ADC values for DWI with DLR and standard reference values were assessed as between −0.07 × 10^{-3} and −0.01 × 10^{-3} mm^2/s. **(b)** Limits of agreement of ADC values for DWI without DLR and standard reference values were assessed as between −0.07 × 10^{-3} and −0.01 × 10^{-3} mm2/s. **(c)** Limits of agreement of ADC values for DWI with and without DLR were assessed as between −0.01 × 10^{-3} and 0.01 × 10^{-3} mm^2/s.

limit of agreement of *D** values for DWI with and without DLR was determined as 1.13 ± 4.04 × 10^{-3} mm^2/s, and the limit of agreement of *f* values for DWI with and without DLR was determined as –0.01 ± 0.07.

Discussion

Our study used *in vitro* and *in vivo* studies to determine the effect of DLR on ADC or IVIM parameter evaluations. This study was also the first to demonstrate that DLR had no effect on ADC evaluations in a QIBA-recommended diffusion phantom. In addition, the *in vivo* study was the first to determine that DLR had little effect on ADC and *D* evaluations using brain DWI or on brain IVIM examinations when *b* values were set at equal to or less than 1500 s/mm^2. However, *D** and *f* values were significantly different for IVIM with and without DLR when IVIM examinations applied the same *b* values. To the best of our knowledge, no other study has assessed the influence of DLR on ADC and IVIM parameter evaluations in *in vitro* or *in vivo* studies.

When the examination time, including reconstruction time, for IVIM with and without DLR was compared, IVIM with DLR exhibited a significantly longer mean examination time than that for IVIM without DLR; however, the acquisition time for IVIM was the same. Therefore, the prolongation of the mean examination time in IVIM with DLR was considered to mainly result from the significantly longer reconstruction time when compared with that of IVIM without DLR.

Our *in vitro* study demonstrated that correlations between ADC values assessed through DWI with and without DLR were significant and strong, whereas the differences between them were non-significant. Moreover, the limit of agreement for DWI with or without DLR compared with that for standard reference values can be considered negligible and small enough for clinical purposes. Therefore, DLR was determined to have little or no influence on ADC evaluations in this setting.

As for the *in vivo* study, we determined that DLR could significantly improve the CV% of DWI for *b* values set at equal to or more than 250, 500, 750, 1000, and 1500 s/mm^2. These results suggest that DWI at *b* values equal to or more than 250 s/mm^2 may feature an increase in image noise level and be decreased by it. When considering the equation for CV%, the standard deviation within ROIs may have predominantly Gaussian noise but additionally include spatial variation resulting from the anatomy. More-

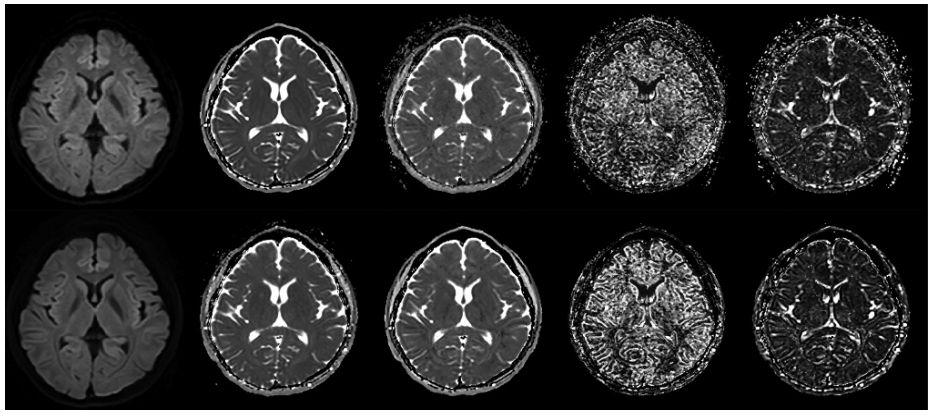

Figure 5. Diffusion-weighted imaging (DWI) (*b* = 1000 s/mm^2) and apparent diffusion coefficient (ADC), *D*, *D**, and *f* maps reconstructed with and without deep learning reconstruction (DLR). Upper row, L to R: DLR. Lower row, L to R: DWI at *b* = 1000 s/mm^2 and ADC, *D*, *D**, and *f* maps reconstructed with DLR. When DLR was applied, the contrast between gray and white matter was improved because of the image noise reduction on the DWI, *D**, and *f* maps. ADC and *D* maps exhibit only a slight reduction in noise. *D*, true diffusion coefficient; *D**, pseudodiffusion coefficient, *f*, percentage of water molecules in micro perfusion within 1 voxel.

Table 3. Comparison of the CV% for diffusion-weighted imaging with and without DLR at various *b* values for the *in vivo* study

b (s/mm^2)	CV% (mean ± standard deviation)		*P* value
	With DLR	Without DLR	
0	6.7 ± 2.2	6.7 ± 1.9	0.34
5	6.2 ± 2.2	6.2 ± 2.0	0.37
10	6.1 ± 2.2	6.1 ± 2.0	0.95
20	6.2 ± 2.1	6.1 ± 1.9	0.97
30	6.1 ± 2.2	6.1 ± 2.0	0.84
50	6.0 ± 2.2	5.9 ± 2.0	0.36
75	5.9 ± 2.0	5.9 ± 1.8	0.10
100	5.8 ± 2.0	5.8 ± 1.8	0.09
250	5.5 ± 1.6	5.6 ± 1.5	<0.001
500	5.3 ± 1.5	5.4 ± 1.4	<0.001
750	5.3 ± 1.4	5.5 ± 1.4	<0.001
1000	5.4 ± 1.5	5.7 ± 1.5	<0.001
1500	6.7 ± 1.7	7.1 ± 1.7	<0.001

CV%, coefficient of variation percentage; DLR, deep learning reconstruction; DWI, diffusion-weighted imaging.

Table 4. Comparison of intravoxel incoherent motion measurements for DWI with and without DLR for the *in vivo* study

	With DLR (mean ± standard deviation)	Without DLR (mean ± standard deviation)	*P* value
ADC (×10^{-3} mm^2/s)	1.04 ± 0.22	1.04 ± 0.21	0.66
***D* (×10^{-3} mm^2/s)**	0.75 ± 0.08	0.74 ± 0.07	0.30
***D** (×10^{-3} mm^2/s)**	11.62 ± 1.84	10.49 ± 1.98	<0.001
f	0.08 ± 0.02	0.09 ± 0.03	<0.001

DWI, diffusion-weighted imaging; DLR, deep learning reconstruction; *D*, true diffusion coefficient; *D**, pseudodiffusion coefficient; *f*, percentage of water molecules in micro perfusion within 1 voxel.

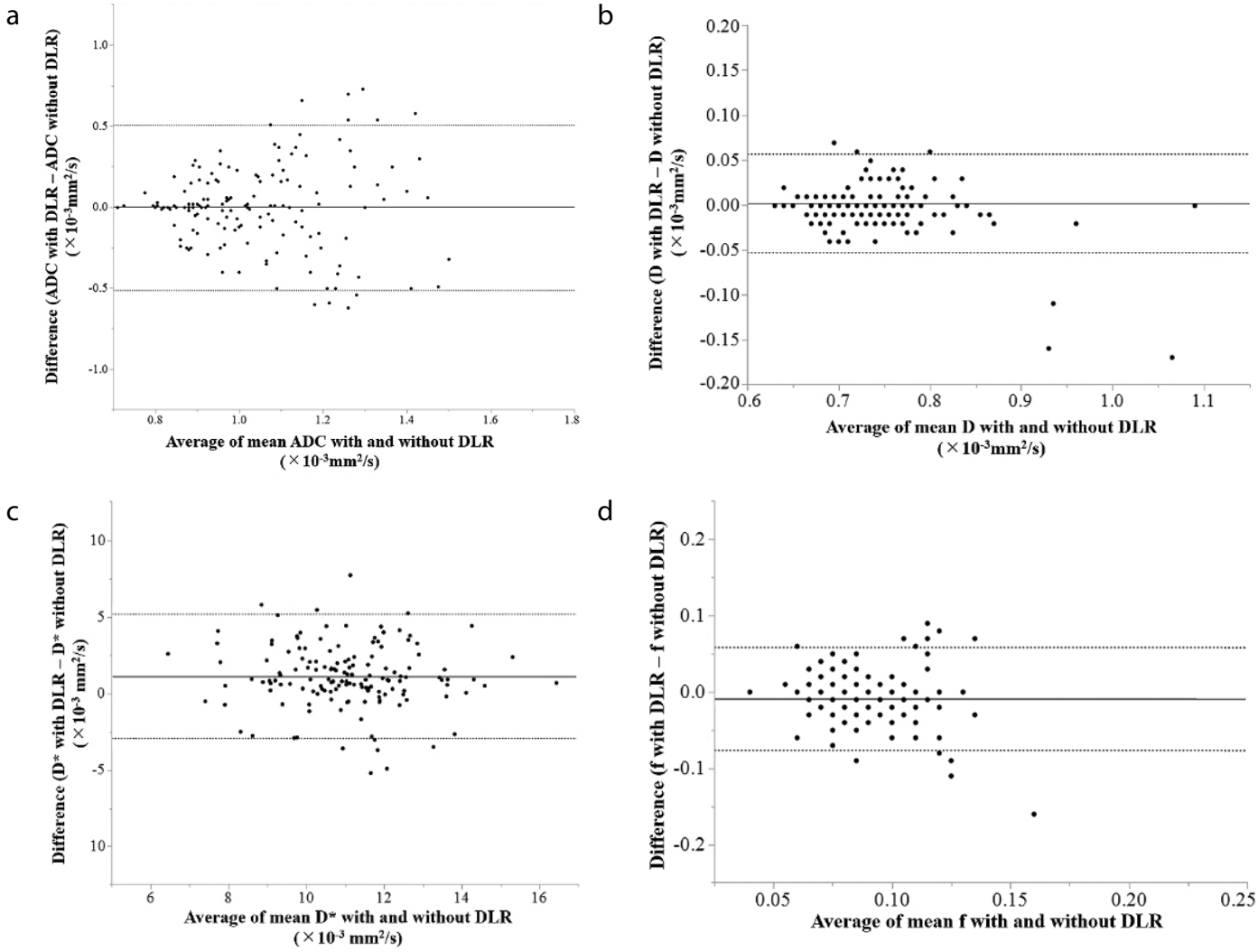

Figure 6. Limits of agreement of apparent diffusion coefficient (ADC), *D*, *D**, and *f* values between diffusion-weighted imaging (DWI) and intravoxel incoherent motion (IVIM) with and without deep learning reconstruction (DLR). Mean difference is denoted by a solid line; upper and lower limits of agreement are denoted by dashed lines at the top and bottom; circles denote data points. **(a)** Mean difference and the limits of agreement of ADC values for DWI with and without DLR. The limits of agreement are determined as $0.00 \pm 0.51 \times 10^{-3}$ mm²/s. **(b)** Mean difference and the limits of agreement of *D* values for IVIM with and without DLR. The limits of agreement are determined as $0.00 \pm 0.06 \times 10^{-3}$ mm²/s. **(c)** Mean difference and the limits of agreement of *D** values for IVIM with and without DLR. The limits of agreement are determined as $1.13 \pm 4.04 \times 10^{-3}$ mm²/s. **(d)** Mean difference and the limits of agreement of *f* values for IVIM with and without DLR. The limits of agreement are determined as −0.01 ± 0.07. *D*, true diffusion coefficient; *D**, pseudodiffusion coefficient, *f*, percentage of water molecules in micro perfusion within 1 voxel.

over, DWI with higher *b* values tends to provide lower signal intensity in brain tissues than that of Gaussian noise; therefore, DLR can improve CV% more effectively when *b* values are higher. Thus, DLR is a viable choice for improving DWI with higher *b* values, such as ≥250 s/mm², which is often used in routine clinical practice. For lower *b* values, such as <250 s/mm², it is widely known that the signal of fluid components, such as cerebrospinal fluid and blood, remains. These components could provide additional spatial variation within ROIs, where reconstruction parameters with and without DLR affect the spatial variation of DWI differently. This situation may impact the statistical significance of the CV% with and without DLR. Our results therefore indicate that DLR should be used for obtaining DWI at *b* values equal to or more than 250 s/mm² to improve image quality in routine clinical practice. Moreover, DLR for denoising MRI has been tested not only for image quality improvement but also for a reduction in acquisition time using compressed sensing or other k-space data acquisition methods for various clinical aims on DWI as well as other MR sequences since 2021.[5,8,10,33-38] Therefore, it would be better for us to clinically apply DLR not only for denoising but also to reduce the examination time when using other techniques, although this study did not apply any techniques to reduce acquisition time.

A comparison of ADC and IVIM indexes for brain DWI with and without DLR in the *in vivo* study revealed that the ADC of DWI for *b* values equal to or less than 1500 s/mm² were not significantly different. This result is compatible with that for our *in vitro* study. Moreover, we identified no significant difference in *D* for DWI with and without DLR when routine *b* values of less than 1500 s/mm² were used. However, *D** and *f* significantly influenced DLR when subjected to the same IVIM examination. The reasons for these results can be easily surmised when the similarity of the mechanisms underlying the models for those previously described are considered.[11-22] Our results for the *in vitro* and *in vivo* studies demonstrate that ADC and *D* measurements for DWI with *b* values equal to or less than 1500 s/mm² can be assumed to have no effect on DLR in this setting. Howev-

er, *b* values of more than 1500 s/mm^2 should be used carefully because these values might have some effect on the DLR results when considering the results of DWI for detecting prostate cancer, for which *b* values equal to or more than 3000 s/mm^2 and DLR are used.[10]

In contrast to the ADC or *D* measurements obtained from DWI and IVIM examinations with and without DLR, we determined that *D** and *f* were significantly affected by DLR, even though there were no significant differences in the CV% of DWI with and without DLR at *b* values lower than 250 s/mm^2. In this study, DWI with and without DLR was generated from the same DWI data obtained from the same sequence and reconstructed with and without DLR. Moreover, all IVIM indexes were measured by means of a commercially available IVIM model. These facts and findings lead us to consider that the differences in *D** and *f* in DWI with and without DLR might be the result of some interaction in the *in vivo* study between signal intensity and image noise within each voxel. Therefore, DLR may be useful for improving the quality of DWI as well as each DWI in the IVIM examinations and have limited influence on quantitative ADC and IVIM parameter evaluations in routine clinical practice.

This study has several limitations. First, we did not have an IVIM phantom or perform animal studies for IVIM in the *in vitro* study. Moreover, the scan parameters for the *in vitro* and *in vivo* studies were not fully matched because of different quantitative DWI index evaluations, and this study is a retrospective study, with no healthy volunteers included. Second, we applied commercially available software, using a mono-exponential model, for IVIM index calculations and assessed the influence of the reconstruction method on these calculations; other models, such as stretched exponential or tri-exponential models, were not tested in this study. Moreover, no comparison between DLR and non-DLR methods for denoising DWI or IVIM images was used, and no standard reference was determined, with only the differences in the ADC or each IVIM index between DWI and IVIM with and without DLR evaluated. To the best of our knowledge, no commercially available MRI phantom exists locally that contains multiple diffusion and circulation compartments and is suitable for IVIM quantification. This type of standardized phantom could be useful for clinicians to validate new advanced techniques in acquisition, reconstruction, and post-processing; therefore, we are now planning to study and develop this type of phantom in the near future. Further investigations are also warranted to determine the effect of DLR on IVIM evaluations using different models for *in vitro* and *in vivo* studies. Third, the study population was too small to allow for evaluations of patients with a variety of brain diseases; the tumor types of the 15 patients involved in our study were highly heterogeneous, which may affect the study results. Further investigations are therefore warranted to determine the influence of DLR on IVIM parameters as well as on clinical outcomes. Fourth, the *b* values used in this study were equal to or less than 1500 s/mm^2 even though *b* values of more than 1500 s/mm^2 are currently and frequently used for brain DWI examinations for various purposes.[10,39-41] Further investigations are therefore warranted that use DLR for brain DWI examinations with *b* values higher than 1500 s/mm^2. Fifth, no comparisons were made in this study of the *D** and *f* values of the DWI with and without DLR and perfusion parameters from other perfusion MR and CT techniques and nuclear medicine studies. Sixth, this study used DLR provided by a single supplier for IVIM calculations in the *in vivo* study; however, the clinical relevance of IVIM examinations is currently evaluated primarily for academic purposes rather than clinical aims. Finally, the IVIM sequence and software used here have not yet been standardized. Multi-center studies using DLR and IVIM software provided by different suppliers are thus warranted for standardization and the determination of clinical relevance for the brain and other organs. Large prospective cohort studies using a variety of MR scanners, DLR algorithms, and IVIM software provided by different suppliers are also warranted, and we will plan these studies to address these issues in the near future.

In conclusion, DLR for MRI has the potential to significantly improve the quality of DWI with higher *b* values. It also has some effect on *D** and *f* values for IVIM examination, whereas ADC and *D* values are less affected by DLR.

Conflict of interest disclosure

The authors declared no conflicts of interest.

Funding

This study was technically and financially supported by the Canon Medical Systems Corporation. Drs Ohno, Murayama, and Toyama had or have research grants from Canon Medical Systems.

References

1. Higaki T, Nakamura Y, Tatsugami F, Nakaura T, Awai K. Improvement of image quality at CT and MRI using deep learning. *Jpn J Radiol*. 2019;37(1):73-80. [CrossRef]
2. Higaki T, Nakamura Y, Zhou J, et al. deep learning reconstruction at CT: phantom study of the image characteristics. *Acad Radiol*. 2020;27(1):82-87. [CrossRef]
3. Kidoh M, Shinoda K, Kitajima M, et al. Deep Learning Based Noise Reduction for Brain MR imaging: tests on phantoms and healthy volunteers. *Magn Reson Med Sci*. 2020;19(3):195-206. [CrossRef]
4. Gavazzi S, van den Berg CAT, Savenije MHF, et al. Deep learning-based reconstruction of *in vivo* pelvis conductivity with a 3D patch-based convolutional neural network trained on simulated MR data. *Magn Reson Med*. 2020;84(5):2772-2787. [CrossRef]
5. Ueda T, Ohno Y, Yamamoto K, et al. Compressed sensing and deep learning reconstruction for women's pelvic MRI denoising: utility for improving image quality and examination time in routine clinical practice. *Eur J Radiol*. 2021;134:109430. [CrossRef]
6. Lin DJ, Johnson PM, Knoll F, Lui YW. Artificial intelligence for MR image reconstruction: an overview for clinicians. *J Magn Reson Imaging*. 2021;53(4):1015-1028. [CrossRef]
7. Matsukiyo R, Ohno Y, Matsuyama T, et al. Deep learning-based and hybrid-type iterative reconstructions for CT: comparison of capability for quantitative and qualitative image quality improvements and small vessel evaluation at dynamic CE-abdominal CT with ultra-high and standard resolutions. *Jpn J Radiol*. 2021;39(2):186-197. [CrossRef]
8. Sagawa H, Fushimi Y, Nakajima S, et al. Deep learning-based noise reduction for fast volume diffusion tensor imaging: assessing the noise reduction effect and reliability of diffusion metrics. *Magn Reson Med Sci*. 2021;20(4):450-456. [CrossRef]
9. Johnson PM, Tong A, Donthireddy A, et al. Deep learning reconstruction enables highly accelerated biparametric MR imaging of the prostate. *J Magn Reson Imaging*. 2022;56(1):184-195. [CrossRef]
10. Ueda T, Ohno Y, Yamamoto K, et al. Deep learning reconstruction of diffusion-weighted MRI improves image quality for prostatic imaging. *Radiology*. 2022;303(2):373-381. [CrossRef]
11. Le Bihan D, Breton E, Lallemand D, Grenier P, Cabanis E, Laval-Jeantet M. MR imaging of intravoxel incoherent motions: application to diffusion and perfusion in neurologic disorders. *Radiology*. 1986;161(2):401-407. [CrossRef]
12. Le Bihan D, Breton E, Lallemand D, Aubin ML, Vignaud J, Laval-Jeantet M. Separation of diffusion and perfusion in intravoxel

incoherent motion MR imaging. *Radiology*. 1988;168(2):497-505. [CrossRef]

13. Turner R, Le Bihan D, Maier J, Vavrek R, Hedges LK, Pekar J. Echo-planar imaging of intravoxel incoherent motion. *Radiology*. 1990;177(2):407-414. [CrossRef]
14. Federau C. Intravoxel incoherent motion MRI as a means to measure in vivo perfusion: a review of the evidence. *NMR Biomed*. 2017;30(11). [CrossRef]
15. Le Bihan D. What can we see with IVIM MRI? *Neuroimage*. 2019;187:56-67. [CrossRef]
16. Iima M, Honda M, Sigmund EE, Ohno Kishimoto A, Kataoka M, Togashi K. Diffusion MRI of the breast: current status and future directions. *J Magn Reson Imaging*. 2020;52(1):70-90. [CrossRef]
17. Zhang JL, Lee VS. Renal perfusion imaging by MRI. *J Magn Reson Imaging*. 2020;52(2):369-379. [CrossRef]
18. Wang YXJ, Huang H, Zheng CJ, Xiao BH, Chevallier O, Wang W. Diffusion-weighted MRI of the liver: challenges and some solutions for the quantification of apparent diffusion coefficient and intravoxel incoherent motion. *Am J Nucl Med Mol Imaging*. 2021;11(2):107-142. [CrossRef]
19. Federau C. Measuring perfusion: intravoxel incoherent motion mr imaging. *Magn Reson Imaging Clin N Am*. 2021;29(2):233-242. [CrossRef]
20. Ma W, Mao J, Wang T, Huang Y, Zhao ZH. Distinguishing between benign and malignant breast lesions using diffusion weighted imaging and intravoxel incoherent motion: a systematic review and meta-analysis. *Eur J Radiol*. 2021;141:109809. [CrossRef]
21. Wang DJJ, Le Bihan D, Krishnamurthy R, Smith M, Ho ML. Noncontrast pediatric brain perfusion: arterial spin labeling and intravoxel incoherent motion. *Magn Reson Imaging Clin N Am*. 2021;29(4):493-513. [CrossRef]
22. Englund EK, Reiter DA, Shahidi B, Sigmund EE. Intravoxel incoherent motion magnetic resonance imaging in skeletal muscle: review and future directions. *J Magn Reson Imaging*. 2022;55(4):988-1012. [CrossRef]
23. Yung JP, Ding Y, Hwang KP, et al. Quantitative Evaluation of apparent diffusion coefficient in a large multi-unit institution using the QIBA diffusion phantom. *medRxiv*. 2020. [CrossRef]
24. Shukla-Dave A, Obuchowski NA, Chenevert TL, et al. Quantitative Imaging Biomarkers Alliance (QIBA) recommendations for improved precision of DWI and DCE-MRI derived biomarkers in multicenter oncology trials. *J Magn Reson Imaging*. 2019;49(7):e101-e121. [CrossRef]
25. Federau C, O'Brien K, Meuli R, Hagmann P, Maeder P. Measuring brain perfusion with intravoxel incoherent motion (IVIM): initial clinical experience. *J Magn Reson Imaging*. 2014;39(3):624-632. [CrossRef]
26. Isogawa K, Ida T, Shiodera T, Takeguchi T. Deep Shrinkage convolutional neural network for adaptive noise reduction. *IEEE Signal Processing Letters*. 2018;25(2):224-228. [CrossRef]
27. Maubon AJ, Ferru JM, Berger V, et al. Effect of field strength on MR images: comparison of the same subject at 0.5, 1.0, and 1.5 T. *Radiographics*. 1999;19(4):1057-1067. [CrossRef]
28. Voroney JP, Brock KK, Eccles C, Haider M, Dawson LA. Prospective comparison of computed tomography and magnetic resonance imaging for liver cancer delineation using deformable image registration. *Int J Radiat Oncol Biol Phys*. 2006;66(3):780-791. [CrossRef]
29. Zierhut ML, Ozturk-Isik E, Chen AP, Park I, Vigneron DB, Nelson SJ. (1)H spectroscopic imaging of human brain at 3 Tesla: comparison of fast three-dimensional magnetic resonance spectroscopic imaging techniques. *J Magn Reson Imaging*. 2009;30(3):473-480. [CrossRef]
30. Spinks TJ, Karia D, Leach MO, Flux G. Quantitative PET and SPECT performance characteristics of the Albira Trimodal pre-clinical tomograph. *Phys Med Biol*. 2014;59(3):715-731. [CrossRef]
31. Bland JM, Altman DG. Statistical methods for assessing agreement between two methods of clinical measurement. *Lancet*. 1986;1(8476):307-310. [CrossRef]
32. Bland JM, Altman DG. Comparing methods of measurement: why plotting difference against standard method is misleading. *Lancet*. 1995;346(8982):1085-1087. [CrossRef]
33. Park JC, Park KJ, Park MY, Kim MH, Kim JK. Fast T2-weighted imaging with deep learning-based reconstruction: evaluation of image quality and diagnostic performance in patients undergoing radical prostatectomy. *J Magn Reson Imaging*. 2022;55(6):1735-1744. [CrossRef]
34. Bae SH, Hwang J, Hong SS, et al. Clinical feasibility of accelerated diffusion weighted imaging of the abdomen with deep learning reconstruction: Comparison with conventional diffusion weighted imaging. *Eur J Radiol*. 2022;154:110428. [CrossRef]
35. Matsuyama T, Ohno Y, Yamamoto K, et al. Comparison of utility of deep learning reconstruction on 3D MRCPs obtained with three different k-space data acquisitions in patients with IPMN. *Eur Radiol*. 2022;32(10):6658-6667. [CrossRef]
36. Tajima T, Akai H, Sugawara H, et al. Feasibility of accelerated whole-body diffusion-weighted imaging using a deep learning-based noise-reduction technique in patients with prostate cancer. *Magn Reson Imaging*. 2022;92:169-179. [CrossRef]
37. Obama Y, Ohno Y, Yamamoto K, et al. MR imaging for shoulder diseases: Effect of compressed sensing and deep learning reconstruction on examination time and imaging quality compared with that of parallel imaging. *Magn Reson Imaging*. 2022;94:56-63. [CrossRef]
38. Afat S, Herrmann J, Almansour H, et al. Acquisition time reduction of diffusion-weighted liver imaging using deep learning image reconstruction. *Diagn Interv Imaging*. 2023;104(4):178-184. [CrossRef]
39. Mardor Y, Roth Y, Ochershvilli A, et al. Pretreatment prediction of brain tumors' response to radiation therapy using high b-value diffusion-weighted MRI. *Neoplasia*. 2004;6(2):136-142. [CrossRef]
40. Kitajima K, Takahashi S, Ueno Y, et al. Clinical utility of apparent diffusion coefficient values obtained using high b-value when diagnosing prostate cancer using 3 tesla MRI: comparison between ultra-high b-value (2000 s/mm^2) and standard high b-value (1000 s/mm^2). *J Magn Reson Imaging*. 2012;36(1):198-205. [CrossRef]
41. Tavakoli AA, Kuder TA, Tichy D, et al. Measured multipoint ultra-high b-value diffusion MRI in the assessment of MRI-detected prostate lesions. *Invest Radiol*. 2021;56(2):94-102. [CrossRef]

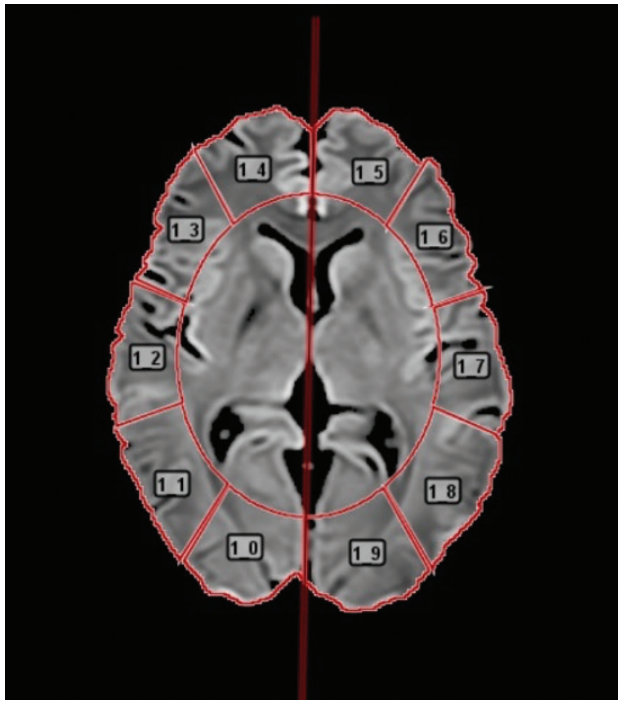

Supplementary Figure 1. Example of image analysis of diffusion-weighted imaging (DWI) with a *b* value of 1000 s/mm^2. To automatically place regions of interest (ROIs), a centerline is initially drawn manually on the DWI with a *b* value of 1000 s/mm^2 per patient. The ROIs are then automatically placed on the normal cortex and white matter in each brain hemisphere on a slice at basal-ganglia level (total of 10 ROIs = 5 ROIs × right and left hemisphere) using a commercially available workstation provided by Canon Medical Systems. The mean and standard deviation of the signal intensity within each ROI is automatically determined. To evaluate each quantitative index from the DWI and perform intravoxel incoherent motion evaluations, all ROIs are copied to the apparent diffusion coefficient (ADC), *D*, *D**, and *f* maps of each patient. Finally, the ADC, *D*, *D**, and *f* values within the ROIs are determined. *D*, true diffusion coefficient; *D**, pseudodiffusion coefficient, *f*, percentage of water molecules in micro perfusion within 1 voxel.

Diagn Interv Radiol 2023; DOI: 10.4274/dir.2022.221615

BREAST IMAGING

ORIGINAL ARTICLE

Use of shear-wave elastography to distinguish complex and complicated fibroadenomas from simple fibroadenomas

Işıl Başara Akın
Hakan Özgül
Canan Altay
Mustafa Seçil
Merih Güray Durak
Duygu Gürel
Pınar Balcı

PURPOSE

Simple fibroadenomas (SFAs), complex fibroadenomas (CFAs), and cellular fibroadenomas (CeFAs) are variants of fibroadenomas. Additionally, some degenerative, hyperplastic, and metaplastic changes may occur in fibroadenomas, forming complicated fibroadenomas. Distinctive ultrasonography (US) features in variants of fibroadenomas and complicated fibroadenomas have not been reported. Shear-wave elastography (SWE) can be applied to effectively discriminate between these variants and complicated fibroadenomas. In this study, we aimed to evaluate SWE findings to discriminate between SFAs and other variants.

METHODS

In total, 48 patients (26 with SFAs, 16 with CFAs, 3 with CeFAs, and 3 with complicated fibroadenomas) participated in this study. The lesions were classified into two groups according to histopathologic diagnoses. The SWE evaluation and lesion elasticity scores (E_{max}, E_{mean}, and E_{min}) were both assessed in m/s and k/Pa, respectively. Two observers measured E_{max}, E_{mean}, and E_{min}. Brightness (B)-mode US findings based on the Breast Imaging Reporting and Data System categorization and elasticity scores were recorded. In the statistical analyses, the chi-square test and non-parametric tests were performed. Fisher's exact test was used to compare independent groups, and Spearman's correlation coefficients were used to correlate the SWE data between the two observers. Additionally, receiver operating characteristic curves were analyzed to evaluate the diagnostic performance of the elasticity values.

RESULTS

The B-mode US features in both groups showed no statistical significance. The set of SWE values of both observers demonstrated strong statistical significance in discriminating between group 1 (SFAs) and Group 2 (CFAs, CeFAs, and complicated fibroadenomas).

CONCLUSION

As the fibroadenoma variants and complicated fibroadenomas have similar US findings, SWE in addition to a conventional B-mode examination can increase the diagnostic performance to discriminate SFAs from other complex and complicated forms of fibroadenomas.

KEYWORDS

Cellular fibroadenoma, complex fibroadenoma, complicated fibroadenoma, shearwave elastography, simple fibroadenoma, ultrasonography

The English in this document has been checked by at least two professional editors, both native speakers of English. For a certificate, please see

http://www.textcheck.com/certificate/J96xm9

From the Department of Radiology (I.B.A. ✉ slbasara@yahoo.com, C.A., M.S., P.B.), Dokuz Eylül University Faculty of Medicine, İzmir, Turkey; Department of Pathology (M.G.D., D.G.), Dokuz Eylül University Faculty of Medicine, İzmir Turkey; Clinic of Radiology (H.O.), Kemalpaşa State Hospital, İzmir, Turkey.

Received 25 April 2022; revision requested 12 Jun 2022; last revision received 30 October 2022; accepted 07 November 2022.

Epub: 23.12.2022

Publication date: 05.09.2023

DOI: 10.4274/dir.2022.221615

You may cite this article as: Başara Akın I, Özgül H, Altay C, et al. Use of shear-wave elastography to distinguish complex and complicated fibroadenomas from simple fibroadenomas. *Diagn Interv Radiol.* 2023;29(5):674-681.

Fibroadenomas are common benign breast lesions, particularly in young and adolescent female patients.[1] Of all the benign breast lesions, 50%–60% are fibroadenomas; when biopsied, 40% are diagnosed as fibroadenomas.[2,3]

Simple fibroadenomas (SFAs) consist of epithelial and stromal histologic components.[4] Fibroadenomas are classified according to their histopathologic components and features,[5] and complex fibroadenomas (CFAs) and cellular fibroadenomas (CeFAs) are two other variants.[5-7] Of all fibroadenomas, 22% are diagnosed as CFAs based on histopathologic evaluation. The rate of development of invasive breast cancer is 3.1 times higher in patients with CFAs than in the normal population. In particular, perilesional benign proliferative changes and a family history of breast cancer increase the risk of malignancy in patients with SFAs and/or CFAs.[8]

CeFAs are characterized by uniform stromal cellularity without stromal atypia, but the diagnosis can be challenging based on histopathologic evaluation because the histopathologic features usually overlap with benign phyllodes tumors.[9]

Degenerative changes, such as hyperplastic changes, squamous metaplasia, focal tubular adenoma, myoid metaplasia, myxoid degeneration, cystic changes, adipose differentiation, infarction, and osteochondroid metaplasia, may occur in fibroadenomas.[6,10,11] In addition, intraductal papillomas, including fibroadenomas, have been reported in the literature.[12] These fibroadenomas are different from the other variants and can be defined as complicated fibroadenomas. If the hyperplasia behaves similarly in normal breast tissue, the risk of developing malignancy can increase within these complicated fibroadenomas.[13]

Main points

- Ultrasonography (US) findings in fibroadenoma variants and complicated fibroadenomas are similar; distinctive US features for each entity have not been reported. Although they have similar US features, clinical evaluations and approaches differ for simple fibroadenomas (SFAs), other variants, and complicated fibroadenomas.
- As brightness-mode US does not have specific distinctive features, unnecessary surgeries and interventional procedures may occur.
- Additional US imaging methods such as shear-wave elastography can assist in discrimination between SFAs, other variants, and complicated fibroadenomas.

Ultrasonography (US) is the main diagnostic method, and lesions are evaluated according to the Breast Imaging Reporting and Data System (BI-RADS).[14] Fibroadenoma variants and complicated fibroadenomas with suspicious US characteristics are categorized as BI-RADS 4, and exact diagnoses are obtained after histopathologic evaluation. Although US findings in fibroadenoma variants and complicated fibroadenomas tend to be similar, distinctive US features for each entity have not been reported in the literature.[14] Although they have similar US features, clinical evaluations and approaches differ for SFAs, other variants, and complicated fibroadenomas.[15,16] For SFAs, follow-up at appropriate intervals is required. For CFAs and complicated fibroadenomas that are suspicious lesions, surgical excision with safe margins is recommended for treatment. Surgery also enables an accurate diagnosis of CeFAs.[1,17,18]

Additional US imaging methods such as shear-wave elastography (SWE) can assist with discrimination between SFAs, other variants, and complicated fibroadenomas. SWE is a quantitative method involving the application of an acoustic radiation force pulse sequence for shear-wave propagation.[19] Tissue stiffness affects quantitative values according to the rapidity of sound changes,[19] with malignant tissues having stiffer components and exhibiting higher velocities than benign areas.[19] These SWE features facilitate discrimination between benign and malignant lesions.[20] In addition, SWE is a useful imaging modality for differentiating benign lesions from those with a low risk of malignancy, which have indistinct brightness (B)-mode US characteristics and the same suspicious BI-RADS features.[21-23]

Although fibroadenomas are benign lesions, they may exhibit suspicious B-mode US features.[15,16] Additional imaging modalities, including SWE, may increase the diagnostic performance of conventional B-mode US.[23] Only one case series in the literature has specifically described the SWE features of CFAs.[7] To the best of our knowledge, no study has specifically evaluated the SWE findings of fibroadenoma variants. In this study, we evaluated the utility of additional SWE findings for differentiating between SFAs and other variants.

Methods

Patients

This retrospective study was approved by our Institutional Review Board, and the requirement for informed consent was waived. The non-interventional ethics committee approval protocol number was 7005-GOA, and the decision number was 2022/13-18. Patients diagnosed with SFAs, CFAs, CeFAs, or complicated fibroadenomas between January 2019 and December 2021 were included in the study. Patients with optimal B-mode US-SWE images and completed histopathologic evaluations were included in the study, whereas patients with artifactual images were not. Additionally, for an optimal histopathologic result evaluation, patients who underwent surgery in another medical center were excluded from the study. A total of 48 patients were reviewed. The patients were divided into groups 1 and 2. Patients with SFAs were classified into group 1, and patients with CFAs, CeFAs, and complicated fibroadenomas formed group 2. B-mode US and SWE images from the picture archiving and communication system (PACS) were evaluated. Lesion sizes, B-mode US findings according to BI-RADS categorization, and elasticity scores were recorded.

Histopathologic diagnosis and evaluation

Most of the lesions were diagnosed using core and/or excisional biopsy. In group 1, 10 lesions were diagnosed through core biopsy and 16 through excisional biopsy. In group 2, 5 lesions (CFAs) were diagnosed using core biopsy, and excisional biopsies were performed on 14 lesions (11 CFAs and 3 complicated fibroadenomas). One CeFA was diagnosed through direct excisional biopsy, and two were diagnosed as phyllodes tumors and one as a juvenile fibroadenoma after core biopsies. In the three CeFAs diagnosed through core biopsies, exact diagnoses were subsequently made after excisional biopsies. In the core biopsies, a 14-Gauge core needle was used. All biopsies were performed under US guidance. In each biopsy session, at least five tissue samples were extracted.

Wire-guided excisional biopsies were performed for non-palpable lesions. The diagnostic method was determined according to the patient's medical condition and preference as well as the surgeon's decision. Patients with SFAs were followed up with after diagnosis. For lesions diagnosed as CFAs or CeFAs via core biopsies, excision with tumor bed resection was performed after the core biopsy.

B-mode US evaluation

The US examinations were performed using an ML6–15 MHz linear transducer (LOGIQ S8; GE Healthcare, Milwaukee, WI, USA). All the relevant images were archived in the Sectra IDS7 PACS system (Sectra AB, Linköping, Sweden) for further evaluation.

The US examinations were performed by 3 different radiologists with 30, 17, and 6 years of breast imaging experience. All the lesions stored in the PACS system were evaluated by two radiologists with 17 and 6 years of breast imaging experience. The B-mode features were determined by consensus between the two radiologists.

The largest diameter of each lesion was measured, and general B-mode US characteristics were evaluated and recorded according to the Fifth Edition of BI-RADS US features. These features included shape (round, oval, or irregular), orientation (parallel or non-parallel), margin (circumscribed, non-circumscribed, indistinct, angular, microlobulated, or spiculated), echo pattern (hyperechoic, hypoechoic, isoechoic, or complex cystic/heterogeneous), and posterior acoustic features (no posterior acoustic features, enhancement, shadowing, or a combination of features). The lesions were then classified according to BI-RADS as follows: BI-RADS 3–probably benign; BI-RADS 4A–low suspicion of malignancy; BI-RADS 4B–intermediate suspicion of malignancy; and BI-RADS 4C–moderate suspicion of malignancy.[24]

Additional imaging evaluation

The patients were evaluated using the additional imaging methods of mammography (MG), tomosynthesis (TS) and magnetic resonance imaging (MRI). The MG and TS examinations were conducted using a MG device (Selenia, Hologic, Bedford, MA, USA). As standard, in MG, each case had four images [right–left craniocaudal and left–right mediolateral oblique (MLO)]. If required, additional positions were also obtained. Digital breast TS was conducted in MLO positions in standard modalities. The MG and TS examinations were applied to patients of appropriate ages. In all these patients, B-mode US examinations were conducted.

The MRI examinations were realized using two different 1.5 T MRI devices: 1. Intera software (version 8.1; Philips Medical Systems, Eindhoven, The Netherlands), 2. Gyroscan Achieva, (Philips, ACS-NT, Bothell, WA, USA). Phased-array breast coils were applied in the prone position. The conventional sequences were as follows: precontrast axial turbo spin echo (TSE) T1-weighted (T1W) [3-mm slice thickness, 3.3 spacing, matrix: 512 × 512, field of view (FOV): 40, repetition time (TR): 516 ms, echo time (TE): 80 ms, echo train length (ETL): 4], axial fat-saturated (SPIR) TSE T2-weighted (3-mm slice thickness, 3 spacing, matrix: 512 × 512, FOV: 40, TR: 6,700 ms, TE: 120 ms, ETL: 30), after contrast material administration (intravenously, 0.1–0.2 mmol/kg), axial dynamic gradient echo, T1W high-resolution isotropic volume examination (2-mm slice thickness, 1 spacing, matrix: 480 × 480, FOV: 40, TR: 50,000 ms, TE: 2,500 ms, ETL: 40), and late postcontrast phase, axial TSE, SPIR T1W (3-mm slice thickness, 3.3 spacing, matrix: 512 × 512, FOV: 42, TR: 550 ms, TE: 80 ms, ETL: 4). The MRI examinations were applied to the patients who had suspicious US and/or MG–TS findings to identify solutions.

SWE evaluation

The elastography features were analyzed after the B-mode US evaluation using a 9L linear transducer (LOGIQ S8; GE Healthcare). All three investigators had been trained by GE Healthcare and subsequently performed at least 20 SWE examinations under their supervision. The most important aspect of the SWE examination is avoiding probe compression to prevent pseudo stiffness. In addition, to prevent motion artifacts, the patients are asked to hold their breath and remain still during the SWE examination, if required.

In the SWE evaluation, the lesions were located within the central part of "elasticity boxes," which were as remote as possible from skin and muscle tissues (unless these tissues exhibited lesion involvement). During the examination, the probe was applied as lightly as possible to prevent pressure on the lesion. The elastography image acquisition time was approximately 10–20 s, and a shear-wave color map was obtained. The colors ranged from dark blue to red, corresponding to the lowest and highest degree of stiffness, respectively. Both B-mode US and additional SWE examinations were performed before histopathologic evaluations.

The regions of interest (ROIs) were placed on the most inelastic areas of the lesions according to the shear-wave color map. The maximum dimensions of the ROI were 3 × 3 mm. Elasticity values [E_{max}, E_{mean}, E_{min}, and standard deviation (SD)] were obtained in m/s and k/Pa. All measurements were made and recorded by radiologists with 17 and 6 years of breast imaging experience, working independently. Both radiologists were blinded to the histopathologic diagnoses of the lesions.

Statistical analysis

The patients' ages, largest lesion diameters, histopathologic diagnoses, B-mode US imaging findings, and final BI-RADS categorizations were recorded. All statistical analyses were performed using Statistical Package for the Social Sciences version 24.0 software.

The chi-square test was performed to evaluate categorical variables, and Fisher's exact test was used to compare independent groups. Non-parametric tests were used for further group analyses. The Kruskal–Wallis test was used to evaluate continuous data, which are presented as mean ± SD. The patients' ages and lesion dimensions were compared between the two groups using the non-parametric Mann–Whitney U test. The mean elasticity values were evaluated through the t-test, and Spearman's correlation coefficients were used to correlate SWE data between the two observers. Receiver operating characteristic curves were analyzed to evaluate the diagnostic performance of the elasticity values. The Youden index was used to define the optimal cut-off value, and cut-off values were then calculated in terms of sensitivity and specificity. The sensitivity, specificity, positive predictive value (PPV), and negative predictive value (NPV) of the cut-off values were measured. Statistical significance was defined as $P < 0.050$.

Results

Patients

A total of 48 patients were included in this study, of whom 26 (54.2%), diagnosed with SFAs, were assigned to group 1. Group 2 comprised 22 (45.8%) patients, including 12 and 7 with diagnoses of CFAs and CeFAs, respectively. Another three patients were diagnosed with complicated fibroadenomas (one each with intraductal papilloma, chondroid metaplasia, and myoid metaplasia).

The median (minimum–maximum) age was 47.3 (24–68) years in group 1 and 42.09 (24–65) years in group 2. There was no statistical difference in age between the groups ($P = 0.722$).

The median (minimum–maximum) diameters of the lesions in groups 1 and 2 were 14.03 (5–30) and 19.04 (9–50) mm, respectively. There was no statistical significance between the groups ($P = 0.130$).

B-mode US findings

The distributions of the B-mode US features of the lesions in both groups are presented in Table 1. There was no statistical significance between the groups. The *P* value of the echo pattern was 0.063. Although the

P value was >0.050, all patients (n = 5) with a complex cystic echo pattern were included in Group 2.

The BI-RADS classification distribution is shown in Table 2; no statistical significance was identified between the two groups in terms of the BI-RADS classification (*P* = 0.783).

Additional imaging findings

Nineteen patients in Group 1 and 14 patients in Group 2 were evaluated using MG–TS. In Group 2, 13 patients had a well-defined nodular lesion, the lesion in 1 patient was an irregular contoured lesion, and 5 patients had no findings from the MG–TS examinations. In Group 2, well-defined nodular lesions were identified in eight patients, and four had no findings.

MRI was performed on 13 patients in Group 1 and on 9 patients in Group 2. In Group 1, no enhancement was observed in two lesions in two patients. All the lesions exhibited enhancement without washout, and in two lesions, slight enhancement was observed. In Group 2, all the lesions had late phase enhancement with no washout, and five lesions were enhanced slightly. Hypointense linear septa were determined in nine patients (five in Group 1 and four in Group 2).

SWE findings

Lesion elasticity was evaluated in terms of both m/s and k/Pa. The elasticity values of E_{max}, E_{mean}, and E_{min} were obtained by two ob-

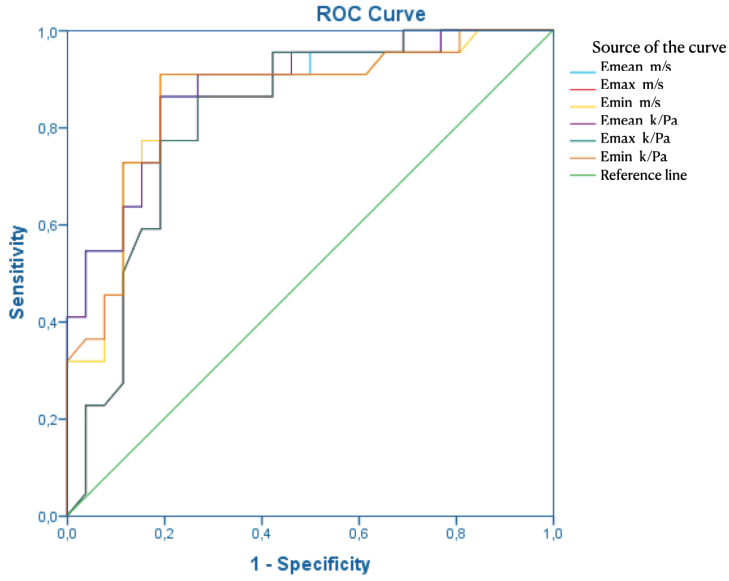

Figure 1. Receiver operating characteristic curves of the elasticity (E_{max}, E_{mean}, and E_{min}) values (in both m/s and k/Pa).

Table 1. Distribution of grayscale ultrasonography features in all groups

Grayscale US features			Group 1 (n - %)	Group 2 (n - %)	*P*
Shape	Oval		16 - (61.5%)	10 - (45.4%)	0.408
	Round		7 - (27%)	10 - (45.4%)	
	Irregular		3 - (11.5%)	2 - (9.2%)	
Orientation	Parallel		16 - (61.5%)	13 - (59.1%)	0.863
	Non-parallel		10 - (38.5%)	9 - (40.9%)	
Margin	Circumscribed		6 - (23.2%)	5 - (22.7%)	0.767
	Non-circumscribed	Indistinct	1- (3.8%)	0	
		Angular	13 - (50%)	9 - (41%)	
		Microlobulated	5 - (19.2%)	7 - (31.8%)	
		Spiculated	1 - (3.8%)	1 - (4.5%)	
Echo pattern	Hypoechoic		16 - (61.5%)	14 - (41%)	0.063
	Hyperechoic		1 - (3.8%)	0	
	Isoechoic		0	1 - (4.5%)	
	Heterogenous		9 - (34.7%)	7 - (31.8%)	
	Complex cystic-heterogeneous		0	5 - (22.7%)	
Posterior acoustic features	No posterior acoustic features		12 - (41.2%)	16 - (72.3%)	0.083
	Enhancement		6 - (23.1%)	1 - (4.5%)	
	Shadowing		5 - (19.2%)	1 - (4.5%)	
	Combined		3 - (11.5%)	4 - (18.2%)	

n, number of patients; US, ultrasonography.

Table 2. Breast Imaging Reporting and Data System classification distribution

BI-RADS classification	BI-RADS 3	BI-RADS 4A	BI-RADS 4B	BI-RADS 4C	*P*
Group 1 (n - %)	3 - (11.5%)	17 - (65.4%)	4 - (15.4%)	2 - (7.7%)	0.783
Group 2 (n - %)	1 - (4.5%)	14 - (63.6%)	5 - (22.7%)	2 - (9.2%)	

n, number of patients; BI-RADS, Breast Imaging Reporting and Data System.

Table 3. Mean elasticity values and P values of both observers' measurements

		Observer 1	Observer 2	*P*
E_{max}	Group 1	5.4573 ± 2.10657 m/s 102.1231 ± 71.41531 k/Pa	5.7354 ± 1.77669 m/s 107.8373 ± 58.36010 k/Pa	<0.001
	Group 2	7.8745 ± 1.32761 m/s 190.8886 ± 58.69822 k/Pa	7.8455 ± 1.30104 m/s 189.4809 ± 57.34698 k/Pa	
E_{mean}	Group 1	4.6096 ± 1.78241 m/s 72.6350 ± 48.21512 k/Pa	4.9742 ± 1.59203 m/s 80.0615 ± 45.99172 k/Pa	
	Group 2	7.0182 ± 1.21245 m/s 151.9655 ± 46.19820 k/Pa	6.8927 ± 1.25090 m/s 146.3909 ± 47.49218 k/Pa	
E_{min}	Group 1	3.6438 ± 1.47768 m/s 46.1835 ± 35.88449 k/Pa	3.7519 ± 1.32861 m/s 46.8531 ± 32.56780 k/Pa	
	Group 2	5.8005 ± 1.31117 m/s 107.0027 ± 42.16296 k/Pa	5.7614 ± 1.37844 m/s 104.7450 ± 42.85316 k/Pa	

E, elasticity.

servers, significantly differentiating between Groups 1 (SFAs) and 2 (CFAs, CeFAs, and complicated fibroadenomas) (all *P* values were <0.001). All data, including the elasticity values and *P* values for the measurements of both observers, are presented in Table 3.

The Spearman's correlation coefficients of the elasticity values (in both m/s and k/Pa), obtained by the two observers, exhibited high compatibility ($P < 0.001$). All the Spearman's correlation coefficient values are shown in Table 4.

Receiver operating characteristic curves were obtained for the E_{max}, E_{mean}, and E_{min} values (in both m/s and k/Pa) (Figure 1). When the cut-off value for E_{max} to discriminate between Groups 1 and 2 was 6.41 m/s, the sensitivity, specificity, PPV, NPV, and area under the curve (AUC) were 86.4%, 80.8%, 72%, 82.6%, and 0.820, respectively. A cut-off value of 131.02 k/Pa for E_{max} produced sensitivity, specificity, PPV, NPV, and AUC values of 81.8%, 73.1%, 69.2%, 81.8%, and 0.820, respectively. A cut-off value of 5.79 m/s for E_{mean} revealed sensitivity, specificity, PPV, NPV, and AUC values of 86.4%, 80.8%, 72%, 82.6%, and 0.874, respectively. When the cut-off value

Table 4. Spearman's correlation coefficient values and *P* values of both observers' measurements

	m/s	kPa	*P*
E_{max}	0.958	0.959	<0.001
E_{mean}	0.970	0.974	<0.001
E_{min}	0.967	0.966	<0.001

E, elasticity.

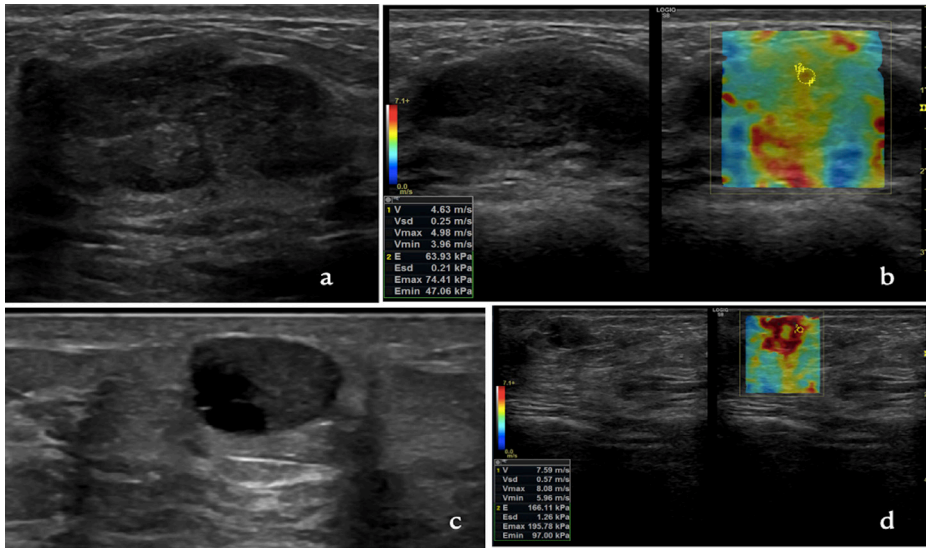

Figure 2. (a) Brightness (B)-mode an ultrasonography (US) image of a 42-year-old female patient with a palpable lesion on her left breast showing an oval-shaped solid breast lesion with indistinct contours and heterogeneous echogenicity. **(b)** Shear-wave elastography (SWE) examination reveals a predominantly green and yellow pattern. Maximum elasticity scores are 4.98 m/s or 74.41 kPa. The lesion was defined as Breast Imaging Reporting and Data System (BI-RADS) 4A, and core needle biopsy was applied. The lesion was diagnosed as a simple fibroadenoma. **(c)** A 46-year-old female patient. In the B-mode US image, the lesion is well-defined with a circumscribed margin. The echo pattern of the lesion is complex cystic. **(d)** In the SWE examination, the lesion has stiffer features with a predominantly red pattern. Maximum elasticity scores were 8.08 m/s or 195.78 kPa. According to these imaging features, the lesion was categorized as BI-RADS 4A. An excisional biopsy was performed at the request of the patient, and the diagnosis was complex fibroadenoma.

Table 5. Distribution of sensitivity, specificity, PPV, NPV, and AUC according to the cut-off values of E_{max}, E_{mean}, and E_{min}

	Cut-off	Sensitivity (%)	Specificity (%)	PPV (%)	NPV (%)	AUC	*P*
E_{max}	6.41 m/s	86.4%	80.8%	72%	82.6%	0.820	0.065
	131.02 k/Pa	81.8%	73.1%	69.2%	81.8%	0.820	0.142
E_{mean}	5.79 m/s	86.4%	80.8%	72 %	82.6%	0.874	0.052
	99.87 k/Pa	86.4%	80.8%	72%	82.6%	0.876	0.064
E_{min}	4.61 m/s	90.9%	80.8%	76%	76%	0.858	0.024
	63.2 k/Pa	90.9%	80.8%	76%	86.9%	0.860	0.015

E, elasticity; PPV, positive predictive value; NPV, negative predictive value; AUC, area under the curve.

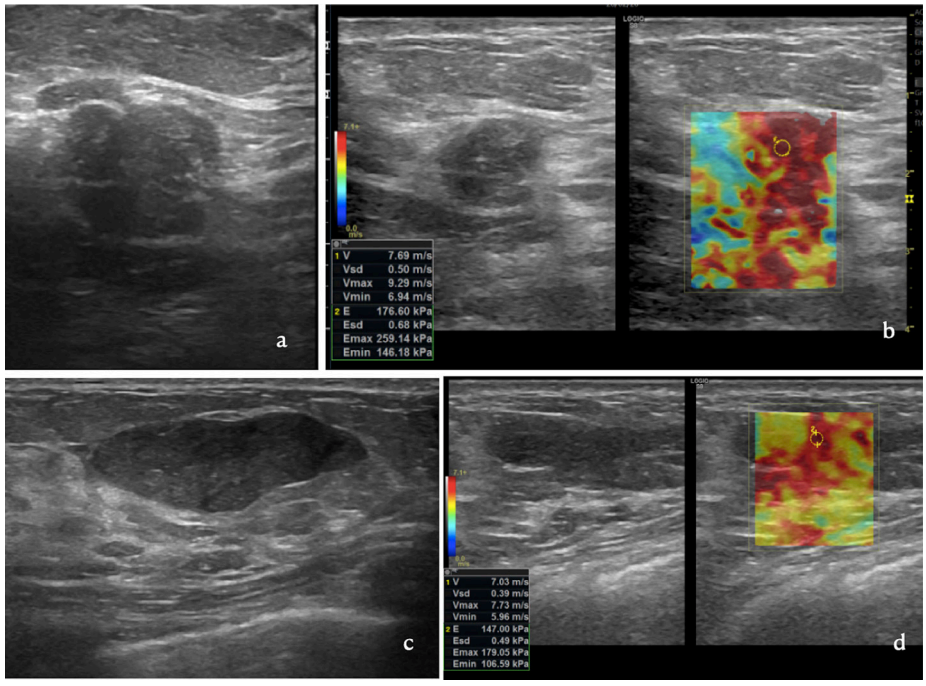

Figure 3. (a) Brightness (B)-mode ultrasonography (US) image of a 51-year-old female patient showing a round, well-defined solid lesion with minimal heterogeneous echo pattern. The orientation of the lesion is vertical. **(b)** The shear-wave elastography (SWE) image shows a predominantly red heterogeneous pattern compatible with a stiff lesion. The maximum elasticity scores are 9.29 m/s or 259.14 kPa. As a result of the combination of the B-mode and SWE findings, the lesion was categorized as Breast Imaging Reporting and Data System (BI-RADS) 4A. The lesion was diagnosed as fibroadenoma including intraductal papilloma after excisional biopsy. **(c)** A 36-year-old female patient with a growing palpable left breast lesion. In the B-mode US image, the lesion is homogeneous hypoechoic. The shape of the lesion is oval with a circumscribed contour and parallel orientation. **(d)** The SWE examination revealed a predominantly red pattern. The lesion was defined as a stiff lesion with maximum elasticity scores of 7.73 m/s or 179.05 kPa. The lesion was classified as BI-RADS 4A through both imaging and clinical findings. The lesion was excised and diagnosed as cellular fibroadenoma.

of E_{mean} was 99.87 k/Pa, the sensitivity, specificity, PPV, NPV, and AUC were 86.4%, 80.8%, 72%, 82.6%, and 0.876, respectively. A cut-off value of 4.61 m/s for E_{min} had sensitivity, specificity, PPV, NPV, and AUC values of 90.9%, 80.8%, 76%, 86.9%, and 0.858, respectively. When the cut-off value of E_{min} was 63.2 k/Pa, the sensitivity, specificity, PPV, NPV, and AUC values were 90.9%, 80.8%, 76%, 86.9%, and 0.860, respectively (Table 5; Figures 2 and 3).

Discussion

This study demonstrated that the addition of SWE to conventional B-mode imaging facilitates the differentiation of SFAs from complex and complicated fibroadenomas. This is significant because B-mode imaging findings in fibroadenomas with suspicious B-mode US features do not discriminate SFAs from suspicious forms or variants. There are pronounced differences in the treatment, follow-up procedures, and potential risk of malignancy between SFAs and other variants;[16] therefore, interventions should be tailored precisely to the diagnosis for optimal patient management.[14] Additional SWE findings enhance the diagnostic performance of B-mode US findings.

The mean age in Group 1 was 47.3 years (range: 24–68 years), whereas in Group 2, it was 42.09 years (range: 24–65 years). The mean age did not significantly differ between the two groups, although the patients in Group 1 were older. Most of the patients in Group 2 were diagnosed with CFAs, and their age distribution was similar to that in the literature. In a study by Pinto et al.[15], the age distribution of patients with SFAs and CFAs was similar to that in our study.[16] However, in another study, patients with CFAs were older than those with SFAs, which was considered to be related to the transformation of complex characteristics with older age.[19] In our study, the younger age of Group 2 patients was related to heterogeneous diagnoses, which included CeFAs and complicated fibroadenomas. Edwards et al.[9] reported that the age of the patients with CeFAs in their study was 35.2–32.7 years. Notably, our institution is a tertiary hospital for breast imaging and treatment, and patients are referred regardless of age.

In this study, the mean diameter of the lesions was smaller in Group 1 (14.03 ± 7.3 mm) than in Group 2 (19.04 ± 11.4 mm), although this was not statistically significant. This is consistent with the literature.[15,17] The smaller mean diameter in Group 1 in our study was attributed to the older age of this group because SFAs decrease in size and regress with age.[15] The larger diameters of the Group 2 lesions were attributed to the transformation of the complex characteristics of fibroadenomas.[19]

In our study, the B-mode US features did not differentiate between the two groups. Most of the lesions in Group 1 were oval. In Group 2, there were equal numbers of oval and round lesions. However, no statistical significance was identified between the two groups in lesion shape, which is consistent with the literature.[15,17] Although there were more lesions with non-circumscribed than circumscribed contours in both groups, the difference was non-significant, which is contrary to the literature.[15] The lesions included in this study were all nominated for histopathologic evaluations according to the BI-RADS categorization. We did not evaluate the SFAs without any changes during the follow-up period, which we believe accounted for the majority of the non-circumscribed lesions. The orientation and posterior acoustic characteristics were not statistically significant between the two groups. In both groups, most lesions were in a parallel orientation, as is reported in the literature.[15] The lesions in our study typically exhibited no posterior acoustic features. Five lesions in Group 2 had a complex cystic echo pattern, which was not detected in any Group 1 lesions. In the studies by Basara Akin et al.[7] and Pinto et al. [15], a complex cystic echo pattern was identified significantly more frequently than any other pattern in CFAs; we attribute this echo pattern to the histopathologic features of CFAs.[8] None of the lesions in either of our groups had parenchymal calcifications.

In our study, 19 patients in Group 1 and 14 in Group 2 were evaluated using MG and TS. In all these images, no specific imaging findings discriminated the groups from each other. The major imaging finding was well-defined nodular lesions. Additionally, MRI was performed in 13 patients in Group 1 and 9 in Group 2. In both groups, the main MRI findings were diffuse enhancement without washout, hypointense linear septa in the lesions, and enhancement in the le-

sions. The ages in each group were similar, and consequently, the menopausal statuses of the patients revealed no differences. Additionally, no specific difference was detected in risk factors. All these imaging findings and demographic features were insufficient to provide a prominent contribution to the diagnoses and prevent unnecessary interventional procedures. The SWE features were the main features that discriminated between the two groups. All the lesions in both groups were benign. In clinical practice, US is the main imaging modality for evaluating solid breast lesions; although benign, they are generally classified as BI-RADS 4.[25] While BI-RADS 4 lesions are suspicious for malignancy, the actual rate of malignancy varies between 3% and 94%. These lesions are diagnosed through either core biopsy or surgical excision, and SFAs should be followed up with appropriate procedures.[17] As CFAs have an increased risk of malignancy, particularly when accompanied by peripheral hyperplastic changes, surgical excision with large and clean surgical margins is recommended for optimal treatment.[17] All CeFAs are challenging to treat. Histopathologic evaluations of core biopsy materials in CeFAs have revealed variations in stroma composition along with glands with a high cellular content.[9] This makes it difficult to distinguish between CeFAs, other fibroadenoma variants, and phyllodes tumors in histopathologic evaluations.[9,26] There are no guidelines for the management and follow-up of CeFAs.[9] The surgical excision of biopsy-proven CeFAs is a logical treatment option for an accurate diagnosis and can also inform follow-up treatment. In the literature, few studies exist on complicated fibroadenomas. Although data regarding these lesions are limited, the increased risk of malignant transformation of such lesions with hyperplastic contents is the most concerning aspect. As the optimal follow-up procedure is unclear, surgical excision is the recommended treatment option.

In the literature, various studies have discussed the diagnostic performance of additional SWE findings for differentiating malignant and benign breast lesions and for evaluating fibroepithelial lesions, including fibroadenomas.[2,23,27-31] Two studies have evaluated the contribution of SWE findings to the diagnosis of fibroadenomas.[2,29] Evans et al.[2] evaluated both B-mode US and SWE features for diagnosing fibroadenomas in the absence of biopsy, concluding that, because clinically benign solid breast lesions with benign B-mode US and SWE findings exhibited no malignant transformation, biopsy and follow-up procedures were unnecessary. In a study of 700 symptomatic breast lesions, none of the lesions were cancerous according to B-mode US and SWE examinations.[32] Another study examined whether SWE and color Doppler US findings could prevent the unnecessary surgical excision of fibroepithelial lesions, including SFAs and phyllodes tumors diagnosed through core biopsies.[29] Lower E_{mean} and E_{max} values were obtained for SFAs than for phyllodes tumors.[29] In the literature, a combination of B-mode US and SWE features has been evaluated to differentiate between SFAs and phyllodes tumors. In our study, different fibroadenoma variants and forms were evaluated, revealing that B-mode US features were ineffective for differentiating SFAs from forms with higher malignant transformation potential. A cut-off E_{min} value of 63.2 k/Pa demonstrated higher sensitivity (90.9%), specificity (80.8%), PPV (76%), and NPV (86.9%) values than all other cut-off values.

Combining SWE and conventional US imaging findings is useful for evaluating, and potentially downgrading or upgrading, BI-RADS 3–4A lesions.[23] A multinational study of 939 breast lesions by Berg et al.[23] revealed that combining SWE features with BI-RADS characteristics improved the specificity and accuracy of the diagnoses. In our study, although all the lesions were benign, additional SWE findings made a major contribution to the differentiation of SFAs from other forms. In our patients, the application of MG and/or TS did not make any difference in the downgrading or upgrading of BI-RADS classifications. The MRI findings were all evaluated using a combination of other imaging modality findings, specifically, B-mode US and SWE findings. Although enhancement patterns had generally unsuspicious features, enhancing lesions with suspicious US and SWE findings were upgraded and histopathologic evaluations were performed.

Our study has several limitations. First and most importantly, the number of patients was limited. In addition, particularly in Group 2, patients were not homogeneous in terms of diagnoses. By increasing the number of patients in both groups and the diagnostic homogeneity of Group 2, SWE findings could be more discriminative. Second, we evaluated quantitative SWE characteristics. In another study, qualitative SWE features, including lesion shape and the homogeneity of elasticity within lesions and surrounding tissue, were evaluated in addition to quantitative features. SWE images were also obtained, and lesion diameter, perimeter, and area were measured. Furthermore, diameter ratios and mass areas on B-mode and SWE images were calculated. These measurements increased the specificity.[23] Adding qualitative elastography features to B-mode and quantitative elastography findings may significantly increase diagnostic performance in larger patient series. As a final limitation, our study was retrospective, only evaluating lesions with known pathologic diagnoses. A prospective study including follow-up could validate our results.

In conclusion, adding SWE to conventional B-mode examinations can increase the ability to differentiate SFAs from more CFAs. To the best of our knowledge, this is the only study to evaluate additional SWE features to diagnose suspicious fibroadenomas. A classification of BI-RADS 4, particularly the BI-RADS 4A subdivision, is associated with low malignancy rates. Although SFAs are benign, for a final diagnosis, interventional methods are required in suspicious cases. Combining non-invasive SWE and B-mode US examinations facilitates discrimination between SFAs, CFAs, and CeFAs. Finally, SWE may be useful for optimizing the diagnosis of fibroadenomas and avoiding unnecessary biopsies, which can cause confusion and anxiety in patients.

Conflict of interest disclosure

The authors declared no conflicts of interest.

References

1. Basara Akin I, Balci P. Fibroadenomas: a multidisciplinary review of the variants. *Clin Imaging*. 2021;71:83-100. [CrossRef]
2. Evans A, Sim YT, Lawson B, Whelehan P. Audit of eliminating biopsy for presumed fibroadenomas with benign ultrasound greyscale and shear-wave elastography findings in women aged 25-39 years. *Clin Radiol*. 2020;75(11):880.e1-880.e3. [CrossRef]
3. Greenberg R, Skornick Y, Kaplan O. Management of breast fibroadenomas. *J Gen Intern Med*. 1998;13(9):640-645. [CrossRef]
4. Hanby AM, Millican-Slater R, Dessauvagie. Fibroepithelial neoplasms of the breast. *Diagnostic Histopathology*. 2017;23(4):149-158. [CrossRef]
5. Humphrey PA, Dehner LP, Pfeifer JD. The Washington Manual of Surgical Pathology. 1st ed. Lippincott Williams & Wilkins; 2008:262. [CrossRef]
6. Kuijper A, Mommers EC, van der Wall E, van Diest PJ. Histopathology of fibroadenoma of

the breast. *Am J Clin Pathol.* 2001;115(5):736-742. [CrossRef]

7. Basara Akin I, Ozgul HA, Guray Durak M, Balci P. Evaluation of elastographic features in complex fibroadenomas with radiologic-pathologic correlation. *J Ultrasound Med.* 2021;40(8):1709-1718. [CrossRef]
8. Dupont WD, Page DL, Parl FF, et al. Long-term risk of breast cancer in women with fibroadenoma. *N Engl J Med*. 1994;331(1):10-15. [CrossRef]
9. Edwards T, Jaffer S, Szabo JR, Sonnenblick EB, Margolies LR. Cellular fibroadenoma on Core needle biopsy: management recommendations for the radiologist. *Clin Imaging*. 2016;40(4):587-590. [CrossRef]
10. Rosen PP. Fibroepithelial neoplasms. In: Rosen PP, eds. Rosen's Breast Pathology. 3rd ed. Philadelphia: Lippincott Williams & Wilkins; 2009:87-201. [CrossRef]
11. Durak MG, Karaman I, Canda T, Balci P, Harmancioğlu O. Cystic fibroadenoma of the breast: a case report. *Turk Patoloji Derg*. 2011;27(3):254-256. [CrossRef]
12. Cummings MC, da Silva L, Papadimos DJ, Lakhani SR. Fibroadenoma and intraduct papilloma--a common pathogenesis? *Virchows Arch*. 2009;455(3):271-275. [CrossRef]
13. Dupont WD, Page DL. Risk factors for breast cancer in women with proliferative breast disease. *N Engl J Med.* 1985;312(3):146-151. [CrossRef]
14. Raza S, Goldkamp AL, Chikarmane SA, Birdwell RL. US of breast masses categorized as BI-RADS 3, 4, and 5: pictorial review of factors influencing clinical management. *Radiographics*. 2010;30(5):1199-1213. [CrossRef]
15. Pinto J, Aguiar AT, Duarte H, Vilaverde F, Rodrigues Â, Krug JL. Simple and complex fibroadenomas are there any distinguishing sonographic features? *J Ultrasound Med*. 2014;33(3):415-419. [CrossRef]
16. Durhan G, Önder Ö, Azizova A, et al. Can radiologist and pathologist reach the truth together in the diagnosis of benign fibroepithelial lesions? *Eur J Breast Health*. 2019;15(3):176-182. [CrossRef]
17. Basara Akin I, Ozgul H, Simsek K, Altay C, Secil M, Balci P. Texture analysis of ultrasound ımages to differentiate simple fibroadenomas from complex fibroadenomas and benign phyllodes tumors. *J Ultrasound Med*. 2020;39(10):1993-2003. [CrossRef]
18. Sklair-Levy M, Sella T, Alweiss T, Craciun I, Libson E, Mally B. Incidence and management of complex fibroadenomas. *AJR Am J Roentgenol*. 2008;190(1):214-218. [CrossRef]
19. Barr RG. Sonographic breast elastography: a primer. *J Ultrasound Med*. 2012;31(5):773-783. [CrossRef]
20. Çebi Olgun D, Korkmazer B, Kılıç F, et al. Use of shear wave elastography to differentiate benign and malignant breast lesions. *Diagn Interv Radiol*. 2014;20(3):239-244. [CrossRef]
21. Shang J, Ruan LT, Wang YY, et al. Utilizing size-based thresholds of stiffness gradient to reclassify BI-RADS category 3-4b lesions increases diagnostic performance. *Clin Radiol*. 2019;4(4):306-313. [CrossRef]
22. Wang M, Yang Z, Liu C, et al. Differential diagnosis of breast category 3 and 4 nodules through BI-RADS classification in conjunction with shear wave elastography. *Ultrasound Med Biol*. 2017;43(3):601-606. [CrossRef]
23. Berg WA, Cosgrove DO, Doré CJ, et al. Shear-wave elastography improves the specificity of breast US: the BE1 multinational study of 939 masses. *Radiology*. 2012;262(2):435-449. [CrossRef]
24. Lee KA, Talati N, Oudsema R, Steinberger S, Margolies LR. BI- RADS 3: Current and future use of probably benign. *Curr Radiol Rep*. 2018;6(2):5. [CrossRef]
25. Raza S, Chikarmane SA, Neilsen SS, Zorn LM, Birdwell RL. BI- RADS 3, 4, and 5 lesions: value of US in management--follow-up and outcome. *Radiology*. 2008;248(3):773-781. [CrossRef]
26. Jacobs TW, Chen YY, Guinee DG Jr, et al. Fibroepithelial lesions with cellular stroma on breast core needle biopsy: are there predictors of outcome on surgical excision? *Am J Clin Pathol*. 2005;124(3):342-354. [CrossRef]
27. Kim GR, Choi JS, Han BK, Ko EY, Ko ES, Hahn SY. Combination of shear-wave elastography and color Doppler: Feasible method to avoid unnecessary breast excision of fibroepithelial lesions diagnosed by core needle biopsy. *PLoS One.* 2017;12(5):e0175380. [CrossRef]
28. Tang Y, Liang M, Tao L, Deng M, Li T. Machine learning-based diagnostic evaluation of shear-wave elastography in BI-RADS category 4 breast cancer screening: a multicenter, retrospective study. *Quant Imaging Med Surg*. 2022;12(2):1223-1234. [CrossRef]
29. Yeo SH, Kim GR, Lee SH, Moon WK. Comparison of ultrasound elastography and color Doppler ultrasonography for distinguishing small triple-negative breast cancer from fibroadenoma. *J Ultrasound Med*. 2018;37(9):2135-2146. [CrossRef]
30. Park SY, Kang BJ. Combination of shear-wave elastography with ultrasonography for detection of breast cancer and reduction of unnecessary biopsies: a systematic review and meta-analysis. *Ultrasonography*. 2021;40(3):318-332. [CrossRef]
31. Shi XQ, Li JL, Wan WB, Huang Y. A set of shear wave elastography quantitative parameters combined with ultrasound BI-RADS to assess benign and malignant breast lesions. *Ultrasound Med Biol.* 2015;41(4):960-966. [CrossRef]
32. Giannotti E, Vinnicombe S, Thomson K, et al. Shear-wave elastography and greyscale assessment of palpable probably benign masses: is biopsy always required? *Br J Radiol.* 2016;89(1062):20150865. [CrossRef]

Diagn Interv Radiol 2023; DOI: 10.4274/dir.2023.221859

CARDIOVASCULAR IMAGING

ORIGINAL ARTICLE

Can left ventricular entropy by cardiac magnetic resonance late gadolinium enhancement be a prognostic predictor in patients with left ventricular non-compaction?

Yun-Ting Ma#
Lu-Jing Wang#
Xiao-Ying Zhao
Yue Zheng
Li-Hui Sha
Xin-Xiang Zhao

#Co-first author Yun-Ting Ma and Lu-Jing Wang contributed to this work equally.

From the Department of Radiology (Y-T.M., X-Y.Z., Y.Z., L-H.S., X-X.Z. ✉ zhaoxinxiang2918@outlook.com), The Second Affiliated Hospital of Kunming Medical University, Kunming, China; Department of Radiology (L-J.W), West China Hospital of Sichuan University, Chengdu, China.

Received 30 August 2022; revision requested 19 September 2022; last revision received 06 January 2023; accepted 31 January 2023.

Epub: 20.03.2023

Publication date: 05.09.2023

DOI: 10.4274/dir.2023.221859

PURPOSE

Left ventricular non-compaction (LVNC) is considered rare; however, the use of cardiac magnetic resonance (CMR) has shown that its incidence is not uncommon, and its clinical presentation remains variable, with an uncertain prognosis. Risk stratification of major adverse cardiac events (MACE) in patients with LVNC remains complex. Therefore, this study aims to determine whether tissue heterogeneity from late gadolinium enhancement-derived entropy is associated with MACE in patients with LVNC.

METHODS

This study was registered in the Clinical Trial Registry (CTR2200062045). Consecutive patients who underwent CMR imaging and were diagnosed with LVNC were followed up for MACE, which was defined by heart failure, arrhythmias, systemic embolism, and cardiac death. The patients were divided into MACE and non-MACE groups. The CMR parameters included left ventricular (LV) entropy, LV ejection fraction (LVEF), LV end-diastolic volume, LV end-systolic volume (LVESV), and LV mass (LVM).

RESULTS

Eighty-six patients (age: 45.48 ± 16.64 years; female: 62.7%; LVEF: 42.58 ± 17.20%) were followed up for a median of 18 months and experienced 30 MACE events (34.9%). The MACE group showed higher LV entropy, LVESV, and LVM and lower LVEF than the non-MACE group. LV entropy [hazard ratio (HR): 1.710, 95% confidence interval (CI): 1.078–2.714, $P = 0.023$] and LVEF (HR: 0.961, 95% CI: 0.936–0.988, $P = 0.004$) were independent predictors of MACE ($P < 0.050$) according to the Cox regression analysis. Receiver operating characteristic curve analysis revealed that the area under the curve of LV entropy was 0.789 (95% CI: 0.687–0.869, $P < 0.001$), LVEF was 0.804 (95% CI: 0.699–0.878, $P < 0.001$), and the combined model of LV entropy and LVEF was 0.845 (95% CI: 0.751–0.914, $P < 0.050$).

CONCLUSION

LGE-derived LV entropy and LVEF are independent risk indicators of MACE in patients with LVNC. The combination of the two factors was more conducive to improving the prediction of MACE.

KEYWORDS

Left ventricular non-compaction, cardiac magnetic resonance, entropy, major adverse cardiovascular events, prognosis

You may cite this article as: Ma YT, Wang LJ, Zhao XY, Zheng Y, Sha LH, Zhao XX. Can left ventricular entropy by cardiac magnetic resonance late gadolinium enhancement be a prognostic predictor in patients with left ventricular non-compaction? *Diagn Interv Radiol.* 2023;29(5):682-690.

Left ventricular non-compaction (LVNC) is a heterogeneous disease that leads to changes in cardiac function and structure. In 2007, the European Society of Cardiology classified LVNC as unclassified cardiomyopathy, affecting mainly the apical, anterior, and lateral walls of the left ventricle (LV).[1] Typical histologic manifestations of LVNC include abnormally thickened trabeculae, deep intertrabecular depression, disordered arrangement of the myofilament bundles, intermyofilament fibrosis, and microcirculatory ischemia.[2] The disease may be asymptomatic at the beginning; however, major adverse cardiovascular events (MACE), such as heart failure (HF), arrhythmias, systemic emboli, and cardiac death, often occur at the end stage. The incidence of MACE in patients with LVNC has been reported to be approximately 38%.[3] Therefore, the long-term prognosis of patients with LVNC is poor, necessitating the search for effective indicators that would aid in assessing the risk of MACE in patients with LVNC, which is crucial for early clinical treatment and intervention.

As the gold standard for the non-invasive assessment of cardiac structure and function,[4] cardiac magnetic resonance (CMR) enables the direct observation of the anatomy of LVNC and provides insight into myocardial perfusion imaging, the visualization of non-compacted myocardium, detection of myocardial fibrosis, and identification of intracavitary thrombi. Therefore, CMR plays a crucial role in the diagnosis, risk stratification, and treatment of patients with LVNC.[5,6] Positive late gadolinium enhancement (LGE) and LV systolic dysfunction [left ventricular ejection fraction (LVEF) <50%] have been used to determine the prognosis of patients with LVNC.[3] However, some investigations have discovered that even individuals with negative LGE and normal LVEF can develop MACE.[7] Therefore, it is necessary to explore improved measures for assessing the prognosis of patients with LVNC. Entropy, a parameter based on the texture analysis of LGE, reflects the heterogeneity of the myocardium by evaluating the complexity of the image signal.[8] The calculation of entropy is based on the distribution of the signal intensity (SI) of the LV myocardium on the LGE images, which elucidates the characteristics of the myocardial tissue. There is no study that investigated the prognostic value of LV entropy in LVNC. Therefore, this study aims to explore the predictive value of LV entropy derived from LGE for MACE in patients with LVNC.

Main points

- Left ventricular (LV) entropy obtained based on cardiac magnetic resonance late gadolinium enhancement was an effective predictor of major adverse cardiac events in patients with LV non-compaction.
- The prognostic value of LV entropy combined with LV ejection fraction was higher than individual indicators.
- The optimal cut-off value for LV entropy was 5.09.

Methods

Study population

This study was approved by the Ethics Committee of the Second Affiliated Hospital of Kunming Medical University (no: PJ2022105, date of the approval: March 18th, 2022), and the requirement for written informed consent was waived. This study was registered in the Clinical Trial Registry (number: CTR2200062045). Patients diagnosed with LVNC using 3.0T CMR between January 2015 and October 2020 were included in this study. The diagnostic criteria followed the Petersen criteria of 2005:[9] 1) a typical bilayered myocardial structure with a thin, compacted epicardial layer and a thick, non-compacted endocardial layer; and 2) the end-diastolic non-compacted/compacted myocardium ratio (NC/C) was >2.3 in any long-axis LV CMR image (Figure 1). The exclusion criteria for the study were as follows (Figure 2): 1) other diseases causing elevated troponin levels (such as pulmonary embolism and aortic dissection); 2) other cardiac diseases (such as myocardial infarction, hypertrophic cardiomyopathy, valvular cardiomyopathy, and congenital heart disease); 3) other severe diseases (such as malignant tumors, chronic kidney disease, liver disease, and severe infectious disease); 4) insufficient imaging quality; and 5) patients lost to follow-up. All patients were followed up by telephone, and the electronic medical records from the last visit were reviewed, with MACE as the endpoint. MACE included 1) HF: hospitalization for HF, cardiac resynchronization therapy implantation, or heart transplantation; 2) arrhythmia: malignant ventricular arrhythmia (ventricular fibrillation, sustained or non-sustained ventricular tachycardia, and implantable cardioverter-defibrillator) and atrial fibrillation; 3) systemic embolism, stroke, myocardial infarction, or peripheral arterial embolism; and 4) cardiac death. The patients were divided into MACE and non-MACE groups based on the presence or absence of MACE during the follow-up period. Elevated values for B-type natriuretic peptide (BNP) (pg/mL) were defined as ≥35 pg/mL and >125 pg/mL for N-terminal pro-BNP (NT-proBNP).

Cardiac magnetic resonance scanning

CMR imaging was performed using a 3.0-T scanner (Philips Achieva, Best, The Netherlands) and an 8-channel phased-array cardi-

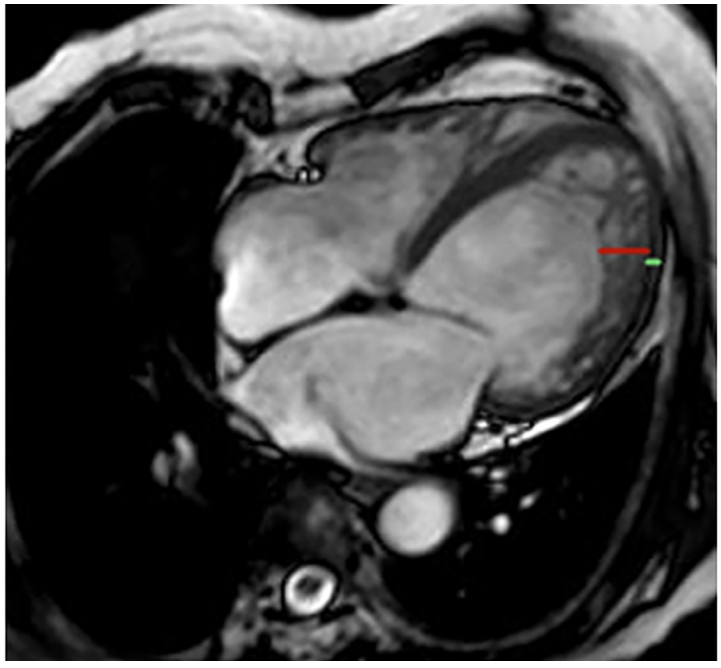

Figure 1. Cardiac magnetic resonance measurements in patients with left ventricular non-compaction. On the four-chamber cine image at the end-diastole, the non-compacted myocardium (red line)/compacted myocardium (green line) was 3.7.

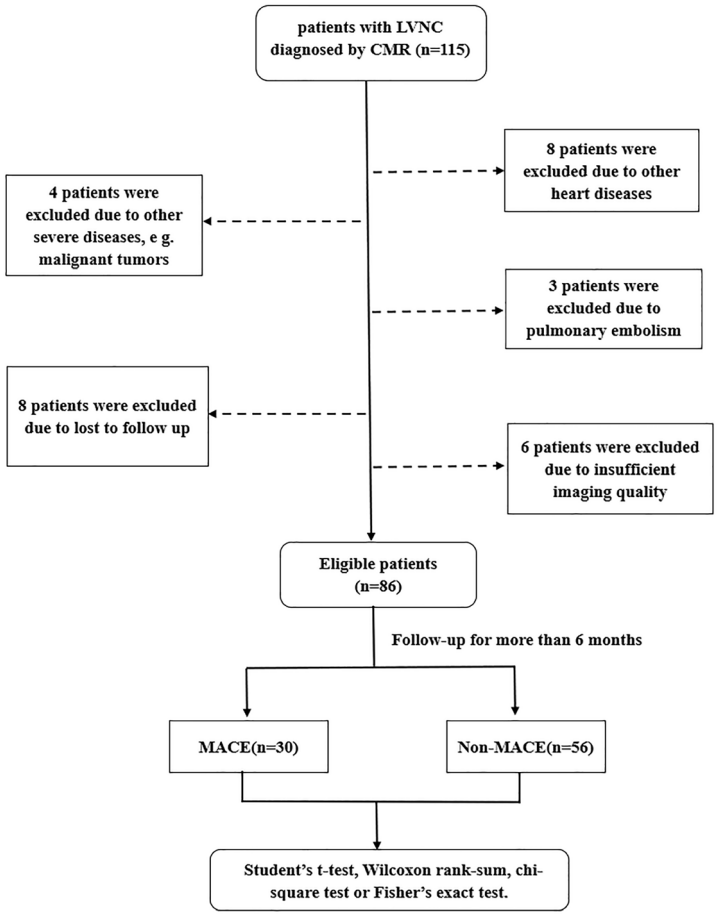

Figure 2. Patient inclusion study flow chart. LVNC, left ventricular non-compaction; CMR, cardiac magnetic resonance; MACE, major adverse cardiovascular events.

ac coil using magnetic resonance imaging (MRI)-compatible chest electrocardiogram gating technology. The true fast imaging with steady-state precession sequence was used for the positioning scan. The scanning parameters were as follows: repetition time (TR), 400 ms; echo time (TE), 1.08 ms; slice thickness, 6 mm; and field of view, 311 mm × 340 mm. Cardiac cine images of the short and long axis (LV of two, three, and four chambers) were obtained using a fast steady-state free precession sequence. The scanning parameters were as follows: TE, 1.52 ms; TR, 3.0 ms; flip angle, 45°; matrix, 178 × 181; and FOV, 350 × 350 mm. In each acquisition, 30 cardiac cycles were collected in each slice, with a slice thickness of 8 mm and a slice interval of 0 mm. The LGE images were acquired in the long-axis (two and four chambers) and short-axis planes 15 minutes after the intravenous administration of 0.2 mmol/kg of gadolinium-based contrast. The scanning parameters were as follows: TE, 2.4 ms; TR, 5.0 ms; flip angle, 25°; FOV, 320 mm × 320 mm; matrix, 168 × 153; slice thickness, 10 mm; and slice spacing, 0 mm.

Cardiac magnetic resonance image analysis

Measurements of the ventricles and atrium were acquired on steady-state free precession sine images according to the protocol used by Kawel-Boehm et al.[10] and Gürdoğan et al.[11] The anteroposterior diameter of the left atrial diameter was measured in the three-chamber cine images parallel to the mitral valve. The LV end-diastolic diameter was obtained at the level of the basal papillary muscles on the short-axis view. The diameter of the right atrium was measured during atrial diastole (maximal size of the left atrium) in the four-chamber cine images. The right ventricular end-diastolic diameter was measured on the four-chamber cine images parallel to the tricuspid valve and 1 cm distal. An analysis of the CMR images was performed using CVI 42 post-processing software (Circle Cardiovascular Imaging, Calgary, Alberta, Canada). The endocardial and epicardial contours of the LV were automatically outlined on the short-axis cine sequence to obtain the CMR parameters, including LVEF, LV end-diastolic volume (LVEDV), LV end-systolic volume (LVESV), and LV mass (LVM). The LV endocardial and epicardial contours were semi-automatically outlined on the LGE short-axis images (LV contouring was performed independently for all patients by two cardiac MRI physicians blinded to the study results; one patient underwent remeasurements at one-month intervals, and the inter- and intra-observer agreements were analyzed). Regions without over-enhancement on the LGE short-axis images were considered normal myocardial regions and were automatically selected as regions of interest (ROI). After the endocardial and epicardial contours were outlined and the ROI were set, the software automatically generated the myocardial enhancement volume percentage (LGE%). LGE was defined as myocardium six standard deviations above the mean SI. The images were subsequently imported into Python 3.8 (MathWorks, Natick, MA) software for the analysis of LV entropy. To compute the probability distribution, $P(x)$, of the SI values in the LV, the SI value of each pixel point was rated from 0 to 255. The $P(x)$ of each SI value was then calculated by counting the frequency of each SI value within the range. The entropy was calculated using the following formula:[12]

$$H(\mathbf{X}) = \mathrm{E}_{x\sim P}[I(x)] = -\mathrm{E}_{x\sim P}[\log P(x)] = \sum_{x} P(x)\log P(x)$$

where x represents the SI of each pixel point and $P(x)$ represents the probability distribution of the SI in the LV. The LV entropy was obtained subsequently (Figure 3a, b). The tissue composition was homogenous (one SI value) when the entropy was zero, whereas an entropy of 10 indicated the most robust heterogeneity.

Statistical analysis

Statistical analysis was performed using SPSS (version 26.0; IBM, Armonk, New York) and MedCalc v 15.8 (MedCalc Software, Ostend, Belgium). The mean ± standard deviation was used for normally distributed variables, whereas the M (P25, P75) was used for non-normally distributed data. The categorical variables were described as frequencies and percentages. The Student's t-test and Wilcoxon rank-sum test were used to compare the continuous variables between the two groups. The categorical variables were compared using the chi-squared test or Fisher's exact test. To assess effective risk variables, those with $P < 0.050$ among the univariable Cox proportional Hazard model were included in the multivariable Cox regression analysis. The hazard ratio (HR) and 95% con-

fidence intervals (CI) for each risk factor were also obtained. The diagnostic performance of various models was evaluated using the receiver operating characteristic (ROC) curve analysis, and the cut-off values of LV entropy were determined. The DeLong test was used to compare the area under the curve (AUC) of different predictive models. Survival analysis of patients with LVNC was performed using the Kaplan–Meier method, and the log-rank test was used to assess differences between the survival curves. Furthermore, $P < 0.050$ was considered statistically significant. The intra- and inter-observer consistency of LV entropy was analyzed using the intraclass correlation coefficient (ICC), and ICC >0.75 indicated good consistency.

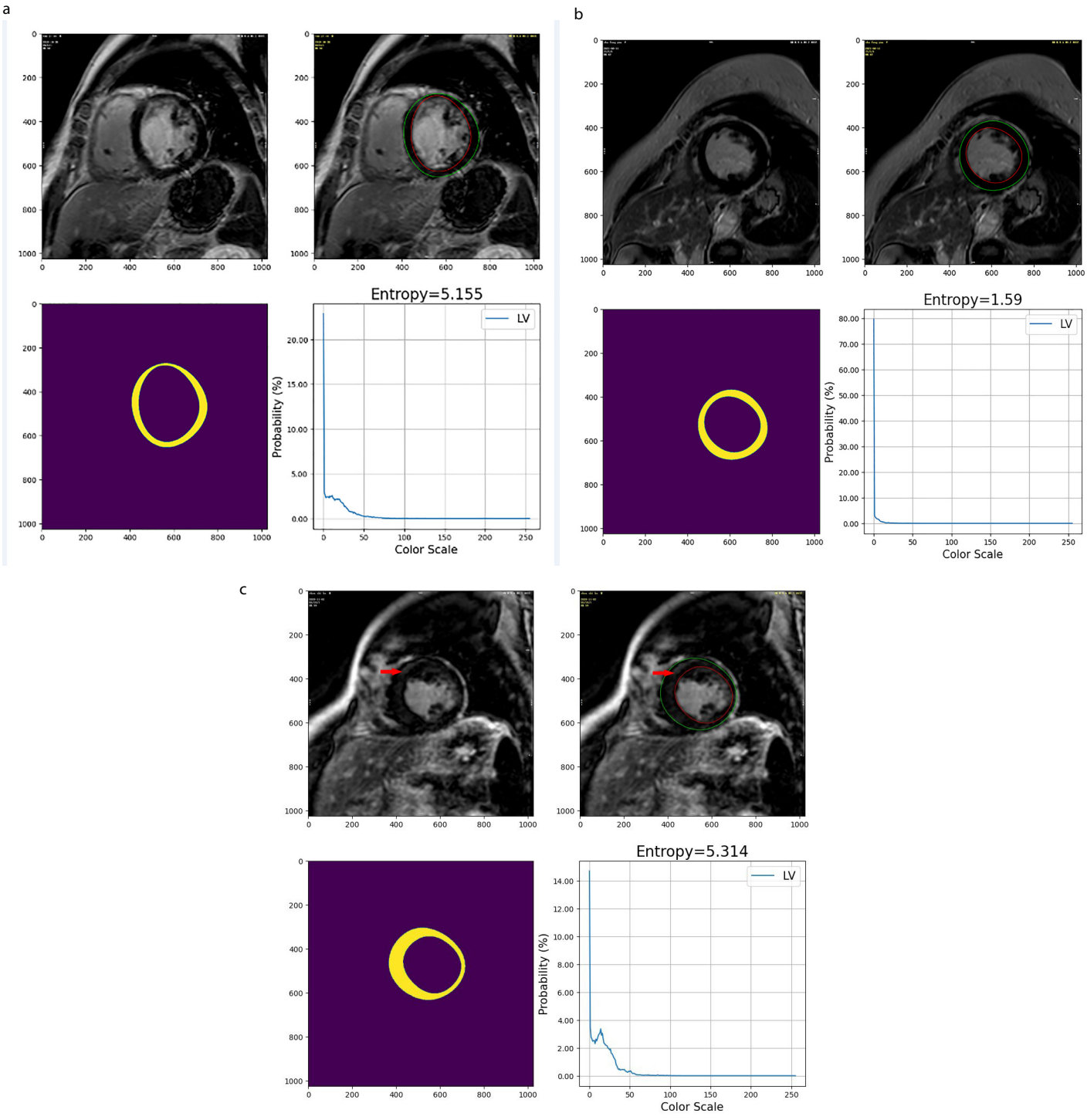

Figure 3. Three patients with left ventricular non-compaction. **(a)** A 46-year-old male patient with LVNC [NC (red line)/C (green line): 2.5], with preserved LVEF (55.46%) and high LV entropy (5.155), had a stroke after 23 months of follow-up. **(b)** A 46-year-old female patient with LVNC [NC (red line)/C (green line): 3.0], with low LVEF (32.47%) and low LV entropy (1.59), had non-MACE during the 10-month follow-up period. **(c)** A 63-year-old male patient with LVNC [NC (red line)/C (green line): 2.4], had non-MACE during the 11-month follow-up period, with preserved LVEF (50.07%) and high LV entropy (5.314). The red arrow showed the LGE. LV, left ventricular; LVEF, left ventricular ejection fraction; MACE, major adverse cardiovascular event; NC, non-compacted; C, compacted; LGE, late gadolinium enhancement.

Results

Baseline characteristics of patients

A total of 115 patients were diagnosed with LVNC using CMR imaging. After excluding 29 cases, 86 patients with LVNC (45.48 ± 16.64 years, 54% men) were enrolled in this trial, including 56 patients without MACE and 30 patients with MACE (including 16 cases of HF, nine cases of arrhythmia, two cases of stroke, two cases of myocardial infarction, and one case of cardiac death). The baseline characteristics of the patients are shown in Table 1. There were 54 (62%) men in this cohort: 23 (76.7%) were in the MACE group, and 31 (55.4%) were in the non-MACE group. The average age of the study cohort patients was 45.48 ± 16.64 years, and the age of the patients in the MACE group was significantly higher than that of the patients in the non-MACE group (52.90 ± 15.66 years vs. 41.50 ± 15.90 years, $P < 0.050$). The differences between the two groups were not statistically significant ($P > 0.050$) for sex, height, weight, body mass index, hypertension, diabetes mellitus, alcohol consumption, smoking, lipid levels, alanine aminotransferase, aspartate aminotransferase, creatinine, uric acid, elevated BNP or NT-proBNP levels, and the New York Heart Association classification.

Cardiac magnetic resonance parameters of the patients

The CMR parameters of the patients with LVNC are shown in Table 2. Compared with the non-MACE group, the LVEF of the MACE group was lower (49.14 ± 13.75% vs. 30.35 ± 16.47%). The MACE group showed higher LV entropy, LVESV, left atrial diameter, LV diameter, and LVM when compared with the non-MACE group (5.08 ± 1.09 vs. 3.72 ± 1.34; 120.27 ± 51.32 mL vs. 94.37 ± 59.55 mL; 39.05 ± 7.57 mm vs. 35.55 ± 7.65 mm; 60.13 ± 11.5 mm vs. 55.45 ± 9.67 mm; 124.97 ± 38.86 g vs. 99.02 ± 35.91 g; $P < 0.050$). There were no significant differences between the two groups in terms of LVEDV, right atrial diameter, right ventricular diameter, NC/C ratio, and LGE% ($P > 0.050$).

Risk factors for major adverse cardiovascular events

The results of univariate and multivariate Cox regression analysis are listed in Table 3. Univariate analysis showed that age, LVEF, LVM, and LV entropy were effective predictors of MACE ($P < 0.050$). After adjusting for age and CMR parameters (LVESV, LA diameter, LV diameter, and LVM), further multivariate analysis revealed that LVEF and LV entropy remained significant predictors of MACE ($P < 0.050$). A negative correlation was found between the risk of MACE and LVEF (HR: 0.961, 95% CI: 0.936–0.988, $P = 0.004$), whereas the risk of MACE was positively associated with LV entropy (HR: 1.710, 95% CI, 1.078–2.714; $P = 0.023$).

Predictive values of indicators

The predictive values of LV entropy, LVEF, and the combined model of the two indicators for MACE in patients with LVNC are shown in Figure 4. The ROC curve analysis revealed that the predictive efficacy of the combined model of LV entropy and LVEF was the highest (AUC: 0.845, 95% CI: 0.751–0.914, $P < 0.050$), followed by LVEF (AUC: 0.804, 95% CI: 0.699–0.878, $P < 0.001$) and LV entropy (AUC: 0.789, 95% CI: 0.687–0.869, $P < 0.001$). The cut-off value of LV entropy was 5.09, with a sensitivity of 63% and a specificity of 86%. The Kaplan–Meier analysis showed that the MACE-free survival of patients with LV entropy <5.09 was significantly higher than that of patients with LV entropy ≥5.09 ($P < 0.001$) (Figure 5a, b). Moreover, the cut-off value of LVEF was 34.22%, with a sensitivity of 70% and a specificity of 84%. However, DeLong's test showed no statistically significant differences in the AUC among the three models ($P > 0.050$).

Intra- and inter-observer variability of LV entropy

The results of the ICC consistency test are presented in Table 4. LV entropy showed good intra- and inter-observer agreements (ICC >0.75).

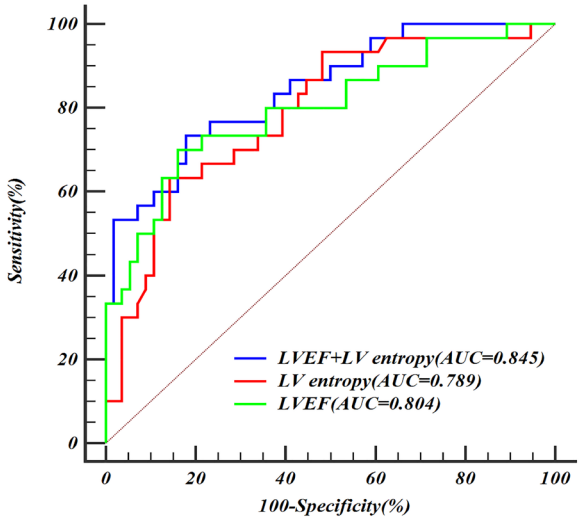

Figure 4. Receiver operating characteristic analysis. The ROC analysis of LV entropy (AUC: 0.789, 95% CI: 0.687–0.869, $P < 0.001$), LVEF (AUC: 0.804, 95% CI: 0.699–0.878, $P < 0.001$), and the combined model of LVEF and LV entropy (AUC: 0.845, 95% CI: 0.751–0.914, $P < 0.050$) for predicting MACE of LVNC. ROC, receiver operating characteristic; AUC, area under the curve; CI, confidence interval; LVEF, left ventricular ejection fraction; LV, left ventricular.

Discussion

The LV entropy obtained based on CMR-LGE was used for the first time in this study to predict the risk of MACE in patients with LVNC. It was demonstrated that LV entropy was a reliable indicator of prognosis in patients with LVNC and that the risk of MACE increased as LV entropy increased. Further, LV entropy could effectively predict the risk of MACE in patients with LVNC when used alone. The cut-off value for LV entropy was 5.09, and LV entropy as a novel predictor of MACE in patients with LVNC could provide valid information for clinical treatment and intervention, which could help improve the prognosis of patients with LVNC. The diagnostic rate of LVNC is rising as imaging technology and knowledge of LVNC advance, and most of the patients are relatively young.[13] Compared with sex–age-matched healthy volunteers, patients with LVNC have a much higher risk of developing MACE,[14] and HF occurs more commonly than other cardiac diseases, including dilated cardiomyopathy.[15,16] In this study, the incidence of MACE in patients with LVNC was 34.9%, with HF occurring most frequently, which was consistent with previous reports.[17-19] Therefore, investigating the prognosis of patients with LVNC has significant clinical implications.

Many studies have been conducted to predict the risk of MACE in patients with LVNC using the thickness of non-compacted myocardium and LV trabeculated mass, atrial size, LVEF, LGE, brain natriuretic peptide, and genes[3,7,19-23] with LVEF and LGE being the most commonly used predictors.[3,24] However, Yu et al.[25] found that even patients with LVEF-preserved LVNC could have impaired LV systolic function and were at risk for MACE. Additionally, although LGE could reflect a certain degree of pathological changes, such as myocardial fibrosis, it relies on a subjective visual evaluation by radiologists and might be erroneous when the degree of myocardial fibrosis is modest or when the myocardium is diffusely fibrotic.[26]

A novel texture analysis method based on CMR-LGE images was developed to quantify the degree of cardiac tissue heterogeneity of the myocardial tissue and entropy.[8]

Table 1. Baseline characteristics of patients with left ventricular non-compaction

	Total (n = 86)	MACE (n = 30)	Non-MACE (n = 56)	χ2/t/Z value	*P* value
Age (years)	45.48 ± 16.64	52.90 ± 15.66	41.50 ± 15.90	3.186	0.002*
Male [n (%)]	54	23 (76.7)	31 (55.4)	3.797	0.063
Height (m²)	1.66 ± 7.55	1.67 ± 6.99	1.65 ± 7.84	0.785	0.435
Weight (kg)	64.80 ± 13.36	65.20 ± 15.56	65.59 ± 12.17	0.201	0.419
BMI (kg/m²)	22.62 [20.74, 25.74]	21.74 [19.69, 26.02]	21.06 [21.06, 25.57]	-1.047	0.295
Hypertension [n (%)]	25	10 (33.3)	15 (26.8)	0.406	0.620
Diabetes [n (%)]	8	3 (10.0)	5 (8.9)	0.000	1.000
Drinking [n (%)]	26	13 (43.3)	13 (23.2)	3.749	0.083
Smoking [n (%)]	27	13 (43.3)	14 (25.0)	3.048	0.093
TC (mmol/L)	4.0 7 ± 1.04	4.11 ± 1.17	4.05 ± 0.97	0.273	0.786
TG (mmol/L)	1.16 [0.95, 1.61]	1.21 [0.93, 1.58]	1.15 [0.96, 1.83]	-0.217	0.828
HDL (mmol/L)	1.08 [0.92, 1.26]	1.01 [0.87, 1.28]	1.10 [0.98, 1.29]	-1.011	0.312
LDL (mmol/L)	2.53 ± 0.77	2.52 ± 0.93	2.53 ± 0.69	-0.070	0.944
ALT	28.00 [19.00, 43.25]	28.50 [22.75, 43.50]	26.50 [18.25, 43.75]	-0.594	0.553
AST	24.50 [18.00, 31.00]	26.00 [19.75, 32.50]	23.50 [18.00, 30.75]	-1.175	0.240
Cr (umoL/L)	80.29 ± 19.20	85.70 ± 15.80	77.39 ± 20.33	1.943	0.055
UA (umoL/L)	427.66 ± 137.90	417.86 ± 123.73	432.91 ± 145.72	-0.480	0.632
NYHA classification	-	-	-	-1.784	0.074
NYHA I, n (%)	42 (48.8)	11 (36.7)	31 (55.4)	-	-
NYHA II, n (%)	34 (39.5)	14 (46.7)	20 (35.7)	-	-
NYHA III, n (%)	9 (10.5)	5 (16.7)	4 (7.1)	-	-
NYHA IV, n (%)	1 (1.2)	0 (0.0)	1 (1.8)	-	-
Elevated BNP or NT-proBNP	35 (40.7)	12 (40.0)	23 (41.1)	0.009	0.923

*Statistically significant. BMI, body mass index; TC, total cholesterol; TG, triglyceride; HDL, high-density lipoprotein; LDL, low-density lipoprotein cholesterol; ALT, alanine aminotransferase; AST, aspartate aminotransferase; Cr, creatinine; UA, uric acid; BNP, B-type natriuretic peptide; NT-proBNP, N-terminal pro-BNP; NYHA, New York Heart Association; MACE, major adverse cardiovascular events; LVNC, left ventricular nonc-ompaction.

Table 2. Cardiac magnetic resonance parameters of patients with left ventricular non-compaction

	Total (n = 86)	MACE (n = 30)	Non-MACE (n = 56)	χ2/t/Z value	*P* value
LVEF (%)	42.58 ± 17.20	30.35 ± 16.47	49.14 ± 13.75	-5.632	<0.001
LVEDV (mL)	179.04 ± 64.06	194.06 ± 53.65	170.99 ± 68.08	1.607	0.089
LVESV (mL)	103.40 ± 57.86	120.27 ± 51.32	94.37 ± 59.55	2.014	0.047*
LA diameter (mm)	36.77 ± 7.76	39.05 ± 7.57	35.55 ± 7.65	2.032	0.047*
LV diameter (mm)	57.09 ± 10.52	60.13 ± 11.5	55.45 ± 9.67	1.998	0.049*
RA diameter (mm)	42.92 ± 7.65	44.80 ± 8.66	41.91 ± 6.92	1.683	0.096
RV diameter (mm)	36.45 ± 11.58	36.85 ± 13.91	36.23 ± 10.26	0.233	0.816
LVM (g)	108.07 ± 38.79	124.97 ± 38.86	99.02 ± 35.91	3.103	0.003*
LV entropy	4.19 ± 1.41	5.08 ± 1.09	3.72 ± 1.34	4.775	<0.001*
NC/C ratio	2.7 [2.4, 3.2]	2.7 [2.4, 3.6]	2.7 [2.4, 3.0]	-1.240	0.215
LGE%	4.69 [2.48, 8.45]	5.31 [3.36, 10.21]	4.21 [2.11, 7.90]	-1.404	0.160

*Statistically significant. LVEF, left ventricular ejection fraction; LVEDV, left ventricular end-diastolic volume; LVESV, left ventricular end-systolic volume; LA, left atrial; LV, left ventricle; RA, right atrium; RV, right ventricular; LVM, left ventricular mass; NC, non-compacted; C, compacted; LGE: late gadolinium enhancement; MACE, major adverse cardiovascular events.

Entropy represents the homogeneity of an image. The entropy of an image with perfectly homogeneous pixels is zero, indicating a homogeneous, single-tissue component. The more different the tissue components of the myocardium, the more heterogeneous the LGE image signal and the higher the entropy value. Therefore, entropy can be used to evaluate the heterogeneity of the myocardial tissue and provide prognostic information objectively and quantitatively. Entropy has also been applied to other cardiac diseases. Androulakis et al.[8] demonstrated that LV entropy is correlated with the prognosis of patients with myocardial infarction. A previous study also confirmed that entropy was a valid predictor of MACE in patients with myocardial infarction.[27] Muthalaly et al.[28] used LV entropy to predict the risk of ventricular arrhythmias in patients with dilated cardiomyopathy and found that LV entropy combined with LGE significantly improved risk prediction. Therefore, the ability of LV entropy to assess the risk of ischemic and non-ischemic heart disease has been validated.

Although the typical pathology of patients with LVNC is characterized by multiple thick myotubular trabeculae,[2,29,30] it has also been suggested that hyper tubularity may only be a physiological alteration.[20,31] Further research has confirmed that the degree of myocardial fibrosis is directly connected to the long-term prognosis of patients with LVNC[32-34] and that the hyper trabeculation of LVNC is not an essential factor affecting prognosis.[15,20] Myocardial histological alterations in patients with LVNC are the pathological basis for the development of MACE. Therefore, LV entropy can quantitatively assess the degree of myocardial fibrosis in patients with LVNC and reflect the prognosis.

In this study, LV entropy was significantly higher in the MACE group than in the non-MACE group, suggesting that the patients in the MACE group had more severe and heterogeneous LV myocardial fibrosis. Further

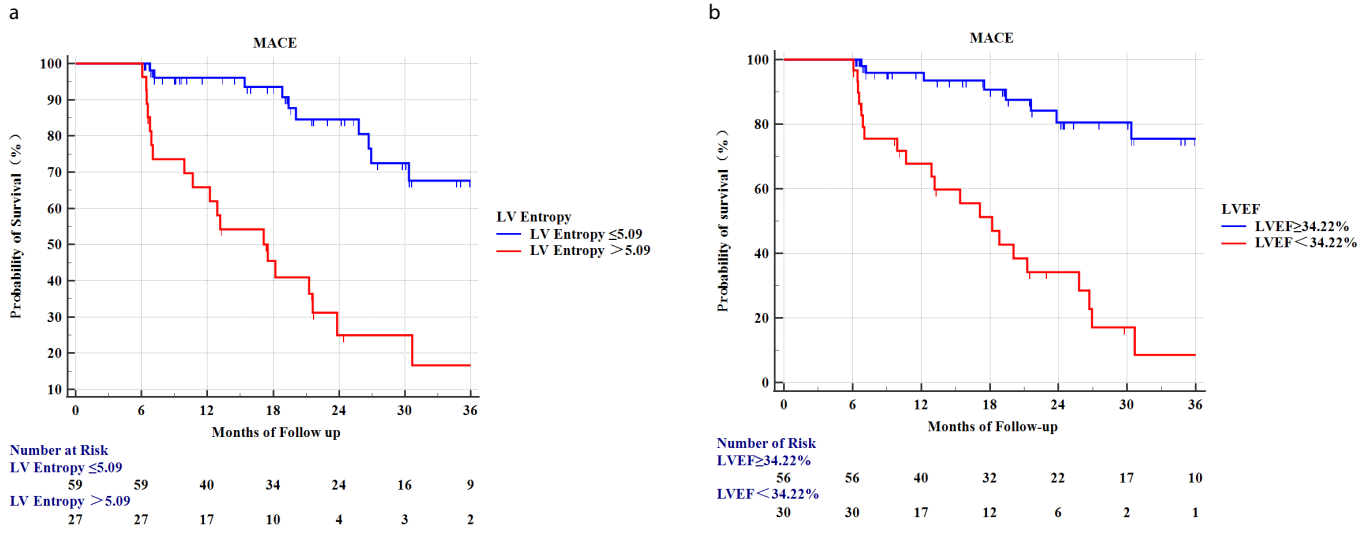

Figure 5. Prognostic value of left ventricle entropy and left ventricular ejection fraction in patients with left ventricular non-compaction. Kaplan–Meier curves showed the difference in non-MACE survival when the patients were stratified according to LV entropy **(a)** and LVEF **(b)**. LV, left ventricular; MACE, major adverse cardiovascular events; LVNC, left ventricular non-compaction.

Table 3. Risk factors for major adverse cardiovascular events in patients with left ventricular non-compaction

	Univariate analysis		Univariate analysis	
Variables	HR (95% CI)	*P* value	HR (95% CI)	*P* value
Age (years)	1.028 (1.007–1.050)	0.008*	1.015 (0.988–1.043)	0.275
LVESV (mL)	1.005 (0.999–1.011)	0.077		
LVEF (%)	0.942 (0.920–0.965)	<0.001*	0.961 (0.936–0.988)	0.004*
LA diameter (mm)	1.033 (0.989–1.080)	0.143		
LV diameter (mm)	1.029 (0.996–1.063)	0.086		
LVM (g)	1.010 (1.002–1.018)	0.013*	1.005 (0.995–1.015)	0.310
LV entropy	2.058 (1.426–2.971)	<0.001*	1.710 (1.078–2.714)	0.023*

*Statistically significant. LVESV, left ventricular end-systolic volume; LVEF, left ventricular ejection fraction; LA, left atrial; LV, left ventricular; LVM, left ventricular mass; HR, hazard ratio; CI, confidence interval.

Table 4. Intra- and inter-observer variability of left ventricle entropy

Parameters	Inter-observer		Intra-observer	
	ICC	95% CI	ICC	95% CI
LV entropy	0.978	0.967–0.986	0.984	0.976–0.990

LV, left ventricular; ICC, intraclass correlation coefficient; CI, confidence interval.

Cox regression analysis showed that LV entropy was a valid predictor of MACE, with a HR >1, indicating that LV entropy was a risk factor for MACE. The risk of MACE in patients with LVNC rises with increasing LV entropy. This study showed that age, LVESV, left atrial diameter, LV diameter, LVEF, LVM, and LV entropy differed significantly between the MACE and non-MACE groups. However, the univariable Cox proportional hazard model indicated that age, LVESV, left atrial diameter, and LV diameter were not predictors of MACE. Although Ramchand et al.[19] suggested that patients with LVNC had a higher risk for the occurrence of MACE, owing to elevated LVESV and LV dilatation, some researchers hypothesized that this mainly responded to myocardial remodeling in the advanced disease stage and was poorly associated with the risk of MACE in patients at the early stage.[35] A further multivariable Cox regression analysis showed that age and LVM were not valid predictors of MACE in patients with LVNC after excluding the effect of confounding factors, while LVEF and LV entropy remained effective predictors of MACE. Previous studies have shown that young age (<18 years) is a risk factor for MACE in patients with LVNC.[24] However, 97% of this study's participants were adults, which may be the reason why age was not a valid predictor of MACE in this study. Additionally, although myocardial remodeling in patients with LVNC could lead to an increase in LVM, it was confirmed that multiple myocardial trabeculae in patients with LVNC could affect the calculation of LVM. Therefore, the assessment of the prognosis may not be accurate.[31] The results of the ROC curve analysis demonstrated that LV entropy and LVEF had good predictive values for MACE in patients with LVNC. The predictive efficacy improved when LV entropy was combined with LVEF. However, DeLong's test revealed no statistically significant difference between the AUC of LV entropy, LVEF, and the combined models of LV entropy and LVEF. This showed that LV entropy as a single prediction model was powerful in predicting MACE in patients with LVNC, which may help simplify the prediction model. The cut-off value for LV entropy was 5.09, indicating that MACE may be more likely to occur in patients with LVNC and LV entropy >5.09. Therefore, more attention should be paid to patients with LVNC and high LV entropy in clinical practice. This study initially verified that LV entropy could be used to predict the risk of MACE in patients with LVNC. However, this study had several limitations. 1) This was a single-center study, and the CMR images of all study populations were obtained using the same device. Whether the difference in the device and field strength could affect the measurement of entropy or not requires further exploration. 2) Among the participants in this trial, 97% were adults. More pediatric patients must be included in follow-up studies. 3) This study did not perform T1 mapping and extracellular volume fraction. Future studies with T1 mapping and extracellular volume fractions are required to validate the findings of this study. 4) Although it was found that LV entropy is a novel parameter that could predict the prognosis of patients with LVNC, the relatively small number of events was a fundamental limitation. Multivariate analysis was considered an exploratory study. Therefore, future prospective studies with larger sample sizes are required to validate these findings.

In conclusion, the LV entropy obtained from CMR-LGE is an effective predictor of MACE in patients with LVNC. The risk of MACE increases with increasing entropy, which could provide a more comprehensive risk stratification for patients with LVNC.

Conflict of interest disclosure

The authors declared no conflicts of interest.

Funding

This research was supported by Major Special Projects in Yunnan Province (202203AC100007), the National Natural Science Foundation of China (82160332), the Kunming Medical University Joint Special Project: Key Project (202201AY070001-097), and the In-Hospital Clinical Research Program of the Second Affiliated Hospital of Kunming Medical University (ynlIT2021010).

References

1. Elliott P, Andersson B, Arbustini E, et al. Classification of the cardiomyopathies: a position statement from the European Society of Cardiology Working Group on Myocardial and Pericardial Diseases. *Eur Heart J*. 2008;29(2):270-276. [CrossRef]
2. Arbustini E, Weidemann F, Hall JL. Left ventricular noncompaction: a distinct cardiomyopathy or a trait shared by different cardiac diseases?. *J Am Coll Cardiol*. 2014;64(17):1840-1850. [CrossRef]
3. Casas G, Limeres J, Oristrell G, et al. clinical risk prediction in patients with left ventricular myocardial noncompaction. *J Am Coll Cardiol*. 2021;78(7):643-662. [CrossRef]
4. Lee SE, Nguyen C, Xie Y, et al. Recent advances in cardiac magnetic resonance imaging. *Korean Circ J*. 2019;49(2):146-159. [CrossRef]
5. Leiner T, Bogaert J, Friedrich MG, et al. SCMR Position Paper (2020) on clinical indications for cardiovascular magnetic resonance. *J Cardiovasc Magn Reson*. 2020;22(1):76. [CrossRef]
6. Paszkowska A, Sarnecki J, Mirecka-Rola A, Kowalczyk-Domagała M, Mazurkiewicz Ł, Ziółkowska L. Imaging features of pediatric left ventricular noncompaction cardiomyopathy in echocardiography and cardiovascular magnetic resonance. *J Cardiovasc Dev Dis*. 2022;9(3):77. [CrossRef]
7. Rocon C, Tabassian M, Tavares de Melo MD, et al. Biventricular imaging markers to predict outcomes in non-compaction cardiomyopathy: a machine learning study. *ESC Heart Fail*. 2020;7(5):2431-2439. [CrossRef]
8. Androulakis AFA, Zeppenfeld K, Paiman EHM, et al. Entropy as a novel measure of myocardial tissue heterogeneity for prediction of ventricular arrhythmias and mortality in post-infarct patients. *JACC Clin Electrophysiol*. 2019;5(4):480-489. [CrossRef]
9. Petersen SE, Selvanayagam JB, Wiesmann F, et al. Left ventricular non-compaction: insights from cardiovascular magnetic resonance imaging. *J Am Coll Cardiol*. 2005;46(1):101-105. [CrossRef]
10. Kawel-Boehm N, Hetzel SJ, Ambale-Venkatesh B, et al. Reference ranges ("normal values") for cardiovascular magnetic resonance (CMR) in adults and children: 2020 update. *J Cardiovasc Magn Reson*. 2020;22(1):87. [CrossRef]
11. Gürdoğan M, Ustabaşıoğlu FE, Kula O, Korkmaz S. Cardiac magnetic resonance imaging and transthoracic echocardiography: investigation of concordance between the two methods for measurement of the cardiac chamber. *Medicina (Kaunas)*. 2019;55(6):260. [CrossRef]
12. Shannon CE. The mathematical theory of communication. 1963. *MD Comput*. 1997;14(4):306-317. [CrossRef]
13. Ross SB, Jones K, Blanch B, et al. A systematic review and meta-analysis of the prevalence of left ventricular non-compaction in adults. *Eur Heart J*. 2020;41(14):1428-1436. [CrossRef]
14. Vaidya VR, Lyle M, Miranda WR, et al. Long-term survival of patients with left ventricular noncompaction. *J Am Heart Assoc*. 2021;10(2):e015563. [CrossRef]
15. Aung N, Doimo S, Ricci F, et al. Prognostic significance of left ventricular noncompaction: systematic review and meta-analysis of observational studies. *Circ Cardiovasc Imaging*. 2020;13(1):e009712. [CrossRef]
16. Sedaghat-Hamedani F, Haas J, Zhu F, et al. Clinical genetics and outcome of left ventricular non-compaction cardiomyopathy. *Eur Heart J*. 2017;38(46):3449-3460. [CrossRef]
17. Cuevas J, Ptaszynski R, Cigarrán H, Calvo J, Martín M. Left ventricular noncompaction

cardiomyopathy: recent advances. *Kardiol Pol*. 2022;2. [CrossRef]

18. Miyake CY, Kim JJ. Arrhythmias in left ventricular noncompaction. *Card Electrophysiol Clin*. 2015;7(2):319-330. [CrossRef]
19. Ramchand J, Podugu P, Obuchowski N, et al. Novel approach to risk stratification in left ventricular non-compaction using a combined cardiac imaging and plasma biomarker approach. *J Am Heart Assoc*. 2021;10(8):e019209. [CrossRef]
20. Femia G, Zhu D, Choudhary P, et al. Long term clinical outcomes associated with CMR quantified isolated left ventricular non-compaction in adults. *Int J Cardiol*. 2021;328:235-240. [CrossRef]
21. Grigoratos C, Barison A, Ivanov A, et al. Meta-analysis of the prognostic role of late gadolinium enhancement and global systolic impairment in left ventricular noncompaction. *JACC Cardiovasc Imaging*. 2019;12(11 Pt 1):2141-2151. [CrossRef]
22. Stämpfli SF, Erhart L, Hagenbuch N, et al. Prognostic power of NT-proBNP in left ventricular non-compaction cardiomyopathy. *Int J Cardiol*. 2017;236:321-327. [CrossRef]
23. Zhou ZQ, He WC, Li X, et al. Comparison of cardiovascular magnetic resonance characteristics and clinical prognosis in left ventricular noncompaction patients with and without arrhythmia. *BMC Cardiovasc Disord*. 2022;22(1):25. [CrossRef]
24. Schultze-Berndt A, Kühnisch J, Herbst C, et al. Reduced systolic function and not genetic variants determine outcome in pediatric and adult left ventricular noncompaction cardiomyopathy. *Front Pediatr*. 2021;9:722926. [CrossRef]
25. Yu S, Chen X, Yang K, et al. Correlation between left ventricular fractal dimension and impaired strain assessed by cardiac MRI feature tracking in patients with left ventricular noncompaction and normal left ventricular ejection fraction. *Eur Radiol*. 2022;32(4):2594-2603. [CrossRef]
26. Iles LM, Ellims AH, Llewellyn H, et al. Histological validation of cardiac magnetic resonance analysis of regional and diffuse interstitial myocardial fibrosis. *Eur Heart J Cardiovasc Imaging*. 2015;16(1):14-22. [CrossRef]
27. Wang L, Peng L, Zhao X, Ma Y, Jin F, Zhao X. Prognostic value of entropy derived from late gadolinium enhancement images to adverse cardiac events in post-myocardial infarction patients. *Acad Radiol*. 2023;30(2):239-247. [CrossRef]
28. Muthalaly RG, Kwong RY, John RM, et al. Left ventricular entropy is a novel predictor of arrhythmic events in patients with dilated cardiomyopathy receiving defibrillators for primary prevention. *JACC Cardiovasc Imaging*. 2019;12(7 Pt 1):1177-1184. [CrossRef]
29. Li Q, Miao L, Xia L, et al. Left Ventricular noncompaction is associated with valvular regurgitation and a variety of arrhythmias. *J Cardiovasc Dev Dis*. 2022;9(2):49. [CrossRef]
30. Wu T, Liang Z, Zhang Z, et al. PRDM16 is a compact myocardium-enriched transcription factor required to maintain compact myocardial cardiomyocyte identity in left ventricle. *Circulation*. 2022;145(8):586-602. [CrossRef]
31. Jacquier A, Thuny F, Jop B, et al. Measurement of trabeculated left ventricular mass using cardiac magnetic resonance imaging in the diagnosis of left ventricular non-compaction. *Eur Heart J*. 2010;31(9):1098-1104. [CrossRef]
32. Liu S, Xie Y, Zhang H, et al. Multiple genetic variants in adolescent patients with left ventricular noncompaction cardiomyopathy. *Int J Cardiol*. 2020;302:117-123. [CrossRef]
33. Takahashi N, Sato N, Takagi K, et al. Clinical usefulness of gated technetium-99m sestamibi myocardial perfusion single-photon emission computed tomography with phase analysis for the management of patients with isolated ventricular noncompaction. *J Cardiol Cases*. 2014;11(4):101-104. [CrossRef]
34. Wengrofsky P, Armenia C, Oleszak F, et al. Left ventricular trabeculation and noncompaction cardiomyopathy: a review. *EC Clin Exp Anat*. 2019;2(6):267-283. [CrossRef]
35. Greutmann M, Mah ML, Silversides CK, et al. Predictors of adverse outcome in adolescents and adults with isolated left ventricular noncompaction. *Am J Cardiol*. 2012;109(2):276-281. [CrossRef]

Diagn Interv Radiol 2023; DOI: 10.4274/dir.2023.232233

CHEST IMAGING

ORIGINAL ARTICLE

Ultra-low-dose spectral-detector computed tomography for the accurate quantification of pulmonary nodules: an anthropomorphic chest phantom study

Xiuxiu Zhou#
Hanxiao Zhang#
Xiaoxing Jin#
Xiaohui Zhang
Xiaomei Lu
Qun Han
Xiaoge Xiong
Tian Liu
Yan Feng
Wenting Tu
Taohu Zhou
Yanming Ge
Peng Dong
Shiyuan Liu
Li Fan

#These authors contributed equally to this work.

From the Department of Radiology (X.Z., T.L., Y.F., W.T., S.L. ✉ radiology_cz@163.com, L.F. ✉ fanli0930@163.com), Second Affiliated Hospital of Naval Medical University, Shanghai, China; Department of Radiology (H.Z.), Xuzhou Medical University, School of Medical Imaging, Xuzhou, China; Department of Radiology Medicine (X.J.), The Second People's Hospital of Linhai, Linhai, China; Department of Clinical Science (X.Zha., Q.H.), Philips Healthcare, Shanghai, China; CT Clinical Science (X.L.), Philips Healthcare, Shanghai, China; School of Statistics and Management (X.X.), Shanghai University of Finance and Economics, Shanghai, China; Department of Radiology (T.Z., Y.G., P.D.), Weifang Medical University, School of Medical Imaging, Shanghai, China.

Received 31 March 2023; revision requested 23 April 2023; last revision received 04 July 2023; accepted 06 July 2023.

Epub: 10.08.2023

Publication date: 05.09.2023

DOI: 10.4274/dir.2023.232233

PURPOSE

To assess the quantification accuracy of pulmonary nodules using virtual monoenergetic images (VMIs) derived from spectral-detector computed tomography (CT) under an ultra-low-dose scan protocol.

METHODS

A chest phantom consisting of 12 pulmonary nodules was scanned using spectral-detector CT at 100 kVp/10 mAs, 100 kVp/20 mAs, 120 kVp/10 mAs, and 120 kVp/30 mAs. Each scanning protocol was repeated three times. Each CT scan was reconstructed utilizing filtered back projection, hybrid iterative reconstruction, iterative model reconstruction (IMR), and VMIs of 40–100 keV. The signal-to-noise ratio and air noise of images, absolute differences, and absolute percentage measurement errors (APEs) of the diameter, density, and volume of the four scan protocols and ten reconstruction images were compared.

RESULTS

With each fixed reconstruction image, the four scanning protocols exhibited no significant differences in APEs for diameter and density (all $P > 0.05$). Of the four scan protocols and ten reconstruction images, APEs for nodule volume had no significant differences (all $P > 0.05$). At 100 kVp/10 mAs, APEs for density using IMR were the lowest (APE_{-mean}: 6.69), but no significant difference was detected between VMIs at 50 keV (APE_{-mean}: 11.69) and IMR ($P = 0.666$). In the subgroup analysis, at 100 kVp/10 mAs, there were no significant differences between VMIs at 50 keV and IMR in diameter and density (all $P > 0.05$). The radiation dose at 100 kVp/10 mAs was reduced by 77.8% compared with that at 120 kVp/30 mAs.

CONCLUSION

Compared with IMR, reconstruction at 100 kVp/10 mAs and 50 keV provides a more accurate quantification of pulmonary nodules, and the radiation dose is reduced by 77.8% compared with that at 120 kVp/30 mAs, demonstrating great potential for ultra-low-dose spectral-detector CT.

KEYWORDS

Spectral computed tomography, chest phantom, pulmonary nodule, low-dose computed tomography, reconstruction algorithm

With increasing public attention on pulmonary nodules and lung cancer, low-dose chest computed tomography (CT) has become an effective modality for the diagnostic screening and prognostic evaluation of lung cancer.[1,2] However, radiation dose remains a key public concern. Image quality in low-dose CT with frequently-used reconstruction algorithms has been widely discussed.[3,4] With advances in reconstruction algorithms, iterative reconstruction (IR) and deep learning image reconstruction technologies have improved image quality.[4-7] In particular, IR decreases image noise and ensures image

You may cite this article as: Zhou X, Zhang H, Jin X, et al. Ultra-low-dose spectral-detector computed tomography for the accurate quantification of pulmonary nodules: an anthropomorphic chest phantom study. *Diagn Interv Radiol.* 2023;29(5):691-703.

quality by optimizing and correcting the raw data. The iDose^4 is a hybrid IR algorithm containing filtered back projection (FBP) and IR components, which could obtain low-noise and high-resolution images with a more complete and comprehensive system model.[8] Additionally, iterative model reconstruction (IMR), another IR algorithm based on the complete model but without FBP components, has been demonstrated to yield sufficiently high-quality images of the chest, abdomen, spine, and other organs.[9-11]

Dual-layer spectral CT (DLCT) with an energy level of 100 kVp is capable of energy analysis. Under a scanning protocol of 100 kVp/10 mAs, an effective radiation dose is reduced to 0.2954 mSv, equivalent to 5–6 times that of chest radiography exposures. The virtual monoenergy of spectral CT ranges from 40 to 200 keV; generally, the lower the keV value is, the higher the contrast and noise. Moreover, DLCT can reconstruct 161 virtual monoenergetic images (VMIs) at different keV levels (40–200 keV), but the accuracy of the quantitative evaluation of new-generation spectral CT is rarely reported. Additionally, studies have revealed that the radiation dose level, virtual monoenergetic level, and kVp tube voltage settings significantly affect the quantitative accuracy and image quality of spectral CT.[12,13] Therefore, this study aimed to assess the impact of different scanning protocols and reconstruction techniques on the quantitative measurement of pulmonary nodules by performing low-dose CT and ultra-low-dose CT scans using different image reconstruction techniques on a chest phantom.[14,15]

Main points

- A 100 kVp/10 mAs scan protocol based on spectral-detector computed tomography (CT) can accurately quantify the diameter and density of pulmonary nodules.
- Iterative model reconstruction (IMR) demonstrated improved image quality under the 100 kVp/10 mAs scan protocol, and virtual monoenergetic images at 50 keV were similar to those obtained with IMR.
- The ultra-low-dose scan protocol (100 kVp/10 mAs) based on spectral-detector CT reduced the radiation dose by 77.8% compared with that at 120 kVp/30 mAs.

Methods

Anthropomorphic chest phantom and synthetic lung nodules

A commercially available multipurpose anthropomorphic thoracic phantom (Lungman; Kyoto Kagaku, Kyoto, Japan; http://www.kyotokagaku.com) was utilized to simulate the human thorax. This phantom consisted of a life-size anatomical model of a human male thorax with substitute materials for soft tissues and synthetic bones. Three-dimensional synthetic pulmonary vessels and bronchi were inserted into the phantom lung.

In total, 12 spherical synthetic pulmonary nodules (Supplementary Table 1 and Supplementary Figure 1) were utilized. The attenuation levels of the ground-glass nodules (GGNs) were –800 and –630 Hounsfield unit (HU) and that of the solid nodules (SNs) was 100 HU. These nodules were randomly placed in the phantom by a technologist with 15 years of experience, and observers were blinded to the placement of the nodules. This retrospective study was approved by the Second Affiliated Hospital of Naval Medical University institutional review board (CZ-20220512-06), and the need for informed patient consent was waived.

Computed tomography image acquisition

All CT images were obtained using second-generation DLCT equipment (Philips spectral CT 7500, Best, The Netherlands). These image acquisitions were performed using four different radiation dose levels (100 kVp/10 mAs, 100 kVp/20 mAs, 120 kVp/10 mAs, and 120 kVp/30 mAs). The effective dose (ED) was determined as dose length product (DLP) × k (0.014), where DLP is the actual value. The scan parameters were as follows: collimation, 128 × 0.625 mm; beam width, 80 mm; slice thickness, 1 mm; pitch, 0.99; rotation time, 0.5 seconds. Each acquisition was repeated three times.

Image reconstruction

The dataset for each scanning dose contained conventional images and monoenergetic images from the original spectral base images data (SBI data) of Compton scattering and photoelectric effects. Conventional images were reconstructed using FBP, iDose^4 (level 5), and IMR (body routine level 2). In addition, VMIs were generated from SBI data obtained at 40–100 keV (iDose^4, spectral level 5) with a 10–keV interval (40/50/60/70/80/90/100 keV). In total, 40 reconstruction imaging datasets were obtained and analyzed.

Quantitative evaluation of nodules and image quality

The diameters and densities of the 12 nodules were manually measured independently by two radiologists with three years of experience in thoracic imaging. The longest nodule diameter on the maximum axial plane was measured. Nodule density was also measured on the maximum axial plane with a region of interest (ROI) large enough to cover the nodule, sparing the nodule margin to eliminate the partial volumetric effect. The images were transmitted to automatic volume measurement software (Infervision Medical Technology, Beijing, China) to automatically determine the volume of the nodules. Image quality was evaluated using the signal-to-noise ratio (SNR) and air noise (AN). The SNR was defined as the ratio of CT attenuation for the lung tissue to the standard deviation (SD) of AN. The ROIs were placed on the right lower lobe for the CT attenuation of the lung and in front of the middle of the sternum for the AN.

Statistical analysis

All statistical analyses were performed using SPSS software (version 26.0; IBM, Armonk, NY, USA) and Python 3. The intraclass correlation coefficient (ICC) was used to analyze overall consistency, and a Bland–Altman analysis was utilized for subgroup consistency. The Kruskal–Wallis test of overall significance was used to assess the significance of image quality. In case of a significant difference in the whole population, a Nemenyi post-hoc test was further applied. The absolute percentage measurement error (APE) was determined for the comparison of meas-

Table 1. Intra-observer agreement and inter-observer agreement of nodule parameters and image quality

Parameter	Intra-observer agreement	Inter-observer agreement
Diameter	0.999	0.986
Density	0.992	0.999
AN	0.887	0.912
SNR	0.965	0.973

AN, air noise; SNR, signal-to-noise ratio.

ured and reference data. The dimension and density of the mold provided by the phantom's manufacturer were used as reference data. The standard for volume was determined based on nodule dimension. The absolute difference and APE were presented as mean ± SD and compared among different scan protocols and reconstruction images. A *P* value <0.05 was considered statistically significant.

Results

Intra-observer and inter-observer consistencies of nodule parameters and image qualities

The ED values for the four scanning protocols were 0.2954, 0.588, 0.4774, and 1.3314 mSv (Supplementary Table 2). The intra-observer agreement levels for nodule diameter and density and the AN and SNR of images between observers were excellent, with ICCs of 0.999, 0.992, 0.887, and 0.965, respectively. The inter-observer agreement levels for nodule diameter and density and the AN and SNR of images between observers were excellent, with ICCs of 0.986, 0.999, 0.912, and 0.973, respectively (Table 1). The measurement results from one scanning are listed in Supplementary Table 3.

Image quality comparison

The image quality obtained using the four different scanning protocols (100 kVp/10 mAs, 100 kVp/20 mAs, 120 kVp/10 mAs, and 120 kVp/30 mAs) revealed statistical differences ($P < 0.05$) among nine of the image reconstruction types (FBP, iDose^4, and seven VMIs), with the exception of IMR ($P = 0.053$) (Table 2). The post-test analysis revealed no significant difference in image quality at 50 keV between 100 kVp/10 mAs and 120 kVp/30 mAs ($P > 0.05$). At doses of 100 kVp/10 mAs, 120 kVp/10 mAs, and 120 kVp/30 mAs, AN and SNR levels among the 10 image types demonstrated statistical differences (all $P < 0.05$).

Under a scanning protocol of 120 kVp/30 mAs, IMR exhibited the best image quality (AN_{-mean}: 6.03 and SNR_{-mean}: 166.32). In addition, at 100 kVp/10 mAs, the image quality of IMR (AN_{-mean}: 9.07 and SNR_{-mean}: 111.22) was better than that of FBP (AN_{-mean}: 31.20 and SNR_{-mean}: 32.27) and iDose^4 (AN_{-mean}: 31.20 and SNR_{-mean}: 32.37), and image quality at 100 keV was the poorest (AN_{-mean}: 38.90 and SNR_{-mean}: 26.11) (Figures 1, 2).

Effects of the four scanning protocols and 10 image reconstruction approaches on the diameter and density of pulmonary nodules

In each scanning group, the nodule volumes revealed no significant differences among the 10 reconstructed images ($P > 0.05$). The four scanning dose groups exhibited no significant statistical differences in the volume, diameter, and density of pulmonary nodules for each reconstruction image (all $P > 0.05$) (Tables 3, 4, Figures 3, 4). Nodules with

Table 2. Air noise and signal-to-noise ratio using 10 reconstruction images

Reconstruction algorithm	Low-dose scanning scheme		AN		SNR	
	kVp	mAs	APEs	*P*	APEs	*P*
40 keV	100	10	18.03 ± 3.87	0.034	57.51 ± 11.07	0.034
		20	28.17 ± 4.97		36.48 ± 5.75	
	120	10	36.63 ± 3.92		27.62 ± 3.07	
		30	24.03 ± 3.62		42.42 ± 6.69	
50 keV	100	10	24.3 ± 2.52	0.044	41.66 ± 4.08	0.044
		20	26.43 ± 1.12		38.11 ± 1.58	
	120	10	28.43 ± 2.15		35.43 ± 2.63	
		30	19.23 ± 1.8		52.45 ± 4.92	
60 keV	100	10	30 ± 2.51	0.023	33.62 ± 2.95	0.023
		20	27 ± 1.5		37.28 ± 2.09	
	120	10	24.63 ± 1.97		40.9 ± 3.15	
		30	17.13 ± 0.84		58.6 ± 2.8	
70 keV	100	10	33.83 ± 3.82	0.023	29.9 ± 3.59	0.023
		20	27.77 ± 2.72		36.39 ± 3.72	
	120	10	22.83 ± 2.03		44.16 ± 3.78	
		30	16.17 ± 0.49		62.04 ± 1.91	
80 keV	100	10	36.33 ± 4.61	0.016	27.9 ± 3.81	0.016
		20	28.4 ± 3.58		35.72 ± 4.8	
	120	10	21.87 ± 1.94		46.11 ± 3.98	
		30	15.8 ± 0.6		63.49 ± 2.38	
90 keV	100	10	37.83 ± 5.11	0.016	26.82 ± 3.93	0.016
		20	28.9 ± 4.17		35.22 ± 5.48	
	120	10	21.33 ± 1.79		47.23 ± 3.85	
		30	15.6 ± 0.72		64.34 ± 2.89	
100 keV	100	10	38.9 ± 5.49	0.016	26.11 ± 4.03	0.016
		20	29.23 ± 4.54		34.91 ± 5.91	
	120	10	21.07 ± 1.68		47.81 ± 3.71	
		30	15.53 ± 0.76		64.62 ± 3.04	
FBP	100	10	31.2 ± 3.92	0.031	32.27 ± 4.11	0.031
		20	23.93 ± 3.89		42.44 ± 6.31	
	120	10	22.67 ± 2.55		44.39 ± 4.71	
		30	15.63 ± 0.38		63.74 ± 1.16	
iDose^4	100	10	31.2 ± 3.92	0.031	32.37 ± 4.12	0.031
		20	23.93 ± 3.89		42.5 ± 6.32	
	120	10	22.67 ± 2.55		44.46 ± 4.7	
		30	15.63 ± 0.38		63.98 ± 1.54	
IMR	100	10	9.07 ± 0.95	0.053	111.22 ± 11.68	0.053
		20	7.77 ± 1.01		130.45 ± 17.46	
	120	10	8 ± 0.52		125.52 ± 8.7	
		30	6.03 ± 0.42		166.32 ± 11.02	

AN, air noise; SNR, signal-to-noise ratio; APEs, absolute percentage measurement errors; FBP, filtered back projection; IMR, iterative model reconstruction; iDose^4, a hybrid iterative reconstruction algorithm.

1.

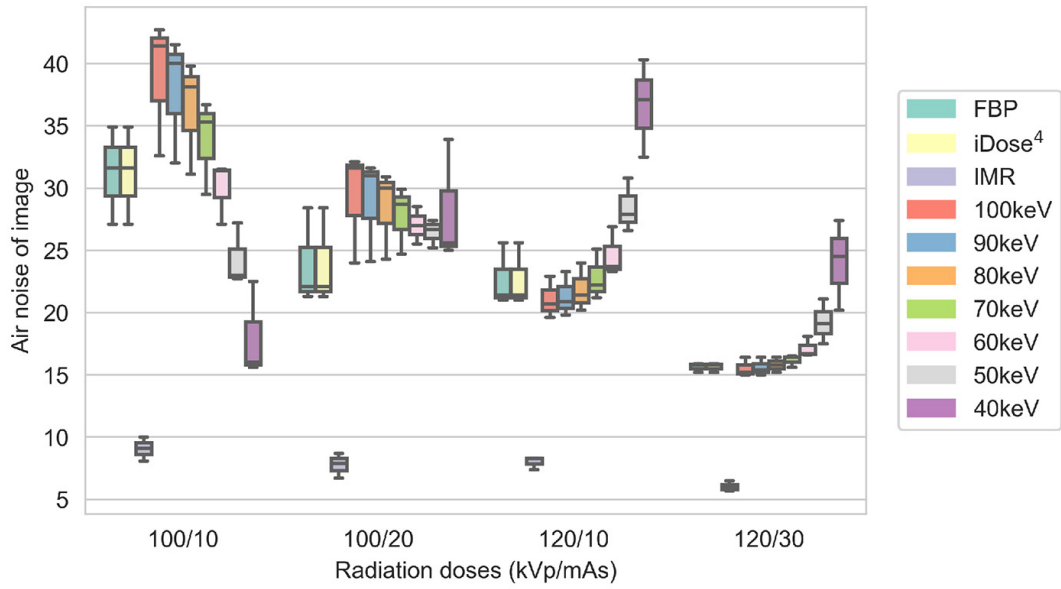

2.

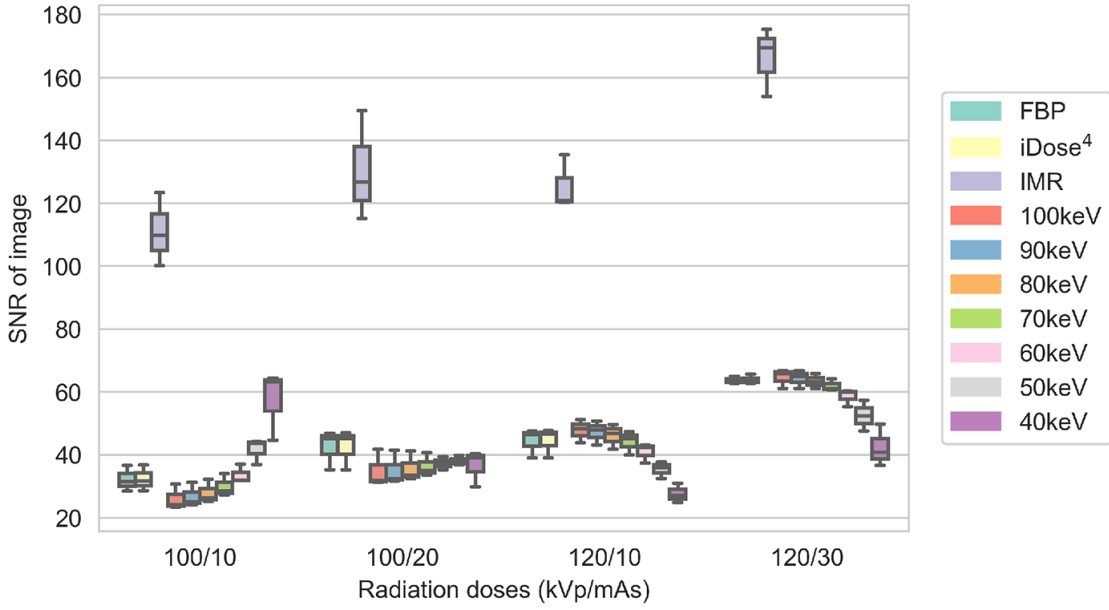

Figures 1, 2. Box plots of air noise and signal-to-noise ratios for 10 reconstruction images using 4 low-dose scanning protocols. SNR, signal-to-noise ratio; FBP, filtered back projection; iDose^4, a hybrid iterative reconstruction algorithm; IMR, iterative model reconstruction.

a size of 5 mm were not detected by the automatic detection software. In three scanning groups (100 kVp/10 mAs, 100 kVp/20 mAs, and 120 kVp/10 mAs), the pulmonary nodule densities obtained using the 10 reconstruction images were statistically different (all $P < 0.05$); however, at 120 kVp/30 mAs, no statistically significant difference was identified ($P > 0.05$). At 100 kVp/10 mAs, APEs for the density in IMR were the lowest (APE_{-mean}: 6.69), and no significant difference was detected between 50 keV (APE_{-mean}: 11.69) and IMR ($P = 0.666$). In each scanning group, nodule diameters were statistically different for the 10 reconstruction images ($P < 0.001$). At 120 kVp/30 mAs, APEs for the nodule diameter in IMR were the lowest (APE_{-mean}: 2.29) and no significant difference was identified between 50 keV (APE_{-mean}: 4.41), and IMR ($P = 0.726$) (Figures 5, 6).

Comparison of quantitative parameters between ground-glass nodules and solid nodules for fixed reconstruction images

For fixed reconstruction images, no significant differences in diameter and density measurements were detected for GGNs at –800 and –630 HU and SNs at 100 HU in the reconstruction images obtained using the four scanning protocols (all $P > 0.05$). However, with the exception of the density of SNs (100 HU), a difference was identified between the 100 kVp/10 mAs and 120 kVp/30 mAs scanning protocols for the 40-keV reconstruction image ($P = 0.036$).

Comparison of quantitative parameters between ground-glass nodules and solid nodules for fixed scanning protocols

For each scanning protocol, the diameters of the SNs at 100 HU measured using the 10 reconstruction images were statistically different ($P < 0.001$), but no significant statistical difference was detected in the diameter of GGNs (CT value: –800 and –630 HU) ($P > 0.05$). Furthermore, the post-

test analysis revealed no significant statistical differences at 100 kVp/10 mAs, 100 kVp/20 mAs, and 120 kVp/30 mAs between 50 keV and IMR in the diameters of SNs (CT value: 100 HU) (all $P > 0.05$). However, at 120 kVp/10 mAs, a statistically significant difference was identified between 50 keV and IMR in the diameters of SNs ($P = 0.029$) (Supplementary Figures 2-4).

Table 3. Mean absolute percentage measurement errors of the volume of pulmonary nodules based on 4 low-dose scanning schemes using 10 reconstruction images

Reconstruction algorithm	Low-dose scanning protocol		Volume	
	kVp	mAs	APEs	*P*
40 keV	100	10	12.43 ± 12.74	0.449
		20	16.64 ± 14.64	
	120	10	13.88 ± 11.02	
		30	9.82 ± 11.75	
50 keV	100	10	13.50 ± 11.50	0.303
		20	13.95 ± 10.26	
	120	10	14.11 ± 13.63	
		30	9.82 ± 11.17	
60 keV	100	10	12.83 ± 10.91	0.352
		20	15.92 ± 13.50	
	120	10	13.83 ± 13.53	
		30	9.39 ± 10.83	
70 keV	100	10	10.72 ± 9.19	0.240
		20	15.86 ± 13.43	
	120	10	13.86 ± 13.69	
		30	8.55 ± 11.29	
80 keV	100	10	9.23 ± 8.05	0.244
		20	15.57 ± 13.15	
	120	10	14.62 ± 13.19	
		30	8.59 ± 11.40	
90 keV	100	10	7.63 ± 7.29	0.338
		20	15.18 ± 13.26	
	120	10	14.35 ± 13.03	
		30	8.67 ± 11.39	
100 keV	100	10	7.94 ± 7.02	0.490
		20	15.14 ± 13.23	
	120	10	14.13 ± 13.27	
		30	8.61 ± 11.44	
FBP	100	10	13.45 ± 12.74	0.440
		20	16.45 ± 14.93	
	120	10	12.99 ± 12.36	
		30	10.21 ± 10.49	
iDose[4]	100	10	11.60 ± 12.12	0.875
		20	14.75 ± 13.25	
	120	10	12.77 ± 11.92	
		30	9.39 ± 10.94	
IMR	100	10	12.39 ± 12.55	0.508
		20	13.33 ± 11.84	
	120	10	7.58 ± 7.18	
		30	8.25 ± 10.52	

APEs, absolute percentage measurement errors; FBP, filtered back projection; IMR, iterative model reconstruction; iDose[4], a hybrid iterative reconstruction algorithm.

For GGNs examined at −630 HU and SNs assessed at 100 HU, all four scanning protocols exhibited statistical differences in density measurements in the 10 reconstruction images ($P < 0.05$). For GGNs examined at −800 HU, scanning protocols at 100 kVp/20 mAs and 120 kVp/30 mAs displayed statistical differences in density measurements in the 10 reconstruction images ($P < 0.05$). For GGNs assessed at −800 HU, scanning protocols at 100 kVp/10 mAs and 120 kVp/10 mAs had no statistical differences in density measurements in the 10 reconstruction images ($P > 0.05$). For SNs assessed at 100 HU and GGNs examined at −630 and −800 HU, no significant differences in density were detected between 50 keV and IMR at 100 kVp/10 mAs ($P > 0.05$) (Supplementary Figures 5-7). The CT images for the pulmonary nodules with different diameters and densities using IMR and the 50-keV reconstruction images under the four scanning protocols are presented in Figure 7.

Discussion

This study elucidated the differences in the accurate quantification of pulmonary nodules using different reconstruction protocols under ultra-low-dose scanning conditions based on spectral-detector CT. Furthermore, the effects of 10 image reconstruction approaches on the diameter and density of lung nodules in a phantom were investigated. Scanning at 100 kVp/10 mAs and 50 keV was applied to GGNs and SNs without affecting the quantification of nodule diameter and density. The image quality obtained using the IMR algorithm was superior; moreover, VMIs at 50 keV exhibited similar performance in the measurement of pulmonary nodules. This protocol reduced the effective radiation dose (ED: 0.2954 mSv) by 77.8% compared with that at 120 kVp/30 mAs (ED: 1.3314 mSv).

The lung is filled with air and receives a lower dose of radiation compared with the other parts of the body. The radiation dose for routine chest radiography in two planes is approximately 0.1 mSv; the radiation dose for conventional chest CT scanning is 5–7 mSv versus only 1–2 mSv for low-dose CT scanning.[16-18] Based on the principle that a dose as low as reasonably achievable should be used, low-dose CT scanning is preferred without affecting the diagnosis.[19,20] Additionally, studies have demonstrated that distinct radiation doses have no significant effects on the measurement of pulmonary nodules.[21] Under different kVp/mAs scanning conditions, the higher the kVp/mAs is, the

better the image quality, but the radiation dose also increases. However, tube voltage has a well-known exponential association with radiation dose; thus, lowering tube voltage can significantly decrease the radiation dose.[22,23] A radiation dose is linearly related to mAs; with decreasing mAs, the radiation dose decreases correspondingly. Four low-dose scanning protocols (120 kVp/30 mAs, 100 kVp/20 mAs, 120 kVp/10 mAs, and 100 kVp/10 mAs) exhibited no significant differences in the diameter and density of GGNs and SNs ($P > 0.05$). Therefore, the 100 kVp/10 mAs protocol may be recommended (ED: 0.2954 mSv) for the evaluation of pulmonary nodules, which would greatly reduce the radiation dose for ultra-low-dose CT (0.13–0.49 mSv).[24]

Table 4. Mean absolute percentage measurement errors of the diameter and density of pulmonary nodules based on 4 low-dose scanning protocols using 10 reconstruction images

Reconstruction algorithm	Low-dose scanning scheme		Diameter		Density	
	kVp	mAs	APEs	*P*	APEs	*P*
40 keV	100	10	4.64 ± 3.33	0.746	32.08 ± 47.46	0.716
		20	4.01 ± 2.92		26.53 ± 37.71	
	120	10	4.91 ± 3.58		17.08 ± 25.19	
		30	4.71 ± 3.64		16.92 ± 24.17	
50 keV	100	10	4.61 ± 2.89	0.741	11.69 ± 19.00	0.841
		20	4.25 ± 3.37		12.92 ± 16.64	
	120	10	4.82 ± 3.85		12.11 ± 15.68	
		30	4.41 ± 3.95		13.89 ± 22.39	
60 keV	100	10	5.03 ± 3.54	0.971	18.64 ± 29.58	0.675
		20	5.28 ± 4.08		14.44 ± 24.94	
	120	10	5.18 ± 3.21		17.25 ± 25.13	
		30	5.66 ± 4.42		17.47 ± 29.68	
70 keV	100	10	5.85 ± 4.61	0.849	26.97 ± 41.99	0.887
		20	5.62 ± 4.94		20.97 ± 33.21	
	120	10	5.47 ± 3.58		22.25 ± 32.52	
		30	6.38 ± 4.87		21.75 ± 34.81	
80 keV	100	10	6.10 ± 4.83	0.997	33.42 ± 50.16	0.826
		20	6.25 ± 5.27		25.81 ± 39.04	
	120	10	5.89 ± 4.05		26.28 ± 37.27	
		30	6.56 ± 5.37		25.03 ± 38.23	
90 keV	100	10	5.64 ± 4.08	0.994	37.47 ± 55.56	0.764
		20	5.66 ± 4.93		29.08 ± 42.92	
	120	10	5.46 ± 4.14		28.81 ± 40.30	
		30	5.85 ± 4.87		27.03 ± 40.44	
100 keV	100	10	6.62 ± 5.21	0.875	42.11 ± 60.15	0.725
		20	6.34 ± 5.61		31.19 ± 45.64	
	120	10	5.82 ± 4.60		30.64 ± 42.39	
		30	6.66 ± 5.01		28.50 ± 42.06	
FBP	100	10	2.76 ± 2.22	0.383	9.61 ± 13.94	0.670
		20	2.96 ± 2.72		10.81 ± 16.98	
	120	10	3.74 ± 2.81		13.83 ± 20.15	
		30	3.04 ± 3.10		17.42 ± 30.37	
iDose[4]	100	10	3.92 ± 3.19	0.764	10.47 ± 15.11	0.788
		20	3.24 ± 2.91		10.89 ± 17.20	
	120	10	3.13 ± 2.96		14.08 ± 20.51	
		30	3.99 ± 3.96		17.39 ± 30.22	
IMR	100	10	2.55 ± 2.26	0.478	6.69 ± 10.06	0.235
		20	2.08 ± 1.77		8.08 ±10.23	
	120	10	2.53 ± 1.83		8.22 ± 9.32	
		30	2.29 ± 2.90		10.86 ± 18.34	

APEs, absolute percentage measurement errors; FBP, filtered back projection; IMR, iterative model reconstruction; iDose[4], a hybrid iterative reconstruction algorithm.

The reconstruction algorithm is critical for CT examination, and image quality varies with different reconstruction algorithms. The traditional FBP has been used in CT image reconstruction for a long time with an obvious disadvantage; its key characteristic is that image noise is related to dose, with image noise increasing significantly when the radiation dose is reduced, affecting the accuracy of diagnosis.[25,26] The IR aims to reduce noise and improve image quality through the cost function, and based on the task, the cost function differs. As a result of technological developments, we are able to obtain low-noise and high-resolution CT images through iDose[4] and IMR technology.[8] This study revealed that under a scanning protocol of 100 kVp/10 mAs, superior image quality can be obtained using IMR (AN_{-mean}: 9.07, SNR_{-mean}: 111.22), and AN and SNR are significantly more effective than FBP and iDose[4], which is consistent with a study by Kim et al.[27] When they applied five scanning protocols at 120 kVp (100/50/20/10 mAs) and 80 kVp/10 mAs, the volume APE and image noise analysis of partly solid nodules (PSNs) and SNs demonstrated that IMR was significantly more effective than iDose[4] and FBP. For GGNs, IMR reduced the diameter measurement error and improved image quality.[28] Gavrielides et al.[29] determined that IMR improved measurement accuracy for 5-mm GGNs (−800 and −630 HU),[30] but its advantage needs to be verified for the measurement of smaller nodules. This study did not measure nodules with a diameter below 5 mm; therefore, the accuracy of IMR for the evaluation of nodules with a diameter below 5 mm also needs to be further elucidated. In the evaluation of nodules larger than 5 mm in diameter, IMR improved image quality in low-dose CT, allowing patients to obtain an accurate diagnosis without increasing the radiation dose. In first-generation DLCT, at the same kVp and mAs, the repeatability of monoenergetic reconstructed images was significantly higher than that of conventional images. The measurement repeatability of

3.

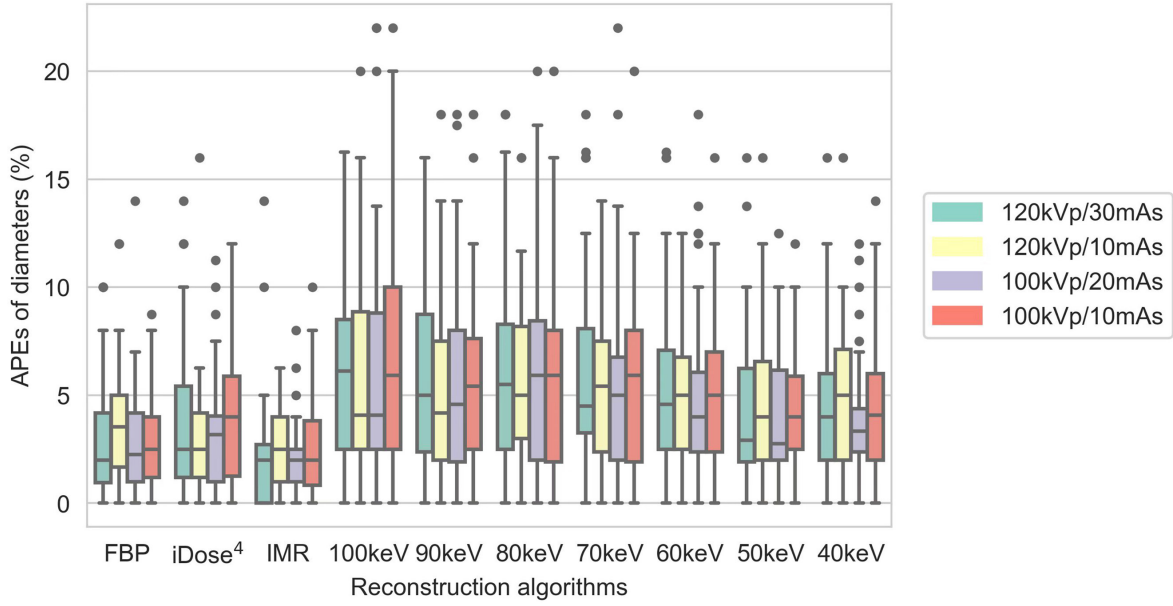

4.

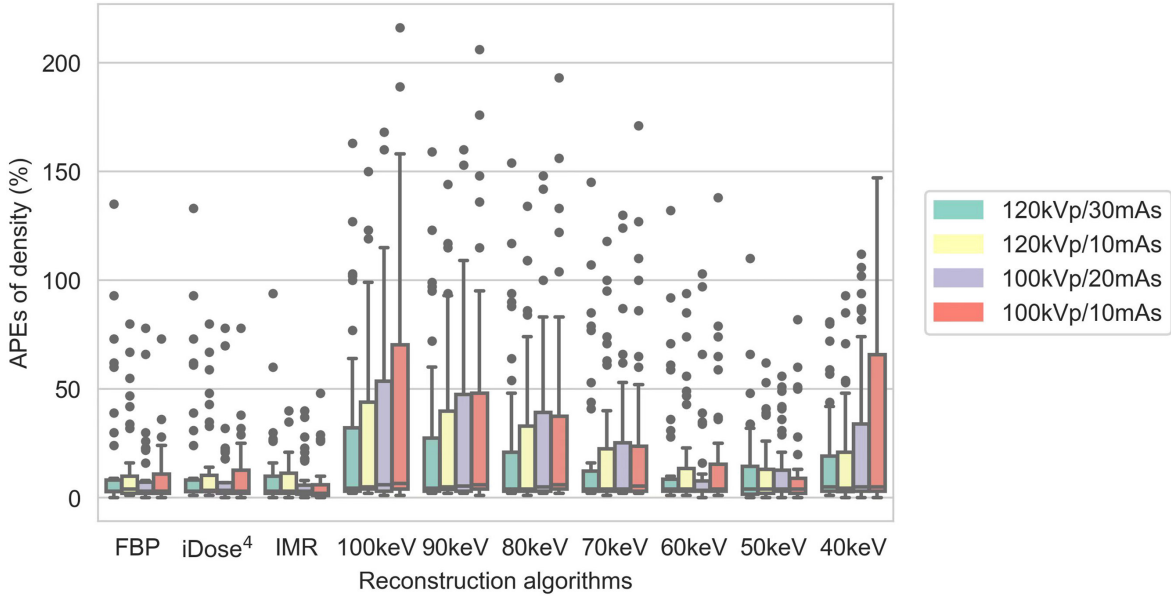

Figures 3, 4. Box plots of the mean absolute percentage measurement errors of the diameter and density of pulmonary nodules for 4 low-dose scanning protocols using 10 reconstruction images. APEs, absolute percentage measurement errors; FBP, filtered back projection; iDose^4, a hybrid iterative reconstruction algorithm; IMR, iterative model reconstruction.

VMIs for pulmonary nodules were equivalent to that of conventional images using the IR algorithm at a standard dose, suggesting the use of monoenergetic images might allow lung cancer screening at a lower radiation dose.[31] Other data revealed that images at a low single-energy level have lower noise and higher image contrast.[32] Regarding spectral CT, low VMIs exhibited better image quality than conventional images from the same system.[33] This outcome is consistent with that of the present study. At a VMI energy level of 50 keV, image quality is not optimal, but 50 keV did not affect the diameter and density of lung nodules in the examined chest phantom.

This study has some limitations. First, the phantom involved in this study was a simple simulation of the adult chest, with a scanning length of 33 cm, which does not represent the actual clinical situation, including the influence of factors such as respiratory movement and patient body shape on the quantitative accuracy and image quality of spectral CT. Additionally, studies have indicated that scan length also affects the radiation dose received by patients,[34,35] which was not evaluated in the present study. Second, second-generation DLCT was applied, and first-generation should be further validated in patients. Third, during scanning, the phantom was scanned 12 times under four scanning conditions (three times for each scanning condition). The positions of nodules in the phantom were inevitably changed when they entered and left the bed, which might impact the measurements. Fourth, the phantom only contained 12 nodules, and pulmonary nodules in this study were circular; however, irregular nodules were not included in the phantom, and PSNs were not evaluated. Therefore, this study may only be applicable to circular GGNs and SNs.

In conclusion, 100 kVp/10 mAs with 50-keV reconstruction demonstrated more accurate quantification of pulmonary nodules than IMR, and the radiation dose was re-

5.

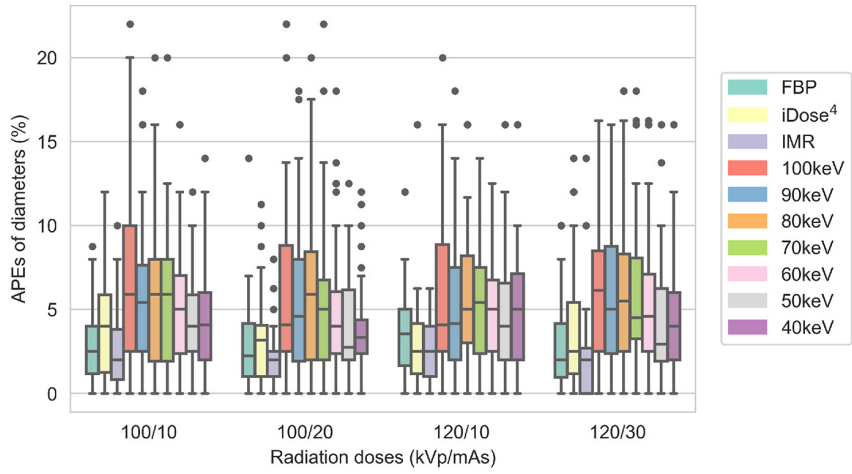

6.

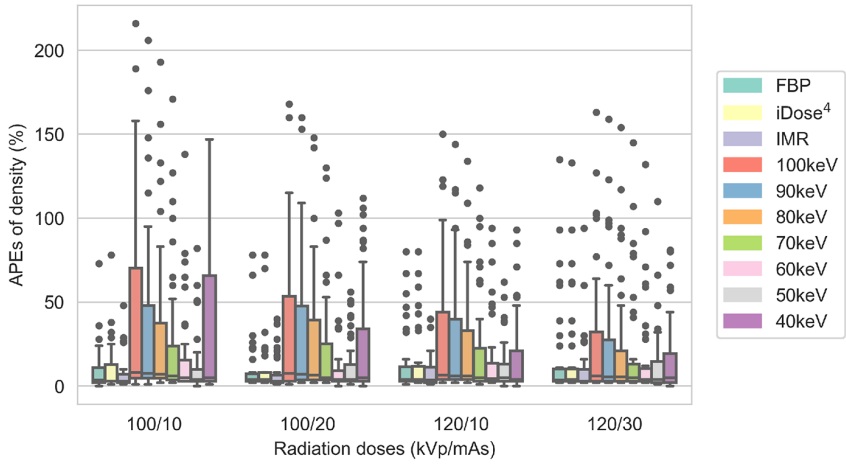

Figures 5, 6. Box plots of mean absolute percentage measurement errors of the diameter and density of pulmonary nodules for 10 reconstruction images and four low-dose scanning protocols. APEs, absolute percentage measurement errors; FBP, filtered back projection; iDose^4, a hybrid iterative reconstruction algorithm; IMR, iterative model reconstruction.

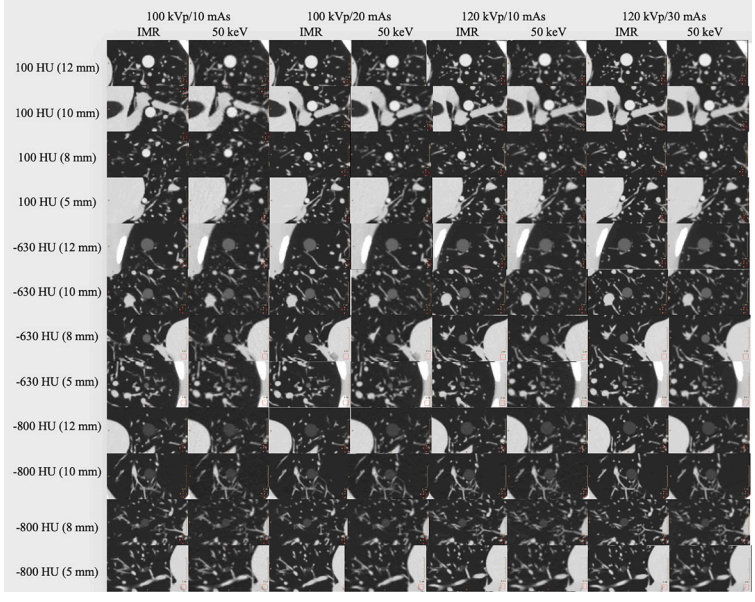

Figure 7. Computed tomography images of pulmonary nodules with different diameters and densities for iterative model reconstruction and 50-keV reconstruction images under four scanning protocols. IMR, iterative model reconstruction; HU, Hounsfield unit.

duced by 77.8% compared with that at 120 kVp/30 mAs, revealing great potential for ultra-low-dose spectral-detector CT.

Acknowledgments

The authors are grateful to Ke Chen and Lijun Wang for providing technical support. Permission was provided by them.

Conflict of interest disclosure

The authors declared no conflicts of interest.

Funding

This work was supported by the National Natural Science Foundation of China (grant numbers: 81871321, 82171926, 81930049, and 82202140); the program of Science and Technology Commission of Shanghai Municipality (grant number 21DZ2202600); National Key R&D Program of China (grant number: 2022YFC2010000, 2022YFC2010002, 2017YFC1308703); the construction of CT standardized database for chronic obstructive pulmonary disease (grant number: YXFSC2022JJSJ002); Science and Technology Innovation Action Plan Project of Shanghai (grant number: 19411951300); Shanghai Sailing Program (grant number: 20YF1449000); Clinical Innovation Project of Shanghai Changzheng Hospital (grant number: 2020YLCYJ-Y24).

References

1. Jemal A, Fedewa SA. Lung cancer screening with low-dose computed tomography in the United States-2010 to 2015. *JAMA Oncol*. 2017;3(9):1278-1281. [CrossRef]
2. Ruano-Ravina A, Pérez-Ríos M, Casàn-Clará P, Provencio-Pulla M. Low-dose CT for lung cancer screening. *Lancet Oncol*. 2018;19(3):e131-e132. [CrossRef]
3. Fleischmann D, Boas FE. Computed tomography--old ideas and new technology. *Eur Radiol*. 2011;21(3):510-517. [CrossRef]
4. Fält T, Söderberg M, Hörberg L, et al. Simulated dose reduction for abdominal CT with filtered back projection technique: effect on liver lesion detection and characterization. *AJR Am J Roentgenol*. 2019;212(1):84-93. [CrossRef]
5. Padole A, Ali Khawaja RD, Kalra MK, Singh S. CT radiation dose and iterative reconstruction techniques. *AJR Am J Roentgenol*. 2015;204(4):W384-W392. [CrossRef]
6. Sun J, Li H, Li J, et al. Improving the image quality of pediatric chest CT angiography with low radiation dose and contrast volume using deep learning image reconstruction. *Quant Imaging Med Surg*. 2021;11(7):3051-3058. [CrossRef]

7. Geyer LL, Schoepf UJ, Meinel FG, et al. State of the art: iterative ct reconstruction techniques. *Radiology*. 2015;276(2):339-357. [CrossRef]
8. Laqmani A, Avanesov M, Butscheidt S, et al. Comparison of image quality and visibility of normal and abnormal findings at submillisievert chest CT using filtered back projection, iterative model reconstruction (IMR) and iDose4™. *Eur J Radiol*. 2016;85(11):1971-1979. [CrossRef]
9. Wu Y, Jiang Y, Han X, Wang M, Gao J. Application of low-tube current with iterative model reconstruction on Philips Brilliance iCT Elite FHD in the accuracy of spinal QCT using a European spine phantom. *Quant Imaging Med Surg*. 2018;8(1):32-38. [CrossRef]
10. Kim C, Lee KY, Shin C, et al. Comparison of filtered back projection, hybrid iterative reconstruction, model-based iterative reconstruction, and virtual monoenergetic reconstruction images at both low- and standard-dose settings in measurement of emphysema volume and airway wall thickness: a ct phantom study. *Korean J Radiol*. 2018;19(4):809-817. [CrossRef]
11. Greffier J, Frandon J, Larbi A, Beregi JP, Pereira F. CT iterative reconstruction algorithms: a task-based image quality assessment. *Eur Radiol*. 2020;30(1):487-500. [CrossRef]
12. Cester D, Eberhard M, Alkadhi H, Euler A. Virtual monoenergetic images from dual-energy CT: systematic assessment of task-based image quality performance. *Quant Imaging Med Surg*. 2022;12(1):726-741. [CrossRef]
13. Dabli D, Frandon J, Belaouni A, et al. Optimization of image quality and accuracy of low iodine concentration quantification as function of dose level and reconstruction algorithm for abdominal imaging using dual-source CT: a phantom study. *Diagn Interv Imaging*. 2022;103(1):31-40. [CrossRef]
14. Zhao R, Sui X, Qin R, et al. Can deep learning improve image quality of low-dose CT: a prospective study in interstitial lung disease. *Eur Radiol*. 2022;32(12):8140-8151. [CrossRef]
15. Du Y, Shi GF, Wang YN, Wang Q, Feng H. Repeatability of small lung nodule measurement in low-dose lung screening: a phantom study. *BMC Med Imaging*. 2020;20(1):112. [CrossRef]
16. Ye K, Zhu Q, Li M, Lu Y, Yuan H. A feasibility study of pulmonary nodule detection by ultralow-dose CT with adaptive statistical iterative reconstruction-V technique. *Eur J Radiol*. 2019;119:108652. [CrossRef]
17. Messerli M, Kluckert T, Knitel M, et al. Ultralow dose CT for pulmonary nodule detection with chest x-ray equivalent dose - a prospective intra-individual comparative study. *Eur Radiol*. 2017;27(8):3290-3299. [CrossRef]
18. Miller AR, Jackson D, Hui C, et al. Lung nodules are reliably detectable on ultra-low-dose CT utilising model-based iterative reconstruction with radiation equivalent to plain radiography. *Clin Radiol*. 2019;74(5):409.e17-409.e22. [CrossRef]
19. Mechlem K, Ehn S, Sellerer T, et al. Joint statistical iterative material image reconstruction for spectral computed tomography using a semi-empirical forward model. *IEEE Trans Med Imaging*. 2018;37(1):68-80. [CrossRef]
20. Ren L, Rajendran K, McCollough CH, Yu L. Quantitative accuracy and dose efficiency of dual-contrast imaging using dual-energy CT: a phantom study. *Med Phys*. 2020;47(2):441-456. [CrossRef]
21. Hein PA, Romano VC, Rogalla P, et al. Linear and volume measurements of pulmonary nodules at different CT dose levels - intrascan and interscan analysis. *Rofo*. 2009;181(1):24-31. [CrossRef]
22. Kalender WA, Buchenau S, Deak P, et al. Technical approaches to the optimisation of CT. *Phys Med*. 2008;24(2):71-79. [CrossRef]
23. Hausleiter J, Meyer T, Hadamitzky M, et al. Radiation dose estimates from cardiac multislice computed tomography in daily practice: impact of different scanning protocols on effective dose estimates. *Circulation*. 2006;113(10):1305-1310. [CrossRef]
24. Carey S, Kandel S, Farrell C, et al. Comparison of conventional chest x ray with a novel projection technique for ultra-low dose CT. *Med Phys*. 2021;48(6):2809-2815. [CrossRef]
25. Laqmani A, Kurfürst M, Butscheidt S, et al. CT pulmonary angiography at reduced radiation exposure and contrast material volume using iterative model reconstruction and iDose4 technique in comparison to FBP. *PLoS One*. 2016;11(9):e0162429. [CrossRef]
26. Willemink MJ, de Jong PA, Leiner T, et al. Iterative reconstruction techniques for computed tomography Part 1: technical principles. *Eur Radiol*. 2013;23(6):1623-1631. [CrossRef]
27. Kim SK, Kim C, Lee KY, et al. Accuracy of model-based iterative reconstruction for CT volumetry of part-solid nodules and solid nodules in comparison with filtered back projection and hybrid iterative reconstruction at various dose settings: an anthropomorphic chest phantom study. *Korean J Radiol*. 2019;20(7):1195-1206. [CrossRef]
28. Kim H, Park CM, Chae HD, Lee SM, Goo JM. Impact of radiation dose and iterative reconstruction on pulmonary nodule measurements at chest CT: a phantom study. *Diagn Interv Radiol*. 2015;21(6):459-465. [CrossRef]
29. Gavrielides MA, Berman BP, Supanich M, et al. Quantitative assessment of nonsolid pulmonary nodule volume with computed tomography in a phantom study. *Quant Imaging Med Surg*. 2017;7(6):623-635. [CrossRef]
30. Maruyama S, Fukushima Y, Miyamae Y, Koizumi K. Usefulness of model-based iterative reconstruction in semi-automatic volumetry for ground-glass nodules at ultra-low-dose CT: a phantom study. *Radiol Phys Technol*. 2018;11(2):235-241. [CrossRef]
31. Kim J, Lee KH, Kim J, Shin YJ, Lee KW. Improved repeatability of subsolid nodule measurement in low-dose lung screening with monoenergetic images: a phantom study. *Quant Imaging Med Surg*. 2019;9(2):171-179. [CrossRef]
32. Sellerer T, Noël PB, Patino M, et al. Dual-energy CT: a phantom comparison of different platforms for abdominal imaging. *Eur Radiol*. 2018;28(7):2745-2755. [CrossRef]
33. Doerner J, Hauger M, Hickethier T, et al. Image quality evaluation of dual-layer spectral detector CT of the chest and comparison with conventional CT imaging. *Eur J Radiol*. 2017;93:52-58. [CrossRef]
34. Kanal KM, Butler PF, Sengupta D, Bhargavan-Chatfield M, Coombs LP, Morin RL. U.S. diagnostic reference levels and achievable doses for 10 adult CT examinations. *Radiology*. 2017;284(1):120-133. [CrossRef]
35. Badawy MK, Galea M, Mong KS, U P. Computed tomography overexposure as a consequence of extended scan length. *J Med Imaging Radiat Oncol*. 2015;59(5):586-589. [CrossRef]

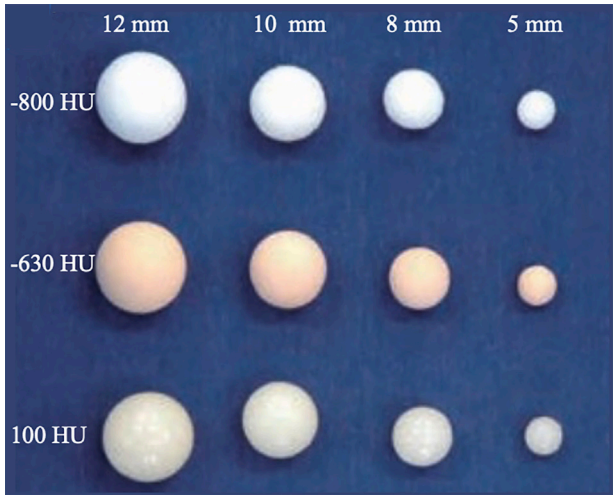

Supplementary Figure 1. Artificial pulmonary nodules with four distinct diameters (5, 8, 10, and 12 mm) and three different densities (–800, –630, and 100 HU). HU, Hounsfield unit.

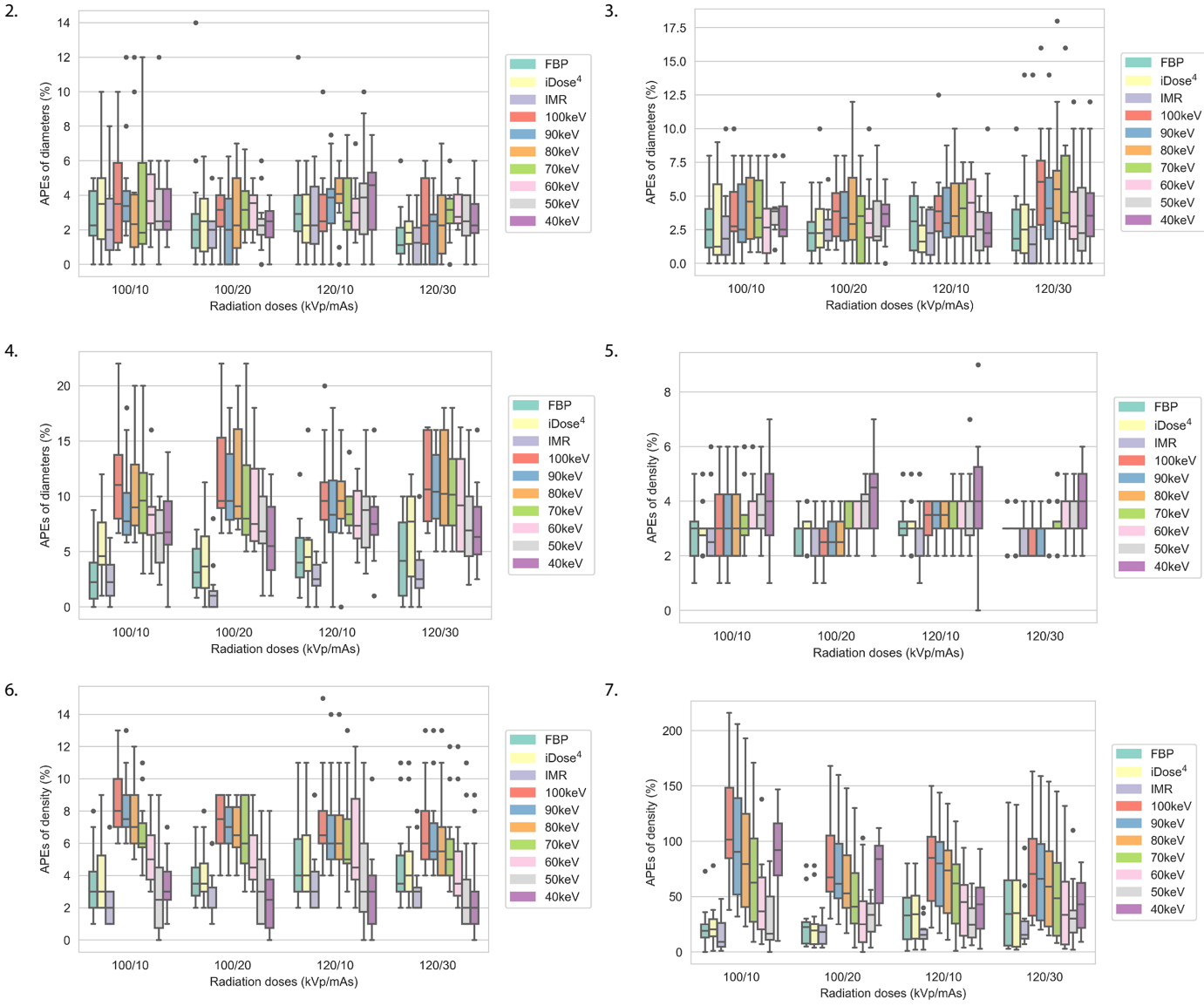

Supplementary Figures 2-7. Diameter and density mean absolute percentage measurement error box plots of nodules obtained at densities of –800, –630, and 100 HU for 10 reconstruction images under 4 scanning protocols. HU, Hounsfield unit; APEs, absolute percentage measurement errors; FBP, filtered back projection; iDose^4, a hybrid iterative reconstruction algorithm; IMR, iterative model reconstruction.

Supplementary Table 1. Characteristics of 12 spherical synthetic lung nodules

Nodule number	Diameter (mm)	Density (HU)	Nodule type
1	12	−800	GGN
2	10	−800	GGN
3	8	−800	GGN
4	5	−800	GGN
5	12	−630	GGN
6	10	−630	GGN
7	8	−630	GGN
8	5	−630	GGN
9	12	100	SN
10	10	100	SN
11	8	100	SN
12	5	100	SN

GGN, ground-glass nodule; SN, solid nodule; HU, Hounsfield unit.

Supplementary Table 2. Estimated radiation dose for various computed tomography protocols

kVp/mAs	CTDIvol (mGy)	L (cm)	DLP_{actual} mGy*cm	ED (mSv)
100 kVp/10 mAs	0.5	32	21.1	0.2954
100 kVp/20 mAs	1	32	42	0.588
120 kVp/10 mAs	0.8	32	34.1	0.4774
120 kVp/30 mAs	2.3	32	95.1	1.3314

CTDIvol, computed tomography dose index; L, length of the exposure; DLP_{actual}, actual value of dose length product; ED, effective dose.

Supplementary Table 3. Nodule parameters and image quality for one scanning protocol

Low-dose scanning scheme	Reconstruction algorithm	Lung tissue (HU)	Air SD	Nodule 1		Nodule 2		Nodule 3		Nodule 4	
				Diameter (mm)	Density (HU)	Diameter (mm)	Density (HU)	Diameter (mm)	Density(HU)	Diameter (mm)	Density (HU)
120 kVp/30 mAs	40 keV	-1001.1	24.5	12.3	-833.9	10.4	-818.1	8.2	-837.6	5.3	-821.7
	50 keV	-1001.8	19.1	12.2	-827.4	10.2	-820.3	8.2	-832	5.2	-825.7
	60 keV	-1001.8	16.6	12.5	-823.7	10.2	-821.4	8.4	-828.8	5.2	-828.2
	70 keV	-1001.9	15.6	12.3	-821.5	10.3	-822.2	8.3	-826.9	5.1	-829.7
	80 keV	-1001.9	15.2	12.1	-820	10.1	-822.7	8.2	-825.6	5.2	-830.7
	90 keV	-1002.1	15	12	-819.1	10	-823.1	8.2	-824.9	5.2	-831.2
	100 keV	-1002.2	15	12.6	-818.4	10.1	-823.3	8.2	-824.3	5.3	-831.5
	FBP	-999.6	15.9	12.4	-824.2	10.1	-822.8	8.1	-820.9	5.1	-825.4
	IDose^4	-999.7	15.9	12.4	-824.5	10.2	-824.4	8.2	-822.1	5.1	-826.6
	IMR	-1000.2	5.9	11.9	-820.8	10.2	-821.8	8	-817.2	5	-821.3
120 kVp/10 mAs	40 keV	-1001.3	40.3	12.5	-821.5	10.5	-805.3	8.5	-830.9	4.9	-827
	50 keV	-1002.6	30.8	12	-819.2	10.2	-816.5	8.5	-826.9	4.5	-828.6
	60 keV	-1003.3	26.9	12.6	-817.8	10.7	-823.1	8.3	-824.5	4.9	-829.6
	70 keV	-1003.8	25.1	12.2	-817	10.7	-827.1	8.2	-823	5	-830.4
	80 keV	-1004	24	12.6	-816.5	10.5	-829.6	8	-822	5.2	-830.8
	90 keV	-1004.3	23.3	12.5	-816.2	10.7	-831.2	8.3	-821.4	4.9	-831.2
	100 keV	-1004.3	22.9	12.5	-816	11	-832.3	8.2	-821.1	5	-831.2
	FBP	-998	25.6	12.4	-819	10.4	-823.4	8.3	-821.4	4.4	-824.7
	IDose^4	-1000.3	25.6	12.2	-819.3	10.2	-825.4	8	-822.4	4.7	-827.5
	IMR	-1002.6	8.3	11.9	-814	10.6	-822.1	8.1	-813.3	4.7	-824.5
100 kVp/20 mAs	40 keV	-1003.8	25.6	12.2	-839.1	10.3	-838.7	8.1	-824.9	4.9	-854.5
	50 keV	-1004.3	25.2	12.3	-830	10.2	-828.4	8	-823	4.7	-841
	60 keV	-1004.5	27	12.3	-824.6	10.5	-822.2	7.9	-821.9	5.1	-833.1
	70 keV	-1004.5	28.7	12.4	-821.5	10.4	-818.6	8.1	-821.2	4.9	-828.4
	80 keV	-1004.5	30	12.4	-819.4	10.2	-816.3	8.1	-820.7	4.9	-825.4
	90 keV	-1004.6	31	12.2	-818.1	10.2	-814.9	8.2	-820.4	5	-823.5
	100 keV	-1004.6	31.6	12.3	-817.3	10.5	-813.8	7.9	-820.4	4.8	-822.1
	FBP	-1000.1	21.3	12.5	-822.3	10.2	-820.5	8.1	-815.2	4.7	-832.1
	IDose^4	-1000.8	21.3	12.4	-823.9	10.1	-822.5	8	-817.4	4.8	-832.9
	IMR	-1001.5	6.7	12.3	-820.9	10	-821.2	7.8	-810.7	4.9	-833.5
100 kVp/10 mAs	40 keV	-1006.8	22.5	12.2	-830.4	8.4	-637.7	8.6	170.9	5.1	-824.5
	50 keV	-1005.3	27.2	12.1	-824.5	8.3	-653.2	8.6	103.1	5.1	-834.8
	60 keV	-1004.4	31.5	12.2	-821.1	7.7	-662.1	8.7	63.1	5.3	-840.8
	70 keV	-1003.8	35.3	12.2	-819	10.1	-820.5	8.9	39.5	5.6	-844.3
	80 keV	-1003.5	38.1	12.2	-817.7	10.1	-816.2	8.8	24.2	5.5	-846.7
	90 keV	-1003.2	40	12.3	-816.9	9.7	-813.3	8.8	14.4	5.1	-848.1
	100 keV	-1003.1	41.4	12.1	-816.3	9.6	-811.6	8.9	7.8	5.5	-849.1
	FBP	-995.8	34.9	12.2	-821.8	9.6	-815.9	7.6	-812.9	5.1	-835.3
	IDose^4	-998.9	34.9	12.2	-821.6	10	-821.3	7.6	-816.7	5.5	-834.1
	IMR	-1000.5	9.1	12.1	-816.8	10	-824.7	7.7	-812.3	5.4	-839.2

SD, standard deviation; FBP, filtered back projection; IMR, iterative model reconstruction; iDose^4, a hybrid iterative reconstruction algorithm; HU, Hounsfield unit.

Nodule 5		Nodule 6		Nodule 7		Nodule 8		Nodule 9		Nodule 10		Nodule 11		Nodule 12	
Diameter (mm)	Density (HU)	Diameter (mm)	Density (HU)	Diameter (mm)	Density (HU)	Diameter (mm)	Density (HU)	Diameter (mm)	Density (HU)	Diameter (mm)	Density (HU)	Diameter (mm)	Density (HU)	Diameter (mm)	Density (HU)
12.2	-617.1	10.4	-631.4	8.2	-619.6	5.6	-688.3	12.6	181.2	10.6	117.1	8.9	144	5.5	91.2
12	-634.1	10	-643.4	8.1	-640.9	5.4	-698.1	12.6	134.3	10.2	87.1	9.1	93.8	5.4	51.9
12.3	-643.8	10.1	-650.5	8.1	-653.5	5.5	-703.8	12.8	106.7	10.5	69.3	9.3	64.4	5.8	28.9
12.4	-659.8	10.1	-654.6	8.3	-661	5.4	-707.3	12.9	90.3	10.8	58.9	9.3	46.9	5.6	15
12.5	-653.6	9.8	-657.4	8.2	-665.9	5.6	-709.4	12.9	79.8	10.6	52.2	9.3	35.6	5.8	6.2
12.3	-655.9	9.9	-659.1	8.1	-668.9	5.2	-710.8	13	72.9	10.8	47.8	9.1	28.4	5.6	0.5
12.3	-657.7	10.3	-660.2	8.5	-671	5.5	-711.9	12.8	68.4	10.8	44.9	9.3	23.4	5.8	-3.4
11.8	-642.1	9.9	-649.4	8	-655.6	5.2	-700.3	12.5	102.8	9.9	75.9	8.6	61.2	5.5	27
12	-644.4	10.1	-650.9	8.2	-656.3	5.4	-700.8	12.5	102.4	10	75.5	8.7	61.3	5.6	27.2
12.1	-642.9	9.6	-645.4	8	-647	5	-682.9	12	115.6	9.8	92.8	8.4	92.5	5	73
12.2	-621.8	10.3	-630.8	8.2	-661.8	5.1	-646.5	12.9	193	10.8	154.1	8.6	126.9	5.3	79.1
12.2	-636.9	10.3	-648	8.4	-666.6	5.2	-667.5	12.9	138.2	10.4	105.8	8.8	74.5	5.6	38.4
12.3	-645.8	10.7	-658.4	8.5	-699.3	5.3	-679.9	12.8	106.1	10.8	77.3	9	43.8	5.4	14.5
12.5	-651.1	10.5	-664.4	8.5	-671	5	-687.2	13.2	86.9	10.8	60.4	8.7	25.6	5.5	0.2
12	-645.5	10.4	-668.4	8.5	-672.1	4.9	-691.9	13.4	74.7	10.8	49.5	8	13.7	5.5	-9
12.2	-656.7	10.8	-670.8	8.6	-672.7	4.9	-695	13.1	66.7	10.6	42.6	8	6.3	5.6	-15
12.3	-658.2	10.6	-672.6	8.4	-673.2	4.8	-696.9	13.2	61.3	10.8	37.8	8.9	1.1	5.5	-18.8
12.1	-649	10.5	-655.7	8.4	-664.2	5.2	-675.8	12.4	107.5	10.4	86.6	8.5	52.9	5.4	32.6
12.1	-649.1	10	-657.6	8.1	-666.2	4.9	-678.5	12.4	105.9	10.6	86.2	8.5	51.7	5.2	32.9
11.9	-644	10.2	-649.5	8	-657.2	4.8	-661	12.3	116.9	10.3	102.3	8.2	80.2	5.1	85.7
12	-608.1	9.7	-627.4	8.1	-611	5.3	-670.3	12.4	212.5	10.1	174.5	8.6	182.1	5.2	126.2
11.9	-633.7	9.8	-646.5	8	-642.1	5.1	-677.5	12.8	141.8	10.1	120.9	8.8	105.7	5.3	48.6
11.8	-648.7	10.2	-657.7	8.1	-660.5	5.5	-681.8	12.7	100.2	10.6	89.3	9	60.7	5.3	3
12.2	-657.6	10	-664.4	8	-671.4	5	-684.4	12.8	75.4	10.7	70.6	9	34	5.3	-24.2
12.4	-663.5	9.9	-668.6	8.2	-678.5	5.3	-686	13	59.5	10.8	58.6	9	16.8	5.4	-41.7
12.2	-667	10	-671.4	8.5	-682.9	5	-687.1	12.8	49.4	10.9	50.8	9.1	5.8	5.5	-52.8
12.2	-669.7	10.1	-673.3	8.4	-686	5.1	-687.8	12.8	42.4	10.9	45.5	8.7	-1.7	5.5	-60.3
12	-647.5	9.7	-646.8	8.1	-655	5.1	-668.3	12.1	104.9	10.1	105	8.3	74.4	4.9	34.1
12	-647.2	9.6	-648.9	8.1	-655.9	5.1	-671.9	12.1	104.4	10.2	103.7	8.6	78.1	5	30.1
12.2	-640.4	9.7	-644	7.8	-644.7	4.9	-656.2	12	117	10.1	118.5	8.1	105.1	4.6	60.4
12	-593.7	9.9	-857.6	8.4	-637.7	5.1	-646.5	12.6	212.5	10	194.2	8.6	170.9	5.7	234.7
11.5	-627.3	9.5	-838.6	8.3	-653.2	5.2	-673.6	12.7	149.8	10.2	112.3	8.6	103.1	5.4	100.1
12	-647.1	9.8	-827.2	7.7	-662.1	5.1	-689.7	13	113.1	10.3	64	8.7	63.1	5.4	21
11.9	-658.8	10.1	-820.5	8.6	-667.5	5.1	-699.1	12.8	91.2	10.3	35.4	8.9	39.5	5.6	-26.6
12.1	-666.4	10.1	-816.2	8.5	-670.9	5.3	-705.3	12.7	77.2	10.6	17	8.8	24.2	5.8	-56.3
12.2	-671.3	9.7	-813.3	8.5	-673.2	5.1	-709.2	12.9	68.1	10.6	5.1	8.8	14.4	5.9	-75.6
12.5	-674.5	9.6	-811.6	8.5	-674.8	5.1	-711.9	13.3	62	10.8	-2.9	8.9	7.8	6	-88.8
12	-640.5	9.9	-646.2	8.1	-657.1	4.9	-679.9	12.3	122.2	10	90	8.4	85.5	5.2	79.4
11.9	-641.1	10	-648.6	8.1	-659.3	5	-686.3	12.5	120.5	10.4	88.3	8.8	81.9	5.6	67.6
12.1	-636.9	10	-824.7	7.9	-647.6	4.5	-674.2	12.3	126.2	9.9	101.3	8.5	106.7	5.2	100.7

SD, standard deviation; FBP, filtered back projection; IMR, iterative model reconstruction; iDose[4], a hybrid iterative reconstruction algorithm; HU, Hounsfield unit.

Diagn Interv Radiol 2023; DOI: 10.4274/dir.2021.211255

INTERVENTIONAL RADIOLOGY

ORIGINAL ARTICLE

Short-term changes of angiogenesis factors after transarterial radioembolization in hepatocellular carcinoma patients

Hüseyin Tuğsan Ballı
Kairgeldy Aikimbaev
İsa Güney Burak
Ferhat Can Pişkin

PURPOSE
To analyze changes in angiogenesis factors after transarterial radioembolization (TARE) with Yttrium-90-loaded resin microspheres in hepatocellular carcinoma (HCC) patients.

METHODS
Interleukin-6, interleukin-8, hepatocyte growth factor, platelet-derived growth factor, fibroblast growth factor, vascular endothelial growth factor-A (VEGF-A), and angiopoietin-2 levels in 26 patients were measured before TARE and on day 1, 7, 14, and 30 after TARE and evaluated regarding radiological response.

RESULTS
In the sixth month of follow-up, 11 (42.30%) patients had a complete or partial response to treatment, while progressive disease was found in 15 (57.69%) patients. The percentage changes in VEGF-A in the non-responders on day 30 ($P = 0.034$) after TARE were significantly more obvious. Peak formation rates of VEGF-A were higher in non-responders ($P = 0.036$).

CONCLUSION
Short-term changes in angiogenesis factors in HCC patients after TARE with Yttrium-90-loaded resin microspheres fluctuate with different amplitudes at different times. The upregulation of growth factors has a prognostic capacity. Changes in VEGF-A after TARE may be helpful for the early recognition of non-responders.

KEYWORDS
Angiogenesis, Hepatocellular carcinoma, Resin microspheres, transarterial Radioembolization, Y-90

Hepatocellular carcinoma (HCC) is the most common primary malignant tumor of the liver; its prevalence increases annually, causing over 600,000 deaths per year.[1] Resection, liver transplantation, and ablations are potential curative treatment options in the very early and early stages, according to the Barcelona Clinic Liver Cancer (BCLC) staging system.[2,3] However, most HCC patients are beyond these stages at the time of diagnosis,[3] and transarterial chemoembolization (TACE) is the standard of care in a palliative manner in the BCLC intermediate stage. For patients with unresectable HCC, who are not appropriate candidates for TACE due to advanced liver disease, multifocal disease, vascular invasion, and portal venous thrombosis, transarterial radioembolization (TARE) with Yttrium-90-loaded microspheres appears to be a safe alternative treatment to TACE with a comparable complication profile and survival rates.[4] United States[5] and Asia-Pacific guidelines[6] endorse TARE as a treatment choice for hepatobiliary malignancies. With transcatheter intra-arterial embolization treatments, the hepatic artery's tumor-feeding branch is selectively targeted; therefore, high-dose therapy can be applied to the index tumor by protecting the tumor-free parenchyma of the liver.[7,8] However, despite technically successful treatment, rapid progression can be detected in some

From the Department of Radiology (H.T.B., K.A., F.C.P. ✉ ferhatcpiskin@gmail.com), Çukurova University Faculty of Medicine, Balçalı Hospital Health Application and Research Center, Adana, Turkey; Department of Nuclear Medicine (İ.G.B.) Çukurova University Faculty of Medicine, Balçalı Hospital Health Application and Research Center, Adana, Turkey.

Received 28 December 2021; revision requested 08 March 2022; last revision received 16 July 2022; accepted 05 August 2022.

Epub: 28.12.2022

Publication date: 05.09.2023

DOI: 10.4274/dir.2021.211255

You may cite this article as: Ballı HT, Aikimbaev K, Burak İG, Pişkin FC. Short-term changes of angiogenesis factors after transarterial radioembolization in hepatocellular carcinoma patients. *Diagn Interv Radiol.* 2023;29(5):704-709.

patients. The cause of this undesirable development in HCC patients depends on many factors, and hypoxia caused by tissue embolization may trigger angiogenesis. It is known that angiogenesis is directly related to tumor progression and metastasis development in hypervascular tumors such as HCC.[9,10] In randomized controlled cohort studies, it was determined that the release of angiogenesis factors after TACE increased, and this escalation was associated with survival duration.[11,12] Since the microspheres used in TARE are smaller (glass or resin microspheres; 20–30 vs. 20–60 microns, respectively) compared with those used in TACE (40–500 microns), TARE is a micro-embolic therapy that maintains hepatic artery patency. Therefore, theoretically, there should be less hypoxia. Thus, triggering the angiogenesis cascade due to hypoxia was not expected in patients undergoing TARE. However, pilot studies reported that the angiogenesis changes are activated after TARE in HCC patients.[13,14] In line with these findings, understanding the short-term serial changes of angiogenesis factors after TARE is important for developing different treatment strategies (for example, TARE combined with systemic anti-angiogenic therapies) to prevent possible rapid progression after TARE.

The aim of this study was to analyze the short-term changes in angiogenesis factors after TARE with Yttrium-90-loaded resin microspheres and their relationship with the radiological response.

Methods

Study design

This study was conducted as a single-center prospective observational investigation in accordance with the 1964 Helsinki Declaration principles and approved by the Institutional Clinical Research Ethical Committee (decision 8-95/2019). Written consent was obtained from all patients before diagnostic and treatment procedures. The study included all consecutive patients with HCC admitted to the hospital between March 2017 and March 2019 and scheduled for TARE in the interventional radiology unit. The multidisciplinary tumor board decided on TARE due to the patients' ineligibility to other treatment modalities for different reasons. The indication for TARE was unresectable HCC for various reasons and a life expectancy of at least three months.[2]

Main points

- The angiogenesis response after transarterial radioembolization (TARE) with Yttrium-90 occurs among hepatocellular carcinoma patients.
- Short-term changes in angiogenesis factor levels fluctuate with different amplitudes at different times.
- The changes in vascular endothelial growth factor-A after TARE may help with the early identification of non-responders to the treatment.

The inclusion criteria for this study were a diagnosis of HCC proven by biopsy or typical imaging findings[15] and meeting the eligibility criteria for TARE.[16] Previously performed liver-targeted thermal ablations or embolization procedures, failure to evaluate radiological response during planned follow-up periods, systemic treatment administered within the first six months after TARE, and extrahepatic metastases detected before radioembolization were the exclusion criteria. TARE with Yttrium-90-loaded resin microspheres was applied to 34 consecutive patients during the study period. During the same period, TARE with Yttrium-90-loaded glass microspheres was applied to five consecutive patients. These five patients were excluded from the study to form a homogeneous group. During the follow-up period, eight patients were excluded from the study (five due to the administration of systemic therapy within the first six months after TARE, two because of their deaths related to non-oncological reasons, and one because of the detection of newly developed extrahepatic metastasis just before treatment). Therefore, 26 patients with HCC were included in the study after applying the inclusion and exclusion criteria.

Radioembolization procedure

Cone-beam computed tomography-guided splanchnic angiographies were performed 7 to 10 days prior to TARE in accordance with reported recommendations.[7] All patients underwent 99m-Technetium-labeled macroaggregated albumin injection into the artery feeding the tumor to determine arteriovenous lung shunt fraction and appropriate dose adjustment. The lung shunt fraction for every patient was calculated with the implementation of a single-photon emission computed tomography γ-camera in the nuclear medicine department. Desired dose calculation was performed using partition model dosimetry.[17] During TARE, standard trans-femoral access was performed for the placement of a 4F or 5F catheter to select the origin of the coeliac axis. A microcatheter was then inserted and selectively advanced to a segmental or sub-segmental tumor-feeding hepatic artery branch. Infusion of the previously calculated dose of the Yttrium-90-loaded resin microspheres was done selectively or super-selectively under fluoroscopic guidance.

Evaluation of the radiological response to radioembolization

All investigated patients were evaluated by dynamic contrast-enhanced magnetic resonance imaging before and after the treatment in the first and third months and then at three-month intervals. The radiological response assessment of the treated tumors was conducted by the modified Response Evaluation Criteria in Solid Tumors.[18]

Regarding the imaging findings obtained at the six-month follow-up visit, the patients were divided into responders (i.e., patients with complete or partial response) and non-responders (i.e., stable disease or progressive disease patients).

Evaluation of the short-terms changes in angiogenesis factors after radioembolization

Blood samples of all patients were taken at baseline (one day before treatment) and on days 1, 7, 14, and 30 after the TARE procedure. The serum levels of commercially available interleukin-6 (IL-6), IL-8, hepatocyte growth factor, platelet-derived growth factor (PDGF), fibroblast growth factor (FGF), vascular endothelial growth factor-A (VEGF-A), and angiopoietin-2 (Ang-2) were measured with a commercially available enzyme-linked immunosorbent assay test. Compared with the baseline levels, the percentage changes of the angiogenesis factors on days 1, 7, 14, and 30 after TARE were calculated. An increase of angiogenesis factor levels at any time more than 50% compared with the relevant baseline values was accepted as a significant peak formation according to Carpizo et al.[13] Rates of significant peak formation and percentage changes regarding baseline values of every angiogenesis factor were registered.

Statistical analysis

Categorical variables were expressed as numbers and percentages, whereas continuous variables were given as means, standard

deviations, medians, and minimum-maximum values where appropriate. The chi-square test was used to compare categorical variables between the response groups. The normality of distribution for continuous variables was confirmed with the Shapiro-Wilk test. The Mann–Whitney U test was used to compare continuous variables between two sets. The statistical level of significance for all tests was considered to be 0.050. All data were analyzed using IBM Statistical Package for the Social Sciences Statistics software (version 20; IBM Corp, NY, US) and the TURCOSA software package (TURCOSA Analytical Ltd, Turkey).

Results

Table 1 shows the patients' demographic and clinical characteristics. In the sixth month of follow-up, eight (30.76%) patients were consistent with a complete response to treatment, while the status of three (11.53%) patients was interpreted as a partial response. During this period, progressive disease was found in 15 (57.69%) patients, which was due to local tumor progression in 12 (46.15%) patients and extrahepatic lung metastasis in 3 (11.53%) patients. Therefore, at 6 months, 11 (42.30%) patients were evaluated as responders, while the remaining 15 patients (n = 15.00; 57.69%) were interpreted as non-responders. The median duration of the entire follow-up period after treatment was 18 (range 6–38) months. During the follow-up period, 12 (46.15%) patients died.

The evaluation of the dynamics of angiogenesis factors after TARE showed that their levels fluctuated from the baseline values at different times (Table 2). Responders had significantly higher initial VEGF-A than non-responders (P = 0.021). No significant difference was found between the baseline values of other angiogenesis factors for the two groups (P > 0.050). The percentage change in VEGF-A values at day 30 in non-responders was significantly more pronounced during

Table 1. Demographic and clinical characteristics of the study population, n = 26

Characteristics	Values Non-Rp (n = 15) vs. Rp (n = 11)	*P*
Age, years; median (min-max)	66.50 (52.00–86.00) vs. 67 (56.00–86.00)	0.867
Gender, n (%) Male Female	 13.00 (86.66) vs. 10 (90.90) 2.00 (13.33) vs. 1.00 (9.10)	0.738
Etiology, n (%) HBV HCV	 10.00 (66.66) vs. 8.00 (72.72) 5.00 (33.33) vs. 3.00 (27.27)	0.931
Child–Pugh score, n (%) A B	 13.00 (86.66) vs. 11.00 (100.00) 2.00 (13.33) vs. 0.00 (0.00)	0.425
BCLC stage, n (%) B C	 9.00 (60.00) vs. 11.00 (100.00) 6 (40.00) vs. 0 (0.00)	0.017
Tumor size, cm; median (min-max)	8.00 (3.00–12.00) vs. 4.50 (2.00–7.20)	0.132
Tumor distribution, n (%) Unilobar Bilobar	 10.00 (66.66) vs. 8.00 (72.72) 5.00 (33.33) vs. 3.00 (27.27)	0.741
Radiation activity, GBq; median (min-max)	1.75 (0.37-2.75) vs. 1.20 (0.45-3.03)	0.652

The chi-square test, Fisher's exact test, and Mann-Whitney U test were used. HBV, hepatitis B virus; HCV, hepatitis C virus; BCLC, Barcelona Clinic Liver Cancer staging system; GBq, Gigabecquerel; min-max, minimum-maximum.

Table 2. Short-term dynamics and comparison of angiogenesis factor levels in the study population after TARE with baseline values, n = 26

Angiogenesis factor*	Baseline	1st day *P*	7th day *P*	14th day *P*	30th day *P*
IL-6	39.80 (12.20–2560.00)	31.30 (7–3020.10) 0.570	39.40 (5.403050.10) 0.949	36.50 (0.10–3000.00) 0.942	35.90 (12.20–3100.20) 0.942
IL-8	41.20 13.20–538.50)	43.70 (4.40–515.80) 0.596	49.20 (14.70–528.90) 0.464	48.20 (6.60–1194.00) 0.701	42.20 (4.40–485.7) 0.687
HGF	19.30 (6.20–1980.10)	21.20 (0.40–772.70) 0.749	21.20 (2.10–803.50) 0.176	19.10 (0.70–820.90) 0.770	18.50 (0.10–566.40) 0.492
VEGF-A	93.60 (0.20–498.90)	72.30 (0.40–474.10) 0.634	47.3 (1.20–449.60) 0.570	30.90 (0.70–480.20) 0.534	52.10 (0.60–486.60) 0.956
FGF	12.20 (2.30–387.20)	13.70 (2.60–267.50) 0.647	16.50 (3.50–299.40) 0.784	15.20 (3.70–258.40) 0.985	18.50 (3.40–203.00) 0.756
Ang-2	59.00 (42.90–191.80)	52.50 (31.50–176.50) 0.421	53.90 (31.70–174.80) 0.297	59.10 (37.00–186.20) 0.621	58.40 (40.70–121.20) 0.898
PDGF	1208.80 (59.30–3665.70)	1662.60 (66.60–3838.50) 0.220	1230.2 (14.90–4322.10) 0.390	1161.50 (14.90–4198.70) 0.942	1184.70 (28–2825.40) 0.701

*pg/mL, median (minimum-maximum), P > 0.050 for all parameters, the Mann–Whitney U test.TARE, transarterial embolization; IL-6, interleukin-6; IL-8, interleukin-8; HGF, hepatocyte growth factor; VEGF-A, vascular endothelial growth factor; FGF, fibroblast growth factor; Ang-2, angiopoietin-2; PDGF, platelet-derived growth factor.

Table 3. Relationship between the percentage changes in angiogenesis factors compared to baseline values with radiological response in the sixth month of follow-up after TARE, n = 26

Angiogenesis factor*	1st day percentage change Non-Rp vs. Rp	*P*	7th day percentage change Non-Rp vs. Rp	*P*	14th day percentage change Non-Rp vs. Rp	*P*	30th day percentage change Non-Rp vs. Rp	*P*
IL-6	−14.72 (−53.60–6.73) vs. 6.10 (−82.80–106.72)	0.897	−113.71 (86.65–1,154.01) vs. 0.00 (−76.60–587.90)	0.815	−30.74 (−99.71–442.24) vs. −4.51 (−85.82–433.04)	0.586	2.44 (−86.53–164.43) vs. 6.41 (−86.31–166.12)	0.897
IL-8	−4.20 (−85.42–208.01) vs. −6.00 (−74.33–95.47)	0.775	11.72 (−51.30–491.31) vs. 8.61 (−25.49–142.52)	0.697	−7.84 (−74.92–1,254.41) vs. 10.71 (35.91–271.04)	0.364	−10.79 (−84.01–451.04) vs. −1.10 (−49.15–120.91)	0.204
HGF	−39.50 (−96.22–508.03) vs. −5.70 (84.80–1,819.02)	0.402	13.92 (−98.95–778.01) vs. 10.51 (−70.79–436.03)	0.921	−10.03 (94.32–3,381.31) vs. 10.12 (−99.21–1169.72)	0.805	−32.90 (−96.01–716.24) vs. 10.41 (−99.91–225.92)	0.657
PDGF	31.00 (−60.73–742.34) vs. 30.20 (−50.40–883.65)	0.856	17.69 (−84.63–552.31) vs. 5.82 (−93.59–897.01)	0.484	−8.51 (−94.74–422.71) vs. −31.02 (−78.93–384.22)	0.204	−22.93 (−92.25–753.39) vs. −22.21 (−73.12–364.24)	0.736
FGF	−10.10 (−78.84–66.69) vs. −20.60 (−69.03–405.01)	0.775	13.53 (−61.49–307.11) vs. 0.71 (−45.25–61.52)	0.186	−6.59 (−68.71–732.32) vs. −11.14 (−53.49–96.42)	0.622	−4.29 (−79.21–584.11) vs. −20.22 (−75.84–108.23)	0.364
VEGF-A	−29.73 (−65.14–3,007.02) vs. −10.21 (−83.01–473.57)	0.659	−15.34 (−83.83–944.01) vs. −36.61 (−76.19–13.49)	0.092	−7.83 (−58.84–44.91) vs. −45.81 (−89.59–15.34)	0.204	2.80 (−43.21–12788.03) vs. −16.11 (−77.92–16.01)	0.034
Ang-2	−9.91 (−58.54–51.92) vs. −6.42 (−19.65–26.61)	0.169	−6.64 (−58.62–74.79) vs. −16.31 (−30.29–7.72)	0.392	1.72 (−58.81–44.91) vs. −16.22 (−49.45–76.09)	0.154	3.31 (−57.72–83.12) vs. −7.61 (−50.24–105.85)	0.169

*Median (minimum-maximum), the Mann–Whitney U test. TARE, transarterial embolization; Non-Rp, non-responders; Rp, responders; IL-6, interleukin-6; IL-8, interleukin-8; HGF, hepatocyte growth factor; PDGF, platelet-derived growth factor; FGF, fibroblast growth factor; VEGF-A, vascular endothelial growth factor; Ang-2, angiopoietin-2.

the 6-month radiological response assessment compared to responders (P = 0.034) (Table 3). However, no significant difference was found between the percentage changes of other angiogenesis factors compared with the baseline values (Table 3).

At the six-month follow-up evaluation, the rates of peak formation of the VEGF-A values of the non-responders were significantly higher than in responders. The rates of the peak formation of the VEGF-A levels in non-responders and responders were 53.33% and 9.00%, respectively (P = 0.036). However, no significant difference was found between the groups for the peak detection rates of other angiogenesis factors according to radiological response findings (Table 4).

Discussion

Angiogenesis is an important factor in the early recurrence and metastasis of vascular tumors such as HCC. Studies have found that angiogenesis activity increases in line with the carcinogenesis steps of liver tumors.[19] In addition, embolization of the hepatic artery with intra-arterial therapies triggers the angiogenesis cascade regardless of the tumor's nature.[20] Suzuki et al.[21] reported that angiogenesis factors increased after bland transarterial embolization of the liver tumors, and the angiogenesis cascade was initiated. Later studies determined a relationship between hypoxia and the tumor parenchyma caused by embolization after TACE. The authors demonstrated the relationship between the strength of angiogenesis launched by hypoxia, the tumor response to the treatment, and the survival time of the patients.[22,23] During TARE, hypoxia occurring in the tumor parenchyma is theoretically more limited compared to other intra-arterial embolization procedures because smaller particles are used for TARE. However, few studies on the existence of the angiogenesis response after TARE have been published.[13,14,24]

Only two studies investigate the angiogenesis response after TARE in patients with HCC. Carpizo et al.[13] applied TARE with Yttrium-90-loaded on resin microspheres to 22 patients with primary and secondary liver tumors (7 HCC and 15 colorectal carcinoma metastases). After the treatment, it was determined that classical (VEGF-A, Ang-2, FGF, and PDGF) and non-classical (IL-8, leptin, and follistatin) angiogenesis factor levels peaked in more than half of the patients compared to the baseline values. Later, Lewandowski et al.[14] applied TARE with Yttrium-90-loaded glass microspheres to 13 patients with HCC and found that all angiogenesis factor levels increased after treatment. However, when compared with baseline values, no significant increase was found in the post-treatment values. When the results of the two aforementioned studies and this study are evaluated together, the hypothesis that TARE triggers the angiogenesis cascade can be considered proven. However, the angiogenesis response after TARE may not be the only factor to consider; external radiotherapy alone also triggers the angiogenesis response in tumors.[25] Therefore, randomized controlled trials with more patients are needed to make a definitive conclusion.

The relationship between the response to TARE and the baseline levels of angiogenesis factors was previously investigated. Carpizo et al.[13] found that the baseline IL-8 and Ang-2 values of patients with shorter overall survival were significantly higher. The authors surmised that baseline levels of angiogenesis factors might have a predictive significance for overall survival durations. However, in the prospective cohort study of Rosenbaum et al.[24] on circulating angiogenesis factors and treatment response after TARE for colorectal cancer and liver metastases, it was determined that baseline angiogenesis values of patients who did not respond to treatment did not differ compared to responders. The authors emphasized that the comparison between patients may be misleading since the baseline levels of angiogenesis factors show wide variations between patients, and there are no standard lower and upper limit levels.

The presented study results showed that levels of angiogenesis factors varied at different times with fluctuating amplitudes within the first month after TARE. In more than half

Table 4. Relationship between the peak formation of angiogenesis factors compared to baseline levels with radiological response after TARE in the study population, n = 26

Angiogenesis factor	Peak formation, n (%) in Rp (n = 11)	Peak formation, n (%) in Non-Rp (n = 15)	*P*
IL-6	5 (45.45)	8 (53.33)	0.691
IL-8	4 (36.36)	6 (40.00)	1.000
HGF	8 (72.72)	12 (80.00)	1.000
PDGF	6 (54.54)	9 (60.00)	1.000
FGF	3 (27.27)	6 (40.00)	0.683
VEGF-A	1 (9.090)	8 (53.33)	0.036
Ang-2	4 (36.36)	1 (13.33)	0.128

*The chi-square test and Fisher's exact test. TARE, transarterial embolization; Non-Rp, non-responders; Rp, responders; IL-6, interleukin-6; IL-8, interleukin-8; HGF, hepatocyte growth factor; PDGF, platelet-derived growth factor; FGF, fibroblast growth factor; VEGF-A, vascular endothelial growth factor; Ang-2, angiopoietin-2.

of the study population, some angiogenesis factors significantly peaked at different times after treatment. In comparison, the same significant increase at various times of some angiogenesis factors was detected in less than half of the patients. The short-term changes of angiogenesis factors after TARE over time show that angiogenesis is a very complex event in HCC patients. The baseline levels of angiogenesis factors show wide variations between patients, and there are no standard lower and upper limit levels.[24] The percentage change of VEGF-A values at day 30 of the non-responders during the 6-month follow-up was significantly greater compared with the responders. The increased angiogenesis factor was VEGF-A in the present study. However, in the literature, VEGF-A and other angiogenesis factors, such as IL-6 and IL-8, were identified as factors that increased after TARE.[13,14,24] The reason for this difference may be the studies' small sample size and the patients' heterogeneity. However, according to the data obtained in the studies in the literature so far, including this one, VEGF-A is an angiogenesis factor that shows an increase after TARE. More data is needed to decide on other factors.

Based on these results, it can be assumed that percentage changes in VEGF-A values may help predict non-responders and shorter overall survival after TARE in HCC patients. This study's results show that the percentage changes of the angiogenesis factors at different times after TARE may help with early recognition of the non-responders to TARE. Thus, TARE can be combined with systemic treatments (anti-VEGF-A) for non-responding HCC patients. More than 50% of HCC patients with disease progression after TARE were ineligible to receive sorafenib due to poor liver function.[26] Therefore, it may be reasonable to begin the therapeutic regimen with a combined approach aimed at effectively treating patients while preserving liver function. Although the SORAMIC trial found no superiority of the TARE plus sorafenib combined treatment over the sorafenib regimen alone, the subgroup analysis indicated a survival benefit in patients aged <65 years, patients without cirrhosis, and patients with cirrhosis of non-alcoholic etiology.[27]

The angiogenesis cascade is regulated by the mechanism of balance in blood levels of angiogenesis and anti-angiogenesis factors.[28] Studies have shown that instantaneous increases in angiogenesis factor levels in the blood are more conducive than chronically high angiogenesis factor levels to recurrence and metastasis development.[29-31] Therefore, determining temporary changes in angiogenesis factor levels may be important for angiogenesis response analysis in patients undergoing TARE. Supporting this hypothesis, the levels of angiogenesis factors in the samples taken from the patients included in this study showed instantaneous increases in non-responders and a continuous decrease in responders. However, the large number of angiogenesis factors and the fact that increasing factors differ from patient to patient make it difficult to determine the accuracy of this hypothesis.

There are a number of limitations to this study. First, it was a single-center (although prospective) observational study, thus reducing its precision. Second, only a relatively small number of patients were included in the study. However, the number of patients was comparable with previously reported studies and the follow-up periods were long enough. Larger multicenter studies should be performed to better assess the changes in angiogenesis factors after TARE in HCC patients. Third, the only anti-angiogenesis factor levels evaluated were Ang-2. Since the cascade is a balance mechanism, angiogenesis and anti-angiogenesis factors should be analyzed together to evaluate the angiogenesis response. Fourth, patients with tumor thrombus were included in this study, whereas Lewandowski et al.[14] stated that the angiogenesis response due to chronic hypoxia might be affected in patients with tumor thrombus. However, in the presented study, changes in the angiogenesis factor levels and not absolute angiogenesis factor levels were emphasized. Therefore, the chronic hypoxia effect due to tumor thrombus can be ignored. Fifth, as all patients received segmental treatment, it was not possible to compare the effects of the lobar and segmental approaches. Segmental therapies would cause more embolic impact and higher radiation doses. In theory, then, growth factor upregulation would be higher in those patients. Last, only resin microspheres were used, characterized by higher particle volume, larger particle size, and lower specific activity. Comparative studies of resin vs. glass microspheres are therefore needed.

In conclusion, the angiogenesis response after TARE with Yttrium-90 occurs among HCC patients. Short-term changes in angiogenesis factor levels fluctuate with different amplitudes at different times. Assessing the changes of VEGF-A after TARE may help with the early identification of non-responders to the treatment. Gradual changes in the angiogenesis factor values, rather than instantaneous changes, are more valuable for evaluating the angiogenesis response after TARE.

Conflict of interest disclosure

The authors declared no conflicts of interest.

References

1. Ozakyol A. Global epidemiology of hepatocellular carcinoma (HCC Epidemiology). *J Gastrointest Cancer*. 2017;48(3):238-240. [CrossRef]

2. Reig M, Former A, Rimola J, et al. BCLC strategy for prognosis prediction and treatment recommendation: the 2022 update. *J Hepatol*. 2022;76(3):681-693. [CrossRef]
3. European Association For The Study Of The Liver; European Organisation For Research And Treatment Of Cancer. EASL-EORTC clinical practice guidelines: management of hepatocellular carcinoma. *J Hepatol*. 2012;56(4):908-943. [CrossRef]
4. Lobo L, Yakoub D, Picado O, et al. Unresectable hepatocellular carcinoma: radioembolization versus chemoembolization: a systematic review and meta-analysis. *Cardiovasc Intervent Radiol*. 2016;39:1580-1588. [CrossRef]
5. Benson AB, D'Angelica MI, Abbott DE, et al. D. Guidelines ınsights: hepatobiliary cancers, version 2.2019. *J Natl Compr Canc Netw*. 2019;17(4):302-310. [CrossRef]
6. Omata M, Cheng AL, Kokudo N, et al. Asia-Pacific clinical practice guidelines on the management of hepatocellular carcinoma: a 2017 update. *Hepatol Int*. 2017;11(4):317-370. [CrossRef]
7. Salem R, Thurston KG. Radioembolization with 90Yttrium microspheres: a state-of-the-art brachytherapy treatment for primary and secondary liver malignancies. Part 1: Technical and methodologic considerations. *J Vasc Interv Radiol*. 2006;17(8):1251-1278. [CrossRef]
8. Salem R, Thurston KG. Radioembolization with 90yttrium microspheres: a state-of-the-art brachytherapy treatment for primary and secondary liver malignancies. Part 2: special topics. *J Vasc Interv Radiol*. 2006;17(9):1425-1439. [CrossRef]
9. Sun HC, Tang ZY. Angiogenesis in hepatocellular carcinoma: the retrospectives and perspectives. *J Cancer Res Clin Oncol*. 2004;130(6):307-319. [CrossRef]
10. Kirsch M, Schackert G, Black PM. Metastasis and angiogenesis. *Cancer Treat Res*. 2004;117:285-304. [CrossRef]
11. Ronald J, Nixon AB, Marin D, et al. Pilot Evaluation of angiogenesis signaling factor response after transcatheter arterial embolization for hepatocellular carcinoma. *Radiology*. 2017;285(1):311-318. [CrossRef]
12. Petrillo M, Patella F, Pesapane F, et al. Hypoxia and tumor angiogenesis in the era of hepatocellular carcinoma transarterial loco-regional treatments. *Future Oncol*. 2018;14(28):2957-2967. [CrossRef]
13. Carpizo DR, Gensure RH, Yu X, et al. Pilot study of angiogenic response to yttrium-90 radioembolization with resin microspheres. *J Vasc Interv Radiol*. 2014;25(2):297-306. [CrossRef]
14. Lewandowski RJ, Andreoli JM, Hickey R, et al. Angiogenic response following radioembolization: results from a randomized pilot study of Yttrium-90 with or without sorafenib. *J Vasc Interv Radiol*. 2016;27(9):1329-1336. [CrossRef]
15. Ayuso C, Rimola J, Vilana R, et al. Diagnosis and staging of hepatocellular carcinoma (HCC): current guidelines. *Eur J Radiol*. 2018;101:72-81. [CrossRef]
16. Giammarile F, Bodei L, Chiesa C, et al. EANM procedure guideline for the treatment of liver cancer and liver metastases with intra-arterial radioactive compounds. *Eur J Nucl Med Mol Imaging*. 2011;38(7):1393-1406. [CrossRef]
17. Kao YH, Tan EH, Ng CE, Goh SW. Clinical implications of the body surface area method versus partition model dosimetry for yttrium-90 radioembolization using resin microspheres: a technical review. *Ann Nucl Med*. 2011;25(7):455-461. [CrossRef]
18. Lencioni R, Llovet JM. Modified RECIST (mRECIST) assessment for hepatocellular carcinoma. *Semin Liver Dis*. 2010;30(1):52-60. [CrossRef]
19. Joo YY, Jang JW, Lee SW, et al. Circulating pro- and anti-angiogenic factors in multi-stage liver disease and hepatocellular carcinoma progression. *Sci Rep*. 2019;9(1):9137. [CrossRef]
20. Shim JH, Park JW, Kim JH, et al. Association between increment of serum VEGF level and prognosis after transcatheter arterial chemoembolization in hepatocellular carcinoma patients. *Cancer Sci*. 2008;99(10):2037-2044. [CrossRef]
21. Suzuki H, Mori M, Kawaguchi C, Adachi M, Miura S, Ishii H. Serum vascular endothelial growth factor in the course of transcatheter arterial embolization of hepatocellular carcinoma. *Int J Oncol*. 1999;14(6):1087-1090. [CrossRef]
22. Sergio A, Cristofori C, Cardin R, et al. Transcatheter arterial chemoembolization (TACE) in hepatocellular carcinoma (HCC): the role of angiogenesis and invasiveness. *Am J Gastroenterol*. 2008;103(4):914-921. [CrossRef]
23. Rahbari NN, Reissfelder C, Mühlbayer M, et al. Correlation of circulating angiogenic factors with circulating tumor cells and disease recurrence in patients undergoing curative resection for colorectal liver metastases. *Ann Surg Oncol*. 2011;18(8):2182-2191. [CrossRef]
24. Rosenbaum CE, van den Hoven AF, Braat MN, et al. Yttrium-90 radioembolization for colorectal cancer liver metastases: a prospective cohort study on circulating angiogenic factors and treatment response. *EJNMMI Res*. 2016c;6(1):92. [CrossRef]
25. Chan LW, Camphausen K. Angiogenic tumor markers, antiangiogenic agents and radiation therapy. *Exp Rev Anticancer Ther*. 2003;3(3):357-366. [CrossRef]
26. Memon K, Kulik L, Lewandowski RJ, et al. Radioembolization for hepatocellular carcinoma with portal vein thrombosis: impact of liver function on systemic treatment options at disease progression. *J Hepatol*. 2013;58:(1):73-80. [CrossRef]
27. Ricke J, Klümpen HJ, Amthauer H, et al. Impact of combined selective internal radiation therapy and sorafenib on survival in advanced hepatocellular carcinoma. *J Hepatol*. 2019;71(6):1164-1174. [CrossRef]
28. Facciorusso A, Paolillo R, Tartaglia N, et al. Efficacy of combined transarterial radioembolization and sorafenib in the treatment of hepatocarcinoma: a meta-analysis. *Dig Liver Dis*. 2022;54(3):316-323. [CrossRef]
29. Risau W. Mechanisms of angiogenesis. *Nature*. 1997;386(6626):671-674. [CrossRef]
30. Chen A, Sceneay J, Gödde N, et al. Intermittent hypoxia induces a metastatic phenotype in breast cancer. *Oncogene*. 2018;37(31):4214-4225. [CrossRef]
31. Dong G, Lin XH, Liu HH, et al. Intermittent hypoxia alleviates increased VEGF and pro-angiogenic potential in liver cancer cells. *Oncol Lett*. 2019;18(2):1831-1839. [CrossRef]

Diagn Interv Radiol 2023; DOI: 10.4274/dir.2022.221473

INTERVENTIONAL RADIOLOGY

TECHNICAL NOTE

Effect of post-pyloric Dobhoff tube retention during gastrojejunostomy for reduction of fluoroscopic time and radiation dose

Tyler S. Thompson
Coulter N. Small
Hugh Davis
Michael Lazarowicz
Jeffrey Vogel
Robert E. Heithaus

ABSTRACT

The purpose of this study was to determine whether retention of a post-pyloric Dobhoff tube (DHT) in position to serve as a visual guide through the pylorus during gastrojejunostomy (GJ) tube placement results in a reduction in fluoroscopy time, procedure time, and estimated radiation dose. A retrospective study evaluated patients who underwent GJ tube placement or gastric to GJ conversion from January 1, 2017, to April 1, 2021. Demographic and procedural data were collected, and results were evaluated using descriptive statistics and hypothesis testing through an unpaired Student's t-test. Of the 71 GJ tube placements included for analysis, 12 patients underwent placement with a post-pyloric DHT in position, and 59 patients underwent placement without a post-pyloric DHT in position. The mean fluoroscopy time and estimated radiation dose were significantly reduced in patients who underwent GJ tube placement with a post-pyloric DHT in position compared with those without (7.08 min vs. 11.02 min, $P = 0.004$; 123.12 mGy vs. 255.19 mGy, $P = 0.015$, respectively). The mean total procedure time was also reduced in patients who underwent GJ tube placement with a post-pyloric DHT in position compared with those who had no post-pyloric DHT, but this finding lacked statistical significance (18.55 min vs. 23.15 min; $P = 0.09$). Post-pyloric DHT retention can be utilized during GJ tube placement to reduce radiation exposure to both the patient and interventionalist.

KEYWORDS

Dobhoff tube, flouroscopy, gastrojejunostomy, radiation, time

Enteral tube feeding via gastric or jejunal routes is an effective method for patients unable to tolerate oral alimentation. When indicated, gastrostomy (G) tube placement is typically the initial intervention at our institution due to physiologic benefits, ease of placement, and low cost. Patients unable to tolerate gastric feeding require post-pyloric enteral feeding via a gastrojejunostomy (GJ) tube. Additionally, patients initially fed via a G tube may require radiographic conversion to a GJ tube when determined to be at high risk for aspiration, as feeding from the jejunal position has been shown to reduce the risk of reflux.[1-3] At our institution, interventional radiologists perform GJ tube placement and G to GJ conversion using fluoroscopic guidance. The principal technical challenge of these procedures lies in the navigation of the guidewire and catheter past the pylorus, accounting for approximately half the total fluoroscopy time in previous studies.[4] Many patients needing GJ tube placement present with a post-pyloric Dobhoff tube (DHT) in place, but this tube is often removed or retracted before GJ tube placement. Occasionally, the DHT is retained in its post-pyloric position, where it functions as a direct visual guide for pyloric access intra-procedurally. The purpose of this study is to investigate if post-pyloric DHT retention during GJ tube placement results in a reduction of fluoroscopy time, procedure time, and radiation exposure.

Technique

The medical records of patients who underwent GJ tube placement or G to GJ conversion from January 1, 2017, to April 1, 2021, were reviewed. The inclusion criteria of this study

From the Department of Radiology (T.S.T. ✉ thompson.t@ufl.edu, C.N.S.), College of Medicine, University of Florida, Gainesville, FL, USA; Division of Interventional Radiology (H.D., M.L., J.V., R.E.H.), University of Florida, Gainesville, FL, USA.

Received 08 Jun 2022; revision requested 14 Jul 2022; last revision received 11 Aug 2022; accepted 11 Aug 2022.

Epub: 11.01.2023

Publication date: 05.09.2023

DOI: 10.4274/dir.2022.221473

You may cite this article as: Thompson TS, Small CN, Davis H, Lazarowicz M, Vogel J, Heithaus RE. Effect of post-pyloric Dobhoff tube retention during gastrojejunostomy for reduction of fluoroscopic time and radiation dose. *Diagn Interv Radiol.* 2023;29(5):710-712.

were procedures performed by one of seven fellowship-trained, board-certified interventional radiology attending physicians alone or with the assistance of an experienced radiology physician assistant. Exclusion criteria were patients who underwent GJ tube exchanges, patients with abnormal gastrointestinal anatomy, insufficient imaging, or procedures performed by medical residents or fellows under the supervision of the attending physician. Demographic and procedural data were collected from the patients' charts, Picture Archiving and Communication System, and procedural flowsheets. Procedural data extracted included procedure type, the presence or absence of a post-pyloric DHT during GJ tube placement, total fluoroscopy time, total procedural time, and estimated radiation dose measured in mean air kerma. Results were evaluated using descriptive statistics and hypothesis testing through an unpaired Student's t-test.

Procedural Technique

Various techniques for GJ tube placement exist; however, the primary technical points remain uniform for each. The indwelling DHT was retained in its post-pyloric position, and a nasogastric tube was placed for gastric insufflation (Figure 1). Two T-fasteners were inserted into the stomach after administering a local anesthetic, and the position of each T-fastener was confirmed with contrast injection. An 18-gauge needle was inserted into the stomach between the two T-fasteners, and the position was confirmed with contrast. A stiff angled glide wire (Terumno Medical Inc., Somerset, New Jersey) was then inserted into the needle and manipulated into the distal duodenum/proximal jejunum using intermittent fluoroscopy and the indwelling post-pyloric DHT for visual guidance through the pylorus. The tract was then serially dilated to the appropriate diameter, and a peel-away sheath was placed. Subsequently, a balloon GJ catheter was inserted into the distal duodenum/proximal jejunum (Figure 2). Post-placement imaging was performed with contrast injection through the port to confirm satisfactory positioning.

Main points

- A significant percentage of fluoroscopic usage during gastrojejunostomy (GJ) tube placement is for obtaining pyloric access.
- Many patients presenting for GJ tube placement have a post-pyloric Dobhoff tube (DHT) already in position; however, this tube is typically retracted into the gastric lumen or removed entirely pre-procedure.
- Retention of a post-pyloric DHT as a visual guide through the pylorus during GJ tube placement can be safely implemented to reduce procedural fluoroscopy time and radiation exposure.

Results

Between 2017 and 2021, 237 GJ tube placements were examined for study eligibility. Of these placements, 133 were excluded from analysis for being performed by resident physicians or fellows under attending physician supervision, as procedural inexperience could confound the analysis of time variables. An additional 22 procedures were identified as GJ tube exchanges and excluded from analysis, as exchanges performed over a guidewire do not require increased fluoroscopic usage. Seven procedures were excluded from analysis due to abnormal patient gastrointestinal anatomy that would confound the analysis of time variables. Four procedures were excluded due to insufficient imaging. The remaining 71 procedures were included in the study analysis (Table 1). The mean air kerma levels were unavailable for 15 patients in the non-DHT group.

The mean fluoroscopy time was significantly reduced in patients who underwent GJ tube placement with a post-pyloric DHT in position compared with those without (Table 2). The mean estimated radiation dose measured in air kerma was significantly reduced in patients who underwent GJ tube placement with a post-pyloric DHT in position compared with those without (Table 2). The mean total procedure time was also reduced in patients who underwent GJ tube placement with a post-pyloric DHT in position compared with no post-pyloric DHT. However, this finding lacked statistical significance (Table 2).

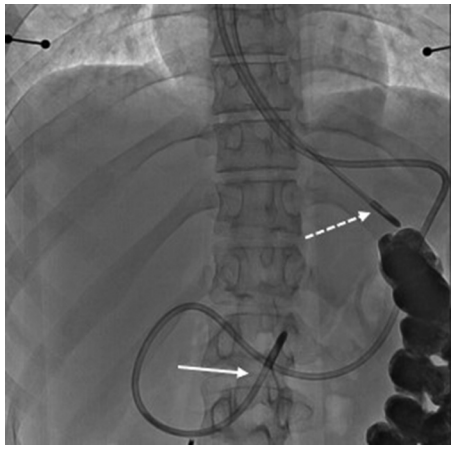

Figure 1. Initial procedural fluoroscopic imaging confirming the presence of a nasogastric tube in the stomach (dashed arrow), and a Dobhoff tube retained in the distal duodenum (solid arrow).

Discussion

There was a greater than 35% reduction in average fluoroscopy time during GJ tube placement when a DHT was retained intra-procedurally for pyloric visualization, which corresponded to significantly reduced radiation exposure to both patient and interventionalist. Although there was an observed decrease in total procedure time in the group with a post-pyloric DHT in position during GJ tube placement, this was not statistically significant, primarily due to statistical underpowering. Further, a component of human error exists in procedural time-keeping; however, this is not a factor for fluoroscopy time, which is strictly tracked by the fluoroscopic equipment during each procedure. Therefore, the total procedure time is subject to slight variation and is not a strict reflection of the actual time the operator spent in the procedure room.

The most common reason for DHT retraction during primary GJ tube placement is gastric insufflation use. The tube may also be removed entirely due to operator preference, with the concern that an additional tube across the duodenum may impede the larger caliber feeding tube following the same course. However, this described technique allows for gastric insufflation without necessitating DHT retraction, and post-procedurally the DHT may be removed to alleviate any concern about GJ tube impediment.

Previously, the use of metoclopramide (Reglan) and domperidone (Motilium) have been studied as potential adjunctive techniques during GJ tube placement to facilitate

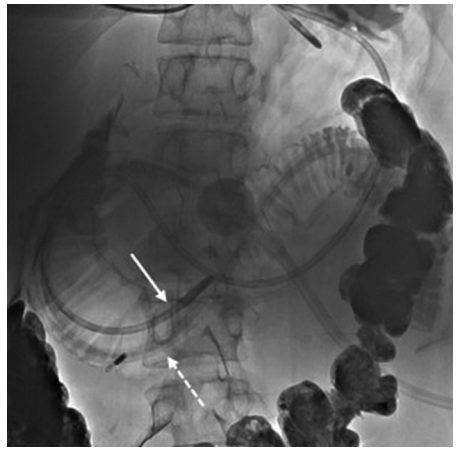

Figure 2. Procedural fluoroscopic imaging demonstrating successful gastrojejunostomy tube placement (dashed arrow) along a tract parallel to the retained post-pyloric Dobhoff tube (solid arrow).

Table 1. Patient characteristics

Cohort	Size	Mean age (years)	Gender distribution
Post-pyloric DHT	n = 12	43.6	4 male, 8 female
No post-pyloric DHT	n = 59	50.7	29 male, 30 female

DHT, Dobhoff tube.

Table 2. Procedural characteristics

Mean	Post-pyloric DHT, n = 12 (SD)	No post-pyloric DHT, n = 59 (SD)	*P*
Fluoroscopy time (min)	7.08 (2.34)	11.02 (9.73)	0.004
Procedure time (min)	18.92 (7.19)	23.25 (18.32)	0.094
Air kerma (mGy)	123.11 (88.42)	255.19 (358.08)	0.015

DHT, Dobhoff tube; SD, standard deviation.

post-pyloric access due to their motility-enhancing pharmacologic properties.[4-7] Our approach does not require medication administration, as these medications contribute to an increased risk of drug–drug interactions and other adverse events, such as neurologic dysfunction.[6-8] This novel technique employs the post-pyloric DHT as a direct visual guide to the pylorus and for dilatation of the pyloric lumen, enabling faster and easier guidewire advancement.

Limitations of this study include a small sample size in the group with a post-pyloric DHT in position during GJ tube placement since this review was performed at a high-volume academic institution, where training residents and fellows place most GJ tubes under attending physician supervision. Some patients in the non-DHT group may have had previous failures at post-pyloric tube placement due to anatomic or physiologic factors, which could confound the observed prolonged fluoroscopy time in the non-DHT group. Additionally, mean air kerma levels were unavailable for 15 patients in the non-DHT group. Therefore, the group's true mean air kerma may be subject to slight variation. Finally, this was a single-institution study, and there is a risk of sampling bias.

In conclusion, this method can be safely implemented as an adjunctive technique to reduce fluoroscopic usage and radiation dose during GJ tube placement. Because many patients presenting for GJ tube placement already have a post-pyloric DHT, this method provides benefits without requiring a significant change in procedural steps. This method can be applied to a broad patient population but shows particular promise for its use in populations where radiation exposure has to be strictly limited.

Acknowledgments

Thanks to Sean Wiley, Denise Kirby-Carlton.

Conflict of interest disclosure

The authors declared no conflicts of interest.

References

1. DiSario JA, Baskin WN, Brown RD, et al. Endoscopic approaches to enteral nutritional support. *Gastrointest Endosc.* 2002;55(7):901-908. [CrossRef]
2. Raha SK, Woodhouse K. The use of percutaneous endoscopic gastrostomy (PEG) in 161 consecutive elderly patients. *Age Ageing.* 1994;23(2):162-163. [CrossRef]
3. Stone B, Hester G, Jackson D, et al. Effectiveness of fundoplication or gastrojejunal feeding in children with neurologic impairment. *Hosp Pediatr.* 2017;7(3):140-148. [CrossRef]
4. DuRocher N, Smith TP, Gazda S, et al. Metoclopramide reduces fluoroscopy and procedure time during gastrojejunostomy tube placement: a placebo-controlled trial. *J Vasc Interv Radiol.* 2020;31(7):1143-1147. [CrossRef]
5. Gupta S, Nihalani ND. Neuroleptic malignant syndrome: a primary care perspective. *Prim Care Companion J Clin Psychiatry.* 2004;6(5):191-194. [CrossRef]
6. Ponte CD, Nappi JM. Review of a new gastrointestinal drug--metoclopramide. *Am J Hosp Pharm.* 1981;38(6):829-833. [CrossRef]
7. Hu B, Ye H, Sun C, et al. Metoclopramide or domperidone improves post-pyloric placement of spiral nasojejunal tubes in critically ill patients: a prospective, multicenter, open-label, randomized, controlled clinical trial. *Crit Care.* 2015;19(1):61. [CrossRef]
8. Reddymasu SC, Soykan I, McCallum RW. Domperidone: review of pharmacology and clinical applications in gastroenterology. *Am J Gastroenterol.* 2007;102(9):2036-2045. [CrossRef]

Diagn Interv Radiol 2023; DOI: 10.4274/dir.2022.221646

INTERVENTIONAL RADIOLOGY

ORIGINAL ARTICLE

Utility of intra-procedural cone-beam computed tomography imaging for the determination of the artery of Adamkiewicz suspected by angiography during transarterial embolization for hemoptysis

Qingmeng Zhang
Jijun Li
Guanghui He
Jun Tang
Guodong Zhang

PURPOSE

To evaluate the role of cone-beam computed tomography (CT) performed for the determination of the artery of Adamkiewicz (AKA) suspected by angiography during trans-catheter bronchial artery embolization for hemoptysis.

METHODS

In this retrospective study, 17 patients with hemoptysis who underwent cone-beam CT for evaluation of the AKA prior to arterial embolization from December 2014 to March 2022 were included. During the angiographic session, two interventional radiologists selected the possible AKAs that were defined as obscured hairpin-curved vessels arising from the dorsal branch of the intercostal arteries and running towards the midline in the arterially enhanced phase. Contrast-enhanced cone-beam CT was performed as an adjunct to angiography to determine whether the indefinite AKA was a real AKA based on whether it was found to connect to the anterior spinal artery.

RESULTS

Selective cone-beam CT was performed at 17 possible AKAs detected by selective arteriogram of the intercostal artery (ICA). Cone-beam CT allowed for the determination of AKAs in 16 cases (94.1%). As a result of cone-beam CT findings, 9 of 16 study arteries (56.3%) were judged as definite AKAs, and the remaining 7 (43.7%) were judged as definitely not AKAs but as the musculocutaneous branching from the dorsal branch of the ICA. In 1 of 17 cases (5.9%), cone-beam CT could not determine the AKA because of poor image quality caused by inadequate breath holding. An additional anterior radiculomedullary artery arising from the dorsal branch of the lower ICA because of the inflow of the contrast medium through the anastomosis was detected in one case by cone-beam CT but not by angiography.

CONCLUSION

Intraprocedural enhanced cone-beam CT performed as an adjunctive technique to angiography is sufficient for confident determination of the AKA, which is essential for the operators to perform accurate and safe arterial embolization for hemoptysis.

KEYWORDS

3-D, angiography, artery, cone- beam computed tomography, hemoptysis, interventional, radiculomedullary artery, radiology, therapeutic embolization

From the Department of Emergency (Q.Z.), Qilu Hospital of Shandong University, Shandong, China; Department of Interventional Radiology (J.L., J.T., G.Z. ✉ guodongbear@sina.com), Shandong First Medical University Affiliated Provincial Hospital, Shandong, China; Department of Thoracic Surgery Division of Interventional Radiology (G.H.), WeiFang People's 2nd Hospital, Shandong, China.

Received 01 June 2022; revision requested 23 June 2022; last revision received 02 August 2022; accepted 16 September 2022.

Epub: 21.02.2023

Publication date: 05.09.2023

DOI: 10.4274/dir.2022.221646

Trans-catheter bronchial artery embolization (BAE) has been widely used for the management of massive and recurrent sub-massive hemoptysis.[1,2] It works on the principle of selective embolization of both the bleeding bronchial arteries and the bleeding non-bronchial systemic collaterals, which usually arise from the intercostal artery (ICA), inferior phrenic artery, and main branches of the subclavian and axillary arteries, such as the internal mammary artery and thyrocervical trunk.

You may cite this article as: Zhang Q, Li J, He G, Tang J, Zhang G. Utility of intra-procedural cone-beam computed tomography imaging for the determination of the artery of Adamkiewicz suspected by angiography during transarterial embolization for hemoptysis. *Diagn Interv Radiol.* 2023;29(5):713-718.

When BAE is performed, the spinal cord blood supply must be considered. The most serious complications associated with BAE are iatrogenic spinal cord ischemia or paraplegia, which are more often related to the inadvertent embolization of the artery of Adamkiewicz (AKA), also known as the dominant anterior radiculomedullary artery.[3] Therefore, accurate identification of the AKA is paramount during BAE.

Anatomically, the AKA is a small artery (caliber 0.5–1.5 mm) that branches from the dorsal branch of the segmental artery (either the ICA or the lumbar artery), ascends to the spinal cord surface, makes a classic "hairpin" arch, then connects to the anterior spinal artery (ASA).[4,5] Digital subtraction angiography is the main imaging modality used during BAE and is also considered the gold standard technique for detecting the AKA because of its high spatial resolution.[6,7] Due to the anatomic features of the AKA, the widely used detection criteria of the AKA by selective segmental arterial angiography is the presence of a characteristic hairpin-curved vessel leading to the ASA.[8,9] However, previous studies have potentially revealed that angiography alone was inadequate to visualize the AKA.[10-15]

During BAE, in the present study, although selective angiography of the catheterized ICA sometimes demonstrated an obscured hairpin-curved vessel running towards the midline, it was impossible to confirm whether this connected to the ASA. In these cases, whether it was a real AKA could not be determined from the angiography images due to the low contrast resolution and the two-dimensional projection. Therefore, imaging modalities with increased contrast resolution and multiple-dimensional projection were required when angiography was insufficient to visualize the minute vessels.

Main points

- Accurate identification of the artery of Adamkiewicz (AKA) is important during bronchial artery embolization for the management of hemoptysis.
- It was very difficult to determine whether the possible arteries of Adamkiewicz were real based on single planar angiography images alone.
- Cone-beam computed tomography is sufficient to provide adequate information for the confident determination of arteries of AKA during arterial embolization for massive hemoptysis.

Intraprocedural cone-beam computed tomography (CT) can provide CT-like images in multiple viewing planes, while eliminating the need to move the patient to the CT room and allow contrast injection into catheterized vessels to offer more subtle vascular and soft tissue information than angiography. Moreover, cone-beam CT provides higher soft-tissue attenuation resolution than angiography.[16-18] Therefore, the present study incorporates intraprocedural cone-beam CT as an adjunct to angiography for the identification of an AKA suspected by angiography.

Methods

Study population

This retrospective study was approved by the institutional review board (decision number of ethics committee approval: JN-2014010021), and informed consent was obtained from each patient or patient's family.

From December 2014 to March 2022, 279 consecutive patients who experienced massive or moderate hemoptysis underwent BAE in the department of interventional radiology. Seventeen of the 279 patients (6.1%) who underwent cone-beam CT for evaluation of an AKA were included in the present study. The mean age of the 17 patients (13 men, 4 women) was 56.3 years (range 32–87 years).

Angiography technique and embolization

All the interventional procedures were performed by two experienced radiologists with 11 and 19 years of experience, respectively. Patients underwent BAE in an interventional angiography suite (Artis Zee; Siemens Healthcare, Germany) equipped with the cone-beam CT option with continuous hemodynamic monitoring. The intervention was performed under local anesthesia through the right-side transfemoral approach. First, a 4FR Cobra (Cook, USA) or Simmons catheter (Cordis, USA) was used to catheterize the bronchial arteries and non-bronchial systemic collaterals. During this step, a coaxial microcatheter (Progreat 2.7F, Terumo, Japan or Stride 2.6F, Asahi Intecc, Japan) used for selective catheterization was useful but not mandatory. The following angiography using a nonionic iodinated contrast medium (Iodixanol, 320 mg I/mL; GE Healthcare, USA) was performed to localize the bleeding site.

A bleeding vessel was defined as a vessel with abnormal angiographic appearances of bronchial or peribronchial hypervascularity, contrast extravasation, arterial enlargement, systemic–to–pulmonary artery or venous shunting, aneurysms or pseudoaneurysms, vessel cut-off, or tortuosity of the bronchial artery. Then embolic agents were injected into the bleeding vessels under continuous fluoroscopic guidance to the point of stasis of flow without reflux. The embolic agents were 300–500 μm-sized polyvinyl alcohol particles (Cook, USA).

Protocol to avoid inadvertent embolization of the artery of AKA.

Of note, when a bleeding bronchial artery branching from the intercostobronchial trunk was visualized during angiography, highly selective catheterization of the bleeding bronchial artery was performed with a microcatheter advancing distally beyond the intercostal branch prior to embolization to avoid reverse flow that may potentially branch off an AKA.

In embolization occurs in the bleeding ICA, care must be taken to ensure whether there is an AKA arising from the ICA detected on pre-embolization angiography. The typical angiographic sign of an AKA is the presence of a hairpin-curved vessel branching from the dorsal branch of the ICA and connecting to the ASA in the arterially enhanced phase (Figure 1). Once an AKA is visualized during selective angiography of the bleeding ICA, the embolization in that ICA should be abandoned.

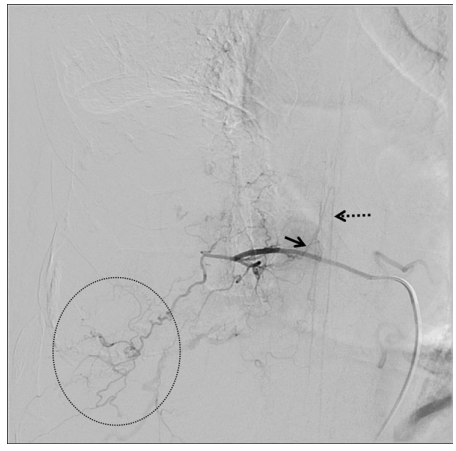

Figure 1. Intraprocedural images of a 45-year-old male patient. Selective angiography of the right tenth intercostal artery (ICA) clearly demonstrated a hairpin-curved vessel (arrow) originating from the dorsal branch of the ICA and connecting to the anterior spinal artery (dotted arrow) in the arterially enhanced phase. This hairpin-curved vessel was considered as an artery of Adamkiewicz. The sign of distal hypervascularity (dotted circle) indicated the ICA was involved in bleeding.

Cone-beam computed tomography protocol

During selective angiography of a bleeding ICA, a possible AKA was defined as an obscured hairpin-curved vessel arising from the dorsal branch of the ICA and running toward the midline in the arterially enhanced phase. Although possible AKAs were suspected from the morphologic "hairpin curve," it was very difficult to confirm the presence or absence of the ASA and to confirm whether the possible AKA connected to the ASA based on the obscured angiographic sign. Thus, whether the possible AKA was a real AKA could not be determined based on the angiography images alone. Selective cone-beam CT was performed when the aforementioned two interventional radiologists simultaneously confirmed the presence of a possible AKA.

Selective cone-beam CT was performed at the catheterized ICA with 6–9 mL of 100% contrast medium injected automatically at a rate of 2–3 mL/s according to the ICA diameter for 3 s with an imaging delay of 2 s. For each cone-beam CT scan, images were acquired during an 8s acquisition time, covering a 208° clockwise rotation. The region of interest was positioned covering the dorsal portion of the aorta from which the ICA rose and the proximal portion of the ICA from which the possible AKA originated. Multiplanar reformation images were reviewed by using 2-mm-thick slices, and three-dimensional visualization was obtained on a dedicated workstation (Leonardo with DynaCT; Siemens Healthcare, Germany).

Image analysis criteria

The two interventional radiologists independently viewed the angiography images and corresponding arterial cone-beam CT images using the paging method to (1) confirm the presence or absence of the ASA, which was defined as a contrast-enhanced vessel on the anterior spinal cord surface, running in the cranio-caudal direction detected on the oblique coronal images or as a dot enhancement continuing cranio-caudally detected on the axial images; (2) confirm or exclude the connection between the study artery and the ASA using the oblique coronal or axial images in the cases in which the ASAs were present; and (3) track the trajectory, distribution, and termination of the study artery using axial images in the cases in which the ASAs were absent.

The study artery was determined by the consensus of the two interventional radiologists using the uniform diagnostic criteria as follows: (1) the study artery was judged as definitely an AKA or definitely not an AKA based on whether it was found to connect to the ASA; and (2) among the study arteries that were judged as definitely not AKAs, a study artery was further considered as a musculocutaneous branch when it ran toward and terminated in the dorsal erector spinae muscle and skin without entering the intervertebral foramen or spinal cord enhancement.

The anatomic level of the ICA was defined as the level of the rib below which the ICA ran. The level of the rib was determined by fluoroscopic examination.

Discrepancies in the evaluations were resolved by consensus. Whether to perform embolization at the bleeding ICA that branched a possible AKA was determined by the cone-beam CT findings as follows: (1) embolization was performed at the bleeding ICA that branched where there was definitely not an AKA, as judged by cone-beam CT acquisitions; (2) embolization was not performed at the bleeding ICA that branched off a definite AKA, as judged by cone-beam CT acquisitions; and (3) embolization was not performed at the bleeding ICA that branched off a possible AKA that was indeterminate from the cone-beam CT.

Results

During the angiographic session, a total of 17 possible AKAs in 17 patients were detected by selective ICA angiography. Selective cone-beam CT was performed for the ICAs with a total of 17 cone-beam CT acquisitions.

Cone-beam CT allowed for the determination of AKAs in 16 of the 17 cases (94.1%). In one case (5.9%), cone-beam CT did not allow for the determination of an AKA because of the poor image quality caused by inadequate breath holding.

As a result, 9 of 16 study arteries (56.3%) were judged as definite AKAs (Figure 2). In these nine cases, both the ASA and the connecting AKA were clearly shown on the cone-beam CT images. The AKA was seen to originate from the left seventh ICA in one case, the left eighth ICA in one case, the left ninth ICA in three cases, the left tenth ICA in two cases, the left eleventh ICA in one case, and the right ninth ICA in one case. The remaining seven study arteries (43.7%) were judged as definitely not AKAs and were further considered as musculocutaneous branches from the dorsal branch of the ICA (Figure 3). In all cases, there was an agreement between the two interventional radiologists.

In one case in which the study artery was judged as a definite AKA, one additional vessel was observed in the cone-beam CT, because of the inflow of the contrast medium through the anastomosis, that originated from the dorsal branch of the lower ICA and ran straight towards the midline. This additional vessel was also evaluated by the two interventional radiologists. As a result, this vessel without the morphologic "hairpin curve" was found to connect to the ASA. Due to the presence of a confirmed AKA (i.e., the dominant anterior radiculomedullary artery), this additional vessel was considered as another anterior radiculomedullary artery by the consensus of the two interventional radiologists (Figure 2). This was in contrast to the angiography, where this anterior radiculomedullary artery was not detected.

The abnormal angiographic appearances of bleeding ICAs were systemic–to–pulmonary artery shunting in 13 cases (76.5%) and marked hypervascularity in 4 cases (23.5%). An abnormal angiographic appearance of contrast extravasation was not found. According to the aforementioned embolization protocol at the bleeding ICA, embolization was performed at the seven bleeding ICAs that branched off where there was definitely not an AKA, as judged by the cone-beam CT acquisitions. Embolization was not performed at the nine bleeding ICAs that branched off the definite AKAs, as judged by the cone-beam CT acquisitions, and at one bleeding ICA that branched off a possible AKA that was indeterminate by cone-beam CT.

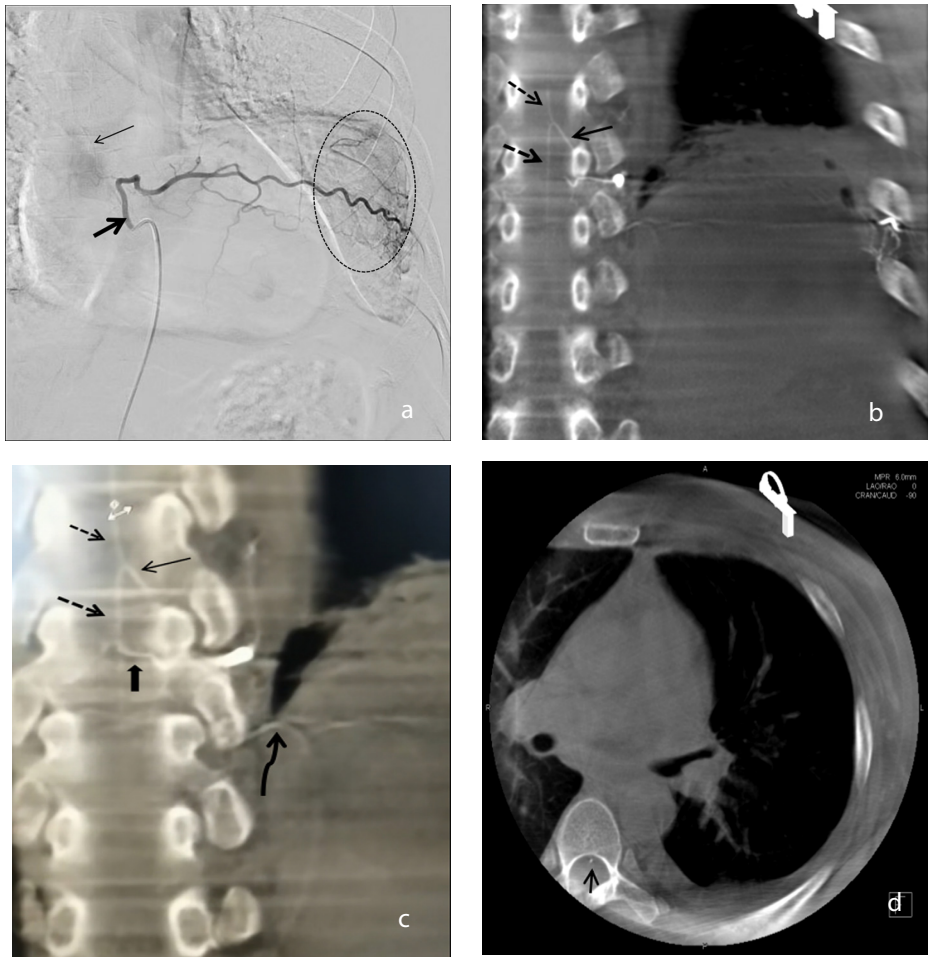

Figure 2. (a-d) Intraprocedural images of a 66-year-old female patient. Selective angiography **(a)** of the left eighth intercostal artery (ICA) (thick arrow) demonstrated the ICA branching off an obscured hairpin-curved vessel (thin arrow) that ran towards the midline in the arterially enhanced phase. This obscured hairpin-curved vessel was barely recognizable with very careful observation and was determined by two interventional radiologists to be a possible artery of Adamkiewicz (AKA). The sign of systemic–to–pulmonary artery shunting (dotted circle) indicated the ICA was involved in bleeding. The corresponding contrast-enhanced oblique coronal cone-beam computed tomography (CT) images **(b, c)** of the left ICA clearly demonstrated the hairpin-curved AKA **(arrow in b, c)** connecting to the anterior spinal artery (ASA) **(dotted arrow in b, c)** and the presence of an additional anterior radiculomedullary artery **(thick arrow in c)** that originated from the dorsal branch of the left ninth ICA **(curved arrow in c)** because of the inflow of contrast medium through the anastomosis, which was not detected on angiography. The corresponding contrast-enhanced axial cone-beam CT image **(d)** of the left ICA demonstrated the ASA, which was considered as a dot enhancement (arrow) continuing cranio-caudally on the anterior spinal cord surface.

Discussion

Cone-beam CT images allow the users to "page through" different planes of images to confirm the accurate correlation of the target vessel with the adjacent vessels and soft-tissue structures. They also allow contrast injection into catheterized vessels to provide more subtle vascular and soft tissue information, which is instrumental in improving the visualization of the selected vessel or structure within a region of interest. Therefore, cone-beam CT has been widely used, especially when the target vessel or structure is invisible or cannot be visualized on angiography.[19,20]

In this study's department, intraprocedural cone-beam CT was routinely used as an adjunct to angiography during BAE for hemoptysis. In the experience of BAEs, most patients received selective embolization in multiple bleeding vessels, including bronchial and non-bronchial systemic arteries. The present study reports the usefulness of cone-beam CT performed as an adjunctive technique to angiography for the determination of the feeding vessels responsible for hemoptysis.[21]

With the anatomic complexity and small vessel size of the AKA anatomy, one of the most important challenges in performing BAE is the pre-embolization identification of the AKA. According to the experience of BAEs, the AKAs were sometimes too small or obscured to be identified confidently. The possible reasons for the inability to visualize the AKAs by angiography were as follows: (1) the AKA caliber was sometimes very small, (2) the AKA was surrounded by high-density osseous formations that sometimes interfered with the recognition of the AKA and its connection with the ASA, and (3) the presence of the other dorsal branches of the segmental artery sometimes curving similarly toward the spinal cord in the anteroposterior view made the AKA less visible. In the present study, all the definite AKAs, as judged by cone-beam CT, were obscured on angiography and were therefore easy to overlook. Furthermore, an additional anterior radiculomedullary artery in one case was visualized by cone-beam CT but was not detected on angiography. These findings are consistent with previous studies in which some AKAs or spinal artery feeders were detected by CT but were invisible on arteriography.[10,11,13] Thus, it is believed the cone-beam CT may be incorporated as a substitute for angiography to identify the AKAs or the fine spinal artery feeders. It is believed that the application of cone-beam CT used in the evaluation of the AKA anatomy has not been reported previously in the literature. Therefore, the present study describes the outcome of cone-beam CT incorporated as an adjunct to angiography for the determination of AKAs.

In the present study, when selective contrast-enhanced cone-beam CT was performed, undiluted contrast medium and only the arterial cone-beam CT scan images were used. A clear visualization of arterial anatomy was desired, and the identification of an AKA was based on arterially enhanced images.

In the present study, cone-beam CT allowed for the visualization of the ASA and its connection with an AKA, and this enabled the determination of AKAs that were suspected by angiography in most cases. As a result of cone-beam CT, 43.7% of possible AKAs were judged as definitely not AKAs but as musculocutaneous branches. The potential reason for the high ratio of vessels judged as definitely not AKAs may be that some angiographic signs might be artifacts resulting from inadequate breath holding or the surrounding high-density osseous formations. Another reason may be that cone-beam CT can provide higher contrast resolution than angiography.

The disadvantages of incorporating the contrast-enhanced cone-beam CT includ-

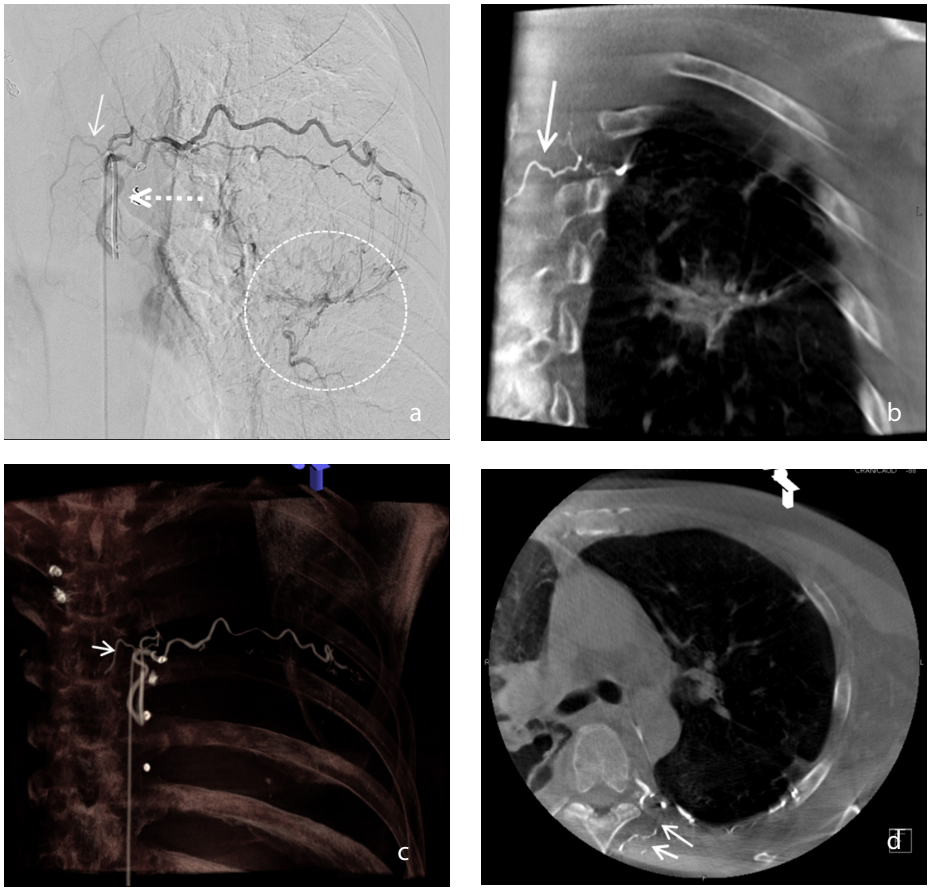

Figure 3. (a-d) Intraprocedural images of a 69-year-old male patient. Selective angiography **(a)** of the left seventh intercostal artery (ICA) (dotted arrow) demonstrated the ICA branching off an obscured hairpin-curved vessel (arrow) running towards the midline in the arterially enhanced phase. This obscured hairpin-curved vessel was determined by two interventional radiologists to be a possible artery of Adamkiewicz (AKA). The sign of systemic–to–pulmonary artery shunting (dotted circle) indicated the ICA was involved in bleeding. The corresponding contrast-enhanced oblique coronal cone-beam computed tomography (CT) image **(b)** and the three-dimensional volume-rendered image **(c)** from the contrast-enhanced cone-beam CT of the ICA clearly demonstrated the possible AKA (arrow) and the absence of the anterior spinal artery (ASA). The corresponding contrast-enhanced axial cone-beam CT image **(d)** of the right ICA demonstrated the absence of intradural enhancement, which indicated the absence of the ASA, and the possible AKA (arrow) running toward and terminating in the dorsal muscle and skin without entering the intervertebral foramen.

ed the additional contrast medium used and motion artifacts caused by inadequate breath holding that sometimes interfered with the image quality. The present study found that adequate breath holding was sometimes difficult for patients suffering from massive or moderate hemoptysis. The poor image quality of cone-beam CT acquisition in one case was attributed to inadequate breath holding.

The present study has four limitations. First, this paper showed angiography alone was found to produce false negatives in 43.7% of the cases, indicating that the reliability of angiography alone was low. Thus, a major limitation was that only suspicious cases were evaluated by cone-beam CT. Second, there may have been potential selection bias due to the retrospective nature of the present study. Third, the sample size was small in the present study. This was because cone-beam CT was only performed in the bleeding ICAs that branched off possible AKAs that were indeterminate by angiography because at that time selective angiography was widely accepted as the gold standard technique for identifying AKAs. Fourth, the exact radiation dose or procedure time was not measured because embolization procedures were performed emergently; therefore, the impact of using cone-beam CT on procedural duration and radiation doses could not be determined.

In conclusion, cone-beam CT performed as an adjunct to angiography is sufficient for confident determination of AKAs, which is essential for the operators to perform accurate and safe embolization during BAE for hemoptysis.

Conflict of interest disclosure

The authors declared no conflicts of interest.

References

1. Mal H, Rullon I, Mellot F, et al. Immediate and long-term results of bronchial artery embolization for life-threatening hemoptysis. *Chest*. 1999;115(4):996-1001. [CrossRef]
2. Panda A, Bhalla AS, Goyal A. Bronchial artery embolization in hemoptysis: a systematic review. *Diagn Interv Radiol*. 2017;23(4):307-317. [CrossRef]
3. Burke CT, Mauro MA. Bronchial artery embolization. *Semin Intervent Radiol*. 2004;21(1):43-48. [CrossRef]
4. Santillan A, Nacarino V, Greenberg E, Riina HA, Gobin YP, Patsalides A. Vascular anatomy of the spinal cord. *J Neurointerv Surg*. 2012;4(1):67-74. [CrossRef]
5. Lazorthes G, Gouaze A, Zadeh JO, Santini JJ, Lazorthes Y, Burdin P. Arterial vascularization of spinal cord: recent study of the anastomotic substitution pathways. *J Neurosurg*. 1971;35(3):253-262. [CrossRef]
6. Savader SJ, Williams GM, Trerotola SO, et al. Preoperative spinal artery localization and its relationship to postoperative neurologic complications. *Radiology*. 1993;189(1):165-171. [CrossRef]
7. Kieffer E, Fukui S, Chiras J, Koskas F, Bahnini A, Cormier E. Spinal cord arteriography: a safe adjunct before descending thoracic or thoracoabdominal aortic aneurysmectomy. *J Vasc Surg*. 2002;35(2):262-268. [CrossRef]
8. Lopez JK, Lee HY. Bronchial artery embolization for treatment of life-threatening hemoptysis. *Semin Intervent Radiol*. 2006;23(3):223-229. [CrossRef]
9. Williams GM, Roseborough GS, Webb TH, Perler BA, Krosnick T. Preoperative selective intercostal angiography in patients undergoing thoracoabdominal aneurysm repair. *J Vasc Surg*. 2004;39(2):314-321. [CrossRef]
10. Kodama Y, Sakurai Y, Yamasaki K, Yokoo K. High false-negative rate of the anterior spinal artery by intercostobronchial trunk arteriography alone compared to CT during arteriography. *Br J Radiol*. 2021;94(1123):20210402. [CrossRef]
11. van den Heuvel MM, Els Z, Koegelenberg CF, Naidu KM, Bolliger CT, Diacon AH. Risk factors for recurrence of haemoptysis following bronchial artery embolisation for life-

threatening haemoptysis. *Int J Tuberc Lung Dis.* 2007;11(8):909-914. [CrossRef]

12. Maramattom BV, Krishna Prasad BP, Padmanabhan S, Baby J. Spinal cord infarction after bronchial artery embolization. *Ann Indian Acad Neurol.* 2016;19(1):156-157. [CrossRef]
13. Maki H, Shimohira M, Hashizume T, et al. Visualization of the spinal artery by CT during embolization for pulmonary artery pseudoaneurysm. *Pol J Radiol.* 2016;81:382-385. [CrossRef]
14. Brown AC, Ray CE. Anterior spinal cord infarction following bronchial artery embolization. *Semin Intervent Radiol.* 2012;29(3):241-244. [CrossRef]
15. Ramakantan R, Bandekar VG, Gandhi MS, Aulakh BG, Deshmukh HL. Massive hemoptysis due to pulmonary tuberculosis: control with bronchial artery embolization. *Radiology.* 1996;200(3):691-694. [CrossRef]
16. Orth RC, Wallace MJ, Kuo MD; Technology Assessment Committee of the Society of Interventional Radiology. C-arm cone-beam CT: general principles and technical considerations for use in interventional radiology. *J Vasc Interv Radiol.* 2008;19(6):814-820. [CrossRef]
17. Wallace MJ. C-arm computed tomography for guiding hepatic vascular interventions. *Tech Vasc Interv Radiol.* 2007;10(1):79-86. [CrossRef]
18. Loffroy R, Lin M, Yenokyan G, et al. Intraprocedural C-arm dual-phase cone-beam CT: can it be used to predict short-term response to TACE with drug-eluting beads in patients with hepatocellular carcinoma? *Radiology.* 2013;266(2):636-648. [CrossRef]
19. Miyayama S, Yamashiro M, Hashimoto M, et al. Identification of small hepatocellular carcinoma and tumor-feeding branches with cone-beam CT guidance technology during transcatheter arterial chemoembolization. *J Vasc Interv Radiol.* 2013;24(4):501-508. [CrossRef]
20. Tacher V, Radaelli A, Lin M, Geschwind JF. How I do it: Cone-beam CT during transarterial chemoembolization for liver cancer. *Radiology.* 2015;274(2):320-334. [CrossRef]
21. He G, Li T, Tang J, Zhang G. Utility of cone-beam CT imaging for the determination of feeding vessels during arterial embolization for massive hemoptysis. *Diagn Interv Radiol.* 2018;24(6):372-377. [CrossRef]

Diagn Interv Radiol 2023; DOI: 10.4274/dir.2023.232262

INTERVENTIONAL RADIOLOGY

ORIGINAL ARTICLE

Artifact characterization of Nitinol needles in magnetic resonance imaging-guided musculoskeletal interventions at 3.0 tesla: a phantom study

Vanessa Franziska Schmidt
Olaf Dietrich
Max Seidensticker
Moritz Wildgruber
Bernd Erber
Jens Ricke
Sophia Samira Goller

PURPOSE

To characterize the artifacts of an 18-gauge coaxial nickel-titanium needle using a balanced steady-state free precession sequence in magnetic resonance imaging-guided interventions at 3.0 tesla.

METHODS

The influence of flip angle (FA), bandwidth, matrix, slice thickness (ST), and read-out direction on needle artifact behavior was investigated for different intervention angles (IA). Artifact diameters were rated at predefined positions. Subgroup differences were assessed using Bonferroni-corrected non-parametric tests and correlations between continuous variables were expressed using the Bravais–Pearson coefficient. Interrater reliability was quantified using intraclass correlation coefficients (ICCs), and a contrast-enhanced target lesion to non-enhanced muscle tissue contrast ratio was quantified.

RESULTS

The artifact diameters decreased with an increase in FA for all IAs ($P < 0.001$) and with an increase in ST for IAs of 45°–90° (all $P < 0.05$). Tip artifacts occurred at low IAs (0°–45°) and gradually increased in size with a decrease in IA ($P = 0.022$). The interrater reliability was high (ICC: 0.994–0.999). The contrast-enhanced target lesion to non-enhanced muscle tissue contrast ratio presented positive correlations with increasing FAs and matrices ($P < 0.001$; $P = 0.003$) and a negative correlation with increasing STs ($P = 0.007$).

CONCLUSION

To minimize needle artifacts, it is recommended to use FAs of 40°–60°, a ST of >7 mm, and, if possible, an IA of 45°–60°. The visibility of the target lesion and the needle's artifact behavior must be weighed up against each other when choosing the ST, while higher FAs (40°–60°) and matrices (224 × 224/256 × 256) are associated with low artifacts and sufficient lesion visibility.

KEYWORDS

Artifact, interventional, MSK, musculoskeletal, real-time sequence

From the Department of Radiology (V.F.S. ✉vanessa.schmidt@med.uni-muenchen.de, O.D., M.S., M.W., B.E., J.R., S.S.G.), University Hospital, LMU Munich, Munich, Germany.

Received 19 April 2023; revision requested 23 May 2023; last revision received 06 June 2023; accepted 11 June 2023.

Epub: 18.08.2023

Publication date: 05.09.2023

DOI: 10.4274/dir.2023.232262

Magnetic resonance imaging (MRI) encompasses excellent characteristics for the image guidance of interstitial interventional procedures, including a lack of ionizing radiation, high soft tissue contrast, and multiplanar needle guidance with quasi-simultaneous acquisition of two or three orthogonal, oblique slices in near real-time.[1-8] In practice, MRI-guided interventions are performed in clinical routines involving a wide range of body regions with a primary focus on the tissues of organs for which MRI is superior to other imaging modalities, such as the liver, prostate, breast, or spine.[6,8-14] However, interventions of peripheral joints for, for example, the purpose of biopsy extraction, are still most likely to be ultrasound-guided, with MRI-guidance of musculoskeletal interventions beyond the spine rarely performed. Nevertheless, there exist a number of approaches that have trialed real-time dynamic MRI in the field of musculoskeletal imaging. For example, Bayer et al.[15] demonstrated that dynamic visualization of the finger anatomy during a full range of motion can be ob-

You may cite this article as: Schmidt VF, Dietrich O, Seidensticker M, et al. Artifact characterization of Nitinol needles in magnetic resonance imaging-guided musculoskeletal interventions at 3.0 tesla: a phantom study. *Diagn Interv Radiol.* 2023;29(5):719-732.

tained by using a balanced steady-state free precession (bSSFP) sequence.

To be MR-compatible and to ensure a safe procedure for the patient and the performing interventionalist, biopsy needles are made of alloys that cause minimal interference with the outer magnetic field, such as nickel-titanium (Nickel Titanium Naval Ordnance Laboratory; Nitinol), titanium, glass fiber, or steel.[16] However, needle artifacts, which mostly present as low intensity signals in the region around the needle's shaft or tip, cannot be completely excluded and can impair accurate visualization of both the needle and the needle-to-target distance. To successfully perform MRI-guided interventions with reliable target localization for musculoskeletal issues at 3.0 tesla (T) units, a thorough understanding of needle artifact behavior is crucial, regardless of the intended biopsy site. The artifact size is influenced by different parameters, which are either related to the individual composition of the needle, such as the alloy, the diameter, and the length, or, to different MRI-related parameters, such as the orientation of the intervention angle (IA) in relation to the static magnetic field (B_0), the strength of the B_0 field, or the pulse sequence type.[5,10,17-22] Therefore, it is important to reassess the technical and methodological fundamentals of musculoskeletal MRI-guided interventions at 3.0 T. This is, on the one hand, because 3.0 T interventional MRI is more demanding in terms of safety and artifact behavior than interventions at lower fields (e.g., at 1.5 T) and on the other hand, because it can provide rewarding superior image quality when considering important aspects in acquisition parameter selections.

Main points

- The use of a flip angle (FA) of 40°–60° and a slice thickness (ST) of 10–17 mm minimized the needle artifacts while maintaining the best possible visualization of the coaxial intervention needle in this musculoskeletal phantom study at 3.0 tesla. To find a compromise, since the ST should not be set too thick to ensure accurate needle placement during the procedure, we ultimately recommend an ST of >7 mm in clinical practice.
- In addition, if possible, the intervention angles should be 45°–60° to specifically avoid tip artifacts.
- The visibility of the target lesion and the artifact behavior of the intervention needle must be weighed up against each other when choosing the ST, while higher FAs (40°–60°) and matrices (224 × 224/256 × 256) were associated with both low needle artifacts and sufficient target lesion visibility.

This paper presents a systematic investigation of the artifact behavior of an 18-gauge (G) commercially coaxial Nitinol needle as a function of the IA and sequence parameter variations using a bSSFP sequence in a muscle phantom model at 3.0 T. The study aims to characterize artifact formation during clinical MRI-guided high-field interstitial interventions, providing valuable guidance for musculoskeletal tissue biopsies.

Methods

Image acquisition

The MRI process was performed using a closed-bore 3.0 T unit (MAGNETOM Vida, Siemens Healthineers, Erlangen, Germany) with a system length (cover-to-cover) of 186 cm and a bore diameter of 70 cm. The gradient system had a maximum gradient strength of 60 mT/m and a slew rate of 200 T/m/s. The MRI protocol was based on an interventional real-time fluoroscopic bSSFP pulse sequence with true fast imaging with steady-state free precession (TrueFISP) contrast ("Needle Intervention Add-in" package, Siemens Healthineers, Erlangen, Germany). This pulse sequence allows for visual real-time updates and interactive graphical modification of the slice geometry during imaging. A four-channel flex coil (Siemens Healthineers, Erlangen, Germany) with a weight of 550 g (516 × 224 mm) was used as the receive coil.

Ethics committee approval was waived for this study due to the exclusively experimental study design without any animals or patients being involved.

Bovine muscle phantom model

A bovine muscle phantom model with a weight of 5.925 kg, a length of 33 cm, a width of 24 cm, a height of 13 cm, and a maximum transverse diameter of 53 cm was used. As expected, the bovine muscle phantom model had an MRI signal intensity comparable to that of human skeletal muscle. The complete scan series could be performed using the same model, ensuring comparability of the results. Before placing the needles, 0.5 mL of 1.0 mmol/mL gadolinium (Gadovist®, Bayer AG, Leverkusen, Germany) diluted at 1:1000 in 0.9% sodium-chloride (B. Braun, Melsungen, Germany) was applied in a 1.0-mL syringe (B. Braun, Melsungen, Germany) centrally into the muscle phantom by using a 20-G Nitinol needle (ITP, Innovative Tomography Products GmbH, Bochum, Germany) to simulate a contrast-enhanced target lesion at the center of the muscle tissue specimen. Thereafter, a total of seven MR-compatible coaxial Nitinol needles (as described below) were positioned at 0°, 15°, 30°, 45°, 60°, 70°, and 90° relative to the B_0 field using the "entry and target points function" within the real-time fluoroscopic MRI software to guarantee an exact and parallel position of the needles in the B_0 field (2° accepted deviation). The experimental setup is shown in Figure 1.

Magnetic resonance-compatible intervention needle

A commercially available MR-compatible coaxial Nitinol needle (ITP, Innovative Tomography Products GmbH, Bochum, Germany) with a size of 18G (outer diameter: 1.25 mm, length: 150 mm, standardized facet cut) was investigated.

Scan series

The phantom was positioned in the isocenter of the *XZ* plane using the light visor of the MR tomograph. The influence of the following five parameters was investigated as a function of the IA on artifact formation: flip angle (FA), receiver bandwidth (BW), matrix, slice thickness (ST), and read-out direction. The IA (the needle angle relative to the B_0 field) varied from 0°–90° (0°, 15°, 30°, 45°, 60°, 75°, and 90°). As one parameter was modified, the others remained constant with the following predefined settings. The matrix was fixed to 128 × 128 voxels, which was a compromise between acquisition time and spatial resolution. Echo time (TE) and repetition time (TR), which yield an influence on acquisition time, were set to a minimum (TE: 1.71 ms, TR: 3.42 ms) as fixed parameters, resulting in an acquisition time of 461 ms per plane. The field of view was uniformly set to 300 × 300 mm^2. The predefined setting was 50° for the FA, 930 Hz/pixel for the BW, and 10 mm for the ST. The fixed read-out direction was right to left. An overview of the default settings is provided in Supplementary Table 1. Starting with these default settings, each of the parameters mentioned above was modified, as described in detail in Supplementary Table 2, resulting in acquisition times of 346–1.148 ms per plane. For each parameter modification, the TrueFISP sequence was performed in the same manner. Prior to the start of the fluoroscopic TrueFISP sequence, the correct angles (accepted deviation of 2°) between the needles and the B_0 field and the position in the isocenter of the MR scanner were verified using test sequences.

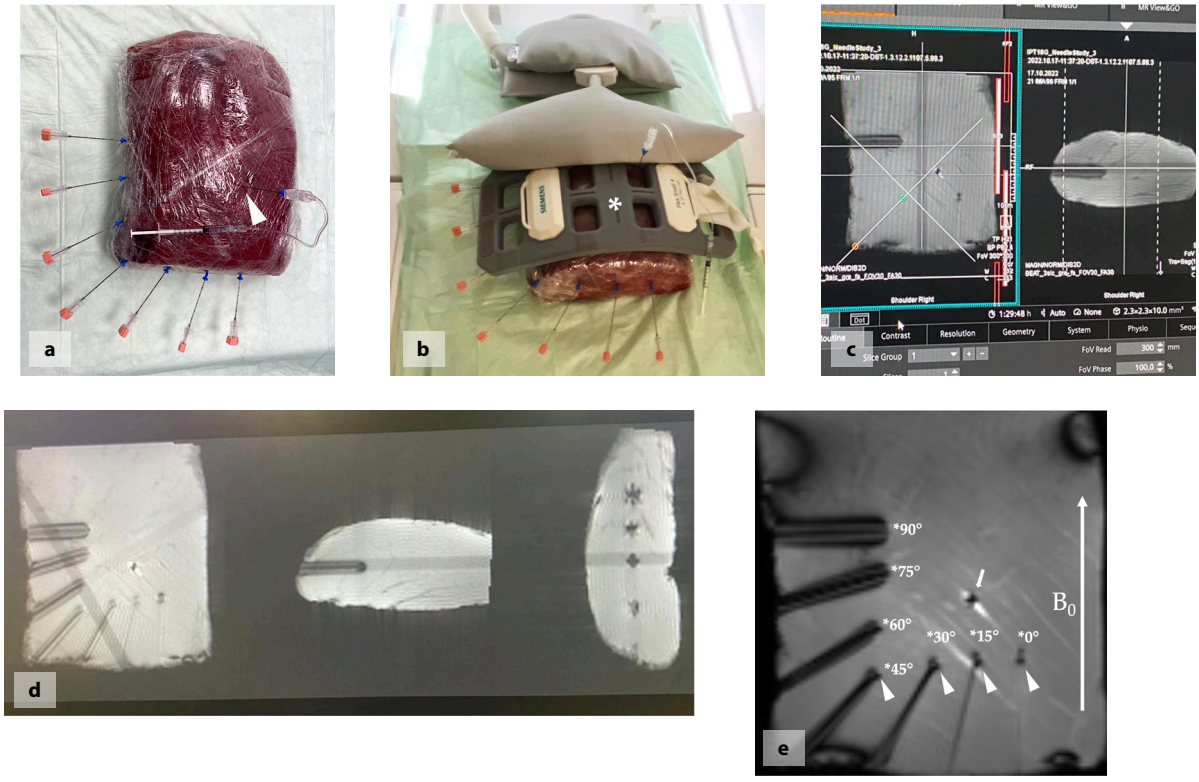

Figure 1. Experimental study set-up. **(a)** Bovine derived muscle phantom model with a 20G Nitinol needle (arrowhead) and linked 1.0-mL syringe for the application of the sodium chloride-diluted-gadolinium centrally into the muscle tissue and seven 18G coaxial Nitinol needles positioned at 0°, 15°, 30°, 45°, 60°, 70°, and 90° relative to the static magnetic field (B_0) field; **(b)** muscle phantom within the 3.0 T magnetic resonance imaging (MRI) scanner covered by a four-channel flex coil (asterisk); **(c)** MRI console illustrating the use of the prototype real-time fluoroscopic MRI software when placing the coaxial needles at defined angles in relation to the B_0 field; **(d)** scan example demonstrating simultaneous acquisition of axial, sagittal, and coronal datasets; **(e)** axial image illustrating the direction of the B_0 field, the simulated contrast-enhanced target lesion at the center of the muscle phantom (small arrow), and the seven coaxial Nitinol needles, which were placed at defined angles relative to the B_0 field (asterisks). Note the ball-like tip artifact at the needle tips at the 0°-, 15°-, 30°-, and 45°-positioned needles (arrowheads). G: gauge; T, tesla.

Artifact diameter measurement

For image acquisition and evaluation of the artifact diameter, Visage Imaging software (Visage Imaging GmbH, Berlin, Germany) was used. The artifact diameters were measured in a standardized plane at two predefined positions (50% and 25% of the inserted needle length measured from the tip of the needle) for every modification of the scan series to ensure comparability. If there was a ball-like tip artifact (IA: 0°, 15°, 30°, and 45°), the maximum diameter of this artifact was determined in the same standardized plane regardless of its two-dimensional direction of largest extension (Figure 2). The needle artifacts were measured by two independent and blinded readers (V.F.S. and S.S.G.) with three and four years of diagnostic MRI experience, respectively, for each modification of the evaluated parameters.

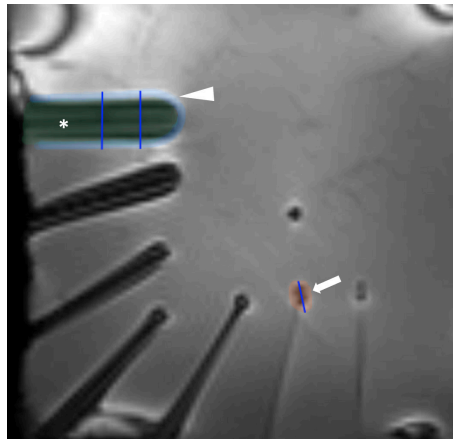

Figure 2. Schematic of the measurement method. The asterisk denotes the hypointense artifact part of the needle artifact at an intervention angle (IA) of 90° (marked in green). The arrowhead presents the additional hyperintense artifact rim around the central hypointense needle artifact occurring at flip angles of 10° and 20° (exemplarily marked in blue for the needle that was inserted at an IA of 90°). The ball-like tip artifact, which occurred at IAs of 0°, 15°, 30°, and 45° is exemplarily shaded orange for the needle that was inserted at an IA of 15°. The three blue lines indicate the measurements of the artifact diameters, first, at two predefined positions (50% and 25% of the inserted needle length measured from the tip of the needle) for every modification of the scan series, and second, as the maximum diameter of the ball-like tip artifact regardless of its two-dimensional direction of largest extension.

Contrast-enhanced target lesion to non-enhanced muscle tissue ratio

For the evaluation of the contrast ratio of the contrast-enhanced target lesion to the non-enhanced muscle tissue, regions of interests (ROIs) with a diameter of at least 5 mm^2 were used to quantitatively assess corresponding signal intensities (SI). The primary ROI was placed inside the contrast-enhanced target lesion and the second ROI within the adjacent non-enhanced muscle tissue at a distance of 20 mm while sparing visible muscle inhomogeneities. In addition,

the latter ROI placement was defined at an identical anatomical depth to the target lesion to avoid any potential influence from surface coil sensitivity profiles. The position, size, and shape of the ROIs were kept almost identical for all measurements. The contrast-enhanced target lesion to non-enhanced muscle tissue contrast ratio (*R*) was defined in terms of the following formula based on the mean SIs in the ROIs:

$$R = SI_{\text{contrast-enhanced target lesion}} / SI_{\text{non-enhanced muscle tissue}}$$

Statistical analysis

Statistical analysis was performed using dedicated statistics software (SPSS version 26, SPSS Inc., Chicago, IL, USA). For the descriptive statistics, the numerical values were presented as means ± standard deviation at 95% confidence intervals. To evaluate the differences between the modified sequence parameters in the related samples, the Wilcoxon signed-rank test (in the case of two values of the modified parameter) and the Friedman test (in the case of more than two values) including post-hoc testing and Bonferroni multiple testing correction were used. Furthermore, possible positive or negative correlations between the values of the modified parameters and the size of the artifact diameter, as well as the contrast-enhanced target lesion to non-enhanced muscle tissue contrast ratio were evaluated. For this purpose, the Bravais–Pearson correlation coefficient was calculated and tested for significance on both sides. To assess the significance of the results, the effect strength, *r*, of the Bravais–Pearson correlation coefficient was additionally presented using Cohen's classification ($r = 0.10$: weak effect, $r = 0.30$: medium effect, $r = 0.50$: strong effect). To determine the differences between the IAs of the MR-compatible needles as unrelated samples, the Kruskal–Wallis test was used. To measure the interrater reliability between the two blinded readers, the intraclass correlation coefficient (ICC) was calculated. A *P* value of 0.05 was set as the limit of statistical significance.

Results

Intervention angle

The seven IAs (0°–90°) exhibited significant differences ($P < 0.001$) in artifact diameters (Figures 3-5), with the artifacts increasing considerably with higher IAs, which also proved to be significant for multiple pairwise comparisons (14 pairs) (Supplementary Table 3). Here, only seven pairwise comparisons of stepwise increased IAs did not show any significant differences (Supplementary Table 3).

Artifact diameters at 50% and 25% of the inserted 18G coaxial Nitinol needle length at various sequence parameters as a function of the intervention angle

The mean values and standard deviations of needle shaft artifact diameters as a function of the IA in relation to the B_0 field of both readers are presented in Table 1.

Flip angle

The artifact size decreased gradually with an increase in FA for each IA (IA_0: 1.40–7.05 mm, IA_{15}: 5.05–7.40 mm, IA_{30}: 7.15–12.35 mm, IA_{45}: 9.85–15.45 mm, IA_{60}: 11.30–16.25 mm, IA_{75}: 14.55–19.45 mm, IA_{90}: 18.90–24.85 mm; $P < 0.001$) (Supplementary Figure 1). The pairwise comparison did not reveal any significant differences among the stepwise increased parameters. However, the multi-

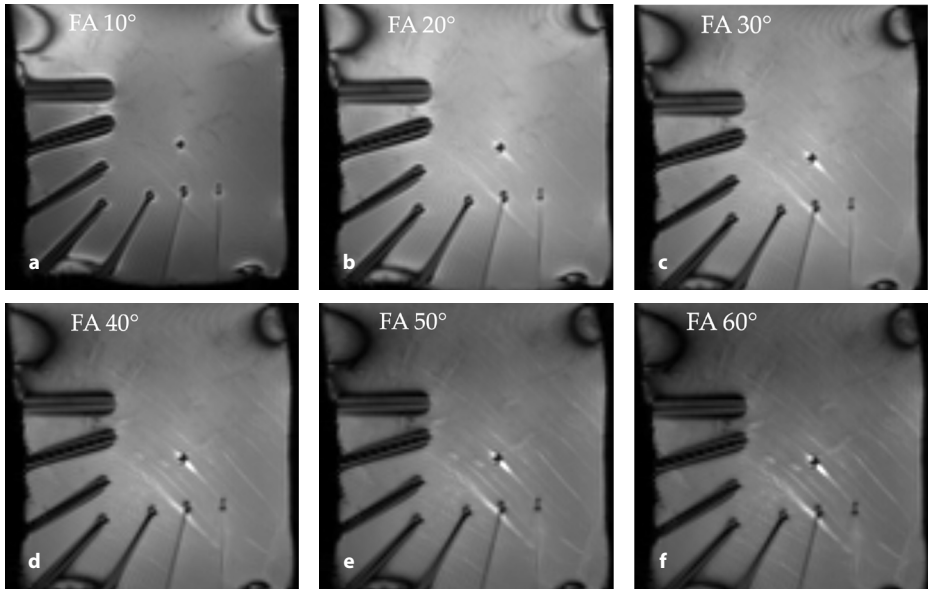

Figure 3. Scan series with flip angles (FA) of 10°–60°. Note the negative correlation of artifact diameters with increasing FAs ($P < 0.001$) **(Supplementary Figure 1)**. **(a-f)** For all seven intervention angles, significant and strong positive correlations between the FAs and the artifact diameters were observed (r = between −0.910 and −0.981; $P < 0.01$). Note the hyperintense peripheral rim around the central hypointense needle artifact occurring at FAs of 10° and 20°.

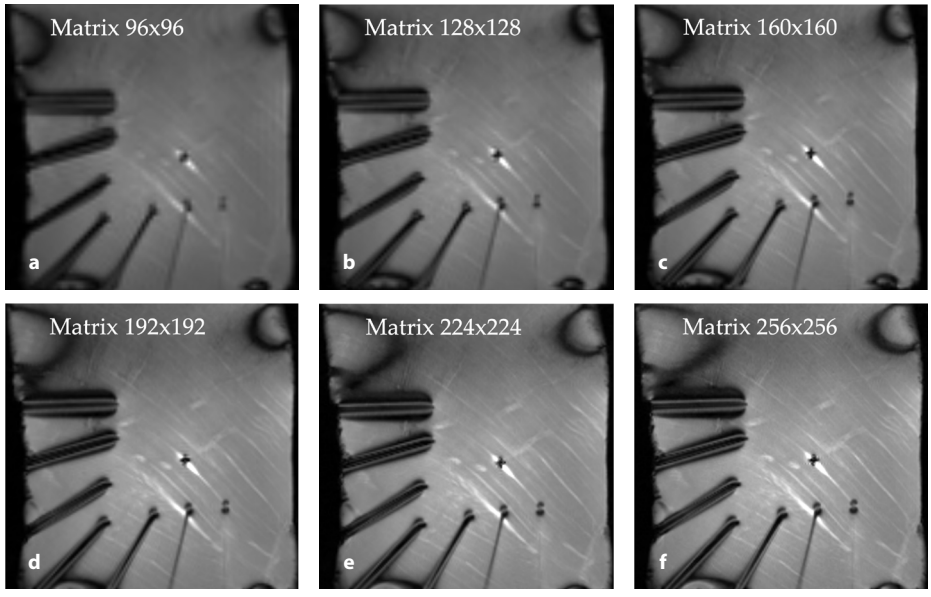

Figure 4. Scan series with matrices of 96 × 96, 128 × 128, 160 × 160, 192 × 192, 224 × 224, and 256 × 256. No significant differences among the artifact diameters were observed when comparing six matrix sizes for all intervention angles (IAs) ($P = 0.035$). However, significant positive correlations were found between the mean artifact diameters of both readers and the matrix size for IAs of 75° and 90° ($r = 0.873$, $P = 0.023$; $r = 0.969$, $P = 0.001$, respectively). In **(a-f)**, the visual correlates are shown. Note an increased differentiation of the actual needle and the needle artifact with larger matrices.

ple testing revealed significant differences among four pairs of FAs (Supplementary Table 4). For all seven IAs, significant and strong positive correlations between the FAs and the artifact diameters were observed (r = –0.973, P = 0.001; r = –0.910, P = 0.012; r = –0.981, P < 0.001; r = –0.970, P = 0.001; r = –0.973, P = 0.001; r = –0.978, P < 0.001; r = –0.919, P = 0.010) (Figure 3). In addition to the central hypointense needle artifact, a hyperintense peripheral rim was observed at FAs of 10° and 20°, which was included in the artifact diameter measurements.

Bandwidth

On modifying the receiver BW, no significant difference in artifact diameter was found for any of the different IAs (IA_0: 3.45–3.90 mm, IA_{15}: 6.15–6.25 mm, IA_{30}: 8.00–8.55 mm, IA_{45}: 11.40–11.75 mm, IA_{60}: 11.90–12.85 mm, IA_{75}: 15.75–15.90 mm, IA_{90}: 18.90–20.25 mm; P = 0.594) and neither was there a sig-

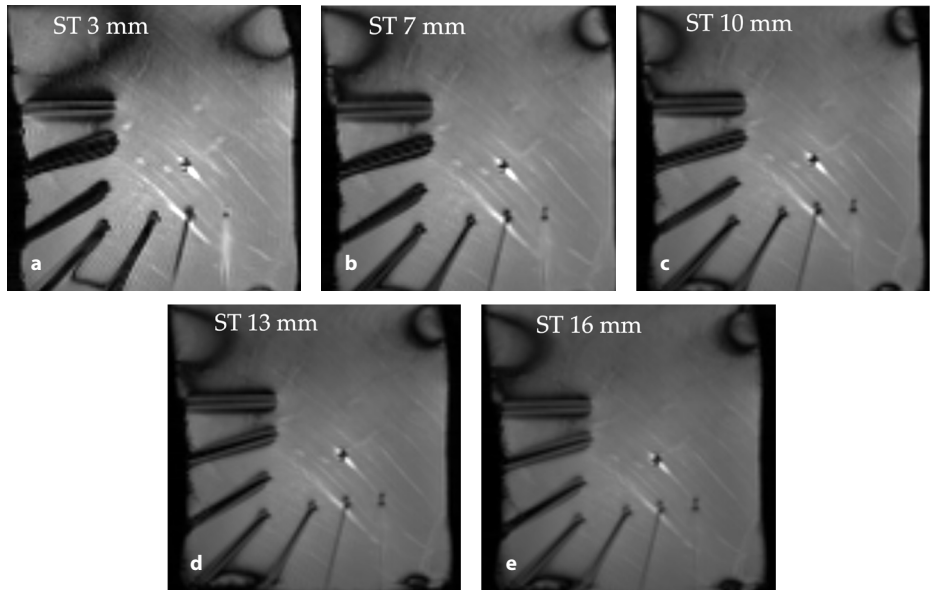

Figure 5. Scan series with slice thicknesses (ST) of 3, 7, 10, 13, and 16 mm. **(a-e)** A significant correlation between the artifact diameters and the ST was found for intervention angles of 45°, 60°, 75°, and 90° (r = –0.943, P = 0.016; r = –0.933, P = 0.020; r = –0.880, P = 0.049, r = –0.955, P = 0.011) **(Supplementary Figure 2)**.

Table 1. Mean artifact diameters measured at 50% and 25% of the inserted needle length

Intervention angle (°)	0	15	30	45	60	75	90	
Parameter								***P* value**
Flip angle (°)								$P < 0.001$[1]
10	7.05 ± 0.07	7.25 ± 0.07	12.35 ± 0.07	15.45 ± 0.07	16.25 ± 0.07	19.45 ± 0.07	24.85 ± 0.07	
20	6.50 ± 0.14	7.40 ± 0.14	10.80 ± 0.14	15.15 ± 0.07	15.45 ± 0.07	17.55 ± 0.07	22.65 ± 0.21	
30	5.70 ± 0.00	7.20 ± 0.00	9.35 ± 0.07	12.65 ± 0.07	13.35 ± 0.07	16.95 ± 0.07	20.25 ± 0.07	
40	2.95 ± 0.07	5.40 ± 0.00	8.60 ± 0.00	12.60 ± 0.00	12.65 ± 0.07	16.30 ± 0.00	19.65 ± 0.07	
50	2.00 ± 0.14	5.35 ± 0.07	8.00 ± 0.00	11.65 ± 0.07	12.30 ± 0.00	14.85 ± 0.07	18.90 ± 0.00	
60	1.40 ± 0.00	5.05 ± 0.07	7.15 ± 0.07	9.85 ± 0.07	11.30 ± 0.00	14.55 ± 0.07	19.10 ± 0.14	
Bandwidth (Hz/pixel)								$P = 0.594$[1]
930	3.90 ± 0.00	6.25 ± 0.00	8.25 ± 0.07	11.75 ± 0.07	11.90 ± 0.00	15.75 ± 0.00	20.25 ± 0.07	
1149	3.45 ± 0.07	6.20 ± 0.00	8.55 ± 0.07	11.65 ± 0.07	12.05 ± 0.07	15.80 ± 0.00	19.95 ± 0.07	
1395	3.55 ± 0.07	6.15 ± 0.07	8.05 ± 0.07	11.45 ± 0.07	12.65 ±0.07	15.85 ± 0.07	18.90 ± 0.00	
1698	3.55 ± 0.07	6.20 ± 0.00	8.00 ± 0.00	11.40 ± 0.00	12.85 ± 0.07	15.90 ± 0.14	19.25 ± 0.07	
Matrix (voxels)								$P = 0.335$[1]
96 × 96	3.90 ± 0.00	6.85 ± 0.07	8.70 ± 0.14	10.35 ± 0.07	13.85 ± 0.07	17.20 ± 0.00	19.70 ± 0.00	
128 × 128	3.95 ± 0.07	6.55 ± 0.07	8.60 ± 0.00	10.30 ± 0.00	13.85 ± 0.07	17.60 ± 0.14	20.75 ± 0.07	
160 × 160	3.95 ± 0.07	5.85 ± 0.07	8.90 ± 0.00	11.95 ± 0.07	14.10 ± 0.00	17.55 ± 0.07	21.45 ± 0.07	
192 × 192	3.95 ± 0.07	5.05 ± 0.07	8.65 ± 0.07	11.65 ± 0.07	13.90 ± 0.14	18.10 ± 0.14	22.10 ± 0.00	
224 × 224	3.25 ± 0.07	6.55 ± 0.00	8.80 ± 0.00	10.90 ± 0.00	12.25 ± 0.07	17.95 ± 0.07	24.75 ± 0.07	
256 × 256	3.25 ± 0.07	4.70 ± 0.00	9.65 ± 0.07	11.05 ± 0.07	13.55 ± 0.07	18.00 ± 0.14	26.40 ± 0.00	
Slice thickness (mm)								$P < 0.001$[1]
3	6.40 ± 0.00	6.80 ± 0.14	9.05 ± 0.07	12.65 ± 0.07	15.65 ± 0.07	19.75 ± 0.07	26.25 ± 0.07	
7	5.05 ± 0.07	6.05 ± 0.07	8.85 ± 0.07	12.15 ± 0.07	13.85 ± 0.07	16.70 ± 0.00	24.60 ± 0.00	
10	5.00 ± 0.00	7.85 ± 0.07	9.25 ± 0.07	11.80 ± 0.00	13.70 ± 0.00	16.40 ± 0.00	22.30 ± 0.14	
13	5.35 ± 0.07	7.70 ± 0.07	8.80 ± 0.00	11.45 ± 0.07	13.50 ± 0.14	16.25 ± 0.07	22.25 ± 0.21	
16	3.20 ± 0.00	4.90 ± 0.14	7.25 ± 0.07	10.10 ± 0.14	11.40 ± 0.00	15.65 ± 0.07	18.10 ± 0.14	
Read-out direction								$P = 0.785$[2]
R >> L	4.30 ± 0.00	6.45 ± 0.07	8.20 ± 0.14	10.70 ± 0.00	13.40 ± 0.14	17.35 ± 0.07	20.80 ± 0.14	
A >> P	4.30 ± 0.00	6.45 ± 0.07	8.35 ± 0.07	10.95 ± 0.00	13.35 ± 0.14	17.20 ± 0.00	20.75 ± 0.07	

Artifact diameters averaged over both readers at 50% and 25% of the needle length measured from the tip of the needle (in mm) at various sequence parameters as a function of the intervention angle in relation to the B_0 field. Values are presented as means ± standard deviation. [1]Friedman test; [2]Wilcoxon signed-rank test; R, right; L, left; A, anterior; P, posterior.

nificant correlation between the artifact diameter and the BW (r = –0.576, P = 0.424; r = –0.575, P = 0.425; r = –0.680, P = 0.320; r = 0.746, P = 0.254; r = 0.573, P = 0.427; r = –0.817, P = 0.188).

Matrix

The Friedman test revealed no significant differences between the artifact diameters when comparing six matrix sizes for each IA (IA_0: 3.25–3.95 mm, IA_{15}: 4.70–6.85 mm, IA_{30}: 8.60–9.65 mm, IA_{45}: 10.30–11.95 mm, IA_{60}: 12.25–14.10 mm, IA_{75}: 17.20–18.10 mm, IA_{90}: 19.70–26.40 mm; P = 0.335). In addition, the pairwise comparisons did not indicate any significant differences (P = 1.000) (Supplementary Table 4). However, significant positive correlations were found between the mean artifact diameters of both readers and the matrix for the IAs of 75° and 90° (r = 0.873, P = 0.023; r = 0.969, P = 0.001, respectively) (Figure 4). For the other IAs, there was no significant correlation between the artifact diameter and the matrix. In addition, an increased differentiation between the display of the actual needle and the surrounding needle artifact was observed with larger matrices.

Slice thickness

On modifying the ST, significant differences in artifact diameter were found for each IA (IA_0: 3.20–6.40 mm, IA_{15}: 4.90–7.85 mm, IA_{30}: 7.25–9.25 mm, IA_{45}: 10.10–12.65 mm, IA_{60}: 11.40–15.65 mm, IA_{75}: 15.65–19.75 mm, IA_{90}: 18.10–26.25 mm; P < 0.001) (Supplementary Figure 2). The multiple testing revealed significant differences between the STs of 3 and 17 mm (P < 0.001) (Supplementary Table 4). A significant correlation between the artifact diameters and ST was found for IAs of 45°, 60°, 75°, and 90° (r = –0.943, P = 0.016; r = –0.933, P = 0.020; r = –0.880, P = 0.049, r = –0.955, P = 0.011) (Figure 5).

Read-out direction

For the two different read-out directions (right >> left, anterior >> posterior), no significant differences in artifact diameters were found during the Wilcoxon signed-rank test (P = 0.785), with generally similar artifact diameters for both read-out directions.

Artifact diameters at the tip of the 18G coaxial Nitinol needle at various sequence parameters as a function of the intervention angle

The mean values and standard deviations of the artifact diameters at the needle tip as a function of the IA in relation to the B_0 field of

Table 2. Mean maximum ball-like tip artifact diameters (regardless of its two-dimensional direction of largest extension)

Intervention angle (°)	0	15	30	45	
Parameter					***P* value**
Flip angle (°)					$P = 0.003$[1]
10	13.10 ± 0.00	13.10 ± 0.00	12.10 ± 0.00	12.25 ± 0.07	
20	11.85 ± 0.07	12.05 ± 0.07	12.75 ± 0.07	11.50 ± 0.00	
30	10.25 ± 0.07	10.50 ± 0.14	9.95 ± 0.07	10.95 ± 0.07	
40	10.25 ± 0.07	9.35 ± 0.07	9.45 ± 0.07	9.65 ± 0.07	
50	10.05 ± 0.07	9.45 ± 0.07	9.30 ± 0.00	8.50 ± 0.14	
60	9.50 ± 0.07	9.10 ± 0.00	9.20 ± 0.00	9.15 ± 0.14	
Bandwidth (Hz/pixel)					$P = 0.082$[1]
930	11.10 ± 0.00	10.80 ± 0.14	10.15 ± 0.07	10.15 ± 0.07	
1149	11.85 ± 0.07	10.40 ± 0.00	9.95 ± 0.07	9.95 ± 0.07	
1395	11.50 ± 0.14	10.15 ± 0.07	10.60 ± 0.14	9.70 ± 0.00	
1698	11.90 ± 0.14	10.80 ± 0.00	10.75 ± 0.07	10.30 ± 0.00	
Matrix (voxels)					$P = 0.614$[1]
96 × 96	13.10 ± 0.00	10.55 ± 0.05	10.30 ± 0.00	10.05 ± 0.05	
128 × 128	12.00 ± 0.10	11.15 ± 0.05	10.60 ± 0.10	10.85 ± 0.05	
160 × 160	11.80 ± 0.00	10.05 ± 0.05	10.35 ± 0.05	10.30 ± 0.00	
192 × 192	10.70 ± 0.10	10.65 ± 0.05	10.75 ± 0.05	9.80 ± 0.10	
224 × 224	12.20 ± 0.00	11.50 ± 0.00	11.20 ± 0.05	9.05 ± 0.05	
256 × 256	11.75 ± 0.05	11.95 ± 0.05	10.15 ± 0.05	10.30 ± 0.00	
Slice thickness (mm)					$P = 0.163$[1]
3	10.30 ± 0.00	11.65 ± 0.05	10.80 ± 0.00	10.65 ± 0.05	
7	10.25 ± 0.05	10.15 ± 0.05	9.90 ± 0.10	9.50 ± 0.10	
10	10.90 ± 0.10	11.05 ± 0.05	10.45 ± 0.05	10.30 ± 0.10	
13	11.05 ± 0.05	10.80 ± 0.10	10.15 ± 0.05	10.30 ± 0.00	
16	11.80 ± 0.00	11.25 ± 0.05	8.45 ± 0.05	8.65 ± 0.05	
Read-out direction					$P = 0.465$[2]
RL	11.00 ± 0.00	10.05 ± 0.05	9.45 ± 0.05	9.65 ± 0.05	
AP	11.20 ± 0.00	10.80 ± 0.10	9.70 ± 0.10	9.30 ± 0.00	

The tip artifact diameters averaged over both readers at various sequence parameters as a function of the intervention angle in relation to the B_0 field. The values are presented as means ± standard deviation; [1]Friedman test; [2]Wilcoxon signed-rank test; R, right; L, left; A, anterior; P, posterior.

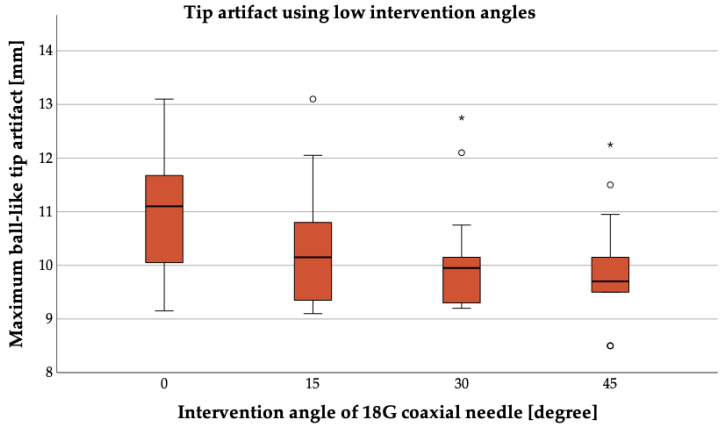

Figure 6. Behavior of the ball-like tip artifact, which occurred at intervention angles (IAs) of 0°, 15°, 30°, and 45°. The maximum diameter of this artifact increased gradually with a decrease in IA (P = 0.022). The pairwise comparisons revealed significant differences between 0° and 30° (P = 0.041), as well as between 0° and 45° (P = 0.047).

Table 3. Interrater reliability

Intervention angle (°)	ICC value	*P* value	95% confidence interval
0	0.998	<0.001	0.995 – 0.999
15	0.994	<0.001	0.985 – 0.997
30	0.995	<0.001	0.989 – 0.998
45	0.999	<0.001	0.997 – 0.999
60	0.997	<0.001	0.994 – 0.999
75	0.998	<0.001	0.995 – 0.999
90	0.998	<0.001	0.996 – 0.999

The ICC values of two blinded readers are shown for intervention angles of 0°–90°. ICC, intraclass correlation coefficient.

both readers are presented in Table 2. A ball-like tip artifact occurred using low IAs of 0°–45°. The maximum diameter of this artifact increased gradually with a decrease in IA ($P = 0.022$) (Figure 6). The pairwise comparisons revealed significant differences between 0° and 30° ($P = 0.041$), as well as between 0° and 45° ($P = 0.047$) (Supplementary Table 5). The modification of the sequence parameters, BW, matrix, ST, read-out direction, had no significant influence on this artifact ($P = 0.082$, $P = 0.614$, $P = 0.163$, $P = 0.465$), while that of the FA did ($P = 0.003$).

Interrater reliability

For the various IAs (0° 15°, 30°, 45°, 60°, 75°, 90°), the ICCs were 0.998, 0.994, 0.995, 0.999, 0.997, 0.998, and 0.998, respectively ($P < 0.001$), indicating excellent interrater reliability (Table 3).

Contrast-enhanced target lesion to non-enhanced muscle tissue contrast ratio

The lesion-to-muscle-contrast ratio, *R*, presented significant positive correlations with an increase in FA and matrices ($P < 0.001$; $P = 0.003$), as well as a significant negative correlation with an increase in ST ($P = 0.007$). No significant correlations were found for the modified BWs ($P = 0.171$). The corresponding data are presented as supplemental information (Supplementary Table 6).

Discussion

In this 3.0 T musculoskeletal phantom study, the influence of different sequence parameters of an interventional real-time fluoroscopic pulse sequence with TrueFISP contrast on the artifact behavior of a commercially available MR-compatible coaxial 18G Nitinol needle was investigated as a function of the IA.

Needle artifacts pose a major limitation to high-field MRI-guided interventions in particular, regardless of the intended target, and are caused by several different physical processes, of which inhomogeneities of the B_0 field experienced by the nuclei are the most important. This needle-induced B_0 inhomogeneity is caused by the geometric characteristics and the individual magnetic susceptibility of the imaged object. Distortions of the spatial geometry, as well as intra-voxel dephasing are caused by these static field errors.[17,23] Among other artifacts, needle artifacts can be caused by radiofrequency effects such as B_1 enhancement.[24] With this background, the present study aimed to analyze artifact formation with a focus on its relevance for MRI-guided high-field musculoskeletal interventional procedures through modifying different sequence parameters (FA, BW, matrix, ST, and read-out-direction) as a function of the IA. Completely erased or too-small artifacts are not always desirable in MR-guided intervention since the needle is visualized by the artifact itself and minimizing artifacts can mean the needle is difficult to recognize.

In general, the technological advances in magnet, coil, protocol, biopsy needle, and probe design have made MRI-guidance a clinically valuable imaging technique for minimally invasive procedures. Due to the continuing innovations in augmented reality, targeting software, and compatible devices, it is crucial to reassess methodological and technical fundamentals, such as needle artifacts. This is especially the case for MRI-guided procedures for musculoskeletal interventions, which is an extremely new field, and specific adaptations need to be made. As such, a phantom that has been adapted to the target tissue in musculoskeletal interventions (muscle phantom) was selected, in contrast to previous studies, which generally employed a 3 T MRI scanner.[25,26] Singh et al.[25] evaluated needle artifact diameters using an acrylic phantom modifying only two parameters: IA and read-out direction. Furthermore, in the present study, contrast medium application was also performed for experimental evaluation of the visibility of the target lesion and to emulate as far as possible the clinical routine, exemplarily imitating contrast-enhanced MR-guided punctures of joint structures in the case of capsulitis.

It is well known that the IA is closely associated with the artifact size.[17,22,27] In line with this, the seven IAs (0°–90°) analyzed in this study exhibited significant differences in artifact diameters, with the artifacts increasing considerably with higher IAs, which also proved to be significant for most of the multiple pairwise comparisons. Elsewhere, Schmidt et al.[20] demonstrated a positive correlation between artifact size and increasing IAs in their 1.5 T-liver phantom study. At this point, it should be noted that it is advantageous to use low susceptibility materials since these can be used at higher IAs. In addition, Frahm et al.[28] analyzed the relationship between the magnetic field strength and the IA. The authors found that the needle artifact growth with an increase in IA was lower with a 0.2-T field strength than with a 1.5-T strength and that at high-field strengths, the artifact size correlated closely with an increase in IA relative to the B_0 field.[28]

In the present study, decreasing artifact diameters were observed with an increase in FA for each IA. At FAs of 10° and 20°, an additional hyperintense peripheral rim artifact was observed around the otherwise hypointense artifact along the shaft of the needle, which was included in the measurements. This artifact consecutively extends the area of potential misinterpretation of the actual needle position and needs to be considered when choosing a FA of 10° or 20° for the TrueFISP sequence. Interestingly, in a previous liver phantom study by Schmidt et al.[20] that analyzed a T1-weighted gradient echo (GRE) sequence at 1.5 T, this hyperintense peripheral rim artifact was observed at high FAs of >45°. Another previous investigation of needle artifacts by Bauch[29], who also modified the FA in a T1-weighted GRE sequence, revealed no relevant changes to the artifact diameter in a stepwise comparison for FAs of <45°, which is in line with both the results of the present study and those obtained by Schmidt et al.[20] However, a T1-weighted GRE sequence was analyzed in these studies and therefore these results cannot be expected to be directly transferrable to ours. This notwithstanding, the multiple testing revealed significant differences between four pairs of FAs, and significant and strong positive correlations between FA and artifact diameter were observed in the present study for all seven IAs. While the previous investigations

demonstrated optimal artifact behavior with FAs of <45° for T1-weighted GRE sequences,[20,29] in contrast, the present study found the smallest artifact sizes with higher FAs (>40°).

No significant correlation was found between artifact diameter and modifications of the BW, although varying the BW is reported in the literature to be a crucial parameter for the minimization of needle artifacts.[30] The physical context is that the Larmor frequencies of the hydrogen protons are altered to a certain amount by a metallic object of a given size and susceptibility. Thus, reducing the BW increases the number of pixels that are visibly affected by the variance in frequencies and consecutively increases the size of the susceptibility artifact.[31] However, this finding using a TrueFISP sequence is consistent with Schmidt et al.'s[20] results when analyzing the BW as a potential influencing parameter on artifact diameters for a T1-weighted GRE sequence, who also did not find any significant differences between different BWs and artifact behavior in a liver phantom. The fact that the BW variations did not significantly influence the needle artifact size may have been because the artifact was too small, meaning potentially significant differences could have remained hidden. However, the BW range in the present study was chosen according to the standard BWs used in clinical practice.

No significant differences in artifact diameter were found when comparing various matrix sizes for each IA, which was also the case with the pairwise comparisons. However, significant positive correlations were found between artifact diameter and matrix for IAs of 75° and 90°. In addition, an increased differentiation between the display of the actual needle and the surrounding needle artifact with larger matrices was observed, which is also in line with Schmidt et al.'s[20] results, who observed smaller artifact diameters at higher matrix sizes in their liver phantom study (not statistically significant). Generally, a higher matrix size reduces the artifact diameters and optimizes the image quality due to decreased voxel volume. In determining the spatial resolution, the matrix is a quality feature of the acquired image data,[28] meaning higher matrices may improve the differentiation of the actual intervention needle and therefore allow for more exact lesion targeting. Nonetheless, the increase in acquisition time is the major reason why matrix sizes cannot be set as high as possible in clinical practice.[29]

The voxel size is not only determined by the matrix, but also by the ST. A decrease in ST is equivalent to a reduction in voxel size and leads to a decreased field inhomogeneity within each individual voxel and subsequently results in lower artifact dependence and the generation of smaller needle artifacts.[28,32] In the present study, significant differences in artifact diameters were observed for each IA when modifying the ST. In addition, the multiple testing revealed significant differences between STs of 3 and 16 mm, and a significant correlation between the artifact diameters and the ST was found for IAs of 45°, 60°, 75°, and 90°. However, in our study setting, smaller artifact sizes were found for higher STs. In this context, it must be noted that the artifact size in the ST-modified scan series appears to be highly influenced by different IAs and that the differentiation of the actual needle shaft and tip is much better with higher STs (>10 mm) when looking at higher IAs. However, it should also be remembered that the ST should not be set too high during the procedure to allow for accurate needle placement. Thus, a potential compromise is selecting a ST of >7 mm. No significant differences in needle artifact sizes were observed for the two different read-out directions (RL or AP) in this study. This is consistent with previous studies on T1-weighted GRE sequences,[18,20,28] but not with a previous study on spin-echo and turbo spin-echo sequences, in which the artifacts were more pronounced when the read-out direction was perpendicular to the needle shafts.[18]

Ball-like tip artifacts were observed with low IAs of 0°–45° and these increased in size with a decrease in IA. Interestingly, this artifact was not significantly influenced by any sequence parameter other than the FA. This artifact at the needle tip particularly impairs the visibility of the tip, which makes precise needle guidance difficult and can be expected to affect the targeting accuracy. Moreover, it is problematic that this tip artifact extends in all directions such that it often resembles a ball; hence the "ball-like" description.[29,33] In line with our results, this tip artifact occurred with low IAs of 0°–10° in a previous study by Schmidt et al.[20] As previously described by Liu et al.[34], the B_0 field is most strongly influenced in the area around the needle tip, which is particularly noticeable in materials with lower magnetic susceptibility, such as carbon fiber or titanium, when compared with other materials (e.g., chromium, cobalt, or nickel).

Regarding clinical routine high-field musculoskeletal interventional procedures, we recommend using a FA of 40°–60° to minimize hypointense artifact formation around the needle shaft and to avoid the occurrence of additional hyperintense artifact formation, which only occurred at low FAs of 10° and 20° in the present scan series. In addition, an ST of 10–16 mm returned the best image quality. To specifically avoid ball-like tip artifacts, IAs of 45°–60° should be selected.

Furthermore, it is important to not only minimize needle artifacts but also to guarantee sufficient visibility of the target lesion. Therefore, the contrast ratio of a gadolinium-enhanced target lesion placed centrally into the muscle phantom and that of the adjacent non-enhanced muscle tissue were evaluated by quantitatively analyzing the corresponding SIs. The contrast-enhanced target lesion was best visualized at higher FAs (40°–60°) and matrices (224 × 224/256 × 256), while a negative correlation between the visibility of the target lesion with increasing STs was observed, which can be explained by the increasing partial-volume effects at higher STs. For small lesions (relative to the ST), this might lead to a potential conflict since higher STs of 10–16 mm minimized the needle artifacts while maintaining the best possible visualization of the coaxial intervention needle. To the best of the authors' best knowledge, there are no comparable previous studies that investigated the visibility of a contrast-enhanced lesion in a similar setting.

However, this study involves a number of potential limitations. First, a fixed phantom was used, which provided an optimal background signal intensity and therefore an optimized depiction of signal voids. In an *in vivo* setting, it must be assumed that both the image quality and the artifact contrast will be worse due to, for example, motion artifacts. Second, this phantom study was performed at a single field strength (3.0 T), and lower field strengths (e.g., 1.5 T) will need to be investigated with this TrueFISP sequence in view of scenarios such as when the patient is not suitable for a high-field intervention due to only 1.5 T-conditional external materials. Nevertheless, 3.0 T is the preferable field strength in the majority of musculoskeletal investigations. Third, only a single alloy (Nitinol) and a single needle size (18G) were investigated. As both alloy and needle size have an impact on artifact behavior,[29,33] further studies are needed to examine these effects. Fourth, the artifact diameters were determined by manual measurements and automatized artifact measurements would minimize any potential reader bias. However, high inter-reader agreement was observed in our study. Furthermore, the artifact di-

ameters were measured in two-dimensional terms and it must be acknowledged that needle artifacts occur three-dimensionally and that the needle artifact volume might be a relevant parameter for exact needle guidance. Nonetheless, depending on the sequence acquisitions, it might not be adequately feasible to conduct such measurements with the available fluoroscopic MRI hardware and software. Fifth, only one single sequence parameter was modified in our scan series to avoid any additional confounding variable; however, the BW was not modified separately but only coupled to the TR since the minimum TR had been systematically chosen in our experimental setting. Furthermore, while the image quality will not be affected by increasing motion artifacts with longer scan times (with an increase in TR) in a phantom model, it may be in real-world settings. Sixth, minimized artifact diameters do not necessarily imply that the "true" position of the needle within the tissue is better known, as it is inherently difficult to be certain about the exact needle position from real-time fluoroscopic MRI visualization. Therefore, further studies with coordinate registration are needed to ensure more accurate verification of the exact needle position and, in particular, the position of the needle tip. In a previous study, Yamada et al.[35] applied real-time ultrasound imaging fused with reformatted static MR images and coordinate registration for needle guidance during MR-guided percutaneous tumor ablations and revealed targeting errors of 1.6 ± 0.6 mm. Last, the investigated sequence parameter settings need to be analyzed and adapted to clinical use cases.

In conclusion, to minimize needle artifacts, it is recommended to use FAs of 40°–60°, a ST of >7 mm, and, if possible, an IA of 45°–60°. The visibility of the target lesion and the needle's artifact behavior must be weighed up against each other when choosing the ST, while higher FAs (40°–60°) and matrices (224 × 224/256 × 256) are associated with low artifacts and sufficient lesion visibility.

Acknowledgements

We would like to thank Siemens Healthineers (Erlangen, Germany) for their support in the development of this manuscript and for providing the real-time sequences and associated software ("Needle Intervention Add-in" package).

Conflict of interest disclosure

The authors declared no conflicts of interest.

References

1. Barkhausen J, Kahn T, Krombach GA, et al. White paper: interventional MRI: current status and potential for development considering economic perspectives, part 1: general application. *Rofo*. 2017;189(7):611-623. [CrossRef]
2. Bock M, Umathum R, Zuehlsdorff S, et al. Interventional magnetic resonance imaging: an alternative to image guidance with ionising radiation. *Radiat Prot Dosimetry*. 2005;117(1-3):774-778. [CrossRef]
3. Elfatairy KK, Filson CP, Sanda MG, Osunkoya AO, Nour SG. In-Bore MRI-guided prostate biopsies in patients with prior positive transrectal US-guided biopsy results: pathologic outcomes and predictors of missed cancers. *Radiol Imaging Cancer*. 2020;2(5):e190078. [CrossRef]
4. Fischbach F, Thormann M, Seidensticker M, Kropf S, Pech M, Ricke J. Assessment of fast dynamic imaging and the use of Gd-EOB-DTPA for MR-guided liver interventions. *J Magn Reson Imaging*. 2011;34(4):874-879. [CrossRef]
5. Jungmann PM, Agten CA, Pfirrmann CW, Sutter R. Advances in MRI around metal. *J Magn Reson Imaging*. 2017;46(4):972-991. [CrossRef]
6. Weiss J, Hoffmann R, Rempp H, et al. Feasibility, efficacy, and safety of percutaneous MR-guided ablation of small (≤12 mm) hepatic malignancies. *J Magn Reson Imaging*. 2019;49(2):374-381. [CrossRef]
7. Winkelmann MT, Archid R, Gohla G, et al. MRI-guided percutaneous thermoablation in combination with hepatic resection as parenchyma-sparing approach in patients with primary and secondary hepatic malignancies: single center long-term experience. *Cancer Imaging*. 2020;20(1):37. [CrossRef]
8. Winkelmann MT, Gohla G, Kubler J, et al. MR-guided high-power microwave ablation in hepatic malignancies: initial results in clinical routine. *Cardiovasc Intervent Radiol*. 2020;43(11):1631-1638. [CrossRef]
9. Dianat SS, Carter HB, Macura KJ. Magnetic resonance-guided prostate biopsy. *Magn Reson Imaging Clin N Am*. 2015;23(4):621-631. [CrossRef]
10. Fischbach F, Bunke J, Thormann M, et al. MR-guided freehand biopsy of liver lesions with fast continuous imaging using a 1.0-T open MRI scanner: experience in 50 patients. *Cardiovasc Intervent Radiol*. 20211;34(1):188-192. [CrossRef]
11. Fischbach F, Eggemann H, Bunke J, Wonneberger U, Ricke J, Strach K. MR-guided freehand biopsy of breast lesions in a 1.0-T open MR imager with a near-real-time interactive platform: preliminary experience. *Radiology*. 2012;265(2):359-370. [CrossRef]
12. Fritz J, Thomas C, Clasen S, Claussen CD, Lewin JS, Pereira PL. Freehand real-time MRI-guided lumbar spinal injection procedures at 1.5 T: feasibility, accuracy, and safety. *AJR Am J Roentgenol*. 2009;192(4):161-167. [CrossRef]
13. Tempany C, Straus S, Hata N, Haker S. MR-guided prostate interventions. *J Magn Reson Imaging*. 2008;27(2):356-367. [CrossRef]
14. Weiss CR, Nour SG, Lewin JS. MR-guided biopsy: a review of current techniques and applications. *J Magn Reson Imaging*. 2008;27(2):311-325. [CrossRef]
15. Bayer T, Adler W, Janka R, Uder M, Roemer F. Magnetic resonance cinematography of the fingers: a 3.0 tesla feasibility study with comparison of incremental and continuous dynamic protocols. *Skeletal Radiol*. 2017;46(12):1721-1728. [CrossRef]
16. Penzkofer T, Peykan N, Schmidt K, Krombach G, Kuhl CK. How MRI compatible is "MRI compatible"? A systematic comparison of artifacts caused by biopsy needles at 3.0 and 1.5 T. *Cardiovasc Intervent Radiol*. 2013;36(6):1646-1657. [CrossRef]
17. Ladd ME, Erhart P, Debatin JF, Romanowski BJ, Boesiger P, McKinnon GC. Biopsy needle susceptibility artifacts. *Magn Reson Med*. 1996;36(4):646-651. [CrossRef]
18. Lewin JS, Duerk JL, Jain VR, Petersilge CA, Chao CP, Haaga JR. Needle localization in MR-guided biopsy and aspiration: effects of field strength, sequence design, and magnetic field orientation. *AJR Am J Roentgenol*. 1996;166(6):1337-1345. [CrossRef]
19. Lüdeke KM, Röschmann P, Tischler R. Susceptibility artefacts in NMR imaging. *Magn Reson Imaging*. 1985;3(4):329-343. [CrossRef]
20. Schmidt VF, Arnone F, Dietrich O, et al. Artifact reduction of coaxial needles in magnetic resonance imaging-guided abdominal interventions at 1.5 T: a phantom study. *Sci Rep*. 2021;11(1):22963. [CrossRef]
21. Thomas C, Springer F, Röthke M, et al. In vitro assessment of needle artifacts with an interactive three-dimensional MR fluoroscopy system. *J Vasc Interv Radiol*. 2010;21(3):375-380. [CrossRef]
22. Thomas C, Wojtczyk H, Rempp H, et al. Carbon fibre and nitinol needles for MRI-guided interventions: first in vitro and in vivo application. *Eur J Radiol*. 2011;79(3):353-358. [CrossRef]
23. Bakker CJ, Bhagwandien R, Moerland MA, Fuderer M. Susceptibility artifacts in 2DFT spin-echo and gradient-echo imaging: the cylinder model revisited. *Magn Reson Imaging*. 1993;11(4):539-548. [CrossRef]
24. Graf H, Lauer UA, Berger A, Schick F. RF artifacts caused by metallic implants or instruments which get more prominent at 3 T: an in vitro study. *Magn Reson Imaging*. 2005;23(3):493-499. [CrossRef]
25. Singh S, Torrealdea F, Bandula S. MR Imaging-Guided Intervention: Evaluation of MR conditional biopsy and ablation needle tip artifacts at 3T using a balanced fast field echo sequence. *J Vasc Interv Radiol*. 2021;32(7):1068-1074. [CrossRef]

26. DiMaio SP, Kacher DF, Ellis RE, et al. Needle artifact localization in 3T MR images. *Stud Health Technol Inform*. 2006;119:120-125. [CrossRef]
27. Wachowicz K, Thomas SD, Fallone BG. Characterization of the susceptibility artifact around a prostate brachytherapy seed in MRI. *Med Phys*. 2006;33(12):4459-4467. [CrossRef]
28. Frahm C, Gehl HB, Melchert UH, Weiss HD. Visualization of magnetic resonance-compatible needles at 1.5 and 0.2 tesla. *Cardiovasc Intervent Radiol*. 1996;19(5):335-340. [CrossRef]
29. Bauch S. Evaluation MR kompatibler Nadeln und interaktiver Sequenzen zur interventionellen Bildgebung an einem offenen 1.0 tesla MR-tomographen (panorama-HFO). Germany: Otto-von-Guericke University Magdeburg; 2013. [CrossRef]
30. Hargreaves BA, Worters PW, Pauly KB, Pauly JM, Koch KM, Gold GE. Metal-induced artifacts in MRI. *AJR Am J Roentgenol*. 2011;197(3):547-555. [CrossRef]
31. Talbot BS, Weinberg EP. MR Imaging with metal-suppression sequences for evaluation of total joint arthroplasty. *Radiographics*. 2016;36(1):209-225. [CrossRef]
32. Müller-Bierl B, Graf H, Lauer U, Steidle G, Schick F. Numerical modeling of needle tip artifacts in MR gradient echo imaging. *Med Phys*. 2004;31(3):579-587. [CrossRef]
33. Reichenbach JR, Wurdinger S, Pfleiderer SO, Kaiser WA. Comparison of artifacts produced from carbon fiber and titanium alloy needles at 1.5 T MR imaging. *J Magn Reson Imaging*. 2000;11(1):69-74. [CrossRef]
34. Liu H, Hall WA, Martin AJ, Truwit CL. Biopsy needle tip artifact in MR-guided neurosurgery. *J Magn Reson Imaging*. 2001;13(1):16-22. [CrossRef]
35. Yamada A, Tokuda J, Naka S, Murakami K, Tani T, Morikawa S. Magnetic resonance and ultrasound image-guided navigation system using a needle manipulator. *Med Phys*. 2020;47:850-858. [CrossRef]

Supplementary Table 1. Default settings

Fixed parameter	Value
FOV (mm^2)	300 × 300
Matrix (voxels)	128 × 128
Slice thickness (mm)	10
Flip angle (°)	50
Echo time (ms)	1.71
Repetition time (ms)	3.42
Bandwidth (Hz/pixel)	930
Read-out direction	RL
Phase oversampling	0
Acquisition time (ms)	461

While one parameter was modified, all others remained unchanged in a predefined setting. FOV, field of view; R, right; L, left.

Supplementary Table 2. MRI acquisition parameters and values.

	Values	Setting	Coupled TR (ms)
Scan series	1	10	
	2	20	
Flip angle (°)	3	30	
	4	40	
	5	50	
	6	60	
Bandwidth (Hz/pixel)	1	930	3.42
	2	1.149	3.28
	3	1.395	3.20
	4	1.698	3.18
Matrix (voxels)	1	96 × 96	
	2	128 × 128	
	3	160 × 160	
	4	192 × 192	
	5	224 × 224	
	6	256 × 256	
Slice thickness (mm)	1	3	
	2	7	
	3	10	
	4	13	
	5	16	
Read-out direction	1	RL	
	2	AP	

Scan series of study profile for intervention angles relative to the B_0 field of 0°–90°. Systematic and sequential modification of the technical parameters of the TrueFISP sequence. TR, repetition time; Hz, Hertz; R, right; L, left; A, anterior; P, posterior; TrueFISP, true fast imaging with steady-state free precession; MRI, magnetic resonance imaging.

Supplementary Table 3. Pairwise comparisons of the artifact diameter depending on the intervention angle

	Sample 1	Sample 2	
Parameter			***P* value**[1]
Intervention angle (°)			
	0	15	*P* = 1.000
	0	30	***P* = 0.027**
	0	45	***P* = 0.000**
	0	60	***P* = 0.000**
	0	75	***P* = 0.000**
	0	90	***P* = 0.000**
	15	30	*P* = 1.000
	15	45	***P* = 0.004**
	15	60	***P* = 0.000**
	15	75	***P* = 0.000**
	15	90	***P* = 0.000**
	30	45	*P* = 1.000
	30	60	*P* = 0.050
	30	75	***P* = 0.000**
	30	90	***P* = 0.000**
	45	60	*P* = 1.000
	45	75	***P* = 0.036**
	45	90	***P* = 0.000**
	60	75	*P* = 1.000
	60	90	***P* = 0.008**
	75	90	*P* = 1.000

[1]Kruskal–Wallis test, *P* values of post-hoc testing including Bonferroni multiple testing correction.

Supplementary Table 4. Pairwise comparisons of the artifact diameter depending on the modified sequence parameters flip angle, bandwidth, matrix size, and slice thickness

	Sample 1	Sample 2	
Parameter			***P* value**[1]
Flip angle (°)			
	60	50	*P* = 1.000
	60	40	*P* = 0.949
	60	30	*P* = 0.064
	60	20	***P* = 0.001**
	60	10	***P* = 0.000**
	50	40	*P* = 1.000
	50	30	*P* = 0.482
	50	20	***P* = 0.015**
	50	10	***P* = 0.001**
	40	30	*P* = 1.000
	40	20	*P* = 0.482
	40	10	*P* = 0.064
	30	20	*P* = 1.000
	30	10	*P* = 0.949
	20	10	*P* = 1.000
Bandwidth (Hz/pixel)			
	1.395	1.698	*P* = 1.000
	1.395	1.149	*P* = 1.000
	1.395	930	*P* = 1.000
	1.698	1.149	*P* = 1.000
	1.698	930	*P* = 1.000
	1.149	930	*P* = 1.000
Matrix (voxels)			
	96 × 96	224 × 224	*P* = 1.000
	96 × 96	128 × 128	*P* = 1.000
	96 × 96	256 × 256	*P* = 1.000
	96 × 96	192 × 192	*P* = 1.000
	96 × 96	160 × 160	*P* = 1.000
	224 × 224	128 × 128	*P* = 1.000
	224 × 224	256 × 256	*P* = 1.000
	224 × 224	192 × 192	*P* = 1.000
	224 × 224	160 × 160	*P* = 1.000
	128 × 128	256 × 256	*P* = 1.000
	128 × 128	192 × 192	*P* = 1.000
	128 × 128	160 × 160	*P* = 1.000
	256 × 256	192 × 192	*P* = 1.000
	256 × 256	160 × 160	*P* = 1.000
	192 × 192	160 × 160	*P* = 1.000
Slice thickness (mm)			
	17	13	*P* = 0.280
	17	10	*P* = 0.068
	17	7	*P* = 0.068
	17	3	***P* = 0.000**
	13	10	*P* = 1.000
	13	7	*P* = 1.000
	13	3	*P* = 0.425
	10	7	*P* = 1.000
	10	3	*P* = 1.000
	7	3	*P* = 1.000

[1]Friedman test, *P* values of post-hoc testing including Bonferroni multiple testing correction; Hz, Hertz.

Supplementary Table 5. Pairwise comparisons of the artifact diameters at the tip (ball-like tip artifact) at various sequence parameters depending on the intervention angle

	Sample 1	Sample 2	
Parameter			***P* value**[1]
Intervention angle (°)			
	30	45	$P = 1.000$
	30	15	$P = 1.000$
	30	0	$\mathbf{P = 0.041}$
	45	15	$P = 1.000$
	45	0	$\mathbf{P = 0.047}$
	15	0	$P = 0.270$

[1]Kruskal–Wallis test, *P* values of post-hoc testing including Bonferroni multiple testing correction.

Supplementary Table 6. Quantitative assessment of contrast-enhanced target lesion to non-enhanced muscle tissue contrast ratio (*R*)

	$SI_{contrast\text{-}enhanced\ target\ lesion}$	$SI_{non\text{-}enhanced\ muscle\ tissue}$	R	
Parameter				***P* value**
Flip angle (°)				$P < 0.001$[1]
10	199.00	154.00	1.29	
20	350.00	246.00	1.42	
30	437.00	273.00	1.60	
40	479.00	259.00	1.85	
50	487.00	235.00	2.07	
60	533.00	154.00	2.29	
Bandwidth (Hz/pixel)				$P = 0.171$[1]
930	528.00	238.00	2.22	
1149	535.00	232.00	2.31	
1395	537.00	225.00	2.39	
1698	536.00	227.00	2.36	
Matrix (voxels)				$P = 0.003$[1]
96 × 96	489.00	246.00	1.99	
128 × 128	484.00	238.00	2.03	
160 × 160	515.00	219.00	2.35	
192 × 192	518.00	216.00	2.40	
224 × 224	584.00	200.00	2.92	
256 × 256	565.00	197.00	2.87	
Slice thickness (mm)				$P = 0.007$[1]
3	633.00	284.00	2.23	
7	564.00	260.00	2.17	
10	486.00	233.00	2.09	
13	449.00	215.00	2.09	
16	421.00	205.00	2.05	
Read-out direction				
RL	484.00	229.00	2.11	
AP	485.00	226.00	2.15	

This ratio was defined in terms of the following formula based on the mean SIs in the ROIs: $R = SI_{contrast\text{-}enhanced\ target\ lesion} / SI_{non\text{-}enhanced\ muscle\ tissue}$. To assess the corresponding signal intensities, defined ROIs of least 5 mm^2 were used. [1]Bravais–Pearson correlation coefficient; SI, signal intensity; ROI, region of interest; R: right; L, left.

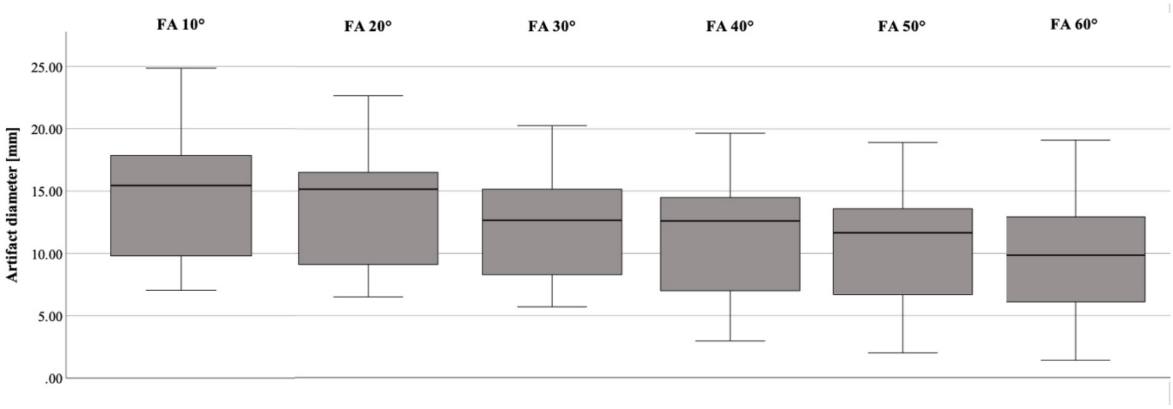

Supplementary Figure 1. Boxplots showing minimum, first quartile, median, third quartile, and maximum for artifact diameter size behavior as a function of the FA (10°–60°) averaged over all intervention angles. Note the gradually decreasing artifact size with the increase in FA ($P < 0.001$). FA, flip angle.

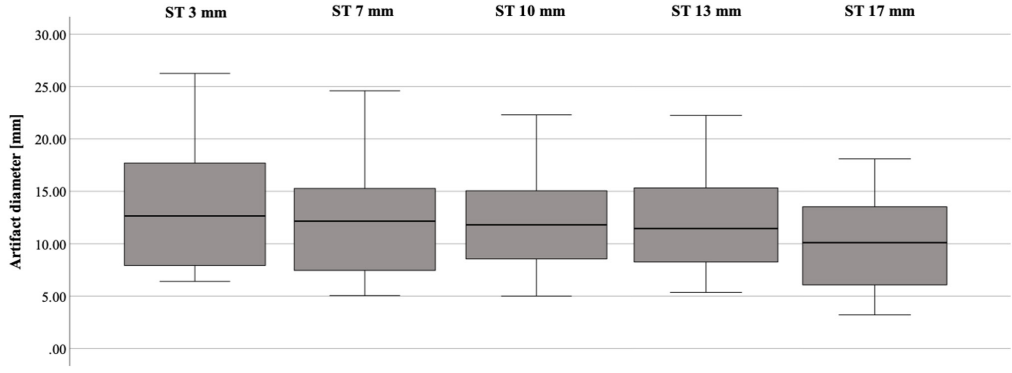

Supplementary Figure 2. Boxplots showing minimum, first quartile, median, third quartile, and maximum for artifact diameter size behavior as a function of the slice thickness (ST) (3–17 mm) averaged over all intervention angles. Note the significant differences in artifact size with the increase in ST ($P < 0.001$).

Diagn Interv Radiol 2023; DOI: 10.4274/dir.2023.232267

INTERVENTIONAL RADIOLOGY

TECHNICAL NOTE

Use of a funneled sheath for embolic protection during removal of thrombosed Simon Nitinol filters

Joshua Cornman-Homonoff
Juan Carlos Perez Lozada
Angelo G. Marino
Hamid Mojibian

ABSTRACT

Inferior vena cava (IVC) filters should be removed when no longer needed, given their association with complications such as thrombosis of the IVC and lower extremities, fracture, migration, and growth into adjacent structures. While this is generally straightforward in the setting of retrievable filters, permanent filters present more of a challenge. In fact, many operators will not attempt to do so for fear of intraprocedural complications, among them, filter fracture and fragment embolization. Despite this, leaving the filters *in situ* places patients at risk of the complications described above. Here, the authors illustrate a novel technique for retrieving permanent filters using a funneled sheath to protect against embolization.

KEYWORDS

Anticoagulant therapy, deep vein thrombosis, inferior vena cava filter, thrombolysis, venography

Inferior vena cava (IVC) filters should be removed when no longer needed, given their association with complications such as thrombosis, filter fracture, filter migration, and IVC perforation.[1] However, patients with permanent filters are at higher risk of retrieval-related complications due to the frequent need for using complex retrieval techniques.[2] The Simon Nitinol filter (Bard Medical, Murray Hill, New Providence, NJ) may be particularly difficult to remove because of its bi-level filtration design. The recently released Protrieve sheath (Inari Medical, Irvine, California) has a retractable nitinol mesh funnel designed to entrap dislodged thrombus, but it can also be used off-label to protect against embolization of other materials. It comprises a sheath with 20-Fr inner and 24-Fr outer diameters; the funnel extends from the distal end of the sheath, measures up to 33.5 mm in diameter, and faces the caval walls when fully deployed (Figure 1). Herein, we describe three cases in which the funneled sheath was used during the removal of thrombosed Simon Nitinol filters, one of which was complicated by the embolization of a filter fragment that was caught by the funnel and subsequently extracted without issue.

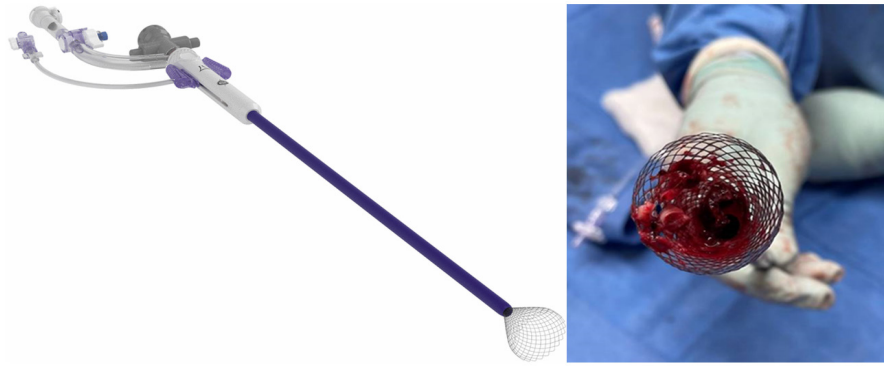

Figure 1. Photograph of the Protrieve sheath (left) and an image of the funnel containing a clot (right).

From the Department of Radiology and Biomedical Imaging, Division of Interventional Radiology (J.C-H. ✉ Joshua.cornman-homonoff@yale.edu, J.C.P.L., A.G.M., H.M.), Yale University School of Medicine, New Haven, United States.

Received 17 April 2023; revision requested 30 May 2023; accepted 12 July 2023.

Epub: 18.08.2023

Publication date: 05.09.2023

DOI: 10.4274/dir.2023.232267

You may cite this article as: Cornman-Homonoff J, Lozada JCP, Marino AG, Mojibian H. Use of a funneled sheath for embolic protection during removal of thrombosed Simon Nitinol filters. *Diagn Interv Radiol.* 2023;29(5):733-735.

Technique

Case 1

A 76-year-old woman who underwent placement of a Simon Nitinol filter nine years prior presented with one day of bilateral leg pain and swelling and was found to have acute thrombus extending from the filter into both lower extremities. Her medical history was notable for morbid obesity, diabetes mellitus type 2 on insulin, and osteoarthritis post bilateral total knee replacements; she was ambulatory with the assistance of a walker. The circumstances of the filter placement were not available, and the patient could provide no further history. She was started on therapeutic heparin; after three days at therapeutic levels, she had not improved so intervention was performed.

Under general anesthesia, bilateral popliteal and double right internal jugular vein accesses were obtained. The funneled sheath was introduced via one internal jugular access and a 16-Fr 45 cm sheath via the other. After deploying the funnel in the suprarenal IVC, the through-and-through wire position was established. Wire position was confirmed using intravascular ultrasound (IVUS), after which the filter was retrieved via the 16-Fr sheath with rigid endobronchial forceps. After confirming the absence of extravasation or other vascular injury, thrombectomy was performed using mechanical (Inari ClotTriever Bold) and aspiration (Inari Triever24 and Protrieve sheath) techniques. Activated clotting time was maintained at approximately 250 seconds throughout the procedure to prevent *in situ* clot formation. Wide patency was restored, and the procedure was terminated without complication. The patient's symptoms improved, and she was discharged on post-procedure day six on apixaban. As of six months later, she has not experienced a recurrence.

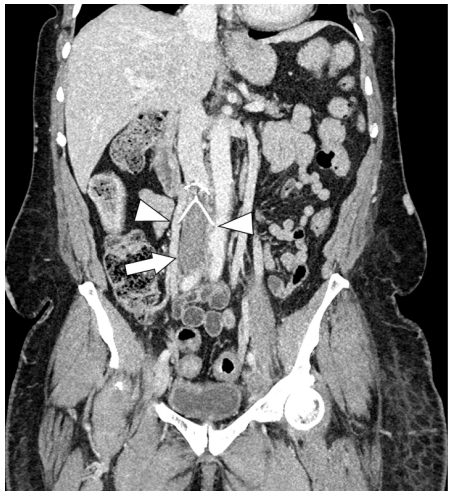

Figure 2. Coronal CT image showing thrombosis of the IVC filter (arrow). The filter extends into adjacent structures (arrowheads). CT, computed tomography; IVC, inferior vena cava.

Main points

- Removal of inferior vena cava filters, permanent or otherwise, may be accompanied by filter fracture and embolization.
- The Inari Protrieve funneled sheath was designed to protect against embolization of thrombus.
- Where there is concern that filter fracture may occur during filter retrieval, the use of the funneled sheath may be indicated to protect against fragment embolization.

Case 2

A 66-year-old woman who underwent placement of a Simon Nitinol filter 10 years prior in the setting of combined deep venous thrombosis (DVT) and pulmonary embolism resented with five days of left-greater-than-right-leg pain and swelling and was found to have acute thrombus extending from the filter into both lower extremities. She had been taking warfarin for many years but switched to rivaroxaban 10 days prior to presentation. Pre-procedural imaging showed that the filter extended beyond the caval wall into adjacent veins and the small bowel (Figure 2). After failure to improve despite two days of therapeutic heparin administration, an intervention was undertaken.

As in case 1, bilateral popliteal and double right internal jugular vein accesses were obtained; both funneled and 16-Fr sheaths were introduced, and through-and-through wire positioning was achieved with the assistance of IVUS (Figure 3). After deploying the funnel in the suprarenal IVC, rigid forceps were used to remove the filter. However, during this process, the filter fractured and one strut remained embedded in the caval wall while a second embolized into the sheath funnel (Figure 4). The former was removed with forceps while the latter was snared and removed through the funneled sheath (Figure 5). Mechanical thrombectomy was then performed as in case 1. Wide patency was restored without complication. The patient recovered uneventfully and was discharged on post-procedure day three on warfarin. As of four months later, no recurrence has occurred.

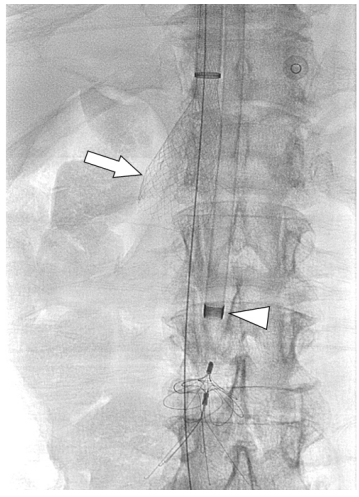

Figure 3. Fluoroscopic image showing the funneled sheath with deployed funnel (arrow) and adjacent 16-Fr sheath (arrowhead). The IVC filter is visible at the bottom of the image. IVC, inferior vena cava.

Case 3

A 56-year-old woman who underwent placement of a Simon Nitinol filter 24 years prior presented with five days of bilateral leg swelling and was found to have acute thrombus extending from the filter into the bilateral iliac veins. Medical history was notable for systemic lupus erythematosus complicated by nephritis, cerebritis, and serositis, as well as prior DVT, for which the filter was placed. Reportedly, she had never previously been on anticoagulation medication. After failure to improve following six days of therapeutic heparin administration, intervention was performed.

Bilateral common femoral, right internal jugular, and right external jugular accesses were obtained. The funneled sheath was placed in the larger internal jugular vein while an 18-Fr 40 cm sheath was placed in

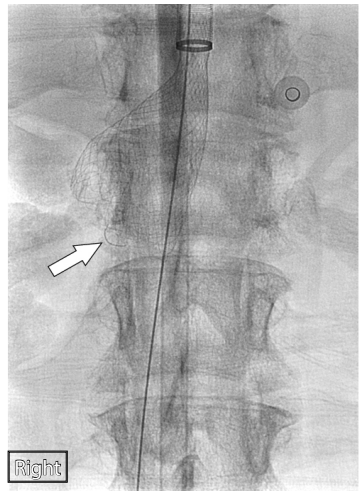

Figure 4. Fluoroscopic image showing a filter fragment (arrow) that was trapped in the funnel sheath.

the smaller external jugular vein. After the achievement of the through-and-through positioning and confirmation of the wire positioning, the filter was removed uneventfully through the 18-Fr sheath with forceps (Figure 6). Mechanical thrombectomy was then completed as in case 1 without complication. The patient's symptoms improved and she was discharged on post-procedure day four on apixaban. As of four months later, no recurrence has occurred.

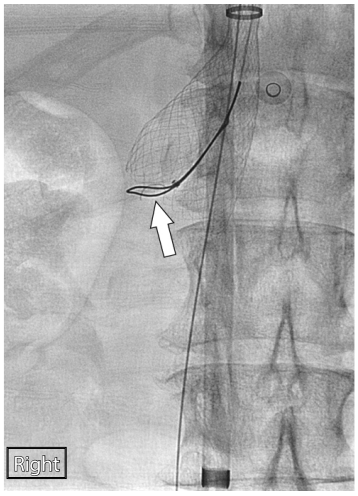

Figure 5. Fluoroscopic image showing snare removal of the filter fragment (arrow) from the sheath funnel.

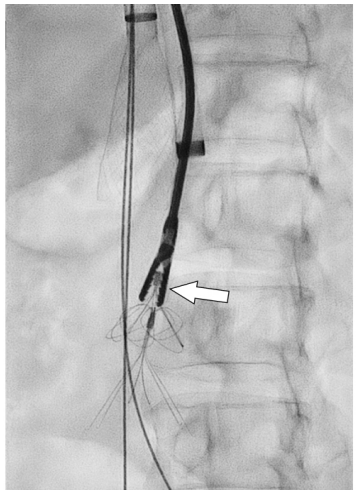

Figure 6. Fluoroscopic image showing forceps retrieval of the 24-year-old Simon Nitinol filter (arrow) through an 18-Fr sheath. The sheath funnel is visible at the top of the image.

Given its retrospective nature, patient consent was not required.

Discussion

Removal of Simon Nitinol IVC filters has only been described in small study series.[3] Although no thrombus or filter fragment embolization was reported, this remains a concern during any complex filter retrieval. Given these risks, the appropriateness of retrieval may be questioned. However, the availability of the Protrieve device potentially tips the balance in favor of removal. In the present series, no patient had a contraindication to anticoagulation medication (on which they continued following the procedure) such that the filters were no longer needed. Despite this, they were left in place given the risk associated with removal. However, these patients had already experienced and were at risk of experiencing further complications from the presence of the filter, and the ability to use the funneled sheath reduced the risks associated with removal. Consequently, in this specific subgroup of patients, filter retrieval with embolic protection was indicated.

Considering the risks associated with removal, this funneled sheath represents a useful adjunct for the removal of Simon Nitinol and, potentially, other permanent, fractured, or severely ingrown filters. However, removal is not without limitations. Because the outer diameter of the sheath is 26-Fr, a vein large enough to accommodate it may not be available. Furthermore, because it measures a total of 50 cm in length, separate access is needed to accommodate rigid forceps, which at the authors' institution, measure 55 cm in length and are thus not long enough to exit the sheath and engage the filter. Although the authors initially placed both sheaths in the same internal jugular vein, subsequent experience has led to the preference for a single puncture of each of the ipsilateral internal and external jugular veins. In either case, the use of parallel sheaths may produce a gap between the funnel and caval wall through which filter fragments could pass. Additionally, small fragments, in particular, could theoretically traverse the holes in the funnel mesh (the holes vary in size depending on the extent of funnel expansion but at 30 mm, these measure 0.90 mm proximally, 1.34 mm in the mid portion, and 2.25 mm distally); however, the implications of the embolization of such fragments are of unclear clinical significance. Despite these limitations, the Protrieve sheath shows potential as an adjunctive device in cases of complex IVC filter retrieval and warrants further study in this role.

Conflict of interest disclosure

The authors declared no conflicts of interest.

References

1. Van Ha TG. Complications of inferior vena caval filters. *Semin Intervent Radiol*. 2006;23(2):150-155. [CrossRef]
2. Tamrazi A, Wadhwa V, Holly B, et al. Percutaneous retrieval of permanent inferior vena cava filters. *Cardiovasc Intervent Radiol*. 2016;39(4):538-546. [CrossRef]
3. Bundy JJ, Chick JFB, Srinivasa RN, et al. Retrieval of Bard Simon Nitinol inferior vena cava filters: approaches, technical successes, complications, and clinical outcomes. *Phlebology*. 2021;36(7):555-561. [CrossRef]